UNIVERSITY OF SOUTHAMPTON

FACULTY OF NATURAL AND ENVIRONMENTAL SCIENCES

Ocean and Earth Science

Using the boron isotope-pH proxy to investigate CO_2 driven retreats of the Antarctic Ice Sheet in the geological past.

by

Rosanna Greenop

Thesis for the degree of Doctor of Philosophy

December 2014

UNIVERSITY OF SOUTHAMPTON

ABSTRACT

FACULTY OF NATURAL AND ENVIRONMENTAL SCIENCES

Ocean and Earth Science

Thesis for the degree of Doctor of Philosophy

USING THE BORON ISOTOPE PROXY TO INVESTIGATE CO_2 DRIVEN RETREATS OF THE ANTARCTIC ICE SHEET IN THE GEOLOGICAL PAST

Rosanna Greenop

Understanding the relationship between atmospheric CO_2 levels and ice sheet stability is of great importance given the anthropogenic emissions of CO_2 over the past 250 yrs. Since the inception of a permanent Antarctic ice sheet at the Eocene-Oligocene transition, fluctuations in global temperature and ice volume are reconstructed to have taken place in the absence of large changes in atmospheric CO_2. However, the output from ice sheet modelling experiments suggest that once large ice sheets have grown on East Antarctica they are inherently stable as a result of a powerful hysteresis effect and consequently higher levels of CO_2 are needed in order to initiate deglaciation. To further investigate this paradox, boron isotope ($\delta^{11}B$) records have here been used to reconstruct CO_2 across two intervals of the Miocene- the middle Miocene climatic optimum (MCO) and the Mi-1 glaciation- both of which coincide with major deglaciation events. In order to calculate CO_2 from $\delta^{11}B$ a number of additional parameters are needed. Here, changes in the boron isotope composition of seawater ($\delta^{11}B_{sw}$) and the life habit of the planktic foraminifera *Globigerina bulloides* (*G. bulloides*) have been investigated through time.

The most useful species of foraminifera for generating $\delta^{11}B$ records across the Mi-1 glaciation is *G. bulloides*, however, its life habit may have been different from the modern. The life habit of *G. bulloides* is investigated using carbon and oxygen isotope ($\delta^{13}C$ and $\delta^{18}O$) data of different size fractions to show that, unlike the modern species, Oligocene-Miocene *G. bulloides* had symbionts. A compilation of published $\delta^{13}C$ data for the Neogene suggests that *G. bulloides* acquired its modern non-symbiotic lifestyle

in the late Miocene. Another essential constraint is the boron isotope composition of seawater. Changes in $\delta^{11}B_{sw}$ through time are investigated here using the $\delta^{11}B$ and $\delta^{13}C$ compositions of planktic and benthic foraminifera. This approach suggests that $\delta^{11}B_{sw}$ was ~ 38‰ at the Oligocene-Miocene boundary before decreasing to ~37 ‰ during the middle Miocene. $\delta^{11}B_{sw}$ then increased by ~ 2.5 ‰ to modern day values (39.61‰). A comparison of this record to the isotopic composition of other major and minor ions in the ocean suggests that variations in riverine input may have been one of the key drivers of the change in $\delta^{11}B_{sw}$ between 14 Ma and the present.

Armed with this improved understanding of the proxy a new $\delta^{11}B$ record from across the Mi-1 glaciation suggests that CO_2 is low (~ 250 ppm) and invariable prior to, and across the Mi-1 glaciation event and, increases to ~ 400 ppm during the deglaciation. A new $\delta^{11}B$ record from between 15.5-17 Ma is also presented that shows CO_2 is elevated to maximum levels of ~ 500 ppm between 15.5 and 16.5 Ma but that it is also extremely variable – regularly oscillating between ~300 ppm and ~500 ppm on orbital timescales. When both of these new records are compared to ice volume and climate records it appears that a dynamic Antarctic ice sheet existed even with a relatively modest CO_2 forcing across the Miocene. Assuming the Miocene can be used as an analogue for the future, this study suggests that the Antarctic ice sheet can be surprisingly dynamic even at relatively low CO_2 (<500 ppm).

Table of Contents

List of tables

List of figures

DECLARATION OF AUTHORSHIP

I, Rosanna Greenop

declare that this thesis and the work presented in it are my own and has been generated by me as the result of my own original research.

'Using the boron isotope-pH proxy to investigate CO_2 driven retreats of the Antarctic Ice Sheet in the geological past.'

I confirm that:

1. This work was done wholly or mainly while in candidature for a research degree at this University;
2. Where any part of this thesis has previously been submitted for a degree or any other qualification at this University or any other institution, this has been clearly stated;
3. Where I have consulted the published work of others, this is always clearly attributed;
4. Where I have quoted from the work of others, the source is always given. With the exception of such quotations, this thesis is entirely my own work;
5. I have acknowledged all main sources of help;
6. Where the thesis is based on work done by myself jointly with others, I have made clear exactly what was done by others and what I have contributed myself;
7. Parts of this work have been published as:

Greenop, R., Foster, G. L., Wilson, P. A., and Lear, C. H., 2014, Middle Miocene climate instability associated with high-amplitude CO_2 variability: Paleoceanography, v. 29, no. 9, p. 2014PA002653.

Signed: .....

Date: .....

Acknowledgements

This PhD research would not have been possible without the help and support of a large number of people. Firstly I can't thank enough my supervisors Paul Wilson and Gavin Foster for all of their guidance and encouragement over the past 4 years. I would like to thank my examiners Chris Pearce and Luc Lourens for their helpful insights into the thesis. I am grateful to Carrie Lear, Sindia Sosdian and Mathis Hain, whose collaboration has greatly enhanced the research output. I have benefited from the input of two panel chairs during this PhD, Steve Bohaty and Heiko Pälike whose insight has been of great value, particularly during the drafting of the published manuscript. I would like to thank both the geochemistry and palaeoclimate/palaeoceanography research groups at NOC for valuable discussions. I would particularly like to thank Anieke Brombacher and Richard Smith for their proofreading of Chapter 3. I am grateful to the Natural Environmental Research Council for funding my PhD project.

I have been lucky to be part of a great laboratory team at NOC- my thanks go to all the B-team members past and present (Miguel Martìnez-Botì, Tom Chalk, Michael Henehan, Marcus Gutjahr, Eleni Anagnostou, Joe Stewart, Sara Fowell, Hannah Donald and Elwyn de la Vega). My particular thanks go to Tom Chalk for what has been a very successful and prosperous 'Greenchalk' partnership over the past 4 years. I am very grateful to Andy Milton, Matt Cooper and Agnes Michalik for all their help in the smooth running of the mass spectrometers and clean labs. I'd like to thank Megan Spencer for all her help in the sediment preparation lab and Richard Pearce for his help on the SEM.

This thesis would not have been possible without the steadfast support of my parents, brother and sister. Their encouragement and good humour has been a life-saver particularly in the final few months. I would like to thank Casey Nixon for his unwavering optimism and strong belief that everything was going to come together in the end. I have also been very lucky to live with some lovely people and make some great friends during my time in Southampton. In particular, I would like to thank my officemates Wendy Kordesch and Tom Chalk (again!) for all their support, tea, proofreading, cake, snacks and distractions.

Chapter 1: Thesis introduction and rationale

1.1 Introduction

The Earth's climate has undergone major changes in the Cenozoic era (past 65 million years, Myrs) with a predominant trend being one of climatic cooling and ice sheet expansion, albeit with a number of key short lived warming events. One of the most established and useful tools available to palaeoclimatologists for unravelling Earth's climate history is the oxygen isotope ratio of foraminiferal calcite, a recorder of both temperature and ice volume. The oxygen isotopic composition of benthic foraminifera shows a long-term increase through the Cenozoic, indicating a general cooling and increase in ice volume (Fig. 1-1). Notable increases in $\delta^{18}O$ (indicative of global cooling and ice sheet expansion) are seen across the Eocene-Oligocene boundary (~ 34 Ma) and the Oligocene-Miocene boundary (~ 23 Ma) (Fig. 1-1). Decreases in $\delta^{18}O$ associated with short-lived climatic optima are seen during the Eocene and mid-Miocene. Broadly coinciding with long-term Cenozoic cooling is a decrease in atmospheric CO_2 levels, from ~1000 ppm in the Eocene to 280 ppm prior to the industrial revolution, indicating a close relationship between climate and CO_2 (Fig. 1-1). In light of the anthropogenic CO_2 increase over the past 250 years, understanding the nature of this relationship is imperative for determining the long-term climatic consequences of rising CO_2 (Meehl et al., 2012; Hansen et al., 2013). The relatively low resolution of the CO_2 data published in the literature means that some major questions remain regarding the role of CO_2 in controlling ice volume and global temperature through time. This is particularly true in the Miocene where, with the exception of the mid-Miocene Climatic Optimum, much of the existing data indicate a relatively invariant CO_2 in the range 300 to 400 ppm. The overarching aim of this thesis is to determine atmospheric CO_2 levels over two key intervals during the Miocene – the middle Miocene Climatic Optimum (14.7-17 Ma) and the Oligocene-Miocene boundary (~ 23 Ma) – and evaluate the role of the greenhouse gas CO_2 in determining ice sheet and climate (in)stability.

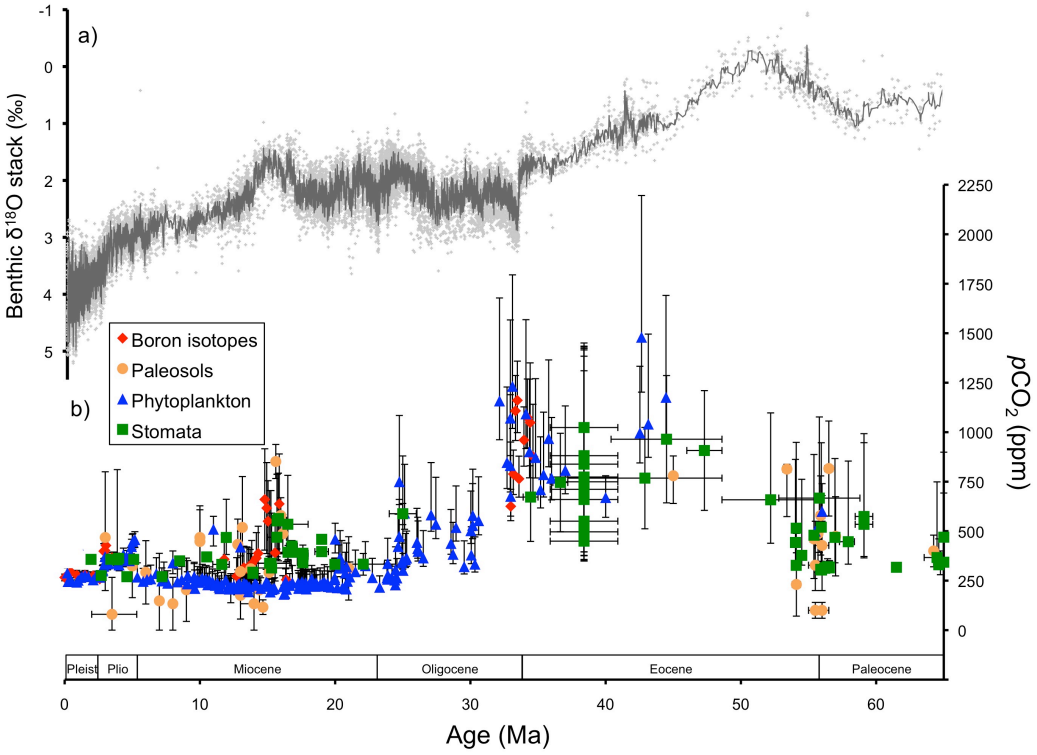

Figure 1-1: An overview of Cenozoic climate and CO_2. (a) Composite benthic $\delta^{18}O$ with 5 point moving average (Zachos et al., 2008). (b) Cenozoic CO_2 reconstructed using boron isotopes (red diamonds), paleosols, (yellow circles) phytoplankton (blue triangles) and stomata (green squares) from Beerling and Royer (2011) and references therein.

1.2 The Miocene epoch

1.2.1 Introduction

Palaeo-records show that the Miocene (5-23 Myrs) is an epoch of relative warmth and reduced ice volume compared with both the preceding late Oligocene and subsequent early Pliocene (Fig. 1-2). Warm conditions peak during the mid-Miocene Climatic Optimum between 14.7 Ma and 17 Ma, which is followed by the re-establishment of full Antarctic glacial conditions similar to those seen in the early Oligocene (and present day). Early alkenone-based records for the Miocene suggested that CO_2 levels remained low, around 200-300 ppm throughout the epoch (Pagani et al., 2005b). In contrast, new CO_2 estimates from a range of different proxies suggest that, while the early and late Miocene were associated with CO_2 in the range of 200-300 ppm, CO_2 during the climate optimum was much higher (up to 500 ppm) (Fig. 1-2) (Kürschner et al., 2008; Foster et al., 2012; Zhang et al., 2013). However, the current records are not of sufficient

resolution and the inconsistency between proxies is too large to assess the variability in CO_2 during this key interval.

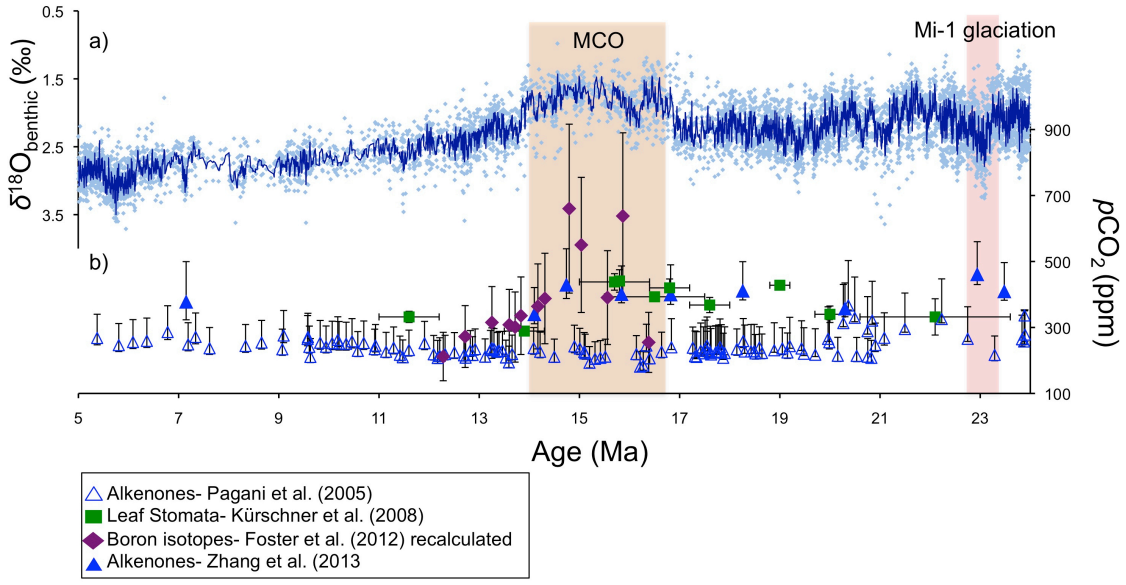

Figure 1-2: An overview of Miocene climate and CO_2. (a) Composite benthic $\delta^{18}O$ with 5 point moving average (Zachos et al., 2008). (b) Miocene CO_2 reconstructed using phytoplankton (open blue triangles) (Pagani et al., 2005b) and (closed blue triangles) (Zhang et al., 2013), leaf stomata (green circles) (Kürschner et al., 2008) and boron isotopes (purple diamonds) from Foster et al., (2012). The CO_2 data from Foster et al., (2012) has been recalculated using the original $\delta^{11}B$ derived pH and alkalinity estimated using a constant surface water omega (see Section 2.3.2.2). Orange and red bands mark the MCO and Mi-1 glaciation respectively.

1.2.2 Early Miocene glaciations

Superimposed on the long term warming and cooling trends of the early Miocene are periodic short term increases in $\delta^{18}O$ (> 0.5‰), first interpreted as glaciation events (Mi 1-7) by (Miller et al., 1987). However, while these events are identifiable in the oxygen isotope records of sediment cores from several ocean basins, the condensed nature of the earlier sequences has prevented the robust correlation of Mi- events in the newer, high-resolution records, yet the nomenclature remains in use (Miller et al., 1991; Wright et al., 1992; Billups et al., 2002; Liebrand et al., 2011). The largest and first of the glaciations that punctuate the early Miocene (Mi-1) coincides with the Oligocene-Miocene boundary (Fig. 1-3). The boundary is identified in sedimentological records by the biostatrigraphic marker *Sphenolithus delphix (Shackleton et al., 2000)*. The Mi-1 glaciation is evident in the oxygen isotope record as a transient, two-step positive excursion in benthic $\delta^{18}O$. Typically the magnitude of this change has been estimated at

approximately 1‰ (Miller et al., 1991; Paul et al., 2000; Pälike et al., 2006a; Pälike et al., 2006b; Liebrand et al., 2011), representing an ice volume change of approximately 50 m sea level equivalent (s.l.e.) and bottom water-cooling of approximately 2ºC (Mawbey and Lear, 2013) (Fig. 1-3). However, a recent re-evaluation of stacked benthic $\delta^{18}O$ records argues that the excursion was smaller (~ 0.6 ‰) and that previous work had placed too much emphasis on the extremes in the interpretation of the individual records (Mudelsee et al., 2014). The Mi-1 glaciation is coincident with an orbital configuration that favours ice sheet expansion suggesting that orbital forcing is an important factor in determining the timing of the event. In particular, the glaciation occurs when obliquity variability is muted, as a result of the 1.2 Myr modulation of the Earth's orbit and axial tilt (node of obliquity), as well as reduced amplitude eccentricity (400 kyr long eccentricity cycle), both of which reduce seasonal extremes and therefore favour ice sheet stability and growth (cool summers) (Zachos et al., 2001b; Pälike et al., 2006a). However, the occurrence of a node in obliquity with low amplitude eccentricity is not unique to the Oligocene-Miocene boundary and consequently other factor(s) are required in order to explain the timing of the climate perturbation (see Chapter 6).

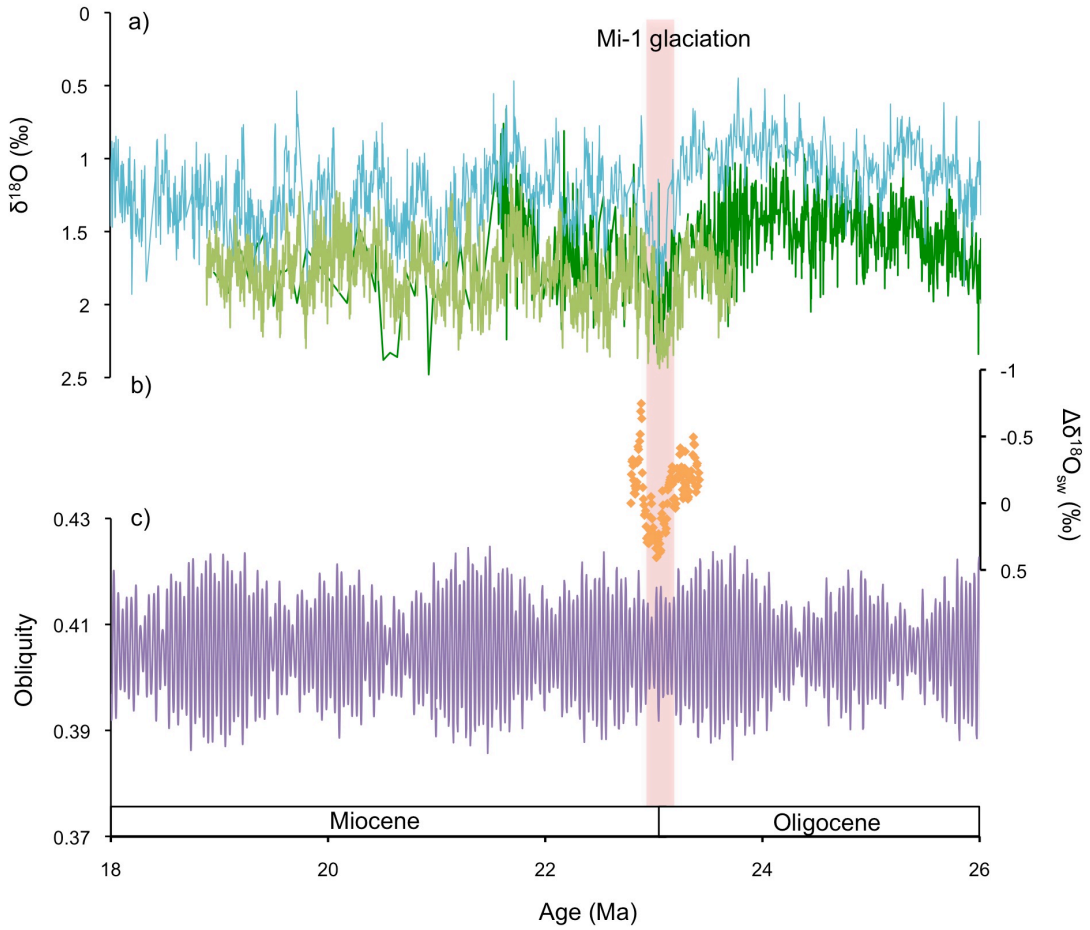

Figure 1-3: Climate and forcing over the Oligocene-Miocene boundary. (a) Oxygen isotope records from Site 926 (blue) (Pälike et al., 2006a), Site 1264 (light green) (Liebrand et al., 2011) and Site 1218 (dark green) (Pälike et al., 2006b) and references therein. (b) Oxygen isotope composition of seawater record from Mawbey and Lear, (2013). Note relative changes are plotted where $\delta^{18}O_{sw}$ at 22.79 Ma is set to zero. (c) Obliquity orbital forcing from Laskar et al., (2004). The Oligocene-Miocene boundary is highlighted in red.

1.2.3 Middle Miocene climate

Two major climatic events characterise the Middle Miocene: the middle Miocene climatic optimum (MCO) and the middle Miocene climatic transition (MMCT). The MCO, between 14.7 Ma and 17 Ma, is a sustained interval of warmer temperatures and reduced ice volume and the MMCT is marked by a 1‰ increase in the oxygen isotope record (Fig. 1-4) interpreted as an interval of major cooling and cryosphere expansion (Flower and Kennett, 1994; Shevenell et al., 2004; Holbourn et al., 2005; Holbourn et al., 2014). Large changes are also seen in the carbon isotope record across the Middle Miocene. A long-lived broad excursion to higher $\delta^{13}C$, known as the Monterey Carbon Excursion, occurs between 13 Ma and 17.5 Ma (Woodruff and Savin, 1991). Superimposed upon this excursion are several short-lived positive $\delta^{13}C$ events,

interpreted to be associated with organic matter burial (CM 1-6; Fig. 1-4). The largest of these events CM 6 coincides with the MMCT and appears to coincide with a decrease in CO_2 (Badger et al., 2013) (Fig. 1-5).

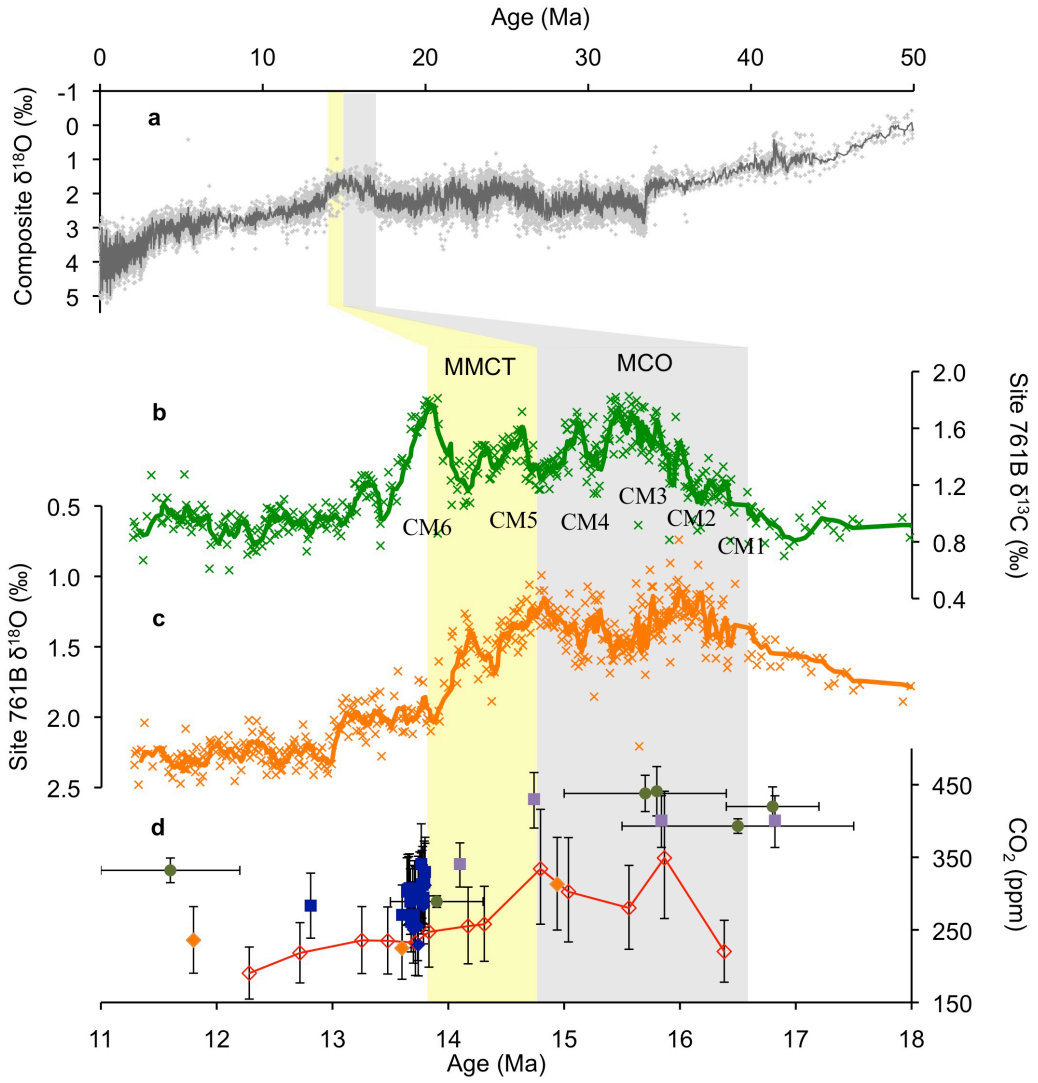

Figure 1-4: Climate and CO_2 across the middle Miocene. (a) Cenozoic oxygen isotope composite (Zachos et al., 2008). (b) $\delta^{13}C$ record from Site 761 (Holbourn et al., 2004; Lear et al., 2010). (c) $\delta^{18}O$ record from Site 761 (Holbourn et al., 2004; Lear et al., 2010). (d) Middle Miocene pCO_2 from (Foster et al., 2012) (red open diamonds); (Badger et al., 2013) (dark blue diamonds/dark blue squares); (Kürschner et al., 2008) (dark green circles) and (Zhang et *al.* 2013) (purple square).

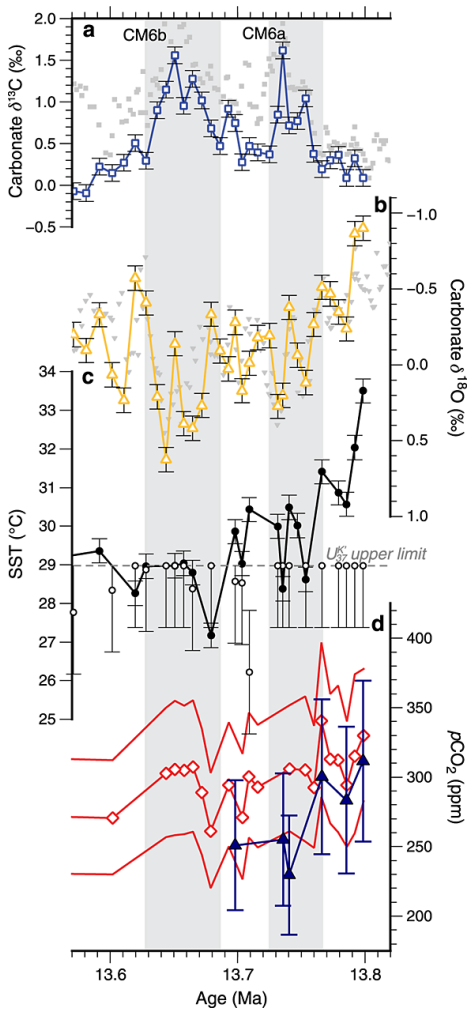

Figure 1-5: Isotope, temperature and CO_2 records across CM6 from the Ras il-Pellegrin section from Badger et al., (2013). a) $\delta^{13}C$ from fine fraction. b) Bulk carbonate $\delta^{18}O$ c) SSTs from *G. trilobus* Mg/Ca (filled black circles) and alkenone unsaturation index (open black circles) (d) atmospheric CO_2 reconstructions from alkenones isotopes (red diamonds with red lines ± 2σ) and from boron isotopes (blue triangles with error bars showing the propagated analytical uncertainty). Grey bars indicate the two carbon maxima peaks of CM6.

The peak of the MCO is characterized by minimum benthic oxygen isotope values of approximately 1‰ (Holbourn et al., 2007; Zachos et al., 2008; Holbourn et al., 2014). Temperature estimates from a range of proxies show that mean temperatures are approximately 6ºC warmer during the MCO than present (Herold et al., 2011 and references therein). Palynological data from the ANDRILL AND-2A sediment core suggests that Antarctic land temperatures reached 10ºC and sea surface temperatures ranged from 0-11.5ºC during the MCO (Warny et al., 2009). The abundance of freshwater palynomorphs combined with evidence of large bedrock channels and scoured terrains suggest that episodic large subglacial floods occurred during the MCO as a result of Antarctic ice sheet instability (Lewis et al., 2006; Warny et al., 2009). Two

discrete intervals of enhanced warming have been identified from counts of freshwater algae and low salinity dinoflagellates at 15.7 Ma and 16.4 Ma (Feakins et al., 2012). The warm intervals are also present in the sedimentary facies analysis (Fig 1-6) and are interpreted as showing intervals of reduced ice volume and increased temperatures (Passchier et al., 2011).

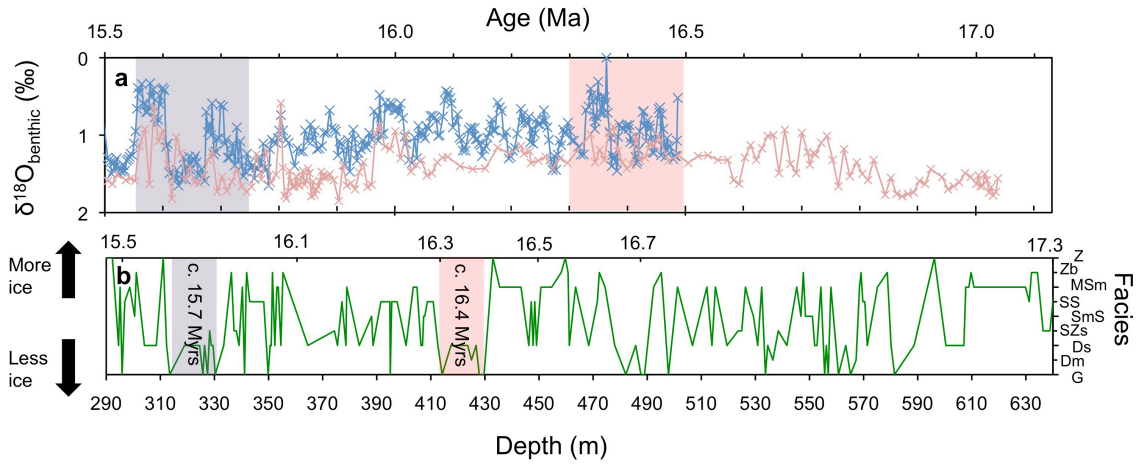

Figure 1-6: MCO ice volume variations. a) Benthic $\delta^{18}O$ record at ODP Site 1146 and ODP Site 1237 (Holbourn et al., 2007). b) Sedimentary facies data from AND-2A core (Passchier et al., 2011) where Z = diatomaceous siltstone, Zb = siltstone, MSm = muddy siltstone, Ss = sandstone, SMs = sandstone/mudstone, SZs = sandstone/siltstone, Ds = diamictite, Dm = Diamictite, G = Conglomaterate/sandstone (for data and full facies description and interpretation see Passchier et al., (2011).

There are now several studies that show the MCO was broadly associated with the highest CO_2 levels of the Miocene (Fig. 1-2) (Kürschner et al., 2008; Foster et al., 2012; Zhang et al., 2013). A possible source of the atmospheric CO_2 is volcanic outgassing of the Columbia River flood basalts. Estimates of the eruption date of the Columbia River Basalt group vary between 16.1-15.0 Ma, which coincides with the peak of the MCO (Hooper et al., 2002). Biogeochemical modeling has shown that the CO_2 associated with 'cryptic degassing' of intruded and crust-contaminated magma is sufficiently large to explain the $\delta^{13}C$ and atmospheric CO_2 change during the core of the Miocene Climatic Optimum, however, additional mechanisms are needed to explain the observed warmth before 16.3 Ma and changes in the calcite compensation depth after ~15.4 Ma (Armstrong McKay et al., 2014).

Following the warmer conditions of the MCO, the MMCT is recorded as an increase of 1‰ in the benthic oxygen isotope record between 14 and 12.5 Ma, interpreted as an

interval of major cooling and cryosphere expansion (Flower and Kennett, 1994; Shevenell et al., 2004; Holbourn et al., 2005; Holbourn et al., 2014). However, the results from numerical modeling studies suggests that the Antarctic land mass has limited capacity for further expansion after the inception of ice on Antarctica at the Oligocene-Eocene (E-O) boundary (Wilson et al., 2013). Consequently a second interval of significant MMCT ice accumulation following the E-O boundary is difficult to explain without a substantial melting event in the interim. Compelling evidence does exist, however, for a change in the thermal regime (determined by the temperature of the ice) on Antarctica at the MMCT. Palaeo glacial till deposits from the western Olympus Range, Antarctica show a permanent shift at around ~13.9 Myrs ago from classic wet-based till to stacked cold-based glacier tills suggesting that the ice sheet was less susceptible to deformation and movement after the MMCT (Lewis et al., 2007).

Evidence from boron isotope, stomatal density and revised alkenone CO_2 records shows that the increase in the benthic oxygen isotope record approximately coincides with a decline in pCO_2 (Fig. 1-7)(Kürschner et al., 2008; Foster et al., 2012; Zhang et al., 2013). Evidence for the removal of carbon from the ocean-atmosphere system is also present in benthic foraminifera trace element ratio records that show bottom water carbonate saturation states increases (Fig. 1-7) at the MMCT as atmospheric CO_2 is declining (Lear et al., 2010; Kender et al., 2014).

While there is a good understanding of the coupling between climate, ice sheet evolution and CO_2 on longer timescales during the Miocene, less is known about the controls of short-term, transient events. This short-term variability is evident both in the benthic oxygen isotope records (Pälike et al., 2006a; Holbourn et al., 2007; Liebrand et al., 2011; Holbourn et al., 2014) and within sediment cores taken from the Antarctic continental shelf margins, which suggest that Antarctic ice volume has varied on orbital timescales during the Miocene (Naish et al., 2001; Passchier et al., 2011; Passchier et al., 2013). Currently the resolution of the CO_2 records is too crude, and the discrepancies among different proxies are currently too large to provide an insight into the possible role of CO_2 in amplifying shorter-term climate variability both across the MCO and the Mi-1 glaciation.

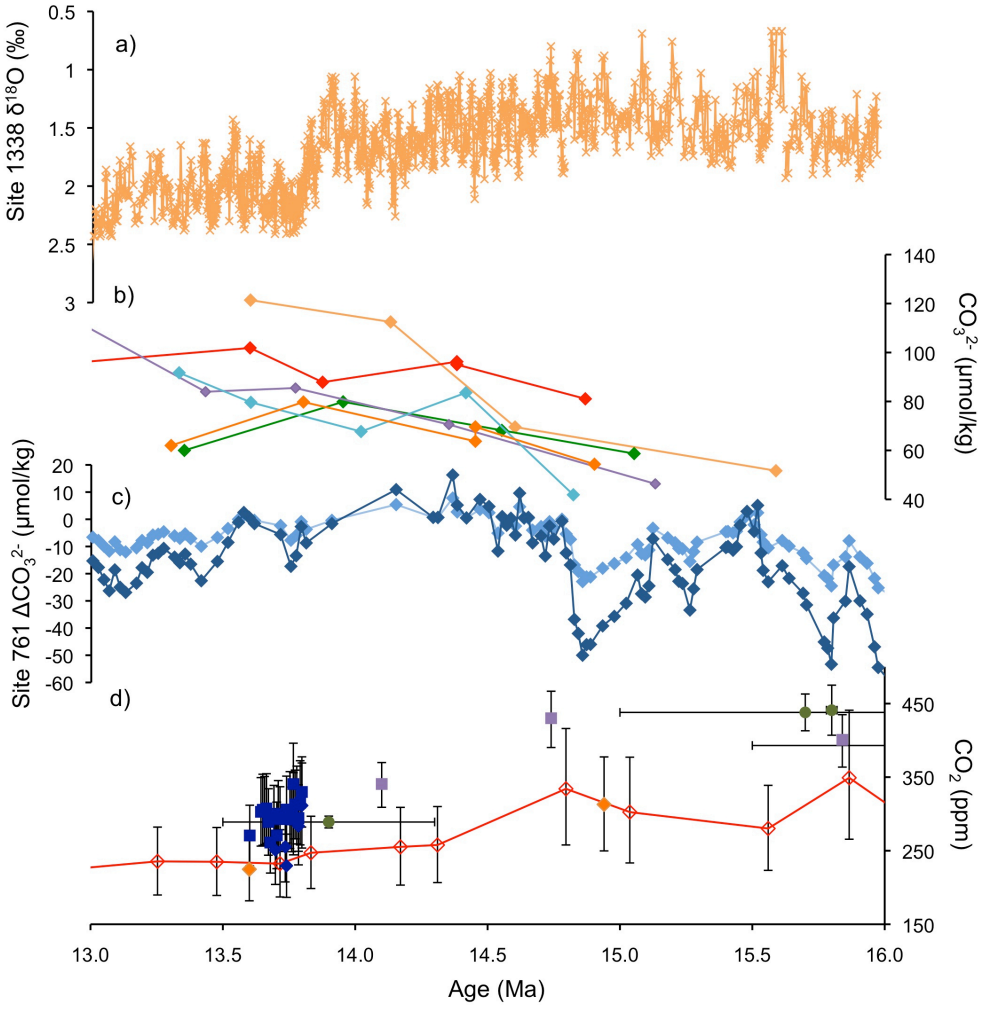

Figure 1-7: Ocean and atmosphere carbonate system changes over MMCT. a) Benthic $\delta^{18}O$ record at ODP Site 1338 (Holbourn et al., 2014). b) Carbonate ion concentration reconstructions at Site 1266 (dark blue), Site 1264 (red), Site 1171 (green), Site 1168 (light blue), Site 1237 (purple), Site 1236 (orange) c) Changes in carbonate ion at Site 761 relative to 16.975 Ma where $[CO_3^{2-}] = 0$ µmol/kg. Dark blue is reconstructed using bottom water temperatures where the record has been adjusted for the carbonate ion effect on Mg/Ca and light blue is reconstructed using bottom water temperatures without a carbonate ion correction (Lear et al., 2010). (d) Middle Miocene pCO_2 from Foster et al., (2012) (red open diamonds); Badger et al., (2013) (dark blue diamonds/dark blue squares); Kurschner et al., (2008) (dark green circles) and Zhang et *al*. (2013) (purple square).

1.3 Ice volume proxies

1.3.1 Introduction

No direct method of measuring palaeo-ice volume exists but several proxies have been used to either independently assess the temperature and ice volume components of the

benthic $\delta^{18}O$ signal or to determine ice volume fluctuations from the physical properties of continental margin sediment cores. The methods most commonly used to assess long-term ice volume changes include coupled Mg/Ca-derived temperature and $\delta^{18}O$ records, analysing the sediments from ice-proximal ocean drilling expeditions, numerical modelling and sequence stratigraphy of continental margin records (Fig. 1-8).

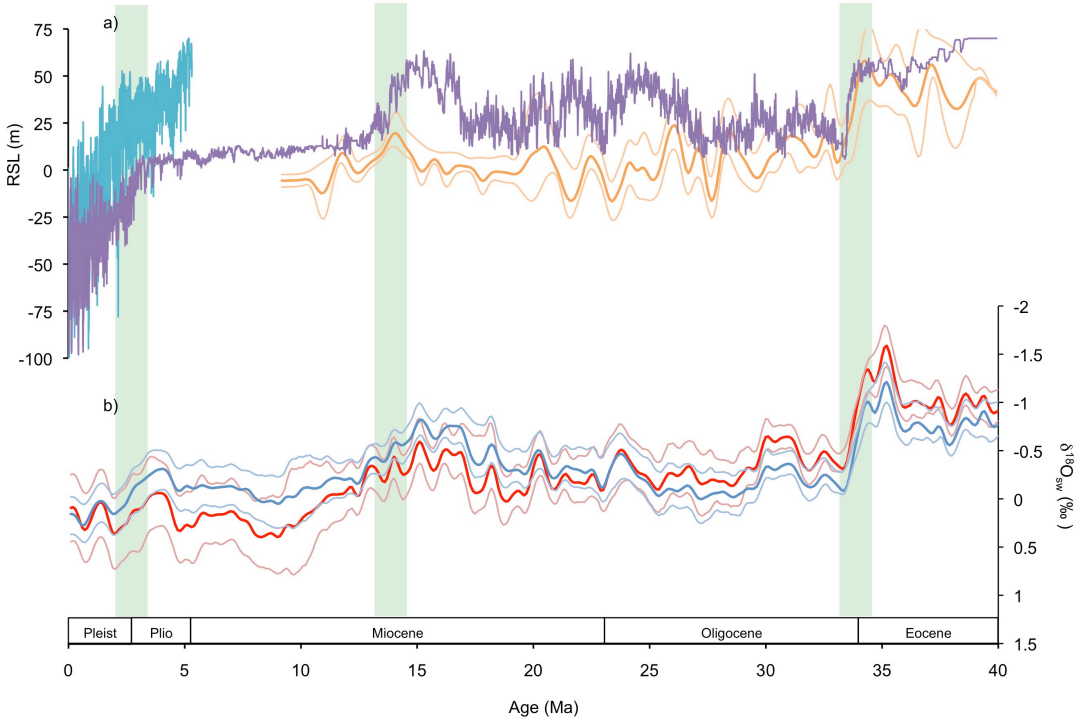

Figure 1-8: Summary of relative sea level variations over the past 40 Ma. a) The reconstructions based on backstripping of the New Jersey Margin and $\delta^{18}O_{benthic}$ are shown in orange (note the records are smoothed to show only variations on >5 Myr timescales) (Cramer et al., 2011), from inverse modelling in purple (De Boer et al., 2010) and the Mediterranean relative sea level record from Rohling et al., (2014) in light blue. b) Reconstructions based on $Mg/Ca_{benthic}$ and $\delta^{18}O_{benthic}$ calculated by Cramer et al., (2011) using the *O. umbonatus* calibration from Lear et al., (2010) are shown in red and using the *O. umbonatus* calibration from Rathmann et al., (2004) in blue. Note the $\delta^{18}O_{sw}$ records are smoothed to show only variations on timescales of >5 Myr. Green bars indicate major intervals of ice growth.

1.3.2 The use of Mg/Ca paleothermometry in estimating ice volume changes

The partition coefficient of Mg into the test of planktic and benthic foraminifera is temperature-dependent and therefore with the application of an appropriate calibration, temperature can be determined (Rosenthal et al., 1997). There are several issues, however, with the utility of the Mg/Ca temperature proxy in benthic foraminifera.

Firstly, the limitations of the analytical technique (e.g. 1σ 0.08–0.02 mmol/mol) can mean it is difficult to resolve small changes in temperature (Sadekov et al., 2014). For instance, the combination of low temperature sensitivity (10-15%/ºC) and low Mg/Ca (~ 1 mmol/mol) in *Cibicidoides wuellerstorfi* means it is difficult to resolve temperature change on the order of 1ºC (0.1–0.15 mmol/mol differences) (Sadekov et al., 2014). In addition, over the past ten years it has been shown that, at low levels of carbonate saturation, Mg/Ca in benthic foraminifera also apparently responds to changes in bottom water carbonate ion concentration (Elderfield et al., 2006). Consequently a re-evaluation of some of the earlier palaeo-ice volume records created using this method is needed (Lear et al., 2000). One way to correct for the effect is to use a carbonate ion proxy such as Li/Ca, however, uncertainties remain regarding the species-specific sensitivities and thresholds to both temperature and saturation state (Lear et al., 2010). A global compilation of Mg/Ca measurements with corrections made for species, carbonate ion effect and the Mg/Ca ratio of seawater (Mg/Ca_{sw}) confirms the results of earlier studies that there were three major periods of ice accumulation during the Cenozoic: 1) across the Eocene-Oligocene boundary (2) the mid-Miocene climatic transition and (3) the Pliocene-Pleistocene boundary (Cramer et al., 2011) (Fig. 1-8). The Mg/Ca of planktic foraminifera also confirms that the Eocene-Oligocene boundary is associated with the emplacement of an Antarctic ice sheet with a size approximately equivalent to the modern-day (Lear et al., 2008; Bohaty et al., 2012).

1.3.3 Ice sheet proximal sediment cores

Sediment cores taken from the Antarctic continental shelf margins have yielded sedimentological evidence for changes in Antarctic climate and ice sheet dynamics. Ice sheet advance and retreat results in the deposition of distinctive sedimentary sequences (Naish et al., 2001), however, the extent to which inferred ice sheet variability from one site can be applied across the whole ice sheet is unknown. Since the early 1980s, the McMurdo Sound area of the Ross ice sheet has been the focus of several projects aiming to drill the sediments below the ice sheet. This part of the Antarctic ice sheet is fed by both the East Antarctic Ice Sheet (EAIS) and West Antarctic Ice Sheet (WAIS) outlet glaciers (Naish et al., 2008). Today, the two ice sheets on Antarctica have different configurations and susceptibilities to melting. The WAIS is grounded below sea level and stabilised by ice shelves around the perimeter, whereas, the EAIS is

stabilised by key bedrock pinpoints above sea level although some overdeepened basins exist (Fig. 1-9). Assuming the record of ice sheet dynamics from one site is representative of general conditions across the ice sheet, this technique may give some insight into Antarctic ice sheet extent. However, evaluating changes in the volume or configuration of the two different ice sheets, which may be reacting differently to a given climatic event, is more difficult. Provenance determination on clasts from the ice margin drill cores, however, may prove a useful method for disentangling the signal from the two ice sheets (Bart, 2003; Chow and Bart, 2003; Talarico and Sandroni, 2009).

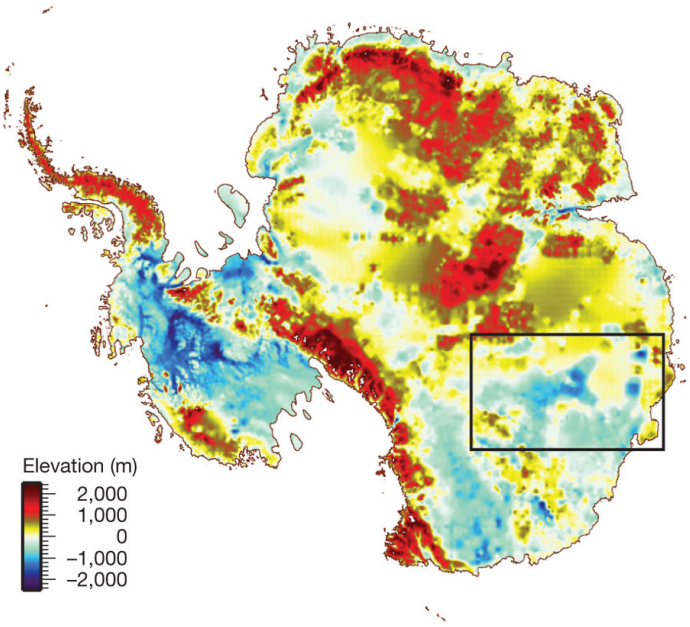

Figure 1-9: Antarctic be topography from Young et al., (2011). The blue areas represent Antarctica's major marine subglacial basins. The box highlights the Aurora subglacial basin.

While cyclic changes in ice sheet growth and retreat are evident in the results from earlier drilling projects such as CIROS-1 and McMurdo Sound Sediment and Tectonic Studies Project (MSSTS-1) (Ehrmann, 1998), the better recovery rates from more recent drilling programs has provided sediments that can be dated and correlated with events in the deep sea sediment records (Barrett, 2008). The Cape Roberts project (CRP) recovered expanded sedimentary sections that provided material for a high-resolution study of orbitally forced fluctuations in the Antarctic ice sheet between 34-17 Ma (Naish et al., 2001; Barrett, 2007). Results confirm evidence from stacked benthic

oxygen isotope record that the Oligocene Antarctic ice sheet is dynamic at orbital timescales (Naish et al., 2001). The Antarctic Drilling Project (ANDRILL) followed the CRP project in 2006-2007 and recovered sediments that span the majority of the Neogene (Barrett, 2008). Preliminary investigations highlight evidence of a colder polar climate dominated by grounding ice across the site in the late Miocene and Pleistocene (Fig. 1-10), warmer conditions and intervals of ice sheet retreat during the MCO (Fig. 1-6) with warmer climates with extended ice free conditions during the Pliocene (Naish et al., 2008; Fielding et al., 2011; Passchier et al., 2011).

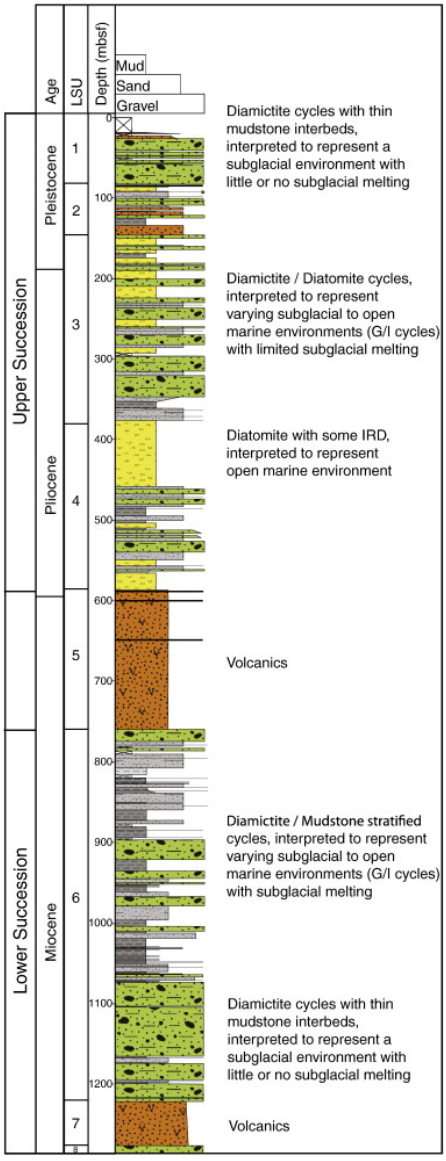

Figure 1-10: Lithostratigraphy of the AND-1B drill core with interpretation of the sedimentary facies (Wilson et al., 2012b).

1.3.4 Sequence stratigraphy

Sequence stratigraphy is a method that determines sea level change from a stratigraphic record, typically a passive continental margin sequence. The two factors that primarily determine the architecture of the depositional sequence are changes in relative sea level and changes in the rate of sediment supply. The inverse technique progressively removes the effects of compaction, loading, and thermal subsidence on the sedimentary record and therefore provides a means of estimating global sea-level (eustasy) changes (Steckler et al., 1988). Independent records of eustasy are obtained from margin stratigraphic records and then converted to apparent sea level change (ASL) by applying a correction factor based on mantle and seawater densities (Kominz and Pekar, 2001). This conversion is necessary because eustasy is the change in sea level with respect to a reference frame that is fixed relative to the centre of the Earth whereas ASL is the observed changes in water depth and includes the crustal loading and unloading that occurs as the volume of water changes.

The use of margin stratigraphic records is hindered by the ice mass self- gravitational effect. The change in mass caused by rapid melting or accumulation of the ice sheet will be accompanied by a deviation from eustatic sea level as a consequence of the corresponding change in gravitational attraction (Woodward, 1888; Farrell and Clark, 1976). For example, when an ice mass accumulates the volume of water attracted to the ice sheet by the gravitational force will increase. The effect of the increased attraction of water to the ice sheet is a local sea level increase when the average sea level is decreasing (Stocchi et al., 2013). The influence of this effect can be far reaching; calculations for a complete melting of the WAIS show sea level will fall within 2000 km of Antarctica, while other far field sites show a sea level rise above the eustatic level (Mitrovica et al., 2009). Consequently, the results of margin stratigraphic records have to be interpreted carefully as self-gravitation affects both the Northern and Southern Hemisphere ice sheets, and consequently very few sites around the world show true eustatic sea level. In addition to the self gravitation effect corrections are also needed to account for shoreline migration, including the inundation and adjustment of regions vacated by grounded, marine-based ice cover, feedbacks on the rotation of the Earth and elastic deformation of the solid Earth (Mitrovica et al., 2009; Conrad, 2013). A Cenozoic compilation of sea level estimates from sequence stratigraphy suggest that sea

level was ~ 50m higher than present prior to the Eocene-Oligocene boundary, before falling to sea levels comparable to the modern for the Oligocene and early Miocene (Fig. 1-8) (Cramer et al., 2011).

1.3.5 Modelling the $\delta^{18}O$ record

Several different models exist that use numerical modelling to decouple the temperature and ice volume components of the benthic oxygen isotope record. The inverse modelling technique derives sea level and temperature using an axisymmetrical one-dimensional (1-D) ice-sheet model that simulates glaciations on both hemispheres using the benthic oxygen isotope record as model forcing (De Boer et al., 2010). This method is based on the assumption that both ice volume and deep-water temperatures are closely related to the mid-latitude-to-subpolar northern hemisphere (NH) temperature. An alternative approach, based on a continuity model, similarly uses a basic ice sheet model to determine the temperature and ice volume components of the benthic oxygen isotope record and is based on the assumption that Antarctic temperature varies in proportion to the deep-sea temperature (Oerlemans, 2004). A comparison of the output from the inverse modelling technique and the continuity model show similar results, however, the deep-water temperatures calculated by the inverse modelling method are 1-2ºC lower during the Oligocene and mid- to late Miocene (De Boer et al., 2010). This offset is attributed to differences in the shape of the ice sheet in the model, which determines how the ice sheet mass balance is maintained and serves as the coupling between temperature and ice volume (De Boer et al., 2010). Sea level reconstructions using this method suggest that Antarctic ice volume was variable (between 0 and 40 m above modern) during the Oligocene and early Miocene before increasing to 60 m above present day during the MCO. Sea level then remained invariant (around the same level as modern day) before decreasing during the late Pliocene/Pleistocene (Fig. 1-8) (De Boer et al., 2010)

An alternative method of combining $\delta^{18}O$ with a modeling approach using planktic $\delta^{18}O$ and a hydraulic control model to determine the sea level controlled variations of seawater input into a semi-restricted basin (Siddall et al., 2003). Sea-level lowering reduces the exchange of water between the semi-restricted basin and open ocean which increases the residence time of water in the basin, causing strong increases in salinity and the $\delta^{18}O$ of basin waters (recorded in the $\delta^{18}O$ of planktic foraminifera) (Siddall et

al., 2003; Rohling et al., 2014). If the rate of water exchange can be characterised and the salinity and $\delta^{18}O$ values are dominated by sea level then the $\delta^{18}O$ of planktic foraminifera can be used to infer sea level changes (Siddall et al., 2003). This approach has been applied to the Red Sea over the past 500 kyrs to show that a strong correlation exists on multi-millennial timescales between global sea level and Antarctic temperature (Rohling et al., 2009). The Mediterranean basin has more recently been used to reconstruct a sea level record over the past 5.3 million years and suggests that in keeping with previous estimates (Miller et al., 2012) sea level was ~10-30 m above present day between 3.3 and 2.9 Myr (Rohling et al., 2014). In addition the study also suggests that sea level may have been as high as 50 m above present day during the early Pliocene (Fig. 1-8) (Rohling et al., 2014).

1.3.6 Implications for Miocene ice volume change

Although some differences exist in the absolute estimations of sea level change during the Miocene, all the sea level proxy records suggest the existence of dynamic ice sheets during the early and middle Miocene. The inverse modelling sea level estimates and $\delta^{18}O_{sw}$ record both suggest that sea level is higher during the Miocene climatic optimum although this rise is not present in the sequence stratigraphy record (Fig. 1-8). Aside from the Mediterranean sea level record (Rohling et al., 2014), which suggests that late Pliocene sea level was similar to the Miocene climatic optimum, the other proxy records suggest that the Miocene climatic optimum was the last interval where sea level was >20m. Consequently understanding the relationship between sea level and CO_2 during this interval is of great importance.

1.4 CO_2 proxies

1.4.1 Introduction

Several techniques have been used to reconstruct the history of CO_2. The $\delta^{13}C$ of alkenone biomarkers, the $\delta^{13}C$ of pedogenic carbonates, the stomatal density of fossilised leaves and the $\delta^{11}B$ composition of biogenic carbonates are the most commonly used techniques to reconstruct Cenozoic pCO_2 and will be discussed here in turn.

1.4.2 The $\delta^{13}C$ of pedogenic carbonates

Soil carbonates form under arid to sub-humid climate and, under certain conditions, the $\delta^{13}C$ composition of the carbonate can be used as a proxy for CO_2 (Cerling, 1991). Prior to the evolution of C4 plants, during the late Miocene, the $\delta^{13}C$ of pedogenic carbonate most likely reflected CO_2 in the atmosphere and CO_2 produced in the soil by plant respiration and microbial activity (Cerling, 1991). This relationship breaks down after the late Miocene as C4 plants have a distinctive $\delta^{13}C$ signature that can complicate the interpretation of the $\delta^{13}C$ signal. To determine atmospheric CO_2 assumptions are made regarding soil temperature, pressure, characteristic CO_2 production depth, soil respiration depth and the $\delta^{13}C$ of atmospheric CO_2 (Bowen and Beerling, 2004). $\delta^{13}C$ of pedogenic carbonates is particularly useful at CO_2 levels > 1500 ppm and can also be used over a larger temporal range than the other available proxies. This proxy is impractical for estimating CO_2 levels during the Neogene, however, because the uncertainties are large at low CO_2 levels. In addition, the slow precipitation rate of the carbonate reduces the temporal resolution of the proxy (Royer et al., 2001). Cenozoic CO_2 level estimates determined using this proxy suggest that CO_2 remained between 500 and 1000 ppm during the Eocene and were around 500-800 ppm during the MCO (Beerling and Royer, 2011 and references therein).

1.4.3 Stomatal densities and CO_2 estimates

The stomatal density of fossilised plants has also been used for CO_2 reconstructions. The abundance of stomata is dependent on the need of the plant to obtain CO_2 from the atmosphere for growth versus the requirement to minimise the loss of water that occurs when the stomata are open (Woodward, 1987). The effect of drought conditions on stomatal density is accounted for in the stomatal index (Salisbury, 1928):

$$SI = \frac{SD}{SD + ED}\, x\, 100 \qquad (1.1)$$

Where SD is defined as the stomatal density and ED is the epidermal cell density (which can be used as a measure of the plant's response to drought conditions). Typically the relationship between SI and atmospheric CO_2 is determined from a calibration (or training) dataset that is then applied on the same species from the fossil

record. For atmospheric CO_2 levels greater than present day the response of SI to increasing CO_2 levels is determined experimentally, however, at CO_2 > ~500 ppm the SI response of modern genotypes show reduced sensitivity (Royer et al., 2001; Beerling and Royer, 2002). In addition, the SI-CO_2 calibration is species-specific, reducing the temporal range over which the proxy can be applied (Royer et al., 2001). Cenozoic CO_2 level estimates determined using leaf stomata suggest that CO_2 remained between 500 and 700 ppm during the Eocene before decreasing to values < 500 ppm around 25 Myrs ago (Beerling and Royer, 2011 and references therein).

1.4.4 The alkenone CO_2 proxy

In photosynthetic algae, the degree of carbon isotope fractionation during carbon fixation is dependent on the concentration of $CO_{2(aq)}$ and therefore atmospheric CO_2 (Bidigare et al., 1997). However, the $\delta^{13}C$ of bulk organic matter is also likely to be affected by the specific growth rate of the autotroph and source of the organic material. To ensure that the carbon isotope signature of organic matter primarily records carbon fractionation as a function of varying CO_2(aq), specific alkenones from haptophyte algae are used (Pagani, 2002). As the $\delta^{13}C$ of alkenones also record variations in the concentration of phosphate, cell size and temperature, corrections have to be applied to the measured $\delta^{13}C$ to account for these parameters (Bidigare et al., 1997; Pagani et al., 1999; Pagani, 2002; Henderiks and Pagani, 2007). Over the Cenozoic, alkenone CO_2 levels remained between 1000-1500 ppm during the Eocene before decreasing dramatically during the Oligocene (Fig. 1-1) and reaching modern levels during the late Oligocene (Pagani et al., 2005b).

1.4.5 The boron isotope composition of biogenic carbonates

The boron isotope composition ($\delta^{11}B$) of biogenic carbonates has also been used to calculate Cenozoic CO_2 and is the dominant method used here (see Chapter 2). One of the main advantages to this technique is the solid theoretical understanding underpinning the proxy. The current Cenozoic boron isotope records suggests that atmospheric CO_2 levels have fallen from more than 2000 ppm in the late Palaeocene/early Eocene to below 500 ppm since the early Miocene (Pearson and Palmer, 2000). Although the boron estimates for the later Cenozoic agree with the

alkenone CO_2 estimates, the values for the earlier Cenozoic are up to 500 ppm higher. However, uncertainties in the reliability of the analytical technique and uncertainties in the reconstruction of the second carbonate system parameter and the fractionation factor (Klochko et al., 2006) that are needed alongside boron isotopes to calculate pCO_2 has raised question marks over the validity of the record (see Chapter 2) (Demicco et al., 2003; Foster, 2008). A new analytical method of measuring boron isotopes has reduced some of the uncertainty in this technique, and has resulted in the reconstruction of more reliable pCO_2 at higher resolution (Foster, 2008). This new method has been used to reconstruct CO_2 levels for the mid-Pliocene climatic optimum, the mid-Miocene climatic optimum and the Eocene-Oligocene boundary (Pearson et al., 2009; Seki et al., 2010; Foster et al., 2012). This thesis aims to gain further insight into some of the key assumptions needed to calculate CO_2 from $\delta^{11}B$ and increase the resolution of $\delta^{11}B$-CO_2 records during the Miocene.

1.5 Neogene ice sheet dynamics

1.5.1 Ice Sheet Initiation

Numerical modelling experiments of the Eocene-Oligocene boundary using a global climate model (GCM) coupled to a dynamic ice-sheet model suggest that CO_2 was the primary factor controlling Southern Hemisphere glaciation (DeConto and Pollard, 2003b). In addition to CO_2, both geochemical data and modelling studies suggest that orbital forcing may have also played a role in ice sheet initiation at the Eocene-Oligocene boundary (DeConto and Pollard, 2003a; Coxall et al., 2005; Ladant et al., 2014a). In this view, declining CO_2 acts as a preconditioning factor for ice sheet growth and then ice sheets are initiated when the orbital forcing favours cool summers. Modelling results suggest that when the threshold CO_2 level for Southern Hemisphere glaciation is reached, the system flips from one quasi-stable state (small dynamic ice sheet) to full EAIS conditions very rapidly. Once initiated, strong positive feedbacks result in full ice sheet conditions developing rapidly due to snow/ice-albedo and ice-sheet height/mass-balance feedbacks (DeConto and Pollard, 2003b). Numerical modelling of the Oligocene-Eocene transition suggests that CO_2 levels need to drop below 750 ppmv for full Southern Hemisphere glaciation to be initiated, whereas CO_2 needs to decline below 280 ppm for the Northern Hemisphere to glaciate (DeConto et

al., 2008). Proxy records across the Eocene-Oligocene boundary have since shown that ice sheet inception coincided with atmospheric CO_2 levels declining to between ~450 and ~1,500 ppm, with a central estimate of ~750 ppm (Pearson et al., 2009; Pagani et al., 2011). However, it has been shown the modelled CO_2 threshold for Antarctic ice sheet inception is dependent upon the initial bedrock topography, the internal hydrology of the ice sheet and the type and configuration of the climate model (Lythe et al., 2001; Langebroek et al., 2009; Wilson and Luyendyk, 2009; Gasson et al., 2014), suggesting that it may be possible that some ice was stable on Antarctic prior to the Eocene-Oligocene boundary and/or that the threshold for Antarctic ice sheet growth may have varied through time (Fig. 1-11) .

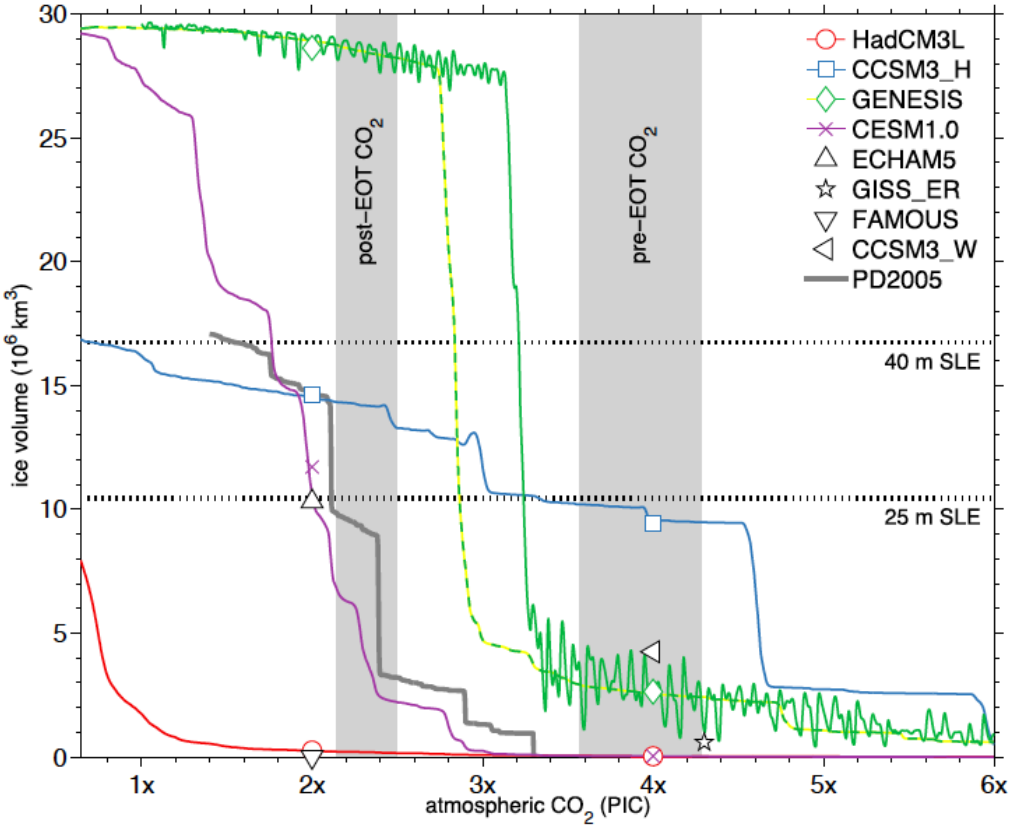

Figure 1-11: Transient CO_2 ice sheet model experiments using climate output from a range of models from Gasson et al., (2014). Horizontal dotted lines are the thresholds for an intermediate (defined here as 25 m Eocene SLE) and a large ice sheet (40 m Eocene SLE). For GENESIS, simulations are shown with (solid green) and without (yellow and green) orbital forcing. Also shown is the simulation of Pollard and DeConto (2005) (PD2005) for a reduction in CO_2 and without orbital forcing. The vertical bars are the pre- and post-EOT CO_2 estimates from Pagani et al., (2011).

1.5.2 Ice Sheet Hysteresis

The step-wise changes in the benthic oxygen isotopes that punctuate the Cenozoic suggests that ice sheet mass increases and decreases non-linearly with changing CO_2 (DeConto et al., 2008; Gasson et al., 2012; Foster and Rohling, 2013). Non-linearity exists within the ice sheet system due to the different mechanisms of ice build-up and decline. This hysteresis effect is a geometric consequence of the non-linear response of ice sheet accumulation versus ablation to the increasing elevation of the ice sheet (Weertman, 1961; Oerlemans, 1982). Geometric hysteresis is primarily found in two instances. Firstly, small ice sheets on sloping terrain are unstable below a certain size (Weertman, 1976; Pollard and DeConto, 2005). The second type of hysteresis exists only on continental ice sheets bound by the ocean. In these circumstances ice sheet inception requires the snowline to descend to the ice-free surface (Fig. 1-12). Ice will then grow over the entire surface, forming an ice sheet, with a positive mass balance, over a large areal extent. Once this threshold has been reached ice will accumulate quickly over a large area. To ablate the ice sheet the snowline must ascend significantly, to the elevation of the outer ice sheet flanks, to produce substantial melt (Pollard and DeConto, 2005). Consequently the altitude above which snow will persist through the summer (equilibrium line altitude) must rise far above the initial bedrock elevation in order to initiate ice sheet decline (Fig. 1-12).

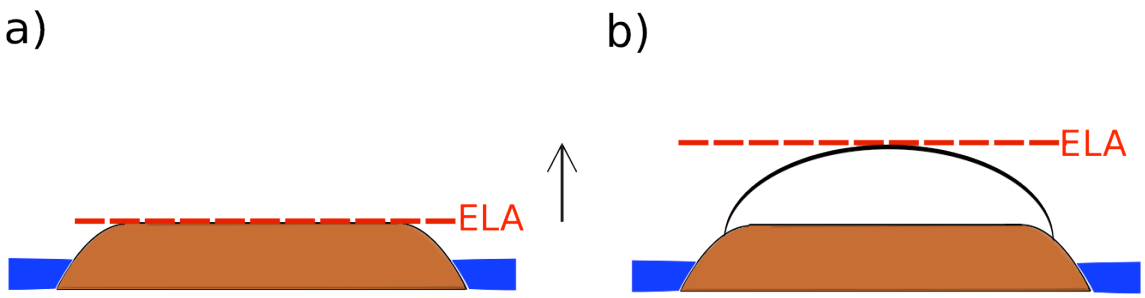

Figure 1-12: The cause of geometric ice sheet hysteresis (a) The height of the equilibrium line altitude (ELA) during ice sheet initiation. (b) The height the ELA must reach in order to initiate ice sheet ablation. The ELA elevates far above the bedrock surface to cause ice sheet decay.

While hysteresis exists during both the Northern and Southern Hemisphere glacial cycles (Pollard and DeConto, 2005; Abe-Ouchi et al., 2013), due to geographical location and Antarctic topography, it is more pronounced in the Southern Hemisphere. In particular, the sub aerial position of the EAIS, coupled with its higher overall

elevation, means it is particularly susceptible to ice sheet hysteresis (Pollard and DeConto, 2005). The predominantly submarine WAIS is more prone to melting by rising ocean temperature given subtle changes in temperature and CO_2 (Pollard and DeConto, 2009).

In order to increase atmospheric temperatures and overcome the hysteresis effect, higher CO_2 levels are needed to cause ice sheet ablation than ice sheet initiation. Coupled ice sheet-global climate model (GCM) simulations show a delay in the main transition from full ice expansion to limited ice sheet coverage when CO_2 is increased linearly from 2x to 4x pre-industrial atmospheric levels (PAL) when compared with the forward run from small to continental ice sheets (Fig. 1-13). Higher CO_2 levels must be attained to cause a change in stable state from a large to a small ice sheet because the ice sheet topography is much higher than the groundmass topography (Pollard and DeConto, 2005).

Continental wide ice sheet initiation begins at 615 ppm in an ice sheet-climate model including Miocene orbital variations, with smaller ice sheets existing between 640-700 ppm (Langebroek et al., 2009). Deglaciation occurs at 725 ppm resulting in a hysteresis window of 110 ppm (Langebroek et al., 2009). While the absolute values approximated by Pollard and DeConto, (2005) differ from the study by Langebroek et al., (2009), the size of the hysteresis window is consistent across the different models. Similar to the CO_2 threshold for ice sheet inception, the size of the hysteresis window is dependent on other parameters such as orbital variations, bed topography and vegetation-climate and ice-albedo feedbacks (Pollard and DeConto, 2005; Pollard et al., 2005; Thorn and DeConto, 2006; Gasson et al., 2012).

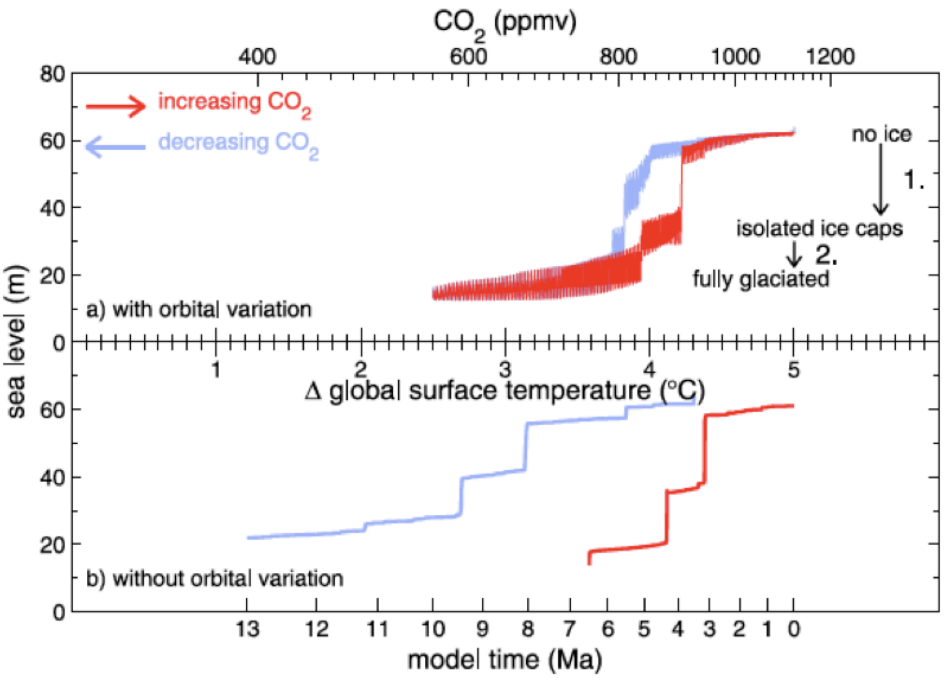

Figure 1-13: Antarctic ice volume simulations (a) Blue curve is the forward integration with ice volume increasing as CO_2 decreases from 4x to 2x PAL (pre-industrial atmospheric levels). Red curve is the reverse integration starting with a large ice sheet and increasing CO_2. (b) Same simulation as (a) without orbital parameters. From Gasson et al., (2012) using the simulations of Pollard and DeConto, (2005).

While clear differences in the nature of the East Antarctic and West Antarctic ice sheets has been evident over the past 5 million years (Pollard and DeConto, 2009), reconstructions of past Antarctic topography suggests that the elevation of West Antarctica was ~20% higher at 34 Ma, than the modern day, and the EAIS and WAIS were more similar in nature (Wilson et al., 2013). The higher elevation of West Antarctica at 34 Ma, in the new topographic reconstructions, is mainly a result of additional corrections for glacial erosion and thermal contraction in the West Antarctic rift system (Wilson and Luyendyk, 2009; Wilson et al., 2012a). A climate-ice sheet model based on the updated topographic reconstructions shows that the WAIS first formed at the Eocene-Oligocene transition, at the same time as the expansion of the EAIS (Wilson et al., 2013).

The results of coupled ice sheet-GCM models described above and reconstructed CO_2 during the late Paleogene and Neogene suggest that the Antarctic ice sheet should have remained stable since it's inception at 34 Ma. However, recent work on Antarctic ice-proximal International Ocean Drilling Program (IODP) sediment cores suggests that the

Pliocene warm period was associated with a partially dynamic EAIS (Cook et al., 2013). Analysis of detrital material deposited during the Pliocene warm period at Site U1361, located on the Wilkes Land margin, suggests that erosion of continental bedrock, caused by the retreat of the ice sheet margin by several hundreds of kilometers, occurs from within the Wilkes Subglacial Basin, an area covered by the East Antarctic ice sheet today (Cook et al., 2013). Although this retreat of the East Antarctic ice sheet is still to be replicated in coupled climate and ice sheet models, a parallel ice sheet model has simulated a similar destabilization of the Wilkes Basin ice sheet through the removal of a specific coastal ice volume that acts as a plug, and prevents accelerated discharge of the ice sheet (Mengel and Levermann, 2014).

1.6 The long term relationship between sea level and CO_2

A compilation of sea level and CO_2 proxy records over the past 34 Myrs shows a relatively consistent relationship between sea level and CO_2 irrespective of the time interval (Foster and Rohling, 2013). Between 200 and 300 ppm there is a linear relationship between sea level and CO_2, primarily as a consequence of the strong sensitivity of Northern Hemisphere ice sheets to CO_2 forcing (Fig. 1-15). Between 300 and 400 ppm there is some additional increase in sea level (~ 20 m), however at CO_2 levels > 400 ppm there is no additional change in ice volume until CO_2 values of ~ 600 ppm are reached (Foster and Rohling, 2013). A crossplot of sea level and temperature records over the past 40 million years similarly suggests that a non-linear relationship exists between the different parameters of the climate system (Gasson et al., 2012). However, the results of this synthesis cannot distinguish whether a one-step or two-step function best describes the data. Aside from the late Pleistocene, in both of these studies, the data are predominantly from intervals of global cooling and consequently it is difficult to assess the presence or absence of hysteresis within the system. To be truly relevant to the future it is important to study time intervals of global warming and ice sheet deglaciation.

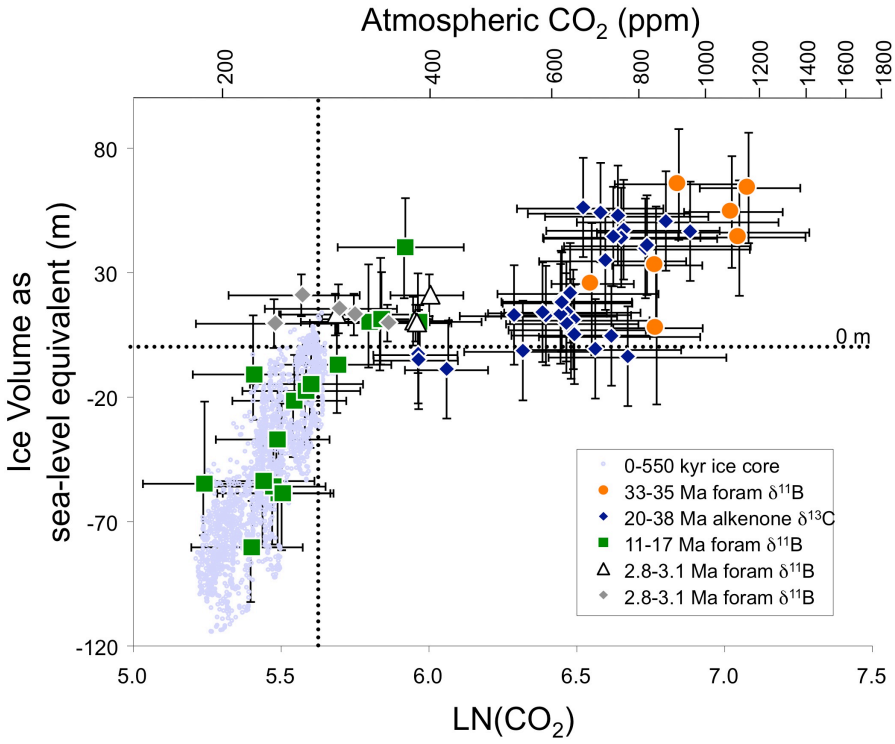

Figure 1-14: Cross-plot of estimates of atmospheric CO_2 and coinciding sea level from Foster and Rohling, (2013). Data are split according to time period and technique used. Note for the Eocene–Oligocene from $\delta^{11}B$ and $\delta^{18}O$, only data that form a decreasing CO_2 trend are plotted for clarity.

1.7 Key Research Aims

Aim 1: To produced $\delta^{11}B$ based CO_2 reconstructions for two Miocene intervals

In order to produce $\delta^{11}B$ based CO_2 reconstructions during the Miocene it is important to constrain some of the other parameters needed to calculated CO_2. Here, in order to allow the conversion of $\delta^{11}B$ in CO_2 for the Miocene records, two of these parameters have been further investigated.

Question 1: To what extent can modern calibrations be used on foraminifera with a long temporal range further back in time? In order to answer this question the life habit of *G. bulloides* is assessed through time. This study can be used to determine the extent to which it is important to test the ecology of other species when producing long-term geochemical records.

Question 2: What are the key controls on the $\delta^{11}B_{sw}$ and how many these have varied through time? The $\delta^{11}B_{sw}$ remains one of the largest sources of uncertainty in absolute

reconstructions of CO_2 prior to the Pliocene. Given the disagreement between the existing $\delta^{11}B_{sw}$ records, additional constraints on this parameter are needed.

Aim 2: To assess the role of CO_2 during intervals of deglaciation

Question 3: What is the role of CO_2 in climate variability during the Miocene climatic optimum? While low-resolution CO_2 records have shown that the MCO is associated with higher CO_2 than the preceding early Miocene, little is known about the causes of climate and ice volume variability within the climatic optimum. This record allows us to determine the relationship between CO_2, climate and ice volume across this interval and compare it to the relationship between these parameters during the late Pleistocene.

Question 4: What is the role of CO_2 in the initiation of the Mi-1 glaciation and subsequent deglaciation? Controls on the timing of the glaciation and the transient nature of the event are not fully understood. Current CO_2 records are not sufficient resolution to determine the role of CO_2 in the glaciation event. Understanding the deglaciation of the Mi-1 glaciation could provide an important insight into ice sheet instability during the Neogene.

1.8 Thesis Outline

Chapter 2 – documents the $\delta^{11}B$ method with a particular focus on elements of the process that have been further developed as part of this PhD. Methods are included in each chapter to describe the specific details of the assumptions made as part of each component of the study.

Chapter 3 – details the life habit of *Globigerina bulloides* through the Neogene, documenting the change in lifestyle of the foraminifera from a symbiont-bearing to a symbiont-barren species. SEM images and $\delta^{13}C/\delta^{18}O$ changes with size fraction are used to analyse changes in the foraminifer's mode of life and suggest that the species changed from a symbiotic to asymbiotic mode of life during the late Miocene.

Chapter 4 – the relative merits of the currently available $\delta^{11}B_{sw}$ records are examined and a new $\delta^{11}B_{sw}$ record is calculated using the difference in $\delta^{11}B$ and $\delta^{13}C$ between benthic and planktic foraminifera. The potential controls of the $\delta^{11}B_{sw}$ are then examined through comparing the new record to changes in the isotopic composition of other key

major and minor ocean ions through time. The new $\delta^{11}B_{sw}$ record shows striking similarity, between 0 and 15 Ma, to changes in the isotopic composition of Li and Ca (and to a lesser extent Mg) suggesting that there is a common control on all 4 elements across this time interval.

Chapter 5 – a new $\delta^{11}B$ derived CO_2 record from across the middle Miocene is presented. This record is then compared to previously published records of ice sheet stability/ice volume change across the same time interval to gain further understanding of the relationship between ice volume and CO_2. The reconstructed CO_2 record suggests that CO_2 is highly variable across this interval, varying between 300 and 500 ppm.

Chapter 6 – presents a new $\delta^{11}B$ derived CO_2 record from across the Oligocene-Miocene boundary. This record is then used to ascertain the extent to which CO_2 controlled the timing of the glaciation. The role of CO_2 in the deglaciation phase of the event is also discussed. The reconstructed CO_2 record suggests that CO_2 is low (~ 250 ppm) and invariable prior to, and during, the glaciation before increasing to ~ 400 ppm during the deglaciation.

Chapter 7 – the results outlined in chapters 3-6 are further discussed with a particular focus on the implications of chapters 5 and 6 for other time intervals, including into the future. One of the key conclusions from this study is that the Antarctic ice sheet is remarkably dynamic at CO_2 levels < 500 ppm. In addition, other potential areas of further work are presented.

Chapter 2: Methodology

2.1 Introduction

Boron has two stable isotopes in the ocean, ^{11}B and ^{10}B, which occur in an approximate 4:1 ratio. Seawater is enriched in ^{11}B relative to the continental input of B due to the preferential removal of the light isotope through processes such as preferential adsorption of ^{10}B onto clays, oceanic crust exchange and preferential substitution of ^{10}B into biogenic calcium carbonate (Lemarchand et al., 2002b). The two major dissolved species of boron in seawater are trigonally coordinated boric acid $B(OH)_3$ and the tetrahedrally-coordinated borate ion $B(OH)_4^-$. The proportions of these two species is pH dependent where at low pH (<6) virtually all dissolved boron is in the $B(OH)_3$ form and at high pH (>11) almost all dissolved boron is in the $B(OH)_4^-$ species (Fig. 2-1) (Zeebe and Wolf-Gladrow, 2001). The following equilibria describes this relationship:

$$B(OH)_3 + 2H_2O = B(OH)_4^- + H_3O^+ \qquad (2.1)$$

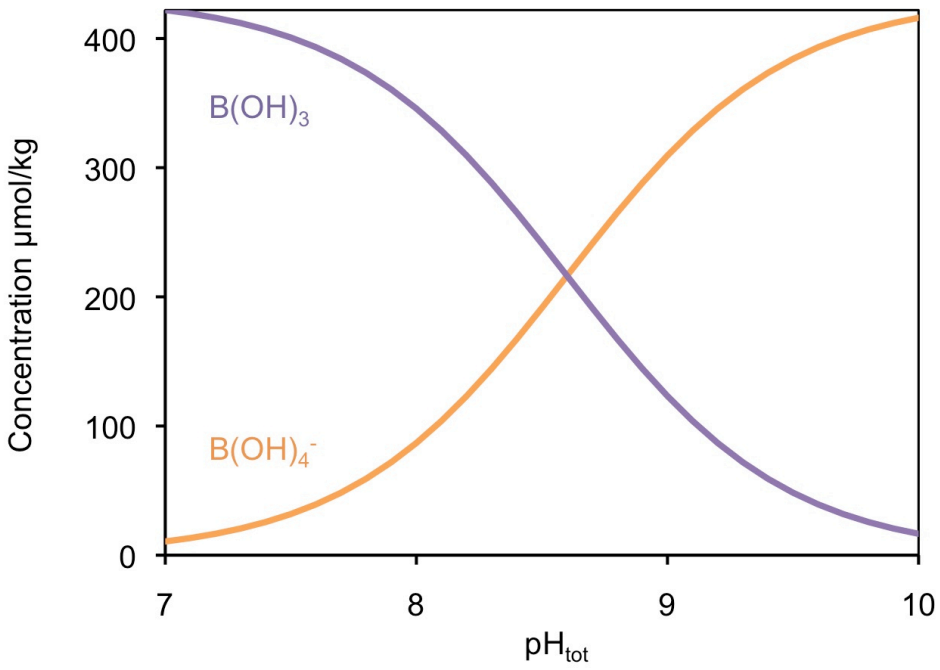

Figure 2-1: Concentration of borate ion [$B(OH)_4^-$] and boric acid [$B(OH)_3$] with seawater pH (total scale). Graph is plotted for T= 25°C S= 35, P= 0 dbar following Dickson, (1990). A total boron content of the ocean of 432.6 µmol/kg is used (Lee et al., 2010).

The proportion of the two species is also dependent on temperature, pressure and salinity. The equivalence point (the intersection of the two curves in Fig. 2-1; pK_B^*) is at pH ~8.6 in seawater at 25ºC, 35 psu salinity and atmospheric pressure (Dickson, 1990). A pronounced isotopic fractionation exists between the two aqueous boron species as a consequence of the differences in coordination and vibration frequencies (Urey, 1947). Consequently given a change in pH both the proportion of the two species and the isotopic composition re-equilibrates (Fig. 2-2). The isotope fractionation between the two species is described by the isotope exchange reaction:

$$^{10}B(OH)_3 + {}^{11}B(OH)_4^- \leftrightarrow {}^{11}B(OH)_3 + {}^{10}B(OH)_4^- \qquad (2.2)$$

Described by the equilibrium constant:

$$\propto_B = \frac{{}^{11}B(OH)_3 \times {}^{10}B(OH)_4^-}{{}^{10}B(OH)_3 \times {}^{11}B(OH)_4^-} \qquad (2.3)$$

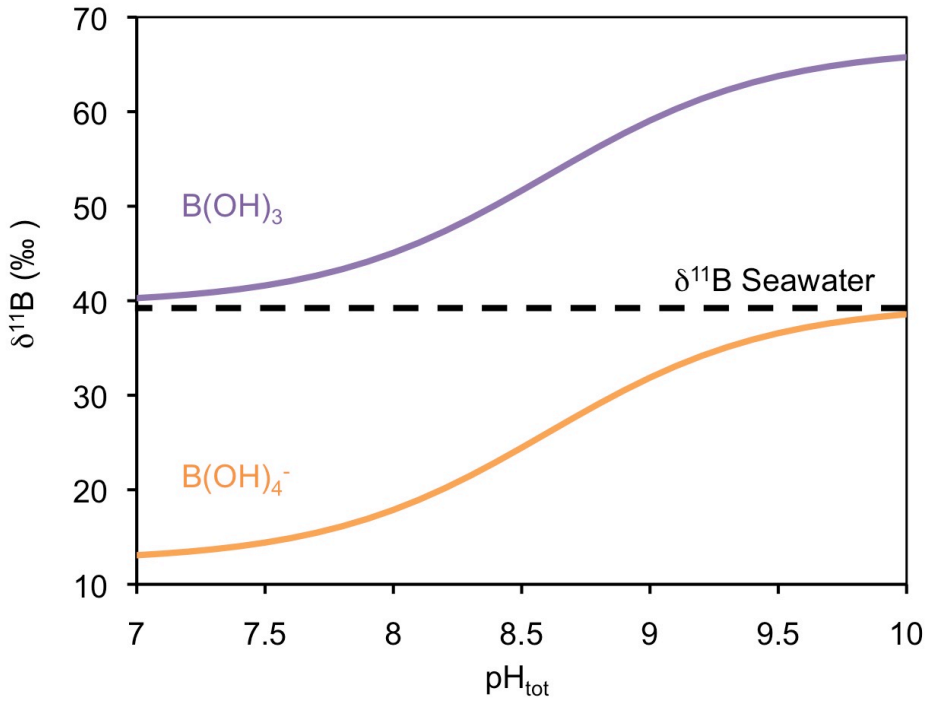

Figure 2-2: $\delta^{11}B$ evolution of borate ion [$B(OH)_4^-$] and boric acid [$B(OH)_3$] with seawater pH (total scale). Calculated using a $\delta^{11}B_{sw}$ of 39.61‰ (Foster et al., 2010), Total boron concentration = 432.6 µmol/kg (Lee et al., 2010) and α_B= 1.0272 (Klochko et al., 2006).

The ratio of ^{11}B to ^{10}B is typically measured and reported in delta notation relative to NIST 951 standard where $^{11}B/^{10}B$= 4.04367 (Catanzaro et al., 1970):

$$\delta^{11}B\ (‰) = \left[\left(\frac{^{11}B/^{10}B_{sample}}{^{11}B/^{10}B_{NIST951}}\right) - 1\right] \times 1000 \qquad (2.4)$$

Since there is an isotopic fractionation between the dissolved species and the abundance of each of the dissolved species is pH dependent, in order to maintained a constant total boron isotopic composition of seawater of $\delta^{11}B$ = 39.61 ‰ (Foster et al., 2010) the boron isotopic composition of the species is also pH dependent (Fig. 2-3):

$$\delta^{11}B_{(B_T)} \times B_T = \delta^{11}B_{(B(OH)_3} \times [B(OH)_3] + \delta^{11}B_{(B(OH)_4^-)} \times [B(OH)_4^-] \qquad (2.5)$$

Where the isotopic composition of the seawater or the $\delta^{11}B$ of either aqueous species can be determined by rearrangement of equation 2.5.

If the isotopic composition of boron in seawater ($\delta^{11}B_{sw}$), $\propto_B$ and K_B^* are known the boron isotope composition of either boron species can be used to calculate pH. For instance, pH is related to the $\delta^{11}B_{borate\ ion}$ by the following equation:

$$pH = pK_B^* - \log\left(\frac{\delta^{11}B_{SW} - \delta^{11}B_{(B(OH)_4^-)}}{\delta^{11}B_{SW} - \propto_B . \delta^{11}B_{(B(OH)_4^-)} - 1000\,.(\propto_B - 1)}\right) \qquad (2.6)$$

2.2 Boron isotopes as a pH proxy

2.2.1 Introduction

A large body of evidence, based on the isotopic measurements of marine carbonates, suggests that only the charged species is incorporated into the foraminifer shell and consequently pH can be calculated using equation 2.6 where $\delta^{11}B_{borate}$ is determined from $\delta^{11}B_{calcite}$ (Hemming and Hanson, 1992; Sanyal et al., 1996; Sanyal et al., 2000; Sanyal et al., 2001; Foster, 2008; Henehan et al., 2013). However, ^{11}B NMR suggests that 36-46% of the boron in the test is trigonally coordinated, although the presence of boric acid within the calcite could be a result of reconstructive surface processes during mineralization (Klochko et al., 2009). As pointed out in Rae et al., (2011), the large isotopic offset between the two species means that the incorporation of small amounts

of boric acid would have a noticeable effect on the $\delta^{11}B_{calcite}$ and consequently another process must be acting to explain the majority of the trigonally co-ordinated boron.

2.2.2 Determining the fractionation factor ($\propto_B$)

Early attempts to calculate the $\propto_B$ relied on theoretical estimates. A value of 1.0194, estimated by relating the frequencies of molecular vibration to the forces in the molecule, was applied to much of the early boron work (Kakihana et al., 1977). However, it was later shown that the value was heavily dependent on the vibrational frequencies of the involved molecule and the theoretical methods used to calculate the forces in the molecule (Pagani et al., 2005a; Zeebe, 2005). The first purely experimental approach to calculate the fractionation factor yielded a value of 1.0272 ± 0.0006 (Klochko et al., 2006). This value was calculated using a spectrophotometric procedure where $\propto_B$ is determined empirically from the difference in dissociation constants between solutions containing solely ^{11}B and ^{10}B for a range of conditions (Fig. 2-3) (Klochko et al., 2006). Subsequent improvements to a theoretically determined fractionation factor are also in agreement with the results of the empirical method (Rustad et al., 2010) and consequently this value is used throughout this thesis.

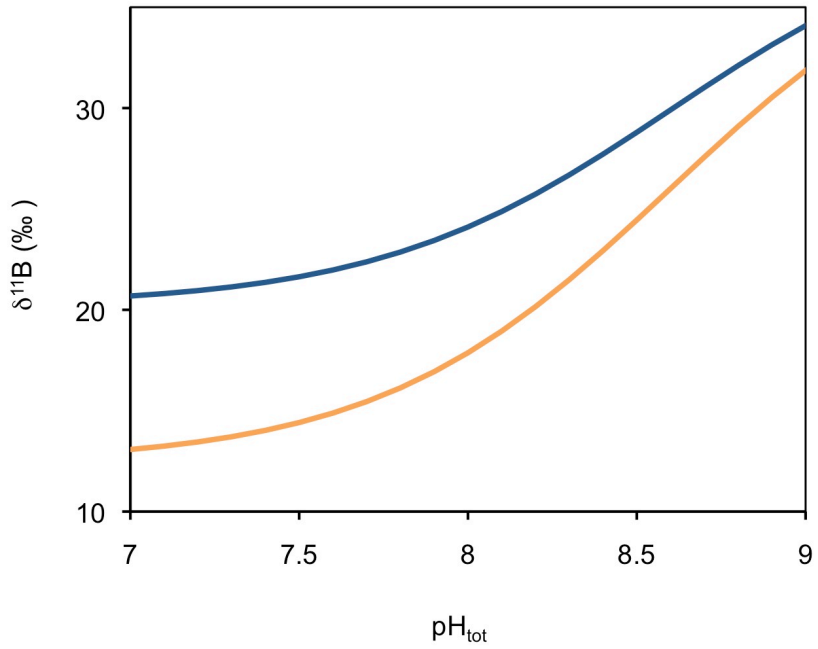

Figure 2-3: $\delta^{11}B$ of $B(OH)_4^-$ in seawater modified from Klochko et al., (2006). Based on theoretical $^{11\text{-}10}K_B$= 1.0194 from Kakihana and Kotaka, (1977); Kakihana et al., (1977) (blue line) and empirical $^{11\text{-}10}K_B$ obtained by Klochko et al., (2006) (orange line).

2.2.3 Vital Effects in Foraminifera

While there is compelling evidence that only the borate ion is incorporated into biogenic calcite (Hemming and Hanson, 1992; Sanyal et al., 1996; Sanyal et al., 2000; Sanyal et al., 2001; Foster, 2008; Henehan et al., 2013), the $\delta^{11}B$ of the carbonate typically lies close to, but not on the $\delta^{11}B_{borate.}$ This effect has been widely documented in core top studies and culture experiments for a range of foraminiferal species (Sanyal et al., 1996; Foster, 2008; Henehan et al., 2013; Yu et al., 2013), with the notable exception of epi-benthic foraminifera, which lie directly on the $\delta^{11}B_{borate}$ line (Rae et al., 2011). The offset between $\delta^{11}B_{borate}$ and $\delta^{11}B_{calcite}$ is not constant and foraminifer $\delta^{11}B$ often shows a different sensitivity to pH than suggested by the theoretical $\delta^{11}B_{borate}$ (Fig. 2-4). The offset between the $\delta^{11}B$ of different species and the theoretically expected $\delta^{11}B$ of borate ion has been attributed to vital effects. The term "vital effects" covers the action of all biological processes that result in an offset between the ambient water conditions and the calcite test. Microenvironment effects, including symbiont photosynthesis, respiration and calcification have been used to explain the observed $\delta^{11}B$ vital effects. The results from a diffusion reaction model have been used to argue that the $\delta^{11}B$ of foraminiferal calcite is controlled by the pH of the microenvironment, which is itself a function of the ambient pH, modified by the foraminifera's internal processes (Zeebe et al., 2003). In detail, the model shows that symbiont-bearing species are generally enriched in ^{11}B over symbiont-barren species because of an elevated pH in the microenvironment caused by photosynthesis (Zeebe et al., 2003). The modeled patterns are also broadly reflected in the measured $\delta^{11}B$ of symbiont-bearing and symbiont-barren species (Hönisch et al., 2003; Foster, 2008; Henehan et al., 2013; Yu et al., 2013). However, the microenvironment theory cannot fully explain the difference in the gradient of the $\delta^{11}B$-pH relationship in foraminifera and the theoretical borate ion (Henehan, 2013). While the controls on the $\delta^{11}B$-pH relationship in foraminifera is still not fully understood, use of the correct calibration is key for the accurate determination of pH. While this is relatively straightforward for the recent past, the applicability of modern calibrations needs to be more thoroughly assessed for extinct species and those with a long lineage. Chapter 3 assesses changes in *G. bulloides* through time, using oxygen and carbon isotopes, to determine the applicability of the calibration for the modern, asymbiotic species.

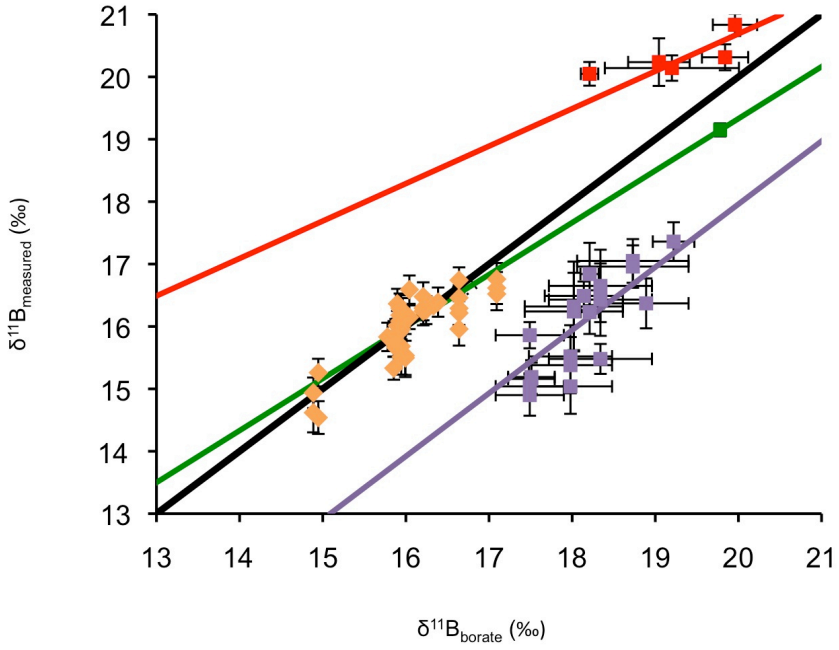

Figure 2-4: Offset between $\delta^{11}B_{measured}$ and $\delta^{11}B_{borate}$ for a range of modern species. The 1:1 line is the $\delta^{11}B$ of the borate ion calculated using a fractionation factor of 1.0272 (Klochko et al., 2006). The calibration for *G. ruber* (red) is from Henehan et al., (2013) and the intercept is modified to go through the 250-300 µm size fraction data (red squares) from the same study. The calibration for *G. sacculifer* (green) is from Sanyal et al., (2001) and the intercept is modified to go through the 300-355 µm size fraction core top value (green square) from Seki et al., (2010). The calibration for *G. bulloides* is from Martinez-Boti et al., (2015b) and core top data are a mix of size fractions (purple squares) from the same study as there is no systematic change in $\delta^{11}B$ with size fraction in this species. The epi-benthic foraminifera (orange diamonds) from Rae et al., (2011) plot on the theoretical $\delta^{11}B_{borate}$ line.

2.2.4 The boron isotope composition of seawater

A second parameter needed to obtain pH from foraminiferal calcite is the boron isotopic ratio of seawater. The present day isotopic content of $\delta^{11}B_{sw}$ is 39.61 ± 0.04 ‰ (Foster et al., 2010). This value is complied from 26-28 samples from a range of ocean basins, salinities, temperatures and water depths. Due to the long residence of boron there is no significant variation in the $\delta^{11}B$ of the seawater samples from different sites (Foster et al., 2010). The residence time of boron in the ocean is estimated at approximately 10-17 million years giving a typical rate of change of ~ 0.1 ‰ Ma^{-1} (Lemarchand et al., 2002b). Consequently to apply the boron-pH proxy further back than the Pliocene, changes in the boron isotope composition of seawater need to be quantified. A number of different methods have been used to determine $\delta^{11}B_{sw}$ changes through the Cenozoic including geochemical modeling of the sources and sinks of boron in the ocean,

analysing the boron isotopic composition of marine halites and sea salts, interpreting trends in the $\delta^{11}B$ of benthic foraminifera and using systematic variations in ocean pH and $\delta^{13}C$ to estimate $\delta^{11}B_{sw}$ (Fig. 2-5) (Pearson and Palmer, 2000; Lemarchand et al., 2002b; Paris et al., 2010; Foster et al., 2012; Raitzsch and Honisch, 2013). While these records show some agreement in the more recent past, large discrepancies still remain in the older parts of the record. In Chapter 4, the relative merits of the different approaches are discussed and a new $\delta^{11}B_{sw}$ record is presented.

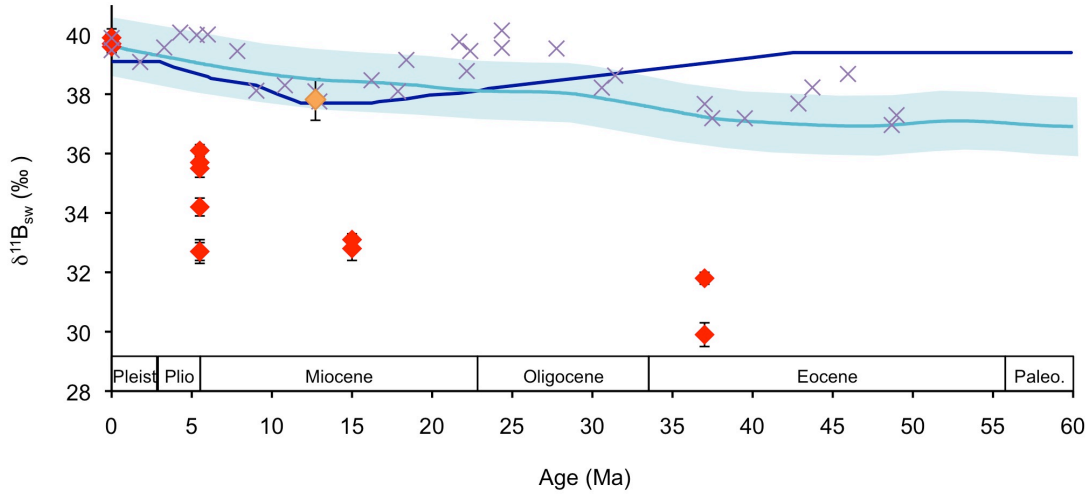

Figure 2-5: A compilation of published $\delta^{11}B_{sw}$ records. Seawater composition measured in halites (red diamonds) from Paris et al., (2010), reconstructed from foraminifera depth profiles (dark blue line and orange diamond) from Pearson and Palmer, (2000) and Foster et al., (2012) respectively, numerical modeling (light blue line) with light blue shaded area showing ± 1 ‰ confidence interval, (Lemarchand et al., 2002b) and benthic $\delta^{11}B$ (purple crosses) from Raitzsch and Honisch, (2013).

2.2.5 The influence of diagenetic alteration

The term 'diagenetic alteration' encompasses several different processes that result in the modification of the foraminifer's primary calcite after deposition on the sea floor. Recrystallisation (or neomorphism) is the process of replacement of a primary calcite (Sexton et al., 2006a). Cementation relates to the addition of new inorganic material, precipitated from porewaters. The third diagenetic process is partial dissolution caused by acidic porewaters. It is well known that diagenetic alteration affects the $\delta^{13}C$ and $\delta^{18}O$ of planktic foraminifera (Sexton et al., 2006a), however, until recently less was known about the effect of diagenesis on planktic foraminifera $\delta^{11}B$. The effect of diagenesis on $\delta^{11}B$ has now been tested across a range of sedimentary environments and

time intervals (Badger et al., 2013; Edgar et al., in review; Foster et al., 2012; Penman et al., 2014). There is little evidence of a diagenetic effect on $\delta^{11}B$ across three sites during the middle Miocene. The $\delta^{11}B$ is similar whether measured from the deeply buried Site 926 sediments, shallowly buried Site 761 or well preserved foraminifera from the clay-rich Ras-il Pellegrin section in Malta (Fig. 2-6) (Badger et al., 2013; Foster et al., 2012). A similar lack of diagenetic overprint from recrystallisation has also been found in $\delta^{11}B$ records with different diagenetic histories across the Paleocene/Eocene Thermal Maximum and prior to the Mid-Eocene Climatic Optimum (Penman et al., 2014; Edgar et al., in review). A possible explanation for the lack of diagenetic effect on $\delta^{11}B$ is that the inorganic carbonate precipitated from the pore water, as the foraminifera recrystallises during burial, has a low B/Ca and therefore only comprises a small proportion of the analysed foraminifera (Edgar et al., in review). However, if dissolution, rather than recrystallization, is the dominant diagenetic process, there is some evidence the altered foraminifera exhibit lower $\delta^{11}B$ values (higher CO_2) (Seki et al., 2010). This is particularly evident in a depth transect of core top foraminifera that shows the $\delta^{11}B$ of *G. sacculifer* declines by ~ 0.7‰ from the shallowest to the deepest site (Seki et al., 2010). This effect is species dependent, however, and no such diagenetic signal is seen in *G. ruber*.

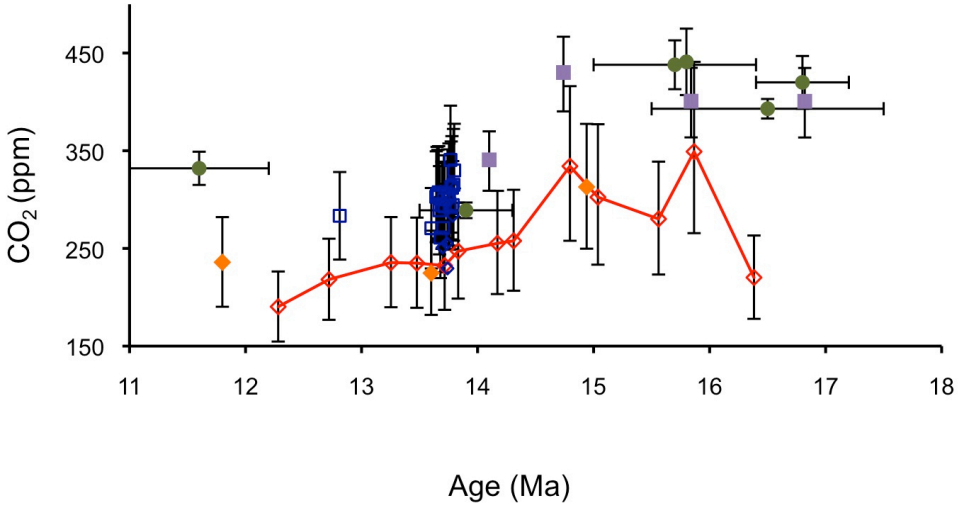

Figure 2-6: $\delta^{11}B$-derived CO_2 estimates are in good agreement with other proxy records across the middle Miocene. CO_2 from boron isotopes ($\delta^{11}B$); (red open diamonds (Site 761B) (Foster et al., 2012) orange solid diamonds (Site 926) (Foster et al., 2012), and open dark blue diamonds (Badger et al., 2013) stomata (dark green circles (Kürschner et al., 2008)); and alkenones (open dark blue squares (Badger et al., 2013) and purple squares (Zhang et al., 2013)).

2.3 pH to CO_2

2.3.1 Introduction

In the ocean CO_2 exists in three different inorganic forms: carbonate ion (CO_3^{2-}), bicarbonate ion (HCO_3^-) and free carbon dioxide (CO_2 (aq)). The carbonate species are related to each other by the following equilibrium:

$$CO_2(aq) + H_2O \leftrightharpoons HCO_3^- + H^+ \leftrightharpoons CO_3^{2-} + 2H^+ \qquad (2.7)$$

The sum concentration of all the dissolved carbon species is called the total dissolved carbon (DIC):

$$DIC = [CO_2(aq)] + [HCO_3^-] + [CO_3^{2-}] \qquad (2.8)$$

The other key parameter needed to determine changes in the ocean carbonate system is total alkalinity (TA), which is a measure of the charge balance in the ocean. Numerous definitions of alkalinity exist and in this thesis we use the following approximation that does not include the full range of charged ions that contribute to total alkalinity but is a good estimate of this parameter at pH >8 (natural seawater) (Zeebe and Wolf-Gladrow, 2001).

$$TA = [HCO_3^-] + 2[CO_3^{2-}] + [B(OH)_4^-] + [OH^-] - [H^+] \qquad (2.9)$$

Using the equations outlined above (2.7-2.9), it is possible to define any parameter of the marine carbonate system if two out of the six components: $CO_{2\ (aq)}$, HCO_3^{2-}, CO_3^{2-}, pH, total alkalinity (TA) and total dissolved inorganic carbon (DIC)) alongside temperature, salinity and depth are known (Zeebe and Wolf-Gladrow, 2001). The calculated CO_2 (aq) is then related to CO_2 (atm) by Henry's law:

$$CO_2(atm) \leftrightharpoons CO_2\ (aq) \qquad (2.10)$$

While a second carbonate system parameter is needed to calculate atmospheric CO_2, the close relationship between pH and $CO_{2\ (aq)}$ highlights the strong dependence of calculated CO_2 on pH, as derived from $\delta^{11}B$ (Fig. 2-7). Therefore, even when there are large uncertainties in the 2nd carbonate parameter (Table 2-1), the $\delta^{11}B$-derived pH in itself provides important constraints on CO_2 changes.

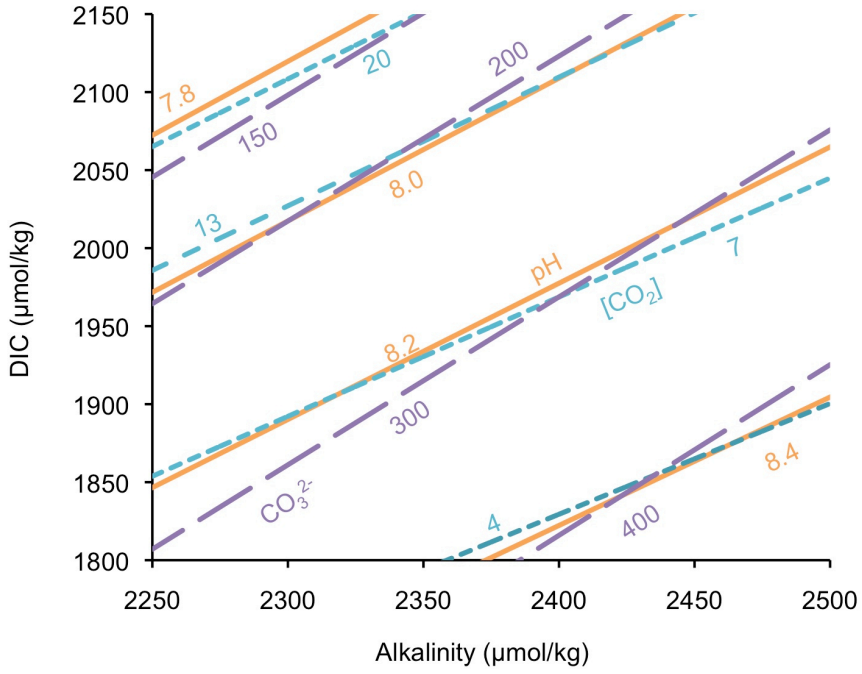

Figure 2-7: Changes in ocean carbonate system parameters as a function of DIC and alkalinity at a temperature of 25°C and a salinity of 35 psu (surface ocean conditions). Note the contours of $[CO_2]$ (light blue), pH (orange) and CO_3^{2-} (purple) are all closely parallel.

2.3.2 Calculating the 2nd carbonate system parameter

2.3.2.1 The B/Ca ratio of foraminifera

In foraminiferal calcite the charged species of boron $B(OH)^-_4$ is substituted into the carbonate lattice by the following mechanism (Hemming and Hanson, 1992):

$$CaCO_3 + B(OH)_4^- \leftrightarrow Ca(HBO_3) + HCO_3^- + H_2O \qquad (2.11)$$

The exchange distribution coefficient for the equation above is shown in equation 2.12 (Zeebe and Wolf-Gladrow, 2001; Yu et al., 2007).

$$K_D = \frac{[B/Ca]_{solid}}{[B(OH)_4^-/HCO_3^-\}_{seawater}} \qquad (2.12)$$

On the basis of this exchange distribution coefficient, the B/Ca ratio in marine carbonates will be a function of the $[B(OH)_4^-]/[HCO_3^-]$ in seawater, which is itself pH dependent (Yu et al., 2007). If the $[B(OH)_4^-]$ is known through an independent

reconstruction of pH, such as boron isotopes, then theoretically an estimate of [HCO_3^-] can be made allowing the carbonate system to be fully constrained (Foster, 2008). However, the B/Ca ratio in planktic foraminiferal calcite is not solely controlled by the [$B(OH)_4$]/[HCO_3^-] in seawater (Yu et al., 2007; Allen et al., 2011; Allen and Honisch, 2012; Allen et al., 2012; Naik and Naidu, 2014; Henehan et al., in review). Instead, some culture studies have shown that K_D in planktic foraminifera is influenced by salinity, the boron concentration in seawater and the presence of other pH sensitive ions such as CO_3^{2-} (Yu et al., 2007; Allen et al., 2011; Allen and Honisch, 2012; Allen et al., 2012; Naik and Naidu, 2014). A recent core top and culture study has found [PO_4^{3-}] and salinity are the dominant controls on B/Ca ratios and that while B/Ca responds strongly to carbonate system variations in culture studies, these patterns are not reproduced in the open ocean (Henehan et al., in review).

2.3.2.2 Calculating alkalinity from surface water saturation state

Surface water calcite saturation state ($\Omega_{calcite}$) is controlled by the concentration of carbonate ion [CO_3^{2-}] and calcium ions [Ca^{2+}] in seawater and the solubility constant of calcite (K_{sp}), which is dependent on pressure, temperature and salinity.

$$\Omega_{calcite} = \frac{[Ca^{2+}].[CO_3^{2-}]}{K_{sp}} \qquad (2.13)$$

If $\Omega_{calcite}$ and [Ca^{2+}] are known then [CO_3^{2-}] can be calculated and used as the 2nd carbonate system parameter. A modeling approach has been used to analyse changes in the surface water saturation state through time. This approach uses the deep-sea sediment core record of calcite compensation depth and the concentration of Mg and Ca in seawater to determine this parameter (Tyrrell and Zeebe, 2004). The results from this study and others suggest that surface water calcite saturation state ($\Omega_{calcite}$) is well regulated varying by only around +0.5 units from the modern value of approximately 5.4 over the past 100 million years (Fig. 2-8) (Tyrrell and Zeebe, 2004; Ridgwell, 2005).

Within a snapshot in time [CO_3^{2-}] is determined by DIC, the partitioning of which is controlled by pH (the concentration of H^+ ions) and alkalinity (the buffering capacity of the ocean) (Honisch et al., 2012). Alkalinity can therefore be calculated using the pH derived from $\delta^{11}B$ and assuming a constant omega. While the carbon cycle models

consistently show long term $\Omega_{calcite}$ has remained constant, on timescales < 100 kyrs it is unlikely the system has time to re-equlibrate to a change in pH and constantly this assumption is not valid (Fig. 2-9) (Honisch et al., 2012). For instance, using the alkalinity determined using this approach in calculations of Pleistocene glacial-interglacial CO_2 overestimates the variations compared to that seen in the ice cores. Ultimately $\delta^{11}B$-CO_2 records are determined on discrete samples, which represent short intervals of time, when omega could have deviate from the modeled long-term value. When using this approach, therefore, it is important to have sufficient uncertainties on the calculated alkalinity, in order to account for short-term deviations in omega.

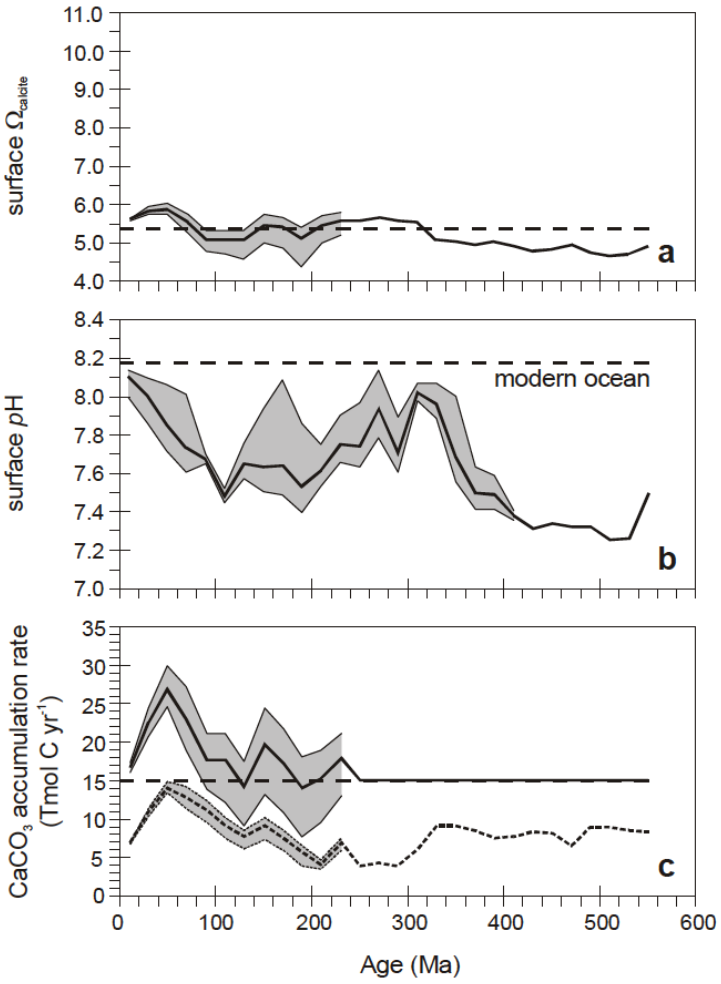

Figure 2-8: Cenozoic carbonate system changes based on modern mode of carbonate cycling from Ridgwell, (2005). (a) Mean (area-weighted) surface saturation state with respect to calcite ($\Omega_{calcite}$). The shaded band represents the uncertainty in $\Omega_{calcite}$ due to the uncertainty in weathering input. The horizontal dotted line indicates the simulated present-day value. (b) Mean surface pH. The shaded band represents the uncertainty in pH due to the uncertainty in atmospheric CO_2. The horizontal dotted line indicates the simulated present-day value. (c) Total (solid line) and neritic (dotted) rates of carbonate accumulation.

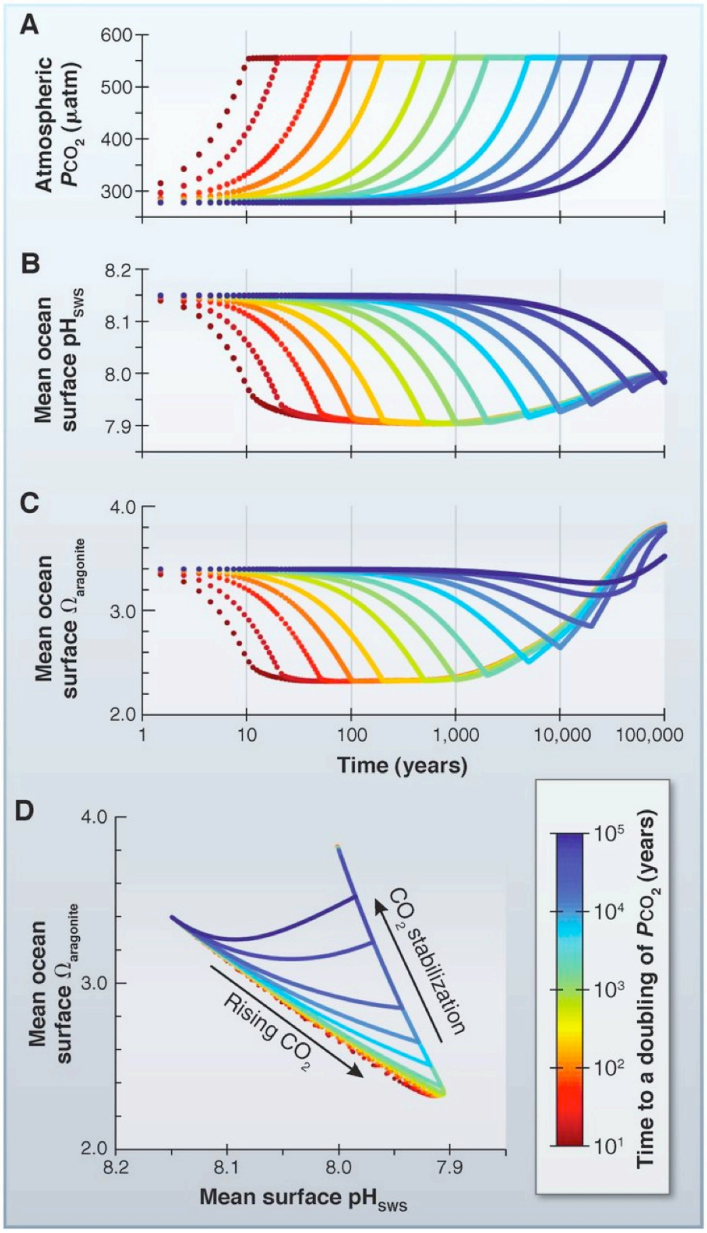

Figure 2-9: The trajectories of mean ocean surface pH and aragonite saturation ($\Omega_{aragonite}$) as the rate of atmospheric CO_2 change increases from Honisch et al., (2012). The four panels show the results of a series of experiments in an Earth system model. (a) Prescribed linear increases of atmospheric CO_2 from ×1 to ×2 preindustrial CO_2, with the different model experiments spanning a range of time scales (but experiencing the same ultimate CO_2 change). (b) Evolution of mean surface pH in response to rising CO_2. (c) Evolution of mean surface $\Omega_{aragonite}$. (d) A cross-plot illustrating how $\Omega_{aragonite}$ is progressively decoupled from pH as the rate of CO_2 increase slows. These model results include both climate and long-term (silicate) weathering feedbacks.

2.3.2.3 The alkalinity-salinity relationship

The linear relationship between alkalinity and salinity can be used in order to define the second variable (Pearson and Palmer, 2000; Honisch and Hemming, 2005; Foster, 2008; Honisch et al., 2009). Surface salinity and alkalinity are closed related in the modern ocean because the charge difference between conservative cations and anions varies with salinity (Zeebe and Wolf-Gladrow, 2001). The primary controls on salinity are precipitation, evaporation, freshwater input, and formation or melting of sea ice and all cause consistent changes in total alkalinity. One approach to calculating surface salinity in the past uses the $\delta^{18}O$ of foraminiferal calcite and removes the ice volume and temperature signals in order to obtain $\delta^{18}O_{sw}$ at the site of analysis (Schmidt et al., 2004c; Honisch and Hemming, 2005). The calibration of $\delta^{18}O_{seawater} = 0.20 * \text{salinity} - 6.73$, based on the modern relationship between salinity and $\delta^{18}O_{seawater}$, is applied to obtained salinity (Schmidt et al., 1999) and then converted to alkalinity. However, the relationship between $\delta^{18}O_{seawater}$ and salinity outlined above is likely to be too simplistic and additional factors may control the two parameters across a range of timescales (LeGrande and Schmidt, 2011). Global relative sea level change can also be used to estimate salinity as a result of the dependence of salinity on the volume of water in the ocean. Salinity estimates using this method would, however, produce a global signal, and wouldn't include local changes (Honisch and Hemming, 2005). The alkalinity-salinity approach is also limited by the assumption that the alkalinity-salinity relationship remained constant through time. This is unlikely further back in time given that whole ocean calcium carbonate compensation changes have occurred (Palike et al., 2012), which would affect whole ocean alkalinity independently of salinity.

2.3.2.4 Constant alkalinity method

To avoid the uncertainty in past salinity estimations, on shorter timescales, it is possible to assume alkalinity remains relatively constant. Alkalinity can be estimated at the core site from the nearest GLODAP site or by using the linear relationship between salinity and alkalinity (Honisch and Hemming, 2005). This approach has primarily been applied to $\delta^{11}B$ records across the Pliocene and Pleistocene (Honisch et al., 2009; Seki et al., 2010). At constant pH, a 100 μmol/kg increase in alkalinity only results in a <15 ppm increase in pCO_2 (Seki et al., 2010). Consequently a constant TA, with an uncertainty of

100-200 μmol/kg can be used without increasing the uncertainty beyond that of the analytical technique, but capturing the likely variability in TA over a particular interval (Hain et al., 2010). However, this technique may not be as applicable pre-Pliocene, when it is possible that alkalinity has deviated away from the modern by > 100-200 μmol/kg.

2.3.2.5 Planktic-benthic gradients

An alternative method of determining alkalinity uses benthic $\delta^{11}B$ and the CCD depth (Foster et al., 2012). In this method it is assumed that the depth of the calcite saturation horizon (CSH) where $\Omega_{calcite} = 1$ is a function of the calcite compensation depth (CCD) (Bostock et al., 2011). Assuming that deep-water pH is homogenous below an intermediate depth, $\delta^{11}B$-pH from benthic foraminifera can be used to determine the pH at the depth of the CSH. In the modern ocean there is little variation in temperature and pH below the intermediate ocean (Foster et al., 2012). Using these assumptions $[CO_3^{2-}]$ can be calculated from omega and depth, which can then be used alongside pH to calculate alkalinity at the calcite saturation horizon depth. This is then applied to the surface by assuming a surface to deep alkalinity gradient (-200 to 100 μmol/kg). This technique has been applied to middle Miocene (Foster et al., 2012). However, the extent to which the observations in the modern ocean regarding the depth difference between the CSH and CCD can be applied back in time is unknown. In the modern ocean CSH-CCD varies between 200m in the Atlantic to 2600m in Pacific (Bostock et al., 2011). Consequently if ocean circulation changed through time the CSH-CCD over a particularly site would also mostly likely be different.

2.3.3 Reconstructions of CO_2 from $\delta^{11}B$ of foraminiferal calcite

Despite the complications in estimating the 2nd carbonate system parameter (Table 2-1), $\delta^{11}B$ derived CO_2 records show good agreement with other CO_2 proxies over a range of timescales. The success of $\delta^{11}B$ in reconstructing CO_2 levels is particularly evident in late Pleistocene records where the data can be compared to the ice core records (Fig. 2-10). Two independently measured $\delta^{11}B$ derived CO_2 records reconstruct the timing and magnitude of the glacial-interglacial changes in CO_2 as observed in the ice-core record (Luthi et al., 2008; Honisch et al., 2009; Chalk et al., in prep.). Further back into the Cenozoic, a good agreement is also seen between $\delta^{11}B$ derived CO_2 estimates and other

proxy records for the middle Miocene (Fig. 2-6) (Kürschner et al., 2008; Foster et al., 2012; Badger et al., 2013; Zhang et al., 2013) and Eocene-Oligocene boundary (Pearson et al., 2009; Pagani et al., 2011).

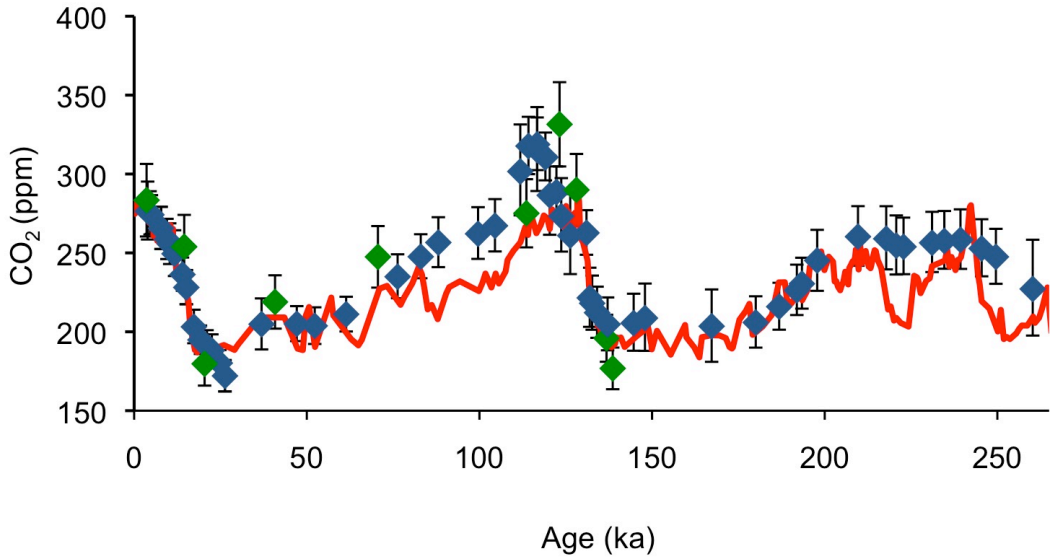

Figure 2-10: The good agreement between the boron isotope derived CO_2 records and the EPICA ice core record over the past two glacial- interglacial cycles. The $\delta^{11}B$ derived estimates from (Honisch et al., 2009) (green diamonds) and Chalk et al., (in prep.) with recalculated data from (Foster, 2008) (blue diamonds) show good agreement in both the timing and magnitude of change when compared to the ice core record (red line) (Luthi et al., 2008).

Parameter	Approximate Uncertainty on CO_2	Comment
Boron isotope measurement	~20-60 ppm	Typical 2σ of 0.2-0.6 ‰
Temperature	~10-15 ppm/°C	
Salinity	~8 ppm/psu	
Calibration	~ 10ppm- ??	Difficult to parameterise calibration uncertainty for extinct species.
Diagenesis	Unknown	The majority of studies shows little effect of diagenesis on $\delta^{11}B$
Fractionation factor	Negligible	The uncertainty of 0.0006 on the fractionation factor is not included in CO_2 calculations
Disequilibrium	Maximum modern disequilibria ±80 ppm	It is difficult to monitor changes in disequilibrium through time.
Boron isotope composition of seawater	± ~ 0-150 ppm	This parameter is well constrained for the modern, the uncertainty increases further back in time.
2nd carbonate system parameter	± ~ 10-300 ppm	This parameter is well constrained for the modern, the uncertainty increases further back in time.

Table 2-1: Approximate uncertainties associated with calculating CO_2 from $\delta^{11}B$. Note that the uncertainties change with both time and absolute CO_2 level (the non-linear relationship between $\delta^{11}B$ and pH means that the uncertainties are larger at higher CO_2).

Analytical methodology for measuring $\delta^{11}B$

2.3.4 Introduction

Several different analytical techniques have been used to measure boron isotopes in foraminiferal calcite. Until recently the analytical method used was dictated by the limited amount of boron within the foraminiferal tests. As a consequence negative-ion thermal ionization mass spectrometry (NTIMS) has been widely used due to the high ionisation efficiency of the technique (Foster et al., 2006). In the NTIMS methodology natural matrices can be loaded directly on to the filament meaning no separation of the boron is needed prior to analysis avoiding additional blank contribution (Ni et al., 2010). However, loading in this manner can lead to matrix related fractionation (Hemming and Hanson, 1994). As the NTIMS method uses natural matrices as activators to produce a BO_2^- beam, the NIST SRM 951 boric acid standard cannot be run without a loading matrix. Most laboratories run the standard with boron-free seawater and also add this to the dissolved carbonate samples in order to maintain a constant matrix between the standard and sample. Despite this, consistency in the

degree of fractionation in the sample and standard is difficult to maintain (Foster et al., 2006). Furthermore instrumental mass fractionation of the dominant species $^{10}B^{16}O_2^-$ and $^{11}B^{16}O_2^-$ can result in poor reproducibility of the results. Attempts to standardise the mass fractionation are made by running the material at similar temperatures and durations as the reference NIST SRM 951 boric acid. However, despite this, unusual fractionation behaviour is still often seen during analysis and triplicate analyses are needed to have confidence in the data.

To improve the accuracy of the boron measurements using the NTIMS method, total evaporation NTIMS (TE-NTIMS) can be applied. The effect of instrumental mass fractionation is greatly reduced in this method as the sample evaporates completely from the filament and the total ion beam of each ion is integrated simultaneously. An additional advantage of this technique is that smaller samples sizes can be used (e.g. Foster et al., 2006 analyse as little as 320 pg of B). However, while a consistent boron isotope composition can be obtained for boric acid and in house standards, reproducibility is still low (~ 0.8‰) when a carbonate matrix is used as the loading material. The presence of residual organic matter within the lattice of foraminiferal calcite is suspected as the cause of the uncertainty (Ni et al., 2010). The organic matter is released during dissolution of the foraminifera and isn't completely removed by either long-term storage in acidic solution or by loading the material in 30% H_2O_2 (Ni et al., 2010). Although some improvements have been made to the NTIMS method, (see examples in Foster et al., 2013), mass spectrometric development over the last decade has lead to the establishment of an analytical approach using a multicollector inductively coupled plasma mass spectrometry (MC-ICPMS), the details of which are outlined below. In order to compare records produced by NTIMS and MC-ICPMS, it is important to have a good understanding of the offsets in $\delta^{11}B$ determined by the two different techniques. Offsets would perhaps be expected as a result of the differences in sample preparation and introduction systems between the two methodologies. A recent interlaboratory comparison has shown that while there was no significant difference between the two analytical techniques when samples have simple matrices (e.g. boric acids, seawater), an offset did exist in samples with a $CaCO_3$ matrix (Foster et al., 2013). However, despite differences in the absolute measured $\delta^{11}B$, evidence suggests that relative changes are consistent between methods. Consequently $\delta^{11}B$ data measured

using NTIMS, such as calibration data, can be used to interpret MC-ICP-MS data, as long as the offset is properly parameterised.

2.3.5 Multicollector inductively coupled plasma mass spectrometry (MC-ICPMS) method

2.3.5.1 Laboratory Protocol

The MC-ICPMS method requires that the $CaCO_3$ sample (in this case foraminiferal calcite) is first cleaned to removed clay particle and organic material and then separated from the Ca (plus trace element) matrix prior to analysis using chromotography. The additional preparatory steps before $\delta^{11}B$ analyses mean that maintaining a low laboratory blank is of great importance. Boron blank is typically derived from 3 sources: (1) fall-in from airborne boron (2) Boron in reagents (3) Boron adhered to sample vessels.

Fall in from airborne boron can be reduced, but not totally eradicated, by using boron free HEPA filters within the clean laboratory. The fall-in boron blank is most significant during column chemistry, which typically takes between 5 and 6 hours. Covering the columns with plastic lids between pipetting acts to minimise this. The magnitude of B contamination during column chemistry is determined using a total procedural blank (TPB). During each batch of columns a solution containing 0.5 M nitric acid and buffer solution, in the same proportions as the sample, is passed through the columns. This is then analysed for boron concentration and an approximate isotope composition is determined. The amount of fall-in blank is relatively low (8 pg/hr), however, the light isotopic composition of the blank (0 to -20 ‰) can mean it's significant for smaller samples (>10 ppb). This is discussed further below. The two main reagents used in sample preparation are MilliQ (MQ) water treated with © EMD Millipore pack and 0.5 M nitric acid. The MQ unit is fitted with a Milli-Q Q-guard (© EMD Millipore) pack, to remove boric acid, which is not removed by conventional reverse-osmosis water purification techniques that primarily target charged species. The 0.5 M nitric acid is made by diluting 14.2 M analytic grade nitric acid that has undergone Teflon distillation. All standards used during the analysis are also made from the same 0.5 M nitric acid and MQ, maintaining a constant blank level and molarity between sample and the standard, therefore reducing the risk of a sample-standard offset. The Na-acetate

buffer required for column chemistry (see below) is cleaned using Amberlite IRA 743 resin prior to use. All Teflon is cleaned using the protocol in Appendix A.

2.3.5.2 Foraminiferal cleaning protocol

Foraminiferal cleaning is based on the approach of Barker et al., (2003). Foraminifera are cracked open to ensure all the chambers are exposed to the cleaning treatment. The foraminifera are then ultrasonicated for 30 seconds and rinsed using MQ water (18.2 MΩ) to remove clays. Clay removal is important as $\delta^{11}B$ decreases as clay content increases as a result of the release of isotopically light boron from within the sheets of the clay mineral (Deyhle and Kopf, 2004). This is then repeated between five and ten times. The precise ultrasonicating time and number of repeats is dependent on the wattage of the ultrasonic bath. After finding an 80 W bath was not sufficiently removing the clays and a 285W bath destroyed the foraminifera we used a 200 W bath following the instructions above. Typically older samples required more clay removal steps and planktic foraminifera were more susceptible to clay contamination than benthics.

Next organics are removed by oxidative cleaning. A 500 µl solution of analytical grade 1% H_2O_2 in 0.1 M NH_4OH_4 is added to each sample and heated in a water bath to 80 ºC for 3 x 5 mins. Between each 5 minute step the samples were tapped and ultrasonicated for 15 seconds to remove any CO_2 bubbles produced during the oxidation of organic material. Removal of organic material is not only important in terms of removing boron isotope contamination but also to ensure the longevity of the columns. Organic material can retard the flow of the liquid through the columns, reducing the yield of boron eluted from the columns. Samples are then subject to a weak acid leach in 0.0005 M HNO_3 for 30 seconds to remove any readsorbed contaminants. To dissolve, 200 µl of Milli-Q and 50 µl of 0.5 M HNO_3 is added to each sample. Additional acid is added in increments of 25 µl until dissolution is completed, with additional ultrasonication as required. A minimum amount of acid is added to the samples to both reduce the risk of leaching boron from any remaining particulate matter and reduce the volume of cleaned buffer that is added before column chemistry (see below). Using a heated ultrasonic bath during dissolution can reduce the volume of acid needed. To ensure no contaminant particulate matter is added to columns, samples are centrifuged for ~ 5 min at 1400 rpm, and the bottom 20-50 µl is not taken for analysis. The supernatant is removed and

transferred to clean screw top teflon for storage prior to columns. Reductive cleaning is not conducted as boron is not present in Fe-Mn oxides in large quantities.

To assess the effect of incomplete cleaning, the $\delta^{11}B$ and trace element composition of cleaned and uncleaned foraminifera from both the Holocene and the Miocene were measured. The samples consisted of single species *G. sacculifer* and *G. sicanus* from Site 999 and Site 761 for the Holocene and Miocene respectively. For the Miocene samples, foraminifera were crushed and homogenised before undergoing different treatments. For the Holocene sample, 27 foraminifera were analysed for each treatment, with double the quantity used for the partial dissolution test. Firstly, the effect of no cleaning on the $\delta^{11}B$ of the sample was analysed. An uncleaned foraminifer has an isotopic ratio 5 ‰ and 4 ‰ lighter for the Holocene and Miocene samples respectively (Fig. 2-11, 2-12). Typically the lighter isotope (^{10}B) preferentially adheres to the clay particles and is incorporated into organic matter, explaining the offset of the $\delta^{11}B$ to lighter values. Clays, removed between no cleaning and clay cleaning, have the largest influence on the isotopic signal causing a 3 ‰ shift in $\delta^{11}B$ in both cases. Organic material removed between clay cleaning only and full clean, causes a 1 ‰ shift in the Miocene sample and a 2 ‰ shift in the Holocene sample, the difference most likely a consequence of more organic matter remineralisation with time and depth within the sediment column. It has been well documented that Mg/Ca is distributed as high and low bands in foraminiferal calcite and consequently full dissolution of samples is needed to ensure an average signal (Sadekov et al., 2005). Here the effect of partial dissolution on $\delta^{11}B$ was tested by removing dissolved carbonate from a fully cleaned sample after the addition of 30 µl of acid (Partial cleaning 1). Partial cleaning (2) is the rest of the sample, dissolved after removal of the material dissolved in the first acid addition. It was found that the isotopic value of the partially dissolved calcite and the remnant calcite, dissolved after the partially dissolved fraction was removed, were the same, suggesting that for $\delta^{11}B$ at least this effect may not be as large (Fig. 2-12).

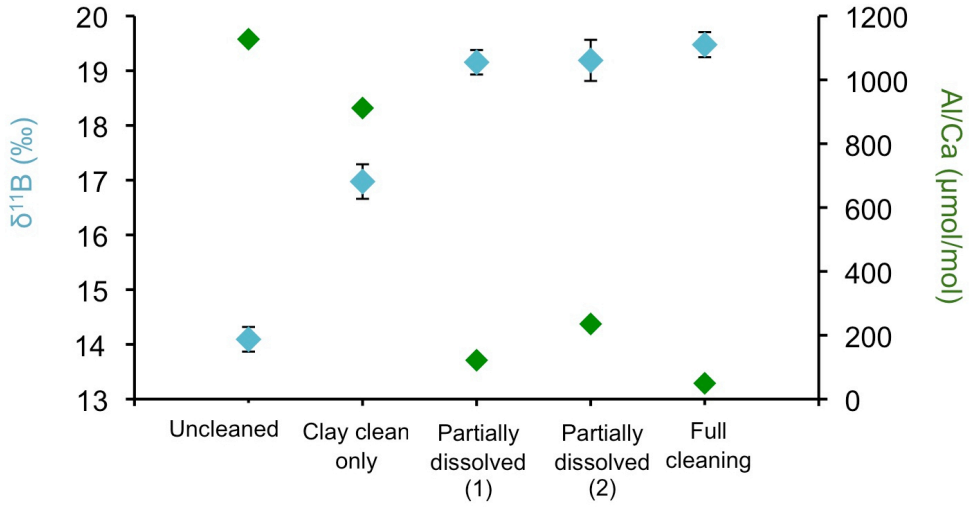

Figure 2-11: The evolution of $\delta^{11}B$ (blue diamonds) and Al/Ca (green diamonds) with each cleaning step on *G. sacculifer (with sac)* from Holocene ODP sample 668B 1 1W 8-10cm. Samples were uncleaned, clay cleaning only and both partially dissolved (1) and (2) underwent full cleaning. Partial cleaning (1) was removed from a fully cleaned sample after the addition of 30 µl of acid. Partial cleaning (2) is the rest of the sample, dissolved after removal of the material dissolved in the first acid addition. Error bars show 2 s.d. external reproducibility.

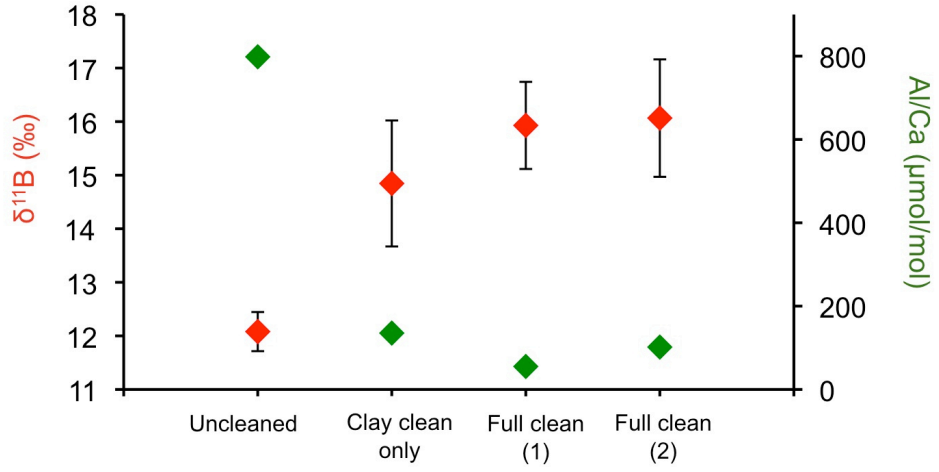

Figure 2-12: The evolution of $\delta^{11}B$ (red diamonds) and Al/Ca (green diamonds) with each cleaning step on *Gs. sicanus* from combined Miocene ODP samples 761B 6 3W 118-120 cm, 123-125 cm 4W 28-30 cm, 33-35 cm, 5W 8-10 cm. Samples were uncleaned, clay cleaning only and full clean (1) and (2). Full clean (1) has an Al/Ca of 55 µmol/mol and full clean (2) has an Al/Ca of 102 µmol/mol. Both $\delta^{11}B$ estimates are within uncertainty of each other suggesting that Al/Ca in this range at least does not affect $\delta^{11}B$. Error bars show 2 s.d. external reproducibility.

2.3.5.3 Column chemistry

In order to measure $\delta^{11}B$ by MC-ICPMS, the boron is removed from the calcium carbonate matrix using boron specific Amberlite IRA-743 resin (Lemarchand et al.,

2002a). The approach described in Foster et al., (2013) is followed, and is briefly described here. At high pH, the partitioning coefficient between the Amberlite resin and the boron is high and consequently practically 100% of the boron is bound (Fig. 2-13) (Lemarchand et al., 2002a). To maintain an elevated pH and ensure high levels of boron absorption on to the Amberlite IRA 743, the dissolved samples are buffered to a pH of 5. To ensure this is achieved for each sample, Na-acetate buffer equivalent to two times the amount of acid used during dissolution is added. The buffered samples are loaded on to columns and washed in using MQ water (Table 2-2). The sample is collected from the resin by decreasing the pH through addition of 0.5 M HNO_3. At low pH the partitioning coefficient of the resin for boron decreases and the boron is eluted (Lemarchand et al., 2002a). The samples are eluted by pipetting between 96 µmol and 120 µmol of 0.5M HNO_3 on to the resin (Table 2-2). The elution volume is dependent on the uptake rate of the MC-ICPMS nebulizer (see below) but should be kept to a minimum in order to maximize the concentration of the sample. This step is repeated five times with approximately 5 minutes between each acid addition to ensure full equilibration of the resin to the decrease in pH. Isotopic fractionation occurs during the elution process and consequently it is important complete elution takes place. This procedure typically results in column yields of approximately 99.9 %. An acceptable level of elution is tested for by passing additional acid through the columns (column 'tails'), equivalent to 4x column volume following sample collection and measuring the boron concentration.

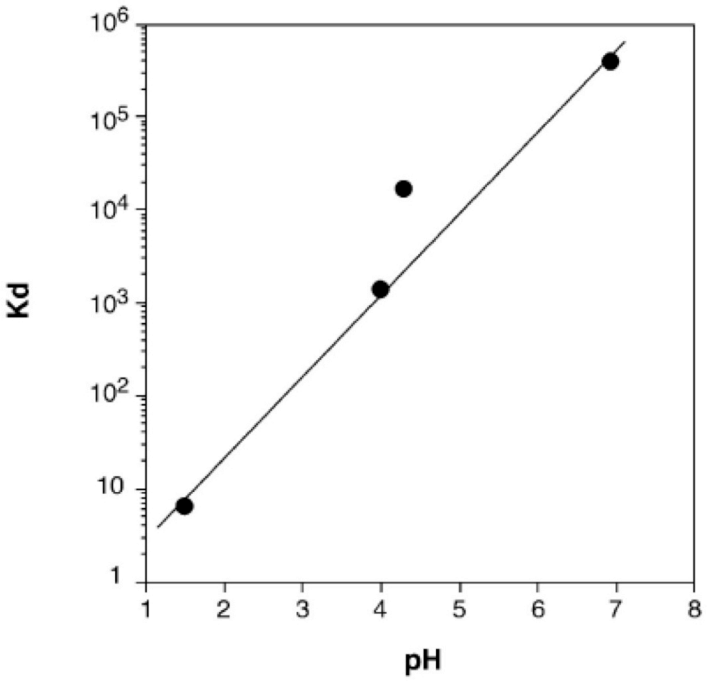

Figure 2-13: Changes in the partition coefficient between boron and the N-methyl-glucamine groups of Amberlite IRA 743 resin versus value of pH from (Lemarchand et al., 2002a). Results from batch experiments. Note the high affinity of the resin for boron at high pH.

Step	Reagents	Directions
Clean columns	0.5 M HNO_3	Repeat 2 times. 1st step- fill reservoir, 2nd step - add 1 ml
Precondition columns	MQ	Repeat 2 times- add 1 ml for both steps
Load sample	Buffered sample	Pipette directly on to resin
Wash in sample	MQ	Repeat 8 times adding 200 µl-drip MQ around the reservoir to wash in sample off the walls.
Elute samples	0.5 M HNO_3	Repeat 5 times adding 96-120 µmol directly on to resin
Collect tail	0.5 M HNO_3	Add 96-120 µmol directly on to resin
Clean columns	0.5 M HNO_3	Repeat 2 times. 1st step- fill reservoir, 2nd step - add 1 ml
Rinse columns	MQ	Repeat 2 times- add 1 ml for both steps

Table 2-2: Column chemistry protocol. The entire process takes between 5 and 6 hours. After collection the samples are stored in screwtop Teflon vial that have been cleaned according to the protocol in Appendix A.

Typically a set of columns needs to be reconditioned every 6-8 months as the liquid no long effectively drips through the column and the resin degrades. In most cases an increase in the % of boron in the columns 'tails' occurs before the isotopic composition of the samples is compromised and is therefore a good indicator of when the columns need reconditioning. The steps involved in column reconditioning include removing all the resin through ultrasonication, cleaning the columns following the Teflon cleaning protocol (Appendix A) and reloading new resin. Ways to increase the lifetime of the columns include ensuring complete removal of organic matter from the samples. This has proved particularly important in coral samples. Cleaning the columns with MQ after use and storing the columns in MQ can slow down the degradation of resin as a result of exposure to acid.

2.3.5.4 $\delta^{11}B$ measurement using MC-ICPMS

The $\delta^{11}B$ samples have been analysed using the Thermo Neptune MC-ICPMS at the University of Southampton following (Foster, 2008; Foster et al., 2013; Henehan et al., 2013). Samples are introduced into a teflon barrel spray chamber using a fused ESI Ltd. PFA 75µl/min teflon nebuliser. The aspiration properties of the nebuliser are key to good machine stability as this determines the rate and stability of the delivery of the sample to the plasma. To ensure good boron sensitivity the sample gas flow was typically set above the maximum limit for the teflon nebuliser consequently reducing the lifetime of the nebuliser to 6 months. Ammonia gas is also added into the spray chamber (2-3 ml/min NH_3) to improve boron washout (Al-Ammar et al., 2000). The machine is tuned for a combination of sensitivity and stability using NIST SRM 951 (Catanzaro et al., 1970). Torch position, sample gas, and source lenses are tuned for maximum sensitivity (Table 2-3). Peak shape is optimised using source lenses and shape to ensure a broad flat-topped peak with limited tailing on either side (Fig. 2-14). The sample gas is then tuned for maximum stability by changing the sample gas and monitoring the change in isotopic ratio until a stability plateau is identified where the ratio no longer changes with changing sample gas (Fig. 2-15). This plateau changes as the machines warms up and between analytical sessions. Typically a 50 ppb solution produces a maximum signal of 700-750 mV and a sample gas stability plateau signal of 500-600 mV.

Inlet System		Lenses	
X	~3.1	X	4.23
Y	~2.6	Y	-4.5
Z	~1	Focus	-550
RF Power	1425	Shape	210
Aux. Gas	0.9	Source Offsets	-42
Cool. Gas	15.25	Focus Quad	~4-7
Sample Gas	~ 1.2	Rotation Quad	0
Ammonia	0.04	Dispersion Quad	0

Table 2-3: Typical machine parameters for the Thermo Neptune MC-ICPMS used at NOCS for boron isotope analysis. Gas fluxes are in L/min. Note that these settings often change between machines and analytical sessions.

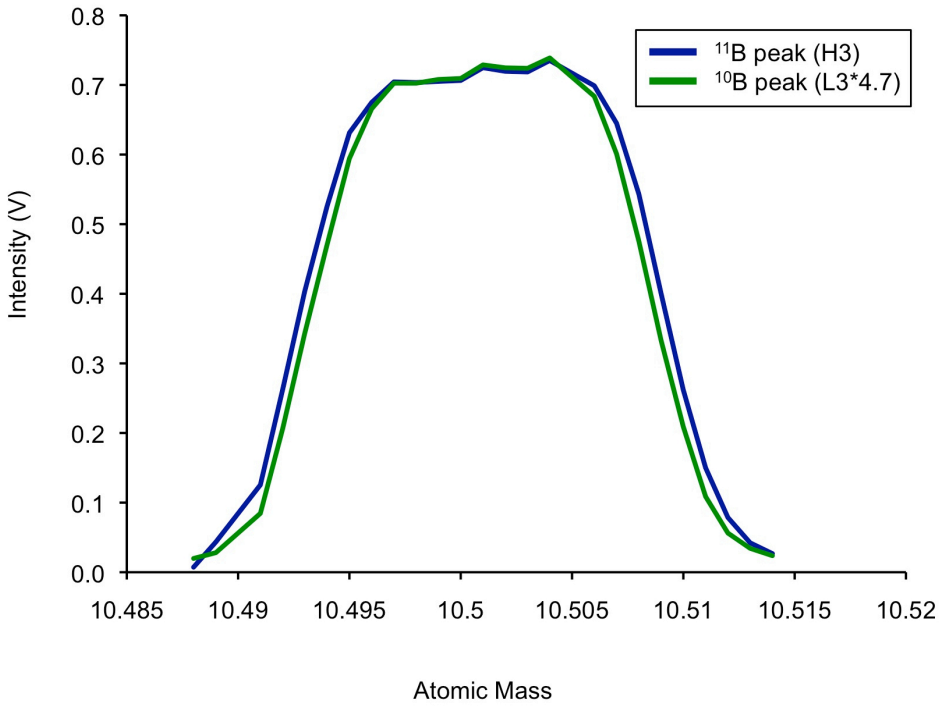

Figure 2-14: Example of a good ^{11}B and ^{10}B peak shape. Note flat top and limited 'tails' on each side of the peak. Both ^{11}B and ^{10}B peaks are plotted, the intensity of the ^{10}B peak has been multiplied by 4.7 so both can be viewed on the same scale.

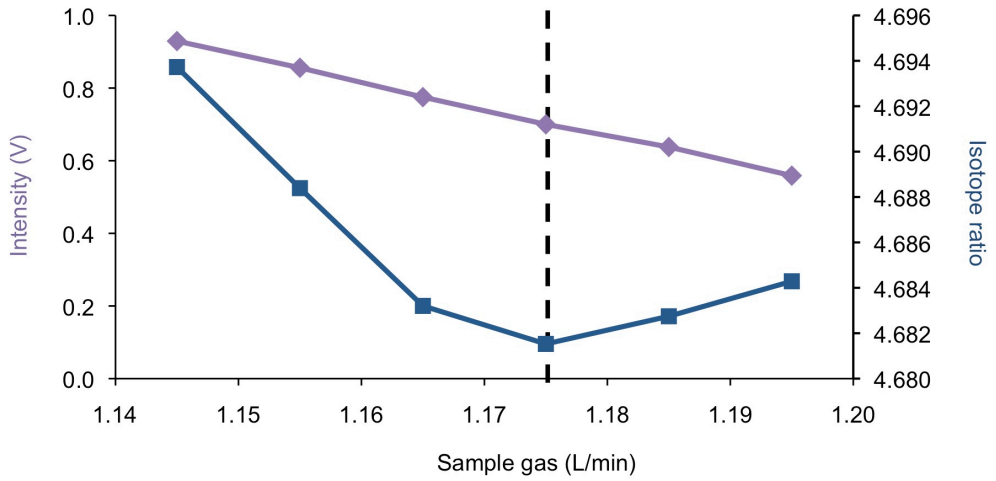

Figure 2-15: The typical output from a sample gas test. The isotope ratio (blue squares) tends to decrease as the sample gas is increased. The stability plateau (black dotted line) is defined by the point where the isotope ratio shows little change as the sample gas is changing. Increasing the sample gas leads to a decrease in intensity. The plateau intensity is usually 20 to 30% lower than the maximum intensity.

The samples are bracketed by standard NIST SRM 951 to allow for accurate correction of machine induced mass fractionation. Standards are run between each sample and blank pots bracket every three samples in order to characterise the nature of fall-in blank during the machine run. The volumes of the blank pots match the samples and contain 0.5 M HNO_3. The blank pot is run using the same method as a sample and the average ^{11}B and ^{10}B from the bracketing blank plots is subtracted from the samples. Within each analytical session two independent measurements of each sample are made (ensuring they don't share blank pots or standards) and an average of the two measurements used to determine the final isotope ratio.

The reproducibility of a dataset can be determined at a range of scales. The most comprehensive investigation of uncertainty accounts for the combined effects of measurement uncertainty and any external uncertainty that arises from sample processing. The long-term external reproducibility is characterised here by the repeat analysis of carbonate reference materials Japanese Geological Survey JCP-1 and JCT-1 (Fig. 2-16a). This standard is also passed through the columns to include uncertainties in column chemistry and therefore represents external precision. Measurements of JCP and JCT are binned into different signal intensities (of 100 mV) and the two standard deviations (2σ) of each intensity group is determined and a line of best fit drawn through the data. In addition, long-term intermediate precision, determined by the repeat

analysis of a previously processed sample either within a single analytical session or during different analytical sessions, is monitored using boric acid, in-house standards BIG D and BIG E and the 2σ is defined in the same way.

The uncertainty on the measurement is controlled by the beam size, which is dependent on the size of the sample and quality of the tuning. The precision and accuracy of small samples is ultimately determined by the detection system of the instrument (Wieser and Schwieters, 2005). In the case of $\delta^{11}B$ analysis the signal is detected using a Faraday cup where the noise is mainly derived from the current amplifer system equipped with a high ohmic resistor to boost the signal. The relationship between signal size and uncertainty is best described using a double exponential where at below a critical level of signal size there is a rapid increase in 2σ (Fig. 2-16a). Two types of noise control the signal size uncertainty relationship: a) Johnson noise caused by inherent electrical noise on the detectors b) Shot noise derived from the statistics of detecting small numbers of ion arrival events at the detectors (Rae, 2011). The threshold beyond which there is a rapid increase in 2σ with decreasing signal size reflects a change in the dominant source of uncertainty from shot noise to Johnson noise (Rae, 2011). The contribution of Johnson to the analytical uncertainty is defined as:

$$\Delta V = \sqrt{\frac{4k_B RT}{t_m}} \qquad (2.14)$$

where ΔV is the 1 standard deviation noise in volts, k_B is the Boltzmann constant, R is the resistor value in ohm, T is the temperature in Kelvin and t_m is the integration time in seconds.

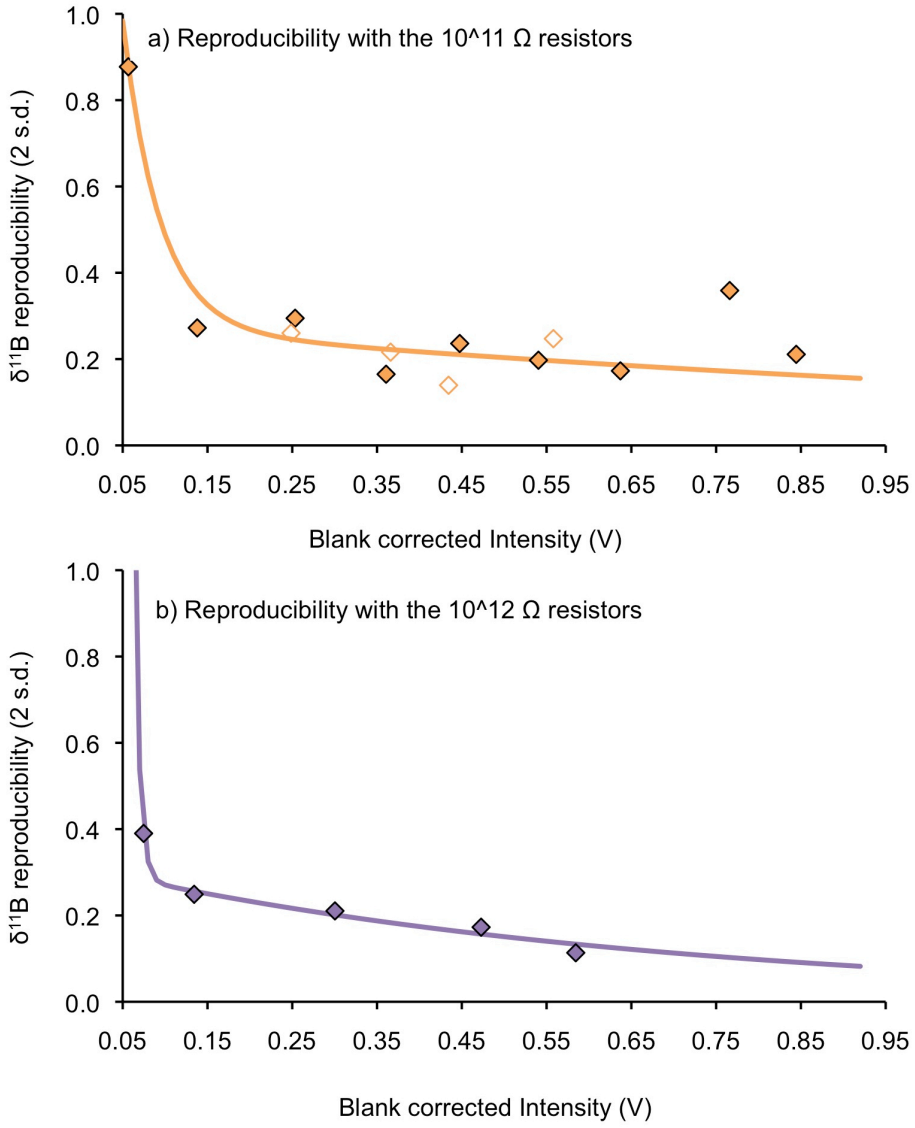

Figure 2-16: External reproducibility curve based on repeat measurements of Japanese Geological Survey JCP-1 (closed diamonds) and JCT (open diamonds) following the method outline in (Rae et al., 2011) across the intensity range of samples in this thesis. JCP measurements were made using (a) 10^11 Ω resistors (b) 10^12 Ω resistors. Samples are run through columns and then analysed incorporating uncertainty in both stages of the procedure. Note the reduced 2 s.d. using the 10^12 Ω resistors in the 75 to 250 mV intensity range.

2.3.5.5 Reproducibility 10^11 vs 10^12 resistors

Typically 10^11 Ω resistors are used on the Faraday cups. However, the recent development of 10^12 Ω resistors has led to a reduction in uncertainties at low signal intensity. The 10^12 Ω resistors increase the signal in volts by a factor of 10. While the noise also increases according the equation above, it does so by only a factor of $\sqrt{10}$

meaning the signal to noise ratio is increase by a factor of 3 (Wieser and Schwieters, 2005; Koornneef et al., 2013). In terms of the $\delta^{11}B$ reproducibility curve this acts to reduce the signal size at which Johnson noise becomes the predominant source of uncertainty and 2σ rapidly increase. To assess the affect of using 10^12 Ω resistors on the intermediate reproducibility of $\delta^{11}B$, repeat analysis of 5 ppb (signal intensity 75 mV) and 10 ppb (signal intensity 150 mV) in-house boric acid standard BIG E ($\delta^{11}B$ = 14.72 ‰) was conducted. Unlike the 10^11 Ω resistors, the 10^12 Ω resistors require a stablisation period before analysis can start and consequently an idle time of two seconds was added to the method between sample uptake and analysis. In the case of both single and repeat analysis, and for both 5 ppb and 10 ppb samples the 2 standard deviations (2σ) with the data set for each concentration improved compared to the uncertainty curve determined using the 10^11 Ω resistors (Fig. 2-17, 2-18; Table 2-4, 2-5). In the case of two repeat analyses on a 5 ppb sample the uncertainty decreased by around half (Fig 2-18; Table 2-5). This has important implications for $\delta^{11}B$ analysis, which is often limited by sample size.

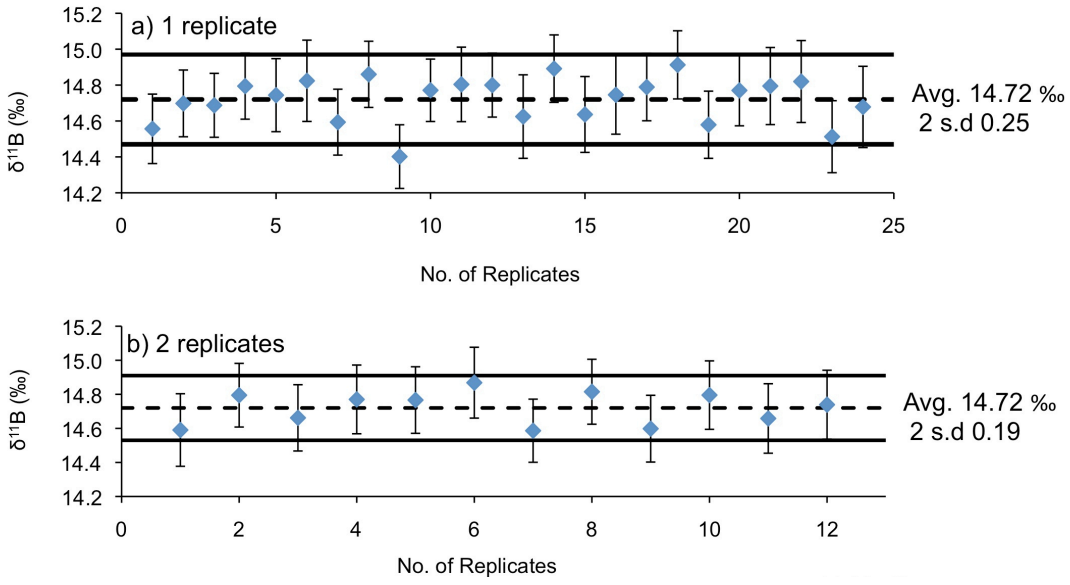

Figure 2-17: $\delta^{11}B$ variability associated with a) 1 replicate and b) 2 replicates of a 10 ppb sample of BIG E measured using 10^12 Ω resistors. Error bars show internal (machine) 2 s.d. reproducibility. Dashed line shows the mean of the replicates. Solid lines show the 2 s.d. external reproducibility of the whole dataset. External 2 s.d. for 1 replicate is 0.25 ‰ and 2 replicates is 0.19 ‰.

	Intensity (volts)	10^11 reproducibility curve 2 s.d.	10^12 2 s.d.
1 replicate	0.15	0.32	0.25
2 replicates	0.15	0.33	0.19

Table 2-4: Mean BIG E and 2 s.d. external reproducibility using 10^11 Ω resistors and 10^12 Ω resistors for a 10 ppb sample (Blank corrected intensity =150 mV).

To test the effect of 10^12 Ω resistors on external reproducibility in $\delta^{11}B$ analysis small JCP samples that had undergone full column chemistry were analysed. The increased precision of these measurements meant it was possible to determine the effect of the $\delta^{11}B$ blank through column chemistry on the $\delta^{11}B$ of small samples. The effectiveness of the total procedural blank (TPB) correction (20-50 pg, mean $\delta^{11}B$ -19 ‰) was also assessed. 5 ppb and 10 ppb samples were measured and the reproducibility of these samples was similarly improved, although more work is needed to characterize the uncertainty at high (>500 mV) and low (< 75 mV) signal intensities (Fig, 2-16b, Table 2-6). However, the JCP mean values were lighter (0.3 ‰ for 10 ppb samples, 0.6 ‰ for 5 ppb samples) than that characterised by using the 10^11 Ω resistors ($\delta^{11}B$ = 24.3 ‰), suggesting that fall-in blank during column chemistry does become significant for smaller samples. Applying the TPB associated with each sample set corrects the 10 ppb JCP back to values determined by the lab in Southampton and other external sources. The 5 ppb samples tend to be overcorrected by the TPB correction, however, are still within uncertainty of the determined value (Table 2-6). At smaller sample sizes the blank forms a larger proportion of the boron in the sample, therefore, inaccuracies in determining the nature of the blank will have a larger influence on the $\delta^{11}B$. The overcorrection of 5 ppb samples may be a result of a mismatch in the volume of different reagents that typically make up a small JCP sample and the TPB. The TPB is made to replicate the composition of the sample (typically 75µl HNO_3, 150 µl buffer). The high B/Ca of JCP coral often means a 5 ppb sample comprises only 7 µl HNO_3 (containing the sample) and therefore 14 µl of buffer. With the improved precision of the 10^12 Ω resistors the offsets in small samples may give additional insights into the nature of the blank $\delta^{11}B$.

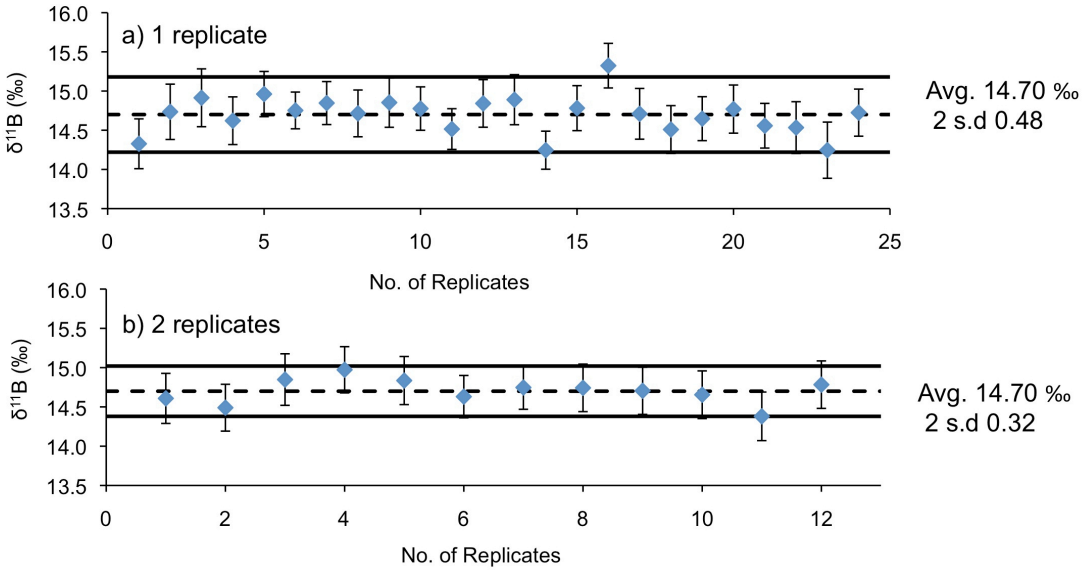

Figure 2-18: $\delta^{11}B$ variability associated with a) 1 replicate and b) 2 replicates of a 5 ppb sample of BIG E measured using 10^12 Ω resistors. Error bars show internal (machine) 2 s.d. reproducibility. Dashed line shows the mean of the replicates. Solid lines show the 2 s.d. external reproducibility of the whole dataset. External 2 s.d. for 1 replicate is 0.48‰ and 2 replicates is 0.32 ‰.

	Intensity (volts)	10^11 reproducibility curve 2 s.d.	10^12 2 s.d.
1 replicate	0.075	0.87	0.48
2 replicates	0.075	0.67	0.32

Table 2-5: Mean BIG E and 2 s.d. external reproducibility using 10^11 Ω resistors and 10^12 Ω resistors for a 5 ppb sample (Blank corrected intensity =75 mV).

	Intensity (volts)	10^11 mean JCP value (‰)	10^11 reproducibility curve 2 s.d.	10^12 mean JCP value (not blank corrected) (‰)	10^12 mean JCP value (blank corrected) (‰)	10^12 2 s.d.
1 replicate	0.07	24.3	0.97	23.64	24.49	0.44
2 replicates	0.07	24.3	0.72	23.64	24.49	0.38
1 replicate	0.121	24.3	0.41	23.96	24.26	0.34
2 replicates	0.121	24.3	0.40	23.96	24.26	0.27

Table 2-6: Mean JCP and 2 s.d. external reproducibility using 10^11 Ω resistors and 10^12 Ω resistors for a 5 ppb (Blank corrected intensity = 70 mV) and 10 ppb sample (Blank corrected intensity = 121 mV). For the samples analysed using 10^12 Ω resistors mean JCP values are shown with and without a TPB correction.

In this thesis data from Chapter 5 are measured using 10^11 Ω resistors and corrected using a TPB of 20 pg and -19‰. The data in Chapter 4 and Chapter 6 are measured using both the 10^11 and 10^12 Ω resistors. The samples measured with the 10^12 Ω resistors are corrected using the concentration of boron measured in the TPB for each

column set and an isotopic ratio of -5 ‰, determined by correcting the small samples back to the mean value of the larger samples.

2.4 Elemental Analysis

Prior to column chemistry a small aliquot of the sample (20 µl) is taken from the cleaned and dissolved sample for elemental analysis. This 20 µl aliquot is then added to 130 µl of 0.5 M HNO_3 and an aliquot of this sample (20 µl) is added to a further 200 µl of acid to test the [Ca] in the sample. The [Ca] test is carried out on either the Thermo Element 2 ICP-MS or the Thermo Scientific XSeries 2 ICP-MS at the National Oceanography Centre, Southampton. Once the [Ca] is known, the sample solution is diluted so that the concentration of the sample matches the bracketing standards. Typically 2mmol [Ca] solutions were ran and bracketed by an in house gravimetric standard (BSGS+B2). For some measurements the samples were bracketed by the Cardiff University in-house standard MCS-B. Three samples are measured between each pair of bracketing standards and washout blank is accounted for by measuring a blank pot containing 0.5 M HNO_3 between each standard/sample. Analysis was carried out for a suite of elements on the Thermo Element 2 ICP-MS (see Appendix F), although the only elemental ratio used in this thesis are Mg/Ca for paleotemperature estimates and Al/Ca to determine the efficiency of sample cleaning. Samples are introduced into a teflon barrel spray chamber using a fused ESI Ltd. PFA teflon nebulizer and ammonia gas is added to the spray chamber in order to improve the boron wash out (Al-Ammar et al., 2000). The instrument is tuned using 0.1 ppb multielement tuning solution with 0.5 ppb of boron. Li, U, In, B and UO are all monitored during tuning to ensure good sensitivity across the entire mass range of elements while minimizing oxides. Consistency standards CS1, 2 and 3 are also analysed during every run to monitor to reproducibility of element ratios.

2.5 Oxygen and Carbon Isotope Analysis

Oxygen and carbon isotope analysis does not require the same degree of cleaning prior to analysis. In the case of the planktic foraminifera in Chapter 3 the samples were ultrasonicated in deionised water prior to analysis. Samples were measured on a gas source mass spectrometer (Europa GEO 20-20, University of Southampton UK)

equipped with automated carbonate preparation device. The majority of planktic and benthic foraminifera pairs in Chapter 4 were measured at Cardiff University on a ThermoFinnigan MAT 252 coupled with a Kiel III carbonate device for automated sample preparation. Additional samples were measured in the lab in Southampton and on a Finnigan MAT 253 gas isotope ratio mass spectrometer connected to a Kiel IV automated carbonate preparation device at the Zentrum für Marine Tropenökologie (ZMT), Bremen. Stable isotope results are reported relative to the Vienna Peedee belemnite (VPDB) standard.

2.6 Scanning Electron Microscopy (SEM)

Images were taken of foraminifera from several sites in Chapter 3, in order to determine changes in the morphology of *G. bulloides* through time. Foraminifera were ultrasonicated for 5 seconds in deionised water in order to remove adhered clays and Coccolithophores. Samples were then mounted on to the stub in the required orientation and gold coated using a Hummer VI A sputter coater. The gold coating improves the backscattering of secondary electrons from the sample, improving image quality. The stub was gold coated between one and four times at 45º angles to ensure good coverage. SEM images were then taken in secondary electron mode on the Leo 1450-VP SEM.

Chapter 3: Morphology and life habit of the planktic foraminifera *G. bulloides* across the Oligocene-Miocene boundary.

Acknowledgements:

The following chapter is written in the style of a research article with the intention of future publication. The contributions of co-authors to this work are detailed below.

Rosanna Greenop: data collection and analysis, SEM imaging, data interpretation, manuscript drafting and production of figures.

Paul A. Wilson: Data interpretation and manuscript drafting

Gavin L. Foster: Manuscript drafting

Abstract:

Understanding the life habits of planktic foraminifera is key to interpreting the trace metal and isotopic composition of their calcareous tests in terms of a reliable indicator of paleo-environment. *Globigerina bulloides* and its predecessor *Globigerina praebulloides* have an evolutionary history stretching back to the late Eocene time. This long stratigraphic range makes these taxa an attractive choice for generating palaeoclimatic records. The physiology of modern *G. bulloides* means, however, that there are large offsets between the isotopic and trace metal composition of the test calcite and the parent seawater. This problem is overcome when working in the relatively recent geological past through the application of suitable calibrations for *G. bulloides*. Uncertainties remain, however, over the applicability of modern calibrations to geochemical records generated for the more distant geological past using *G. praebulloides*. Here we present oxygen and carbon isotope size fraction data and scanning electron microscope images for *G. praebulloides* for snapshots of time across the Oligocene-Miocene transition, OMT (~ 23 Ma). In most samples our data reveal patterns consistent with a foraminifer that houses symbionts, whereas the modern species (*G. bulloides*) is asymbotic. In keeping with work elsewhere, we find that the wall texture of the Oligocene-Miocene species in our samples shows more similarities

to that of a modern '*Globigerinoides* -type' than to a '*Globigerina*-type' foraminifer. These results strongly suggest that geochemical calibrations based on modern day *G. bulloides* are not applicable to use in material of Oligocene-Miocene boundary age. A compilation of published carbon isotope data show that the strong isotope disequilibrium characteristic of present-day *G. bulloides* emerged in late Middle to early Late Miocene times (~ 7 Ma) making this interval attractive for further study in the quest to understand the evolutionary history of this palaeoceanographically useful taxon.

3.1 Introduction

Modern *Globigerina bulloides* is a surface dwelling, non-symbiotic spinose planktic foraminifera typically found in temperate, sub-polar and upwelling environments, where it often makes up a substantial fraction of the planktic assemblage (Prell and Curry, 1981; Hemleben et al., 1989; Sautter and Sancetta, 1992; Peeters et al., 2002). Oxygen and carbon stable isotope studies suggest that, while the species calcifies in surface waters, it does so out of isotopic equilibrium with seawater (Kahn and Williams, 1981; Sautter and Thunell, 1991). A positive relationship between size and $\delta^{18}O$ in *G. bulloides*, has been attributed to a lifecycle involving significant vertical migration with the addition of a gametogenetic calcite crust at thermocline depths in the latter stages (Hemleben et al., 1989). $\delta^{13}C$ disequilibrium for *G. bulloides* is one of the most pronounced seen among modern foraminifera (offset ~ 2 ‰ from the $\delta^{13}C$ of dissolved inorganic carbon) and appears to be correlated with test size (Elderfield et al., 2002; Friedrich et al., 2012; Birch et al., 2013). The relationship between size fraction and $\delta^{13}C$ (Fig. 3-1), and to some extent the correlation of size fraction and $\delta^{18}O$, is suggested to be controlled by the incorporation of progressively less metabolic CO_2 into the test as the foraminifer grows because of slowed growth, reduced metabolic activity and less kinetic fractionation into adulthood (Spero and Lea, 1996; Birch et al., 2013). Modern *G. bulloides* is not alone in showing a positive correlation between $\delta^{13}C$ and test size. A comparable correlation exists in dinoflagellate symbiont-bearing foraminifera (Fig. 3-1), however, in those taxa metabolic CO_2 incorporation is the dominant control on $\delta^{13}C$ in juveniles and photosymbiosis-induced fractionation controls $\delta^{13}C$ in larger tests (Birch et al., 2013). Consequently, while the $\delta^{13}C$ trend with size is the same in both

dinoflagellate symbiont-bearing foraminifera and in asymbiotic *G. bulloides*, the controls on $\delta^{13}C$ fractionation may be different in the larger size fractions.

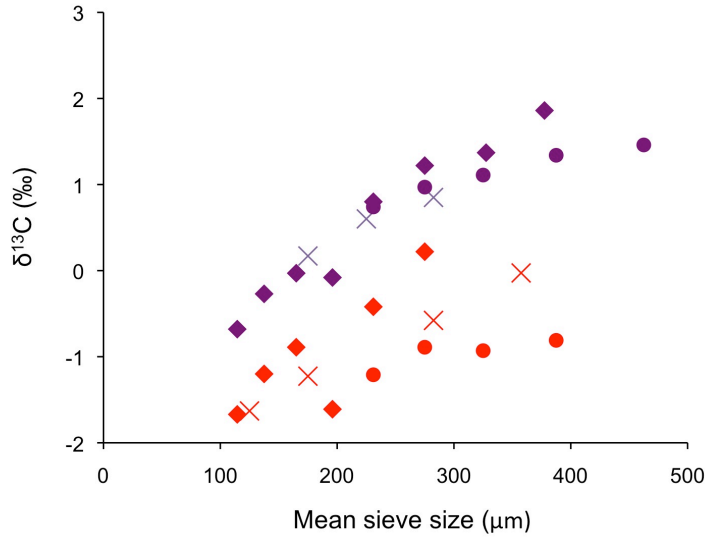

Figure 3-1: $\delta^{13}C$ versus size fraction for modern *G. ruber* (purple) and *G. bulloides* (red). The data are taken from Birch et al., (2013) (diamonds), Elderfield et al., (2002) (circles) and Friedrich et al., (2012) (crosses). The gradient of the $\delta^{13}C$ size fraction relationship is approximately comparable in *G. ruber* and *G. bulloides*.

A long stratigraphic range means that *G. bulloides* and its assumed ancestral form, *G. praebulloides*, have the potential to be extremely useful for palaeoclimatic reconstructions (Grant and Dickens, 2002; Pahnke et al., 2003; Majewski and Bohaty, 2010). Yet considerable uncertainty surrounds the taxonomy, ecology and evolutionary history of these taxa and also, therefore, the applicability to the geological record of the modern calibrations that are used to reconstruct palaeoclimate records from geochemical data sets. Most taxonomic texts state that *G. bulloides* first evolved in the middle Miocene, although *G. praebulloides*, which is morphologically similar, first originated during the late Eocene (Blow and Banner, 1962). Appropriate application of modern calibrations to the fossil record requires consistency of life habit through time. Demonstration of a positive correlation between $\delta^{13}C$ and size fraction in *G. praebulloides* of Oligocene age from outcrops of the Cipero Formation, Trinidad suggests that this taxon may have possessed dinoflagellate symbionts (Pearson and Wade, 2009), however, further work is necessary to investigate the presence of other isotopic patterns characteristic of symbiotic foraminifera and thus discount the possibility that this relationship was caused by size dependent metabolic carbon isotope

fractionation as seen in the modern taxon. Pearson and Wade (2009) also concluded that the morphological differences between *G. bulloides* and *G. praebulloides* are within the range of variability seen in the modern species, raising the question of whether both of these taxa should simply be assigned to *G. bulloides*. Hereafter, therefore, we refer to the modern taxon as *G. bulloides sensu stricto (s.s.)* and the taxon of Oligo-Miocene age as *G. bulloides sensu lato (s.l.)*. We present oxygen and carbon isotope data for *G. bulloides (s.l.)* from three sites for samples of OMT age (~22-25 Ma). The majority of samples analysed show the isotopic patterns that are typically used to identify symbiont-bearing foraminifera. We also present a compilation of published carbon isotope data for both *G. bulloides (s.s)* and *(s.l.)* plotted against time-equivalent other epi-pelagic taxa. These data suggest that the strong carbon isotope disequilibrium characteristic of present-day *G. bulloides* emerged in late middle to early late Miocene times (~ 7 Ma).

3.2 Materials and Methods

Planktic foraminifera were analysed from Ocean Drilling Program (ODP) Site 925 (4°12.249′N, 43°29.334′W, 3042.2 m present water depth), Integrated Ocean Drilling Program (IODP) Site 1264 (28°31.95′S, 2°50.73′E, 2505 m present water depth) and IODP Site 1406 (40°21.0′N, 51°39.0′W, 3798.9 m water depth). The preservation of these foraminifera ranges from frosty (Site 925) to glassy (Site 1406) (Sexton et al., 2006a). Age models are based on Expedition 342 Scientists, (2012), Liebrand et al., (2011) and Stewart et al., (2012) (and references therein) for Site 1406, Site 1264 and Site 925 respectively. *G. bulloides (s.l.)* were picked from narrow size fractions between 180 and 355 μm. Samples were cleaned by ultrasonication in deionised water to remove clays and between 6 and 29 specimens were analysed from each size fraction. The surface dwelling, symbiont-bearing foraminifera *Globigerina primordius* and asymbiotic foraminifera species *Globoquadrina dehiscens*, *Paragloborotalia siakensis/mayeri* and *Paragloborotalia bella* were also analysed at some sites, for comparison. Stable isotopes were determined by a gas source mass spectrometer (Europa GEO 20-20, University of Southampton UK) equipped with automated carbonate preparation device. Stable isotope results are reported relative to the Vienna Peedee belemnite (VPDB) standard with external analytical precision of ±0.05‰.

Foraminifera were prepared for scanning electron microscopy (SEM) by ultrasonication for 5 seconds in deionised water in order to remove adhered clays and Coccolithophores. Samples were then mounted on to the stub in the required orientation and gold coated using a Hummer VI A sputter coater. The gold coating improves the backscattering of secondary electrons from the sample, improving image quality. The stub was gold coated between one and four times at 45° angles to ensure good coverage. SEM images were then taken in secondary electron mode on the Leo 1450-VP SEM.

3.3 Results and Discussion

3.3.1 Wall texture

Similar to observations made in *G. bulloides (s.l.)* from Trinidad (Pearson and Wade, 2009), the SEM images presented here show that the wall texture of *G. bulloides (s.l.)* at Site 1406, Site 1264 and Site 925 exhibits a regular reticulate network akin to a 'honeycomb' texture (Fig. 3-2; 2-4). The lack of much digenetic alteration at Site 1406 makes the SEM images from this site ideal for more in depth analysis of the foraminiferal test. The wall texture of *G. bulloides (s.l.)* at this site is characterised by clearly defined ridges and pores at the junctions of the ridges (Fig. 3-2; 5). The wall texture of modern *G. bulloides (s.s.)* is quite different with flatter walls and pore pits penetrating an unmodified surface (Fig. 3-2; 1) (Steineck and Fleisher, 1978). The pores in modern *G. bulloides (s.s.)* are densely packed, irregular and in some cases ajoining, except in newly formed chambers. The features we describe for *G. bulloides (s.l.)* show more similarity to the *Globigerinoides* (*Genus*) (many species belonging to this Genus host symbionts). Similar to the *G. bulloides (s.l.)* the wall texture in the *Globigerinoides (Genus)* is coarsely perforated, pores are located within pits separated by ridges in a 'honeycomb' arrangement and spines are localised at ridge intersections (Steineck and Fleisher, 1978). The difference in the wall structure of the *Globigerina (Genus)*, which *G. bulloides (s.s.)* belongs to, and the *Globigerinoides (Genus)*, has been attributed to differences in the way the calcite is precipitated (Cifelli, 1982). While both genera are thought to have similar textural development, it is suggested that pore formation occurs at the same time as ridge development in the *Globigerina* group, preventing the formation of an organized honeycomb structure (Cifelli, 1982). The similarity in wall-texture between *G. bulloides (s.l.)* and modern symbiont dwelling foraminifera may

provide some potential evidence, albeit indirect, that *G. bulloides (s.l.)* hosted symbionts. It is important to note, however, the relationship between foraminiferal wall texture and ecology is not well understood (Sexton et al., 2006b). For instance, an analysis of the wall textures and $\delta^{13}C$ and $\delta^{18}O$ inferred depth habitats in late to middle Eocene foraminifera concluded that the wall textures of a planktic foraminifera is an evolutionarily conservative feature of the test, little influenced by habitat or ecology (Sexton et al., 2006b). Consequently while wall texture can be used to highlight morphological differences between *G. bulloides (s.l.)* and *G. bulloides (s.s.)*, we need to turn to geochemical data to further assess the question of symbiont activity.

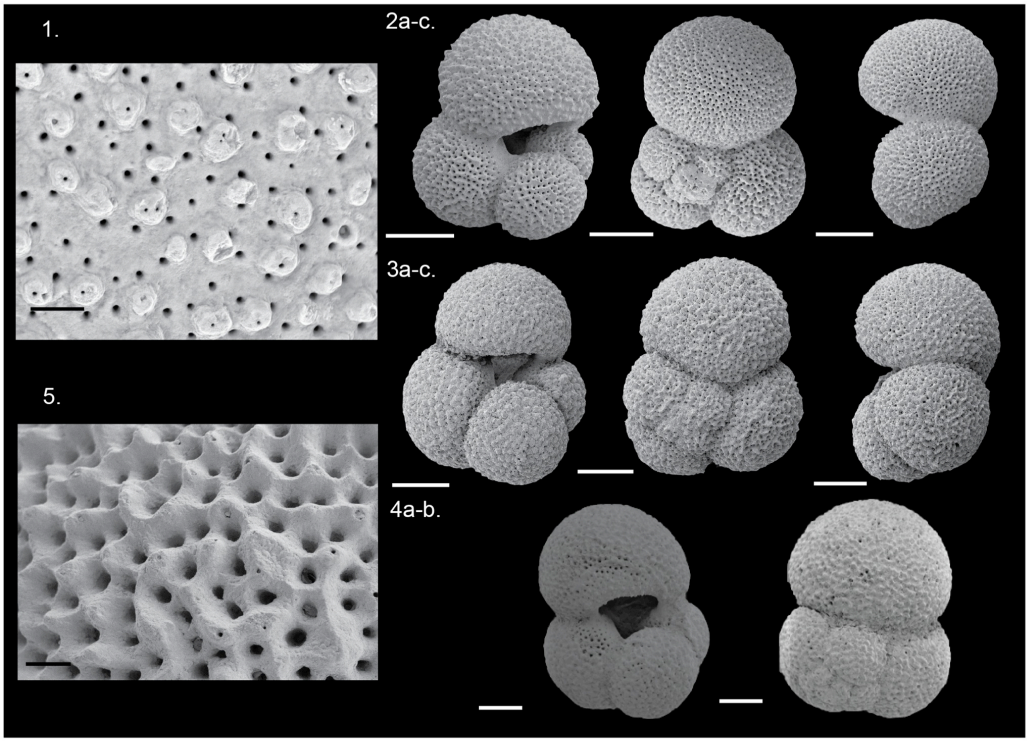

Figure 3-2: *G. bulloides* wall texture and specimens. **1.** Typical '*G. bulloides (s.s.)*' type wall texture from Holocene, north Atlantic specimen (980A 1H 2W 100-102). Photo courtesy of Michael Henehan. **2.** *G. bulloides (s.l.)* from Site 1406. (**a)** umbilical view (1406A 8H 5W 72-74); **(b)** spiral view (1406A 8H 5W 72-74); **(c)** side view (1406A 8H 5W 72-74). **3.** *G. bulloides (s.l.)* from Site 1264. (**a)** umbilical view (1264B 25H 1W 109.5-110.5); **(b)** spiral view (1264B 25H 3W 119.5-120.5); **(c)** side view (1264B 25H 1W 109.5-110.5). **4.** *G. bulloides (s.l.)* from Site 925. (**a)** umbilical view (154-925A-22R-7W, 30–32 cm); **(b)** spiral view (154-925A-22R-7W, 30–32 cm) from Stewart et al., (2012). **5.** Wall texture image of a well-preserved specimen from Site 1406 (1406A 8H 5W 72-74). A *Globigerinoides* type 'honeycomb' wall structure can be identified. For **1** and **5** the scale bar is 10µm. For **2-4** the scale bar is 100µm.

3.3.2 Carbon isotopes: interspecies offsets and body size gradients

Traditionally the presence of four isotope patterns in extinct foraminifera are used as an indicator for dinoflagellate symbionts (Norris, 1996); (1) the lowest $\delta^{18}O$ of the whole foraminifer assemblage, (2) the absence of change in $\delta^{18}O$ with increasing size fraction, (3) the most positive $\delta^{13}C$ in the assemblage, (4) a large increase in $\delta^{13}C$ with increasing size fraction. The relationship between $\delta^{13}C$ and size fraction is most commonly used to determine the presence of symbionts (Berger et al., 1978; Spero and DeNiro, 1987; Spero and Lea, 1993; Edgar et al., 2012), however, this test is not applicable to chrysophyte algal symbionts, which do not demonstrate the size fraction $\delta^{13}C$ relationship in the modern ocean (Norris, 1998; Bornemann and Norris, 2007). We employ these principles modified in light of the findings of a recent re-evaluation of core top and tow data from the modern ocean suggesting that a steep slope in the relationship of size and $\delta^{13}C$ and the lowest $\delta^{18}O$ of the assemblage are likely to be the most reliable of these criteria (Ezard et al., 2015).

Figure 3-3 shows new and published size fraction $\delta^{13}C$ data for *G. bulloides (s.l.)* taken from samples of OMT age from a latitudinal transect of sites in the Caribbean and Atlantic Ocean. Data from north/equatorial Atlantic (I)ODP Sites 1406 and Site 925 show an increase in $\delta^{13}C$ with test size with a gradient ranging between 0.0045 ± 0.002 ‰ μm^{-1} and 0.0102 ± 0.0018 ‰ μm^{-1}. These gradients are at least as great as those seen in the modern dinoflagellate symbiont-bearing foraminifera *Globigerinoides ruber* (0.0031-0.0096 ‰ μm^{-1}) and *Globigerinoides sacculifer* with sac (0.0022-0.0036 ‰ μm^{-1}) (Ravelo and Fairbanks, 1995; Elderfield et al., 2002; Friedrich et al., 2012; Birch et al., 2013). However, the gradients are also comparable to modern *G. bulloides (s.s.)* (0.0022-0.010 ‰ μm^{-1}) (Fig. 3-1) (Elderfield et al., 2002; Birch et al., 2013; Friedrich et al., 2012). The positive correlation between $\delta^{13}C$ and size fraction is not seen in our data set from South Atlantic IODP Site 1264. Figure 3-4a shows the carbon isotopic fractionation between *G. bulloides (s.l.)* and another Oligo-Miocene age surface dweller *G. primordius* for Site 925, Site 1264 and Trinidad. The modern carbon isotope offset between *G. ruber and G. bulloides (s.s.)* is also plotted for comparison. The $\delta^{13}C$ value of *G. bulloides (s.l.)* is comparable to *G. primordius*, which has the most positive $\delta^{13}C$ value in the assemblage during this time interval (Pearson and Wade, 2009). There is

no evidence in *G. bulloides* (*s. l.)* for the large carbon isotope disequilibria that define *G. bulloides (s.s.)* (Fig. 3-3a) (Elderfield et al., 2002; Friedrich et al., 2012).

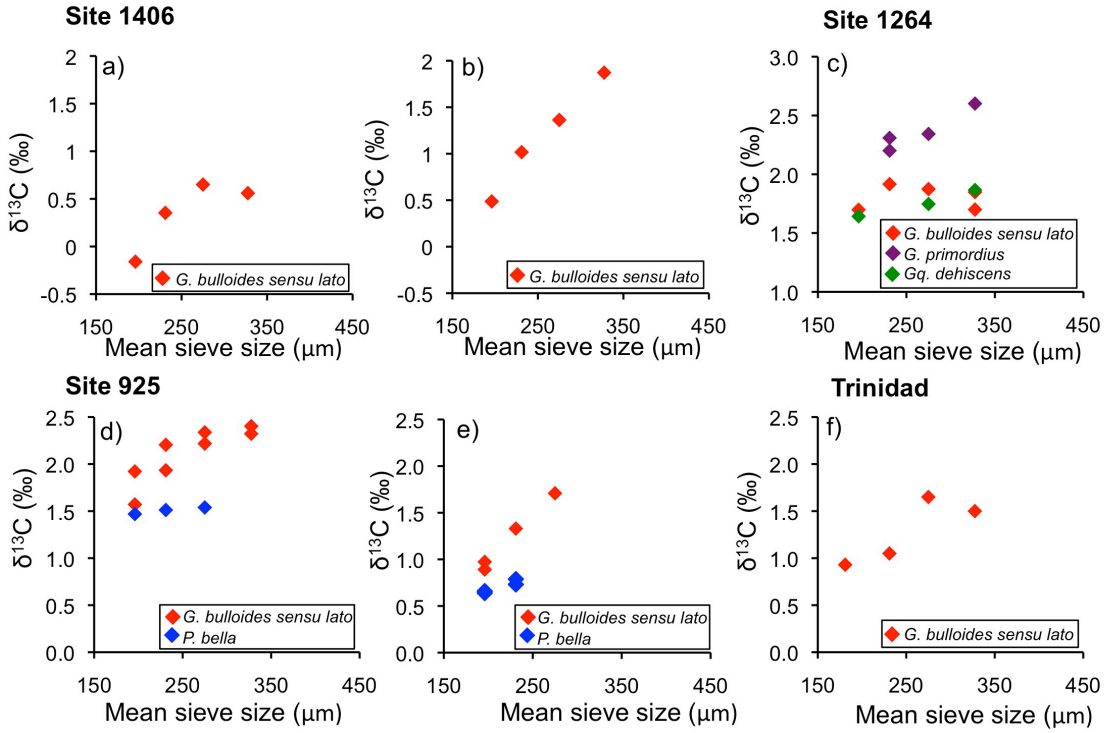

Figure 3-3: *G. bulloides (s.l.)*, *P. bella*, *G. primordius* and *Gq. dehiscens* $\delta^{13}C$ plotted against size fraction for Site 1406 (a) 21.96 Ma (b) 23.08 Ma (this study), Site 1264 (c) 22.5 Ma (this study), Site 925 (d) 22.7 Ma (e) 24.2 Ma (this study and Stewart et al., 2012) and Trinidad (f) O6 (Pearson and Wade, 2009) across the Oligocene Miocene boundary.

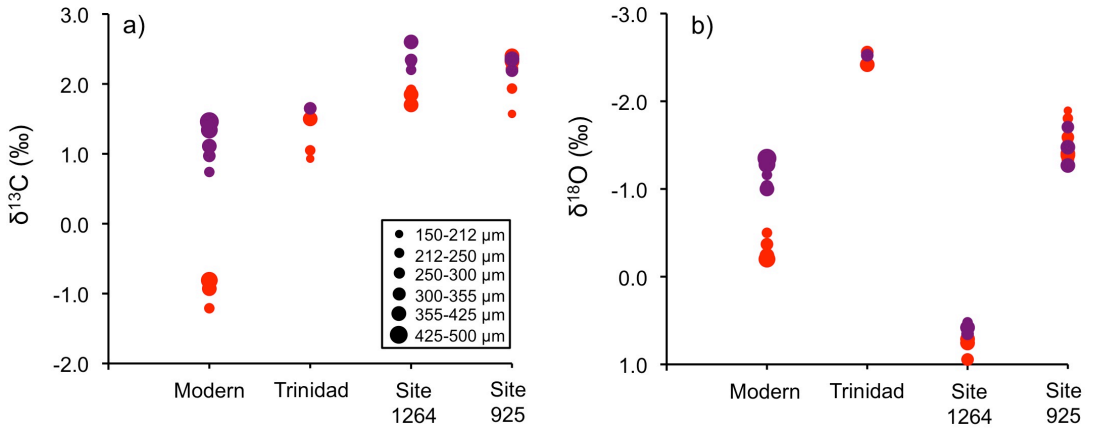

Figure 3-4: (a) $\delta^{13}C$ and (b) $\delta^{18}O$ for *G. bulloides (s.s.)* (red) and *G. ruber* (purple) plotted for the modern from (Elderfield et al., 2002). *G. bulloides (s.l.)* (red) and *G. primordius* (purple) are plotted for Trinidad (Pearson and Wade, 2009), Site 1264 (this study) and Site 925 (this study and (Stewart et al., 2012)). The size of the data point reflects the size fraction the data were analysed from.

The $\delta^{13}C$ -size fraction relationships observed in our data are consistent with data from Trinidad suggesting that the isotope patterns typically associated with dinoflagellate symbiont-bearing foraminifera are not limited to the Indian Ocean (Fig. 3-3) (Pearson and Wade, 2009). However, the correlation between $\delta^{13}C$ and body size in *G. bulloides (s.l.)* cannot be used in isolation to infer the presence of dinoflagellate symbionts across this time interval because of the similar $\delta^{13}C$- body size relationship displayed in asymbiotic *G. bulloides (s.s.)* (Fig. 3-1). In *G. bulloides (s.s.)* the positive relationship between size fraction and carbon isotopes is also accompanied by a large offset in absolute $\delta^{13}C$ values compared to other surface dwelling symbionts. These 'vital effects' cause the $\delta^{13}C$ in the foraminiferal calcite to be offset to the extent that the $\delta^{13}C$ is comparable to that of a thermocline dwelling foraminifera species (Friedrich et al., 2012). Here, we interpret the positive correlation between $\delta^{13}C$ and size fraction in the absence of pronounced $\delta^{13}C$ isotopic disequilibrium present at Site 925, Trinidad and Site 1406 as evidence that *G. bulloides* (*s.l.)* hosts dinoflagellate symbionts. However, the absence of a positive correlation between $\delta^{13}C$ and size fraction at Site 1264 means the same conclusion cannot be drawn for this site and it is possible that the foraminifera here hosts chrysophyte algal symbionts. At Site 1264 *G. primordius*, was analysed in contemporaneous samples and shows a clear relationship between $\delta^{13}C$ and size fraction (Fig. 3-3) making it unlikely that diagenetic homogenisation of the isotopes or oceanographic effects are masking the correlation of $\delta^{13}C$ and size fraction in *G. bulloides* (*s. l.)* (Pearson et al., 2001). An alternative explanation is that the species at Site 1264 may be a different morphotype of *G. bulloides* that does not host symbionts. Morphologically the *G. bulloides* specimens from Site 1264 are within the morphological variability seen in other sites, however, a degree of genetic variability has been found in modern *G. bulloides (s.s.)* in the North Atlantic suggesting that several genotypes may exist within one morphotype (Darling et al., 2003).

3.3.3 Oxygen isotopes and depth habitat

At Site 925, Trinidad and Site 1264 (where data is available) the oxygen isotope values of *G. bulloides (s.l.)* are compared to *G. primordius*, identified as having amongst the most negative $\delta^{18}O$ values in the late Oligocene assemblage (Fig. 3-4b) (Pearson and Wade, 2009; Stewart et al., 2012). The two species show similar values, suggesting that

G. bulloides (s.l.) dwelled in the surface waters as it does in the modern (*G. bulloides (s.s.)*). In figure 3-5, new and published size fraction and oxygen isotopes data are plotted for Site 925, Site 1264, Site 1406 and Trinidad. At Site 1406, Site 1264 and Trinidad there is no clear correlation between $\delta^{18}O$ and body size, whereas, both the samples from Site 925 exhibit a positive correlation between $\delta^{18}O$ and body size (Fig. 3-5). The requirement for symbionts to have access to light means that the depth habitat of symbiont-bearing foraminifera is limited to the surface waters of the ocean. In the modern ocean symbiont-bearing foraminifera have the most negative oxygen isotope values as a result of the warm temperatures found in the surface ocean. The results in this study are consistent with the analysis of the late Oligocene planktic foraminifera assemblage that showed both *G. primordius* and *G. bulloides (s.l.)* have the amongst the most negative oxygen isotope values of all the species measured (Pearson and Wade, 2009). Analysis of foraminiferal depth habitat relationships based on $\delta^{18}O$ show that while the mode of carbon synthesis may have changed through time, *G. bulloides (s.l.)* remained in the surface waters across the Miocene (Gasperi and Kennett, 1992; Majewski and Bohaty, 2010),

Patterns in $\delta^{18}O$ and size fraction are more complicated to interpret than the relationship between $\delta^{13}C$ and size fraction as conflicting explanations exist for the causes of the patterns exhibited. Norris (1996) argued that limited depth migration driven by the requirement of the photosymbionts to remain in the photic zone means that the oxygen isotopes composition of symbiont-bearing foraminifera does not change with size fraction. In contrast, it is hypothesised that the positive correlation between $\delta^{18}O$ and body size in *G. bulloides (s.s.)* is a consequence of depth migration during the life cycle and the decreasing contribution of metabolic CO_2 to the isotopic signal with size (Norris, 1996; Spero and Lea, 1996). The relationship between size fraction and $\delta^{18}O$ may alternatively be linked to the symbiont type (Ezard et al., 2015). In this interpretation a non-linear negative relationship between body size and $\delta^{18}O$ is shown to be associated with dinoflagellate-symbionts, whereas a non-linear positive relationship is indicative of species without symbionts (species with chrysophyte symbionts show a linear slightly positive relationship). The lack of correlation between size fraction and $\delta^{18}O$ at Sites 1406, 1294 and Trinidad suggests one or some combination of the following: (1) *G. bulloides (s.l.)* is not undergoing depth migration with increasing size in the same way as their modern counterparts (*G. bulloides s. s.*) (Norris, 1996). (2) The

species may host chrysophyte symbionts (which only show a slight positive relationship between size fraction and $\delta^{18}O$; Ezard et al., 2015). Whether the interpretation of Norris, (1996) or Ezard et al., (2015) is applied, the positive correlation between $\delta^{18}O$ and body size at Site 925 is consistent with a non-symbiotic foraminifera. However, in size fractions < 300 µm (the size range of the majority of foraminifera in this study), the $\delta^{18}O$ of modern symbiotic foraminifers *Orbulina universa and Globigerinoides sacculifer* positively correlates with size fraction (Birch et al., 2013). Consequently, the positive relationship between $\delta^{18}O$ and size fraction at Site 925 may be as a result of the limited size range of *G. bulloides (s.l.)*, making it difficult to analyse trends in $\delta^{18}O$ and size fraction in the adult foraminifera. However, this hypothesis does not explain why the positive correlation between size fraction and $\delta^{18}O$ is only seen at Site 925. Given the inconsistencies in the $\delta^{18}O$ -size fraction relationship exhibited in the foraminifera in this study and given the need for further validation of the use of $\delta^{18}O$ to determine symbiont type we treat the interpretation of this data with caution.

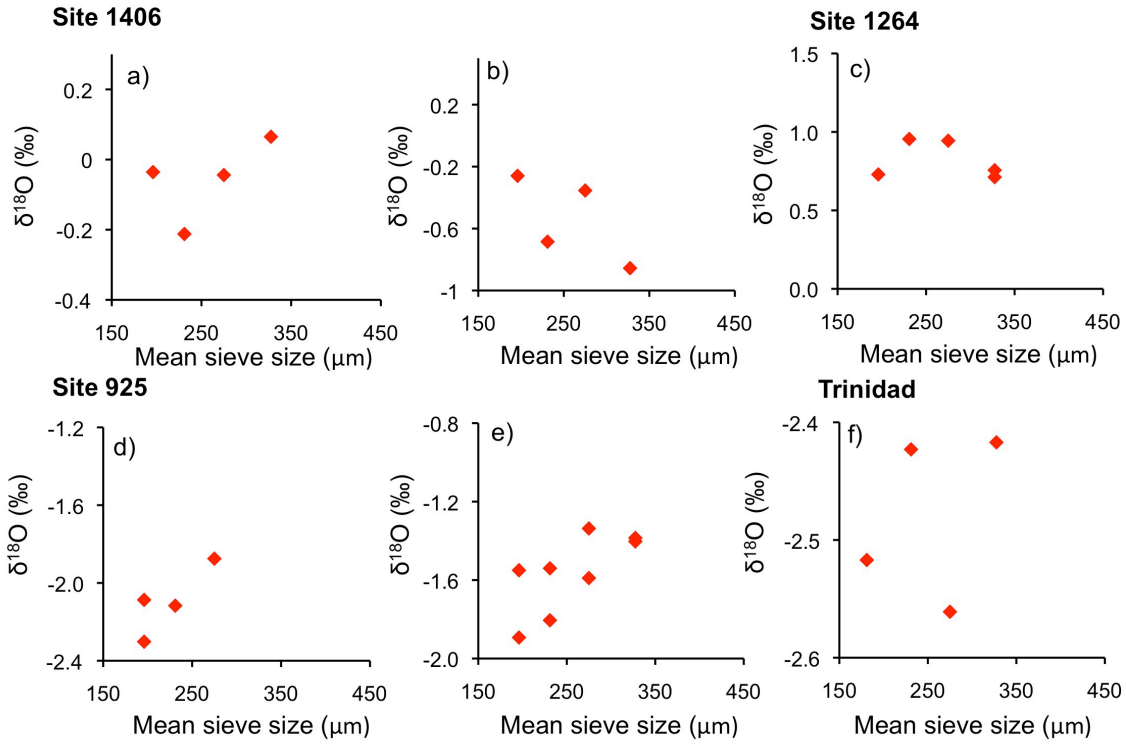

Figure 3-5: *G. bulloides (s.l.)* size fraction plotted against $\delta^{18}O$ for Site 1406 (a) 21.96 Ma (b) 23.08 Ma (this study), Site 1264 (c) 22.5 Ma (this study), Site 925 (d) 22.7 Ma (e) 24.2 Ma (this study and Stewart et al., 2012; see Appendix B for details of data from this study) and Trinidad (f) O6 (Pearson and Wade, 2009) across the Oligocene Miocene boundary.

3.3.4 Potential Causes of Change in Carbon Synthesis Method at 7 Ma

Understanding the extent to which *G. bulloides (s.s.)* and *G. bulloides (s.l.)* coexisted is key to interpreting isotopic and trace metal records produced from analysis of their tests. In Figure 3-6, we plot several datasets from the literature that contain carbon isotope data for both *G. bulloides* and an additional reference surface dweller for the same time intervals (although not in all cases the same sample) (Elderfield et al., 2002; Grant and Dickens, 2002; Ennyu and Arthur, 2004; Pearson and Wade, 2009; Friedrich et al., 2012). The reference surface dweller is plotted to ensure that any changes in the $\delta^{13}C$ composition of *G. bulloides* are not a result of changes in the $\delta^{13}C$ composition of seawater DIC. A compilation of $\delta^{13}C$ measurements (Fig. 3-6) made on dinoflagellate symbiont-bearing foraminifera is also plotted for reference (Roberts and Tripati, 2009). In the absence of SEM images to accompany these studies it is difficult to know precisely which *G. bulloides* type, as defined here, was analysed. However, the distinctiveness of the carbon isotope offset can be used to determine whether the data were generated on *G. bulloides (s.s.)* or *G. bulloides (s.l.)*. Between 7 and 24 Ma there is no discernable carbon isotope offset between *G. bulloides* and the reference surface dweller suggesting that the symbiotic form was dominant during this interval. This finding does not negate the possibility that a *G. bulloides (s.s.)* also existed and follow-up work is needed in order to fully define the prevalence of the two *G. bulloides* types across this interval. Between 0 and 7 Ma the carbon isotope difference between *G. bulloides* and the reference surface dweller is ~ 2 ‰ and in keeping with modern studies. Based on the available data it appears there is an absence of the symbiont-bearing *G. bulloides* after 6.5-7.5 Ma with the exception of one sample at 1.92 Ma. More work is needed to fully map the evolutionary history of this species.

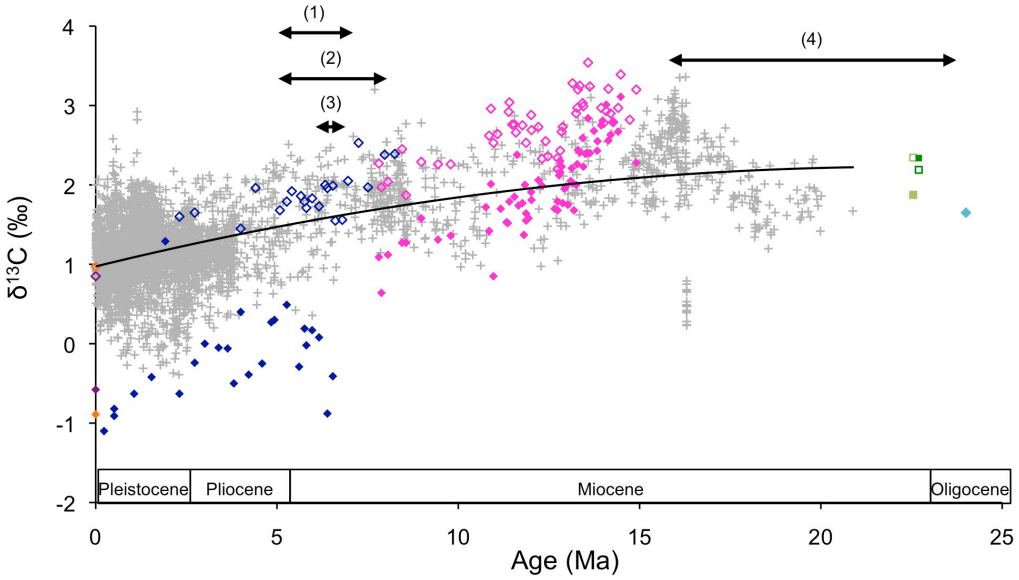

Figure 3-6: *G. bulloides* $\delta^{13}C$ plotted against time (solid diamonds). An alternative surface dweller is also plotted (open diamonds). Dark grey data are from a planktic foraminifera $\delta^{13}C$ compilation by (Roberts and Tripati, 2009). A 2nd order polynomial is fitted through the dataset. Published data for *G. bulloides* and another surface dwelling foraminifera from Friedrich et al., (2012), core MC575/1 (*G. ruber* $\delta^{13}C$ (open purple diamond) and *G. bulloides* $\delta^{13}C$ (closed purple diamond), Elderfield et al., (2002), BOFS core 31K (*G. ruber* $\delta^{13}C$ (open orange diamond) and *G. bulloides* $\delta^{13}C$ (closed orange diamond)), Grant and Dickens, (2002), DSDP Site 590 (*G. sacculifer* $\delta^{13}C$ (dark blue open diamonds) and *G. bulloides* $\delta^{13}C$ (dark blue closed diamonds)), Ennyu and Arthur, (2004), ODP Sites 1170 and 1172 (*O. universa* $\delta^{13}C$ (pink open diamonds) and *G. bulloides* $\delta^{13}C$ (pink closed diamonds)), Pearson and Wade, 2009, Trinidad (*G. primordius* $\delta^{13}C$ (light blue open diamonds) and *G. bulloides* $\delta^{13}C$ (light blue closed diamond)). Data from Site 925 *G. primordius* $\delta^{13}C$ (dark green open square) and *G. bulloides* $\delta^{13}C$ (dark green closed square) and Site 1264 *G. primordius* $\delta^{13}C$ (light green open square) and *G. bulloides* $\delta^{13}C$ (dark green closed square) from this study and Stewart et al., (2012). Key environmental and evolutionary changes are marked. (1) Coccolithophores switch to allocating more inorganic carbon to photosynthesis than to calcification to adapt to lower CO_2 conditions (Bolton and Stoll, 2013). (2) C4 plants develop a carbon-concentrating mechanism to reduce photorespiration rates and the amount of CO_2 needed by the plant (Cerling et al., 1997; Ehleringer et al., 1997). (3) Surface cooling in the mid to high latitudes, which led to strengthened oceanic latitudinal and thermal gradient (Schmidt et al., 2004b). (4) Radiation of the *Globigerinoides* group (Wei and Kennett, 1986).

Despite uncertainties in the evolutionary pathway of *G. bulloides,* there is little isotopic evidence for the presence of *G. bulloides (s.l.)* since ~ 7 Ma. Next we explore some of the potential reasons for the appearance of *G. bulloides (s.s.)* from *G. bulloides (s.l.)* during the late Miocene. The major controls on evolutionary change are separated into two categories: abiotic and biotic. Abiotic controls are primarily related to physical environmental changes whereas biotic controls focus on the processes occurring within a species and interactions between different taxa. If the extinction of *G. bulloides (s.l.)* were associated with biotic changes we would expect to see changes in the diversity or

structure of the surface dwelling community during the late Miocene. During the late Oligocene foraminiferal diversity was low and there were few species inhabiting the surface waters (Pearson and Wade, 2009). As a consequence across the Oligocene-Miocene boundary *G. bulloides (s.s.)*, along with *G. primordius*, were dominant in most surface water assemblages from the tropics (e.g. Site 925) to the high latitudes (e.g. Site 1406). The foraminifera were typically small during the Oligocene compared with modern taxa. Diversification of the *Globigerinoides (Genus)* increased the number of symbiotic surface dwellers during the early Miocene (Wei and Kennett, 1986). This radiation was completed by ~16 Ma, however, suggesting that the changes in *G. bulloides* were not driven by increased surface water planktic foraminiferal diversity. While diversity did not change across the late Miocene, low-latitude foraminiferal sizes increased sharply during the middle-late Miocene (Schmidt et al., 2004a). The maximum test size of modern day *G. bulloides (s.s.)* is, however, comparatively smaller than other low latitude foraminifers suggesting that this species did not undergo a similar increase in size. The increase in test size of foraminifera may have meant the *G. bulloides (s.l.)* was outcompeted for space and light in the surface waters.

The late Miocene is an interval of hypothesised CO_2 decline. Both Coccolithophores and land plants evolved to adapt to photosynthesising under lower CO_2 conditions between 5 and 8 Ma (Cerling et al., 1997; Ehleringer et al., 1997; Zhang et al., 2009; Bolton and Stoll, 2013). In both cases the photosynthesisers adapted carbon concentration mechanisms to increase efficiency. In C4 plants a biochemical carbon-concentrating mechanism meant the plant could reduce its photorespiration rates, reducing the amount of CO_2 needed, and also reducing rates of water loss (Cerling et al., 1997; Ehleringer et al., 1997). In Coccolithophores the phytoplankton allocated more inorganic carbon to photosynthesis than to calcification (Bolton and Stoll, 2013). It is possible the rate of symbiont photosynthesis may also have reduced under low CO_2 conditions, with those species that are better adapted having an evolutionary advantage. There is evidence that some species of Symbiodinium dinoflagellates (found in corals and some benthic foraminifera) grow more rapidly under high aqueous CO_2 (Brading et al., 2011) and consequently a fall in atmospheric CO_2 may have caused a reduction in symbiont photosynthesis. The *Globigerinoides* (*Genus*) continued to prosper during this time interval (Wei and Kennett, 1986). The differences in morphology between the *Globigerinoides (Genus)* and the *Globigerina (Genus)*, for instance the secondary

aperture in the *Globigerinoides (Genus)*, may explain the different success rate of each group.

The alternative hypothesis is that environmental changes may have lead to an increase in the prominence of *G. bulloides (s.s.)*. The late Miocene was dominated by surface cooling in the mid to high latitudes, which led to strengthened oceanic latitudinal thermal gradients (Schmidt et al., 2004a; Schmidt et al., 2004b). In combination all these factors acted to increase the number of ecological niches available to planktic foraminifera (Wei and Kennett, 1986). The rise of *G. bulloides (s.s.)* may therefore have been a result of an increase in the ecological niches, such as the upwelling regions, where the species dominates today and nutrients are abundant so that the presence of symbionts has no functional advantage.

3.4 Conclusions

The life habit of *G. bulloides (s.l.)*, characterised in this study, was fundamentally different to modern taxa. This is evident in the isotope data, which points to the presence of a symbiont-bearing *G. bulloides* across this interval. Consequently modern stable isotope and trace metal calibrations are not directly applicable to the symbiotic *G. bulloides (s.l.)*. Although more work is needed to determine the extent to which the two types of *G. bulloides* coexisted, there is an apparent absence of *G. bulloides (s.l.)* after 6 Ma. The late Miocene was an interval of both environmental and evolutionary changes in the surface water of the ocean that could in combination explain the decline of the *G. bulloides (s.l.)* and the simultaneous rise of the asymbiotic *G. bulloides (s.s.)*.

Chapter 4: The use of benthic and planktic foraminiferal $\delta^{11}B$ and $\delta^{13}C$ to calculate the boron isotope composition of seawater.

Acknowledgements:

The following chapter is written in the style of a research article with the intention of future publication. The contributions of co-authors to this work are detailed below.

Rosanna Greenop: data collection and analysis, calculating $\delta^{11}B_{sw}$, data interpretation, manuscript drafting and production of figures.

Paul A. Wilson: manuscript drafting

Gavin L. Foster: data interpretation and manuscript drafting

Mathis P. Hain: produced the model output from CYCLOPS, formulated matlab code to calculate $\delta^{11}B_{sw}$

Sindia S. Sosdian: Provided $\delta^{11}B$ planktic data, aided in the collection of some of the $\delta^{11}B$ benthic data and $\delta^{13}C$ data

Caroline H. Lear: Provided some of the benthic foraminifera for $\delta^{11}B$ analysis

Abstract:

The boron isotope composition ($\delta^{11}B$) of planktic foraminiferal calcite, which reflects seawater pH, is a well-established proxy for reconstructing atmospheric CO_2. However, in order to translate the $\delta^{11}B$ into pH it is necessary to know the boron isotope composition of the seawater ($\delta^{11}B_{sw}$) the calcite precipitated from. While a number of $\delta^{11}B_{sw}$ reconstructions exist, the discrepancy between the different methods means there are uncertainties in this parameter further back in time. Here we present a new $\delta^{11}B_{sw}$ record based on the $\delta^{11}B$ difference between planktic and benthic foraminifera and the pH gradient between surface and deep. We calculate $\delta^{11}B_{sw}$ two ways: 1) Assuming a constant pH gradient between surface and deep; and (2) Using the $\delta^{13}C$ gradient between surface and deep to account for change is the pH gradient through time (given the coupling between $\delta^{13}C$ and pH in the water column). The $\delta^{11}B_{sw}$ records based on the

fixed pH gradient and the $\delta^{11}B$- $\delta^{13}C$ gradient methods show a good level of consistency with each other and are thus combined to provide the most robust estimate. The $\delta^{11}B_{sw}$ record produced suggests that $\delta^{11}B_{sw}$ is around 1.5 ‰ lower than today at ~ 38 ‰ at the Oligocene Miocene boundary, and decreases to a minimum of ~ 37 ‰ at 14 Ma. From this middle Miocene minimum, $\delta^{11}B_{sw}$ then increases to the modern value (39.61 ‰) through the late Miocene and Pliocene. A similar pattern of change is evident in the seawater isotopic composition of Mg, Li and Ca, a shift in the isotopic composition of all four elements is evident since the middle Miocene. The similarity in the evolution of Li, B, Ca (and to a lesser extent Mg) over at the least the past 15 Myrs and present suggests that the processes responsible must be consistent across the systems. Analysis of the fluxes of the four elements into and out of seawater suggests that the most likely cause of the shift during the middle Miocene is a change in the isotopic composition of the riverine input through time, potentially driven by an increase in secondary mineral formation.

4.1 Introduction

In order to determine the relationship between CO_2 and climate in the geological past, it is key to calculate reliable estimates of absolute CO_2 through time. In recent years the boron isotope composition ($\delta^{11}B$) of foraminiferal calcite has become one of the most commonly used tools to reconstruct CO_2 beyond the last 800 kyrs and throughout the Cenozoic era (Foster, 2008; Honisch et al., 2009; Pearson et al., 2009; Henehan et al., 2013; Greenop et al., 2014; Martinez-Boti, et al., 2015a). Yet long-term change in the boron isotope composition of seawater ($\delta^{11}B_{sw}$) is poorly constrained and represents a major contributor to the uncertainties associated with CO_2 estimates made in this way. In the modern ocean the $\delta^{11}B_{sw}$ is well mixed and a conservative element with an invariant isotopic ratio (39.61‰; Foster et al., 2010), but this value is subject to change through geological time. The residence time of boron in the ocean has been estimated at between 11 and 17 Myrs (Lemarchand et al., 2002b). Therefore we can expect the uncertainty associated with $\delta^{11}B_{sw}$ to be an important factor in CO_2 estimates beyond the late Pliocene.

The ocean boron budget and its isotopic composition are controlled by a number of inputs and outputs (Fig. 4-1). However, the magnitude of the boron fluxes between land,

the ocean and atmosphere are still poorly understood and therefore residence time and changes in both concentration ($[B]_{sw}$) and isotope ratio ($\delta^{11}B_{sw}$) through time are uncertain. Typically the main inputs of B into the ocean are cited as being silicate weathering, delivered to the ocean via rivers (Lemarchand et al., 2002b), hydrothermal vents (Spivack and Edmond, 1987) and fluid expelled from accretionary prisms (You et al., 1993). The major outputs are oceanic crust alteration (Spivack and Edmond, 1987), adsorption onto sediments (Palmer et al., 1987) and co-precipitation into carbonates (Hemming and Hanson, 1992). In all three cases the ^{10}B isotope is preferentially removed and consequently the resultant seawater is isotopically heavier (39.61‰) than the inputs (average ~ 10.4‰). Atmospheric boron may also be an important flux both in and out of the ocean (Park and Schlesinger, 2002). While some studies have suggested that precipitation within the catchment area may be an important factor controlling the $\delta^{11}B$ of rivers (Rose-Koga et al., 2006), other studies have shown atmospheric boron to be a secondary control on riverine boron isotope composition (Lemarchand and Gaillardet, 2006).

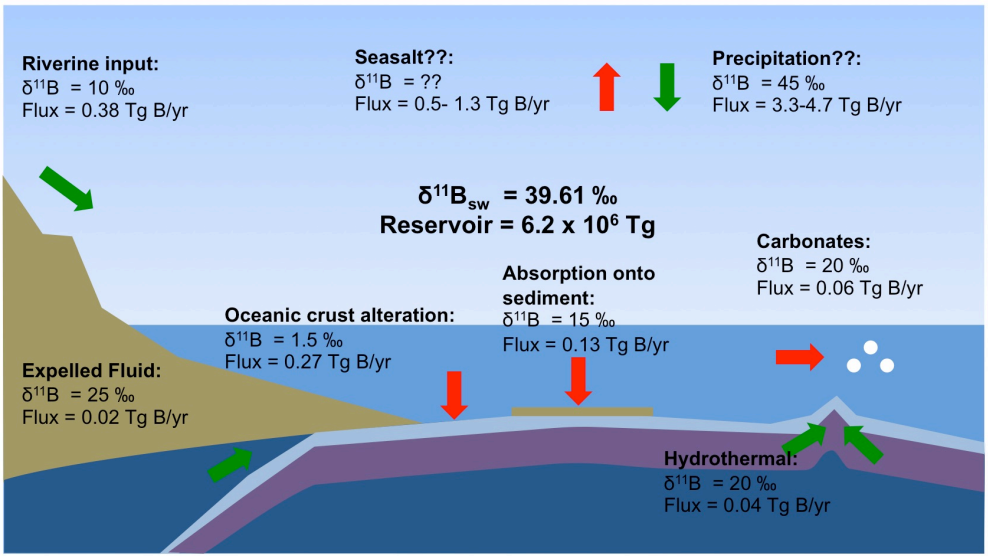

Figure 4-1: The oceanic boron cycle. Fluxes are from (Lemarchand et al., 2002b) and (Park and Schlesinger, 2002). Isotopic compositions are from (Spivack and Edmond, 1987; Hemming and Hanson, 1992; You et al., 1993; Smith et al., 1995; Lemarchand et al., 2002b; Foster et al., 2010).

Unlike many other isotopic systems (e.g. Mg, Ca, Li, Sr) to date no archive has been discovered that simply records the $\delta^{11}B$ of seawater. This, like the basis of the $\delta^{11}B$-pH proxy, is a result of the pH dependency of B speciation in seawater (Zeebe and Wolf-Gladrow, 2001; Chapter 2). Consequently, marine precipitates preferentially

incorporate one of the isotopically distinct aqueous boron species, which imparts a pH dependency. Empirical reconstructions of $\delta^{11}B_{sw}$ must therefore use "indirect" approaches; so far four methods have been applied to the Cenozoic (0-65 Ma) (Fig. 4-2). Firstly, geochemical modelling of the changes in the flux of boron in and out of the ocean through time has been used to suggest that the $\delta^{11}B_{sw}$ increased from 37‰ at 60 Ma to 40‰ +/- 1‰ at the present day (Lemarchand et al., 2002b). However, there are uncertainties associated with quantification of, and controls on, the oceanic inputs and outputs of boron in to the ocean (Lemarchand et al., 2002b). For instance, it is possible that subtle variations in poorly constrained factors such as crustal permeability, lifetime of water-rock interactions and expansion rate of the oceanic ridge can have a large effect (variations between 30‰ and 50‰ at a 10 million year scale) on the amount and isotopic composition of the boron removed from the ocean during oceanic crust alteration (Simon et al., 2006). These issues coupled with uncertainties in the magnitude of the atmospheric boron flux (Park and Schlesinger, 2002), make direct geochemical modelling of the evolution of $\delta^{11}B_{sw}$ an unconstrained practise.

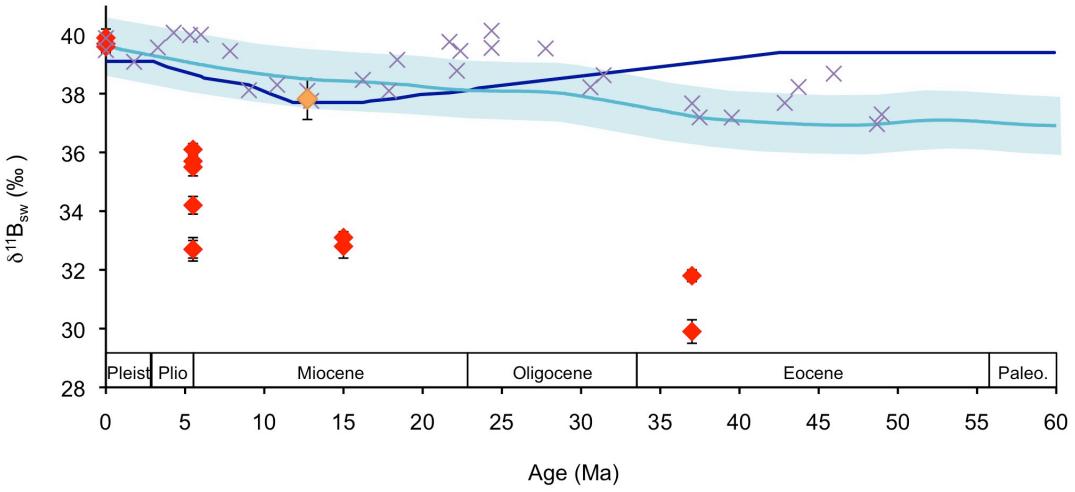

Figure 4-2: A compilation of published $\delta^{11}B_{sw}$ records. Seawater composition measured in halites (red diamonds) from (Paris et al., 2010), reconstructed from foraminifera depth profiles (dark blue line and orange diamond) from (Pearson and Palmer, 2000) and (Foster et al., 2012) respectively, numerical modeling (light blue line) with light blue shaded area showing ± 1 ‰ confidence interval, (Lemarchand et al., 2002b) and benthic $\delta^{11}B$ (purple crosses) from (Honisch et al., 2012).

The boron isotopic composition of marine halites and sea salts has also been used to reconstruct the boron isotope composition of the ocean in the past (Paris et al., 2010). Results from studies employing this method suggest that the $\delta^{11}B_{sw}$ has varied by 8‰

over the Cenozoic (Fig. 4-2) (Paris et al., 2010). However, evaporates, by their very nature are created from a modified seawater solution isolated from the open ocean and it is unknown whether the isotope values are truly representative. Brine and halite fractionation offsets of -20‰ to -30‰ and -5‰ have been found in laboratory and natural environments respectively casting doubt over the validity of the assumption that no fractionation occurs during halite formation (Vengosh et al., 1992; Liu et al., 2000). However, given that these fractionations, and riverine input during basin isolation, will drive the evaporate-hosted boron to lighter isotope values the fluid inclusion record likely provides a constraint on the lower limit for the $\delta^{11}B_{sw}$ through time (i.e. $\delta^{11}B_{sw}$ is heavier than the halite fluid inclusions of (Paris et al., 2010).

An alternative semi-empirical approach uses assumptions regarding the evolution of Cenozoic deep-ocean pH and a benthic $\delta^{11}B$ record to determine changes in $\delta^{11}B_{sw}$ (Fig. 4-2). Based on the muted glacial-interglacial change in the $\delta^{11}B$ of benthic foraminifera *Cibicidoides wuellerstorfi* (Honisch et al., 2008), this method assumes that deep-sea pH variations due to changes in pCO_2 are relatively small compared to those at the surface on short (e.g., glacial/interglacial) time scales, whereas long-term variations in CO_2 that are accompanied by changes in terrestrial weathering will be recorded (Raitzsch and Honisch, 2013). However, an alternative study of glacial-interglacial deep ocean pH change in the Caribbean Sea suggests that benthic $\delta^{11}B$ varied by ~1 ‰ (~ 0.15 pH units) and consequently the assumption of constant deep-sea pH on short timescales may not be valid (Yu et al., 2010). In order to constrain these long-term variations in CO_2, and calculate $\delta^{11}B_{sw}$ from the $\delta^{11}B_{benthic}$, estimates of surface water pH are taken from the model output of Ridgwell, (2005) and carbonate system calculations of Tyrrell and Zeebe, (2004). In Tyrrell and Zeebe, (2004) surface water pH is calculated from $[CO_3^{2-}]$, determined from surface water omega (reconstructed from the CCD, [Ca] and [Mg]) and atmospheric CO_2 (from the GEOCARB-III model; Berner and Kothavala, 2001). In the modeling study of Ridgwell, (2005) the surface water saturation state is calculated from sea level, [Ca], bicarbonate weathering flux and atmospheric CO_2 proxy data. Some of the CO_2 data is derived using the boron isotope-pH proxy, leading to some circularity in the methodology. The average surface water pH output from the two approaches is used (a near linear surface water pH increase of 0.39 over the past 50 myrs). Based on carbon cycle sensitivity experiment that show that an assumption of similar past and modern surface-to-deep gradients in $[CO_3^{2-}]$ is reasonable (Tyrrell and

Zeebe, 2004), a constant surface-to-depth pH gradient of –0.3 units has been used to infer the concurrent change in deep-sea pH (Raitzsch and Honisch, 2013). While this method may shed some light on the evolution of $\delta^{11}B_{sw}$ through time, it cannot be used to determine pH from $\delta^{11}B$ of foraminiferal calcite because the $\delta^{11}B_{sw}$ record is partially determined by the surface water pH estimate derived from ocean carbonate system calculations and modelling experiments. Furthermore, given the close coupling of atmospheric CO_2 levels and surface water pH and the variability in CO_2 proxies through the Cenozoic, the assumption that pH has changed linearly through the Cenozoic is most likely an oversimplification. By applying the linear assumption to benthic $\delta^{11}B$, any variability in the record that is not described by this trend is being attributed to changes in $\delta^{11}B_{sw}$.

One of the big challenges of reconstructing a $\delta^{11}B_{sw}$ record empirically is determining $\delta^{11}B_{sw}$ without relying on independent pH constraints. One way to avoid having to use absolute pH reconstructions is to use the non-linear relationship between $\delta^{11}B$ and pH alongside known pH gradients in the ocean to estimate $\delta^{11}B_{sw}$. The non-linear relationship between $\delta^{11}B$ and pH means that the calculated pH difference between two $\delta^{11}B$ data points varies as a function of $\delta^{11}B_{sw}$ (Fig. 4-3). Consequently if the size of the pH gradient is known the appropriate $\delta^{11}B_{sw}$ value can be assigned so that the $\delta^{11}B$ derived pH gradient matches that known value.

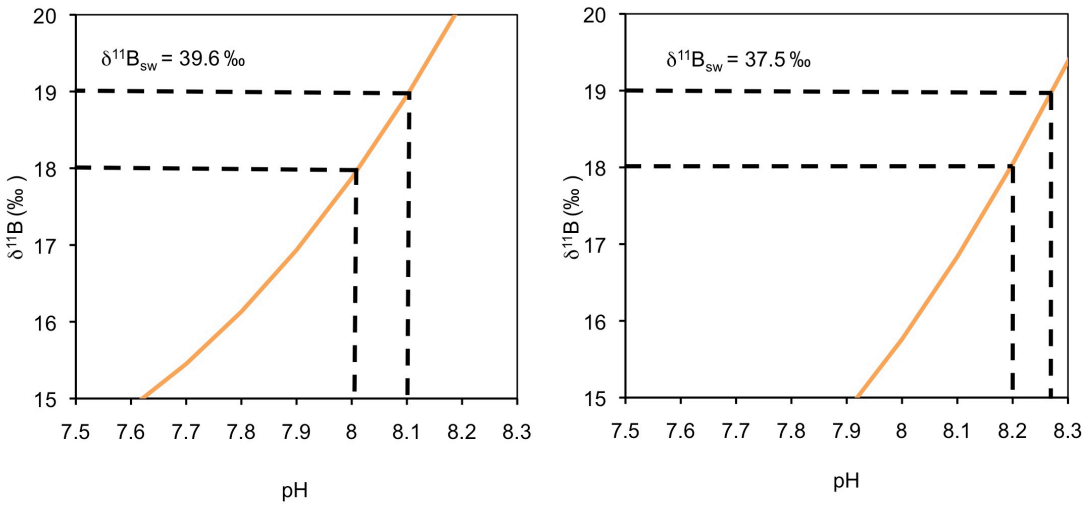

Figure 4-3: The evolution of $\delta^{11}B$ of borate ion with pH for $\delta^{11}B_{sw}$ of 39.61‰ and $\delta^{11}B_{sw}$ of 37.5‰. Calculated using B_T= 432.6 µmol/kg (Lee et al., 2010) and α_B= 1.0272 (Klochko et al., 2006). Note the difference in pH gradient for a given $\delta^{11}B$ difference at the two different $\delta^{11}B_{sw}$.

Previously this approach has been applied to pH variations in the surface ocean (using the $\delta^{11}B$ from surface and thermocline dwelling foraminifera) (Fig. 4-2) (Palmer et al., 1998). High pH exists in oceanic surface waters as a result of the removal of dissolved inorganic carbon during photosynthesis, the sinking and subsequent respiration of the organic matter releases DIC at depth, causing pH to decrease from the surface waters to deeper waters. In a particular water column profile, the minimum pH is found in the oxygen minimum zone. Consequently if the boron isotope value of a mixed layer dwelling species and near oxygen minimum zone dweller is known, a value for $\delta^{11}B_{sw}$ can be calculated that is consistent with the expected pH gradient (Pearson and Palmer, 1999). The resultant curve produced by this method shows $\delta^{11}B_{sw}$ varies between 37.7‰ and 39.4‰ through the Cenozoic (Fig. 4-2) (Pearson and Palmer, 2000). However, a number of problems exist with this record. Firstly, the applicability of this $\delta^{11}B_{sw}$ record (derived from $\delta^{11}B$ data measured using NTIMS) to $\delta^{11}B$ records generated using the MC-ICPMS is questionable. While interlaboratory comparisons have shown that relative changes are consistent for modern carbonate samples (Foster et al., 2013), this has not been tested on an extensive range of samples. In addition, this $\delta^{11}B_{sw}$ record is determined using a fractionation factor of 1.0194 (Kakihana et al., 1977), whereas recent experimental data have shown the value to be higher (1.0272 ± 0.0006, Klochko et al., 2006). Thirdly, given our understanding of the $\delta^{11}B$ difference between species/size fractions (Foster, 2008; Henehan et al., 2013), the mixed species and size fractions used to make the $\delta^{11}B$ measurements may have increased the uncertainty in the reconstructed $\delta^{11}B$ gradients. It is also questionable whether the foraminifera available captured the full surface to thermocline pH range. Consequently, while the estimates from (Pearson and Palmer, 1999) show that the rationale behind this approach yields useful $\delta^{11}B_{sw}$ estimates, the underlying measurements and some of the key assumptions may have led to some uncertainties in the record.

4.2 Rationale

Here we apply the methodology first outlined by Pearson and Palmer (1999), however, instead of analysing gradients within the surface water, we use the pH gradient between the surface (planktic foraminifera) and deep-ocean (benthic foraminifera). This approach has been applied to the middle Miocene where it has yielded a $\delta^{11}B_{sw}$ of 37.82‰ (Foster et al., 2012). The major limitation of this approach concerns the

assumption of a constant pH gradient through time. A useful extension to this method therefore uses $\delta^{13}C$ of foraminiferal calcite to estimate the surface to deep pH gradient and determine $\delta^{11}B_{sw}$ (Foster et al., 2012). While geochemical modeling has shown that it is likely the surface to deep pH gradient of the whole ocean has mostly likely remained constant through time (Tyrrell and Zeebe, 2004), it is difficult to determine the extent to which this is true for a specific site. Following Foster et al., (2012) we use the $\delta^{13}C$ composition of the planktic and benthic foraminifera in order to correct for any changes in the pH gradient. Any process that changes the ratio of total alkalinity to total dissolved inorganic carbon could change the pH depth profile. The main modifying factors are changes in the organic carbon pump and ocean circulation. The organic carbon pump modifies the pH profile as photosynthesis removes DIC from the surface waters and oxidation of organic matter at depth adds DIC therefore the relative rates of these two processes could change the surface to deep pH gradient. Like pH, the carbon isotopic composition of DIC is also largely controlled by the operation of the organic carbon pump as the $\delta^{13}C$ composition of the DIC is typically isotopically heavy in the surface waters (as a result of photosynthesis) and isotopically light at depth (because of the remineralisation of organic matter). A change in the relative rates of these two processes therefore changes the surface to deep gradient of both pH and $\delta^{13}C_{DIC}$ and consequently they are well correlated in the oceans (Fig. 4-4). Ocean circulation can also modify both the pH and $\delta^{13}C_{DIC}$ in the ocean (Fig. 4-5). Typically, the longer a deep water mass has been isolated from the surface the more remineralised organic carbon accumulates (with a light isotopic composition), lowering both the pH and the $\delta^{13}C$. Consequently the age of the water mass bathing the deep ocean (e.g. north Atlantic deep-water versus Antarctic bottom water in the Atlantic; Fig. 4-5) will influence both the surface to deep pH gradient and $\delta^{13}C_{DIC}$ gradient in the ocean.

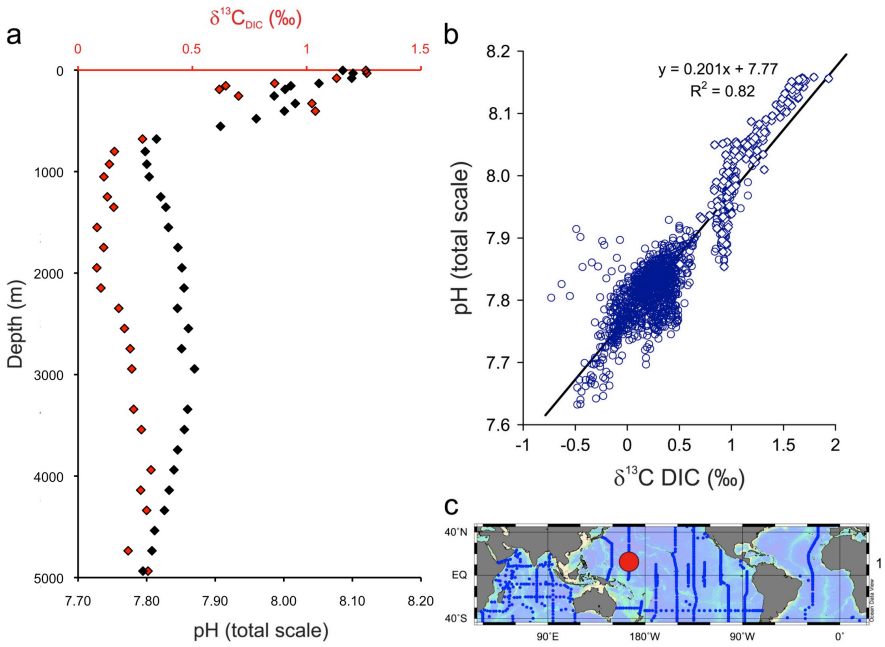

Figure 4-4: pH and $\delta^{13}C_{DIC}$ relationships in the modern ocean adapted from Foster et al., (2012). (a) Depth vs. pH and $\delta^{13}C_{DIC}$ at a site in the eastern Indian Ocean (S15° 58' 15" E111° 18' 10") (Key et al., 2004). (b) Cross plot of pH vs. $\delta^{13}C_{DIC}$ for all the sites shown in (c; open circles). Because of anthropogenic acidification and the Seuss effect only data from >1500 m are plotted in (b). Also shown in (b) are the data from a transect in the North Atlantic (from 0 to 5000 m) where the effects of anthropogenic perturbation on both parameters have been corrected.

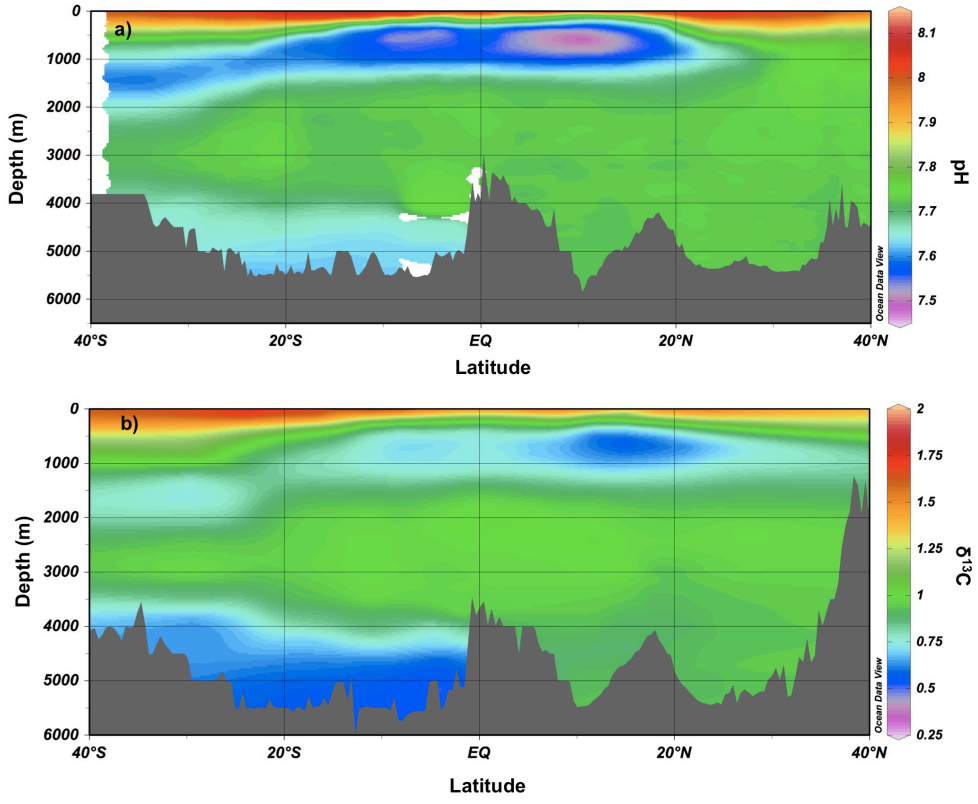

Figure 4-5: Latitudinal cross-section through the Atlantic showing a) pH variations b) the $\delta^{13}C$ composition. Data is plotted using Ocean Data View. pH data is from the CARINA dataset and the $\delta^{13}C$ data is from the GLODAP data compilation (Key et al., 2004).

Based on the rationale outlined above, a change in the $\delta^{13}C$ gradient between benthic and planktic foraminifera can be used (after accounting for vital effects) to determine changes in the surface to deep pH gradient. However, this method relies on the assumption that the relationship between pH and $\delta^{13}C$ has remained constant through time. In Foster et al., (2012) some potential secondary controls on the slope of the pH vs. $\delta^{13}C_{DIC}$ gradient were identified as follows: (i) the strength of the alkalinity pump which changes ALK/DIC (and hence pH) with a ratio of roughly 2/1 but does not significantly influence $\delta^{13}C_{DIC}$ (ii) the extent and temperature of air–sea gas exchange at high latitudes which modifies CO_2 solubility and $\delta^{13}C_{DIC}$ of water masses ventilated in these regions and (iii) the concentration of CO_2 which influences the magnitude of the carbon isotopic fractionation between phytoplankton and $[CO_2]_{aq}$ and the magnitude of the $\delta^{13}C_{DIC}$ gradient that develops.

So far the methods outlined by Foster et al., (2012) have only been used on a single time slice. Here we present a Neogene benthic $\delta^{11}B$ record at approximately 1 Myr resolution. Coupled with planktic $\delta^{11}B$ measurement made on the same samples we use two approaches to calculate $\delta^{11}B_{sw}$ based on $\delta^{11}B$ measured in planktic-benthic pairs. In the first we assume the pH gradient has remained constant at 0.2 units through time. In the second approach we utilise benthic-planktic $\delta^{13}C$ gradients to correct for changes in the strength of organic carbon pump and circulation through time. In addition we use a biogeochemical box model to assess the extent to which the relationship between pH and $\delta^{13}C$ gradients has remained constant under a range of different carbon system and oceanographic perturbations.

4.3 Methods

4.3.1 Site Locations and Age Models

Foraminifera from four sites are used to construct the planktic-benthic $\delta^{11}B$ pairs; ODP Site 758 and ODP Site 999 for the Pleistocene and Pliocene samples and ODP Site 926 and Site 761 for the Miocene. We also incorporate the middle Miocene planktic-benthic pair from Site 761 in Foster et al., (2012). The Site 999 age model for the Pleistocene is from Chalk et al., (in prep.) and for the Pliocene is from Haug and Tiedemann (1998). The age model for Site 758 is based on Chen et al., (1995). The ODP Site 926 age

model for the mid to late Miocene is from Zeeden et al., (2013), middle Miocene is Flower et al., (1997) and for the early Miocene is Pälike et al., (2006). The age model for the middle Miocene at Site 761 is from Holbourn et al., (2004).

4.3.2 Boron Isotope Analysis and pH Calculation

The boron isotope measurements (described in delta notation as $\delta^{11}B$ – permil variation) were made relative to the boric acid standard SRM 951; (Catanzaro et al., 1970). Boron was first separated from the Ca matrix prior to analysis using the boron specific resin Amberlite IRA 743 following (Foster et al., 2013). The boron isotopic composition was then determined using a sample-standard bracketing routine on a ThermoFisher Scientific Neptune multicollector inductively coupled plasma mass spectrometer (MC-ICPMS) at the University of Southampton (closely following Foster et al., 2013). Analysis was conducted on benthic foraminifera *Cibicidoides wuellestorfi* or *Cibicidoides mundulus* from the > 250μm depending on which species were most abundant in each sample. The $\delta^{11}B$ of both *Cibicidoides* species shows no offset from the theoretical $\delta^{11}B$ of the borate ion and therefore no calibration is needed to correct for species-specific offsets (Rae et al., 2011). The planktic species used to construct the benthic-planktic pairs changes through time, as a single species is not available for the entire Neogene (see Appendix C.2 for summary).

In addition to $\delta^{11}B_{calcite}$, temperature and salinity are also needed to calculate pH from $\delta^{11}B$. Here planktic SSTs are calculated from tandem Mg/Ca analyses on planktic foraminifera (with a conservative ± 2ºC, 95% confidence interval). Adjustments were made for changes in the Mg/Ca_{sw} using the record of (Horita et al., 2002) and correcting for changes in dependence on Mg/Ca_{sw} following (Evans and Muller, 2012) using H = 0.41 calculated from *G. sacculifer* (Delany et al., 1985; Hasiuk and Lohmann, 2010; Evans and Muller, 2012) using the equations:

$$Mg/Ca_{sw.c} = (Mg/Ca_{sw.a} / Mg/Ca_{sw.m})^{0.41} \qquad (4.1)$$

Where $Mg/Ca_{sw.c}$ is the correction factor applied to the temperature equation for changing Mg/Ca_{sw}, $Mg/Ca_{sw.a}$ is the estimated Mg/Ca_{sw} for the age of the sample and $Mg/Ca_{sw.m}$ is modern Mg/Ca_{sw}. Temperature is then calculated using the generic planktic

foraminifera calibration of (Anand et al., 2003) and including a correction factor for Mg/Ca_{sw}.

$$Temperature = LN(Mg/Ca_{test}/(0.38 * Mg/Ca_{sw.c}))/0.09 \qquad (4.2)$$

Mg/Ca analysis was conducted on a small aliquot of the sample dissolved for isotope analysis at the University of Southampton using a ThermoFisher Scientific Element 2 XR. Al/Ca was also measured to assess the competency of the sample cleaning (in all cases Al/Ca < 100 μmol/mol). Due to complications with the Mg/Ca-temperature proxy in benthic foraminifera (Elderfield et al., 2006), bottom water temperatures (BWTs) are estimated here by taking the temperature change from the Mg/Ca temperature compilation of (Cramer et al., 2011), using the calibration of Lear et al., (2010) and applying this change to the modern bottom water temperature at each site taken from the nearest GLODAP site (with a conservative ± 2ºC, 95% confidence interval). SSS are held constant at modern values determined from the nearest GLODAP site (± 2 ‰ uncertainty, 95% confidence interval) for the entire record.

The majority of the $\delta^{13}C$ data were measured at Cardiff University on a ThermoFinnigan MAT 252 coupled with a Kiel III carbonate device for automated sample preparation. Additional samples were measured on a gas source mass spectrometer Europa GEO 20-20, University of Southampton UK equipped with automated carbonate preparation device and on a Finnigan MAT 253 gas isotope ratio mass spectrometer connected to a Kiel IV automated carbonate preparation device at the Zentrum für Marine Tropenökologie (ZMT), Bremen. Some of the Pleistocene benthic $\delta^{13}C$ from Site 999 are from Chalk et al., (in prep) and the Pliocene benthic $\delta^{13}C$ from Site 999 was taken from the nearest sample in Haug and Tiedemann, (1998) (A description of the source of $\delta^{13}C$ for each sample is available in Appendix C.3). Stable isotope results are reported relative to the Vienna Peedee belemnite (VPDB) standard. An adjustment for vital effects on the $\delta^{13}C$ of *G. ruber* (+0.94 ‰; Spero et al., 2003), *G. trilobus*/*G. praebulloides* (+0.46 ‰; Spero et al., 2003; Al-Rousan et al., 2004;) and *C. mundulus* (+0.47 ‰; McCorkle et al., 1997) is applied to calculate the $\delta^{13}C$ of DIC. No adjustment is applied to the data from *C. wuellestorfi* (McCorkle et al., 1997).

4.3.3 Modelling the evolution of pH to $\delta^{13}C$ gradient through time

The conversion of $\delta^{13}C$ gradient to pH gradient is determined from numerical simulations using the CYCLOPS biogeochemical box model with the addition of a dynamical lysocline, a subantarctic zone surface box and a polar Antarctic zone box (Hain et al., 2010). The robustness of the relationship between $\delta^{13}C$ and pH in the Atlantic was tested under a range of different oceanographic scenarios including different stratification levels and surface nutrient concentrations in the polar Antarctic zone, 'glacial' versus 'interglacial' circulation regimes and with variable CO_2 air/sea gas-exchange as outlined in (Hain et al., 2010). In addition the model was run under differing [Ca] (1x to 4x modern), CCD depths (3.5-5.5 km Pacific CCD depth) and CO_2 levels (200-1000 ppm). While the $\delta^{13}C$ to pH relationship is only modelled for the Atlantic Ocean and therefore may be less applicable to the Indian Ocean sites, it should still give a first order indication of the extent to which the $\delta^{13}C$ to pH relationship remained stable over time.

4.3.4 Assessing Uncertainty

$\delta^{11}B_{sw}$ was calculated for each timeslice with uncertainties in temperature (± 2 ºC uncertainty), salinity (± 2 ‰ uncertainty), $\delta^{11}B_{planktic}$ (± 0.15-0.42 ‰), $\delta^{11}B_{benthic}$ (± 0.21-0.61 ‰), the fixed pH gradient 0.2 (± 0.05 pH units) and the $\delta^{13}C$-pH gradient relationship (± 0.05 pH units) determined using a Monte Carlo simulation (n = 1000). The Monte Carlo simulation allows us to fully account for the combined effect of the required parameters on the calculated $\delta^{11}B_{sw}$. Given the long (11-17 Ma; Lemarchand et al., 2002b) residence time of boron in seawater, short-term variability can be ascribed to either uncertainty or short-term variability in pH/$\delta^{13}C$ relationship or average pH gradient, which can be smoothed to obtain average $\delta^{11}B_{sw}$ estimates through time. Here a non-parametric regression was used (a locally weighted scatterplot smoothing LOESS function) with a smoothing factor for each record determined using a generalised cross validation approach. To generate a best estimate of $\delta^{11}B_{sw}$ through time a probabilistic approach similar to Foster and Rohling, (2013) was used to fully account for the uncertainty in the calculated $\delta^{11}B_{sw}$. For each data point 10000 realizations of the $\delta^{11}B_{sw}$ time series were generated by randomly perturbing each discrete $\delta^{11}B_{sw}$ estimate within its uncertainty. A LOESS curve was then fitted to each realisation, and the distributions

at each $\delta^{11}B_{sw}$ step, as well as the probability maximum, and the 68% and 95% probability intervals, were determined. The final $\delta^{11}B_{sw}$ record was constructed by combining the output from the LOESS Monte Carlo simulations derived using 1) the fixed pH gradient assumption 2) the $\delta^{13}C$ derived pH gradient approach (n= 20000) and determining the median, 68% and 95% probability intervals from the combined dataset.

4.4 Results and Discussion

4.4.1 $\delta^{11}B$ benthic and planktic data

Surface and deep-ocean, $\delta^{11}B$, $\delta^{13}C$ and temperature broadly show a similar pattern throughout the Neogene (Fig. 4-6). The $\delta^{11}B$ benthic record decreases from ~15 ‰ at 24 Ma to a minimum of 13.28 ‰ at 14 Ma before increasing to ~17 ‰ at present day (Fig. 4-5). This pattern and the range of values in $\delta^{11}B$ benthic is in keeping with previously published Neogene $\delta^{11}B$ benthic records measuring using NTIMS (Raitzsch and Honisch, 2013), suggesting that our deep-water $\delta^{11}B$ record is representative of large scale pH changes in the global ocean. While the surface $\delta^{11}B_{borate}$ remained relatively constant between 24 and 11 Ma at ~ 16 ‰, similar to the deep-water $\delta^{11}B$, there is an increase in $\delta^{11}B$ between the middle Miocene and present (values increase to ~ 20 ‰) (Fig. 4-6b). The surface water temperatures reconstructed show a long-term decrease through the Neogene from ~ 28ºC to 24ºC (Fig. 4-6c). Following Cramer et al., (2011) deep water temperatures decrease from ~ 12ºC to 4ºC at present day. Surface and deep-water $\delta^{13}C_{DIC}$ both decrease and appear to covary through the Neogene (Fig. 4-6e, f).

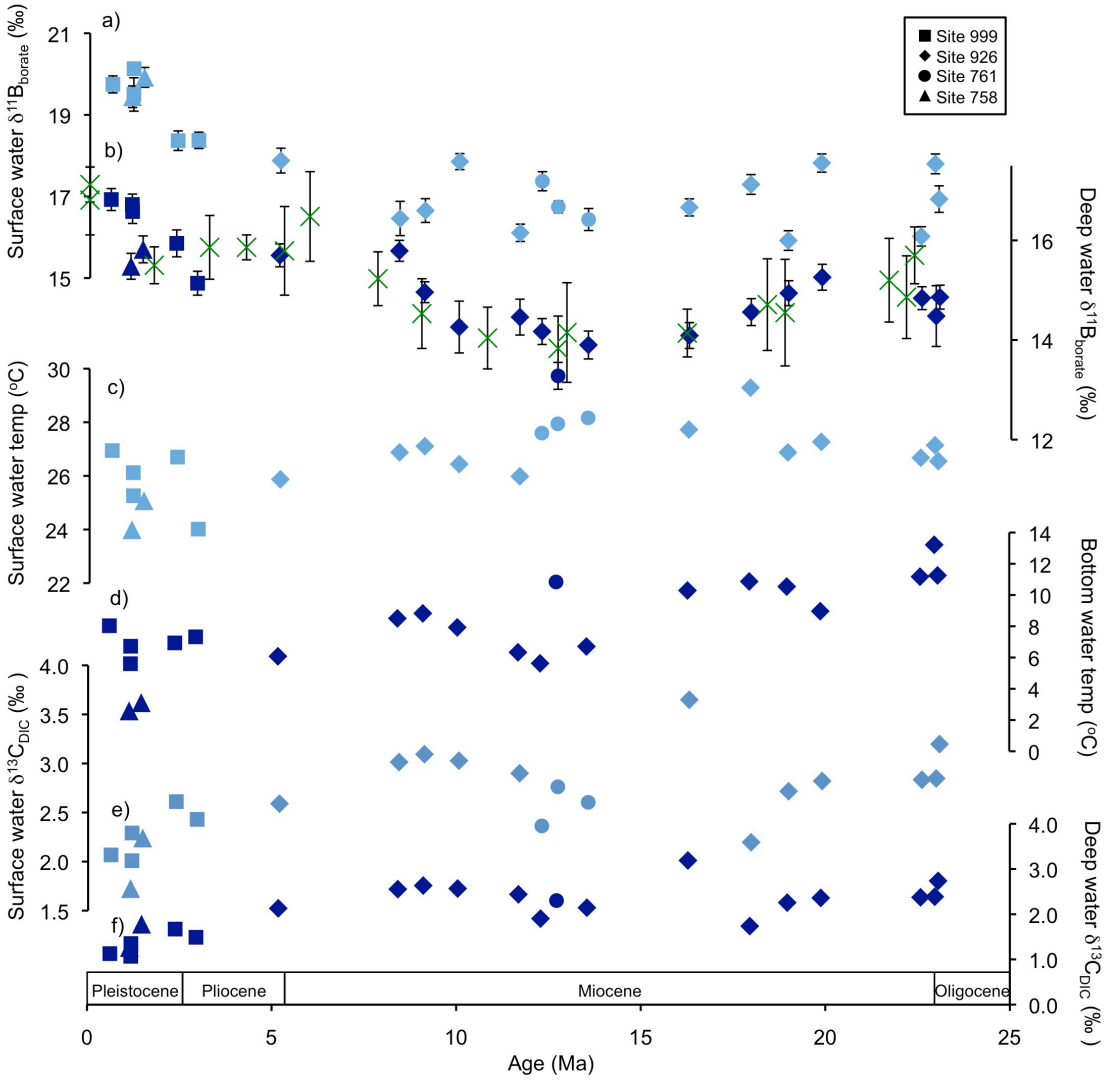

Figure 4-6: $\delta^{11}B_{borate}$, temperature and $\delta^{13}C_{DIC}$ estimates for surface and deep (a) $\delta^{11}B_{borate}$ surface and (b) $\delta^{11}B_{borate}$ deep (blue) from this study and (green) (Raitzsch and Honisch, 2013). $\delta^{11}B$ is plotted on inverted axes and the error bars show the external reproducibility at 95% confidence. (b) Mg/Ca based temperature reconstructions for calculated on tandem measurements of surface dwelling planktic. (c) Deep water temperature estimates from (Cramer et al., 2011). (d) $\delta^{13}C_{DIC}$ surface record (e) $\delta^{13}C_{DIC}$ benthic record. Squares depict Site 999, triangles are Site 758, diamonds are Site 926, circles are Site 761.

4.4.2 The relationship between $\delta^{13}C$ and pH gradients

The results of the global carbon model simulations suggest that the gradient of the relationship between $\delta^{13}C$-pH remains relatively robust in the Atlantic irrespective of atmospheric CO_2 levels or the source of bottom waters (North Atlantic Deep Water versus Glacial North Atlantic Intermediate Water, Fig. 4-7). While the relationship seems robust, there are relatively large uncertainties in the $\delta^{13}C$-pH gradient relationship

under conditions of glacial north Atlantic intermediate water (GNAIW), when the North Atlantic Deep Water (NADW), does not penetrate as deeply as today. This is mainly as a result of the presence of Antarctic bottom water (AABW) in the deep Atlantic Ocean when the overturning circulation is shallower in the North Atlantic. AABW is not as well connected to the surface waters as NADW and consequently the coupling of the surface and deep is not as strong for a given carbon perturbation. When we use the relationship described by the model output to calculate the pH gradient from the $\delta^{13}C$ gradient, variations of 0.2 pH units are evident (Fig. 4-8). The pH gradient varies between 0.15 and 0.34 with the most sustained interval of high pH gradients concentrated in the early Pleistocene and Pliocene.

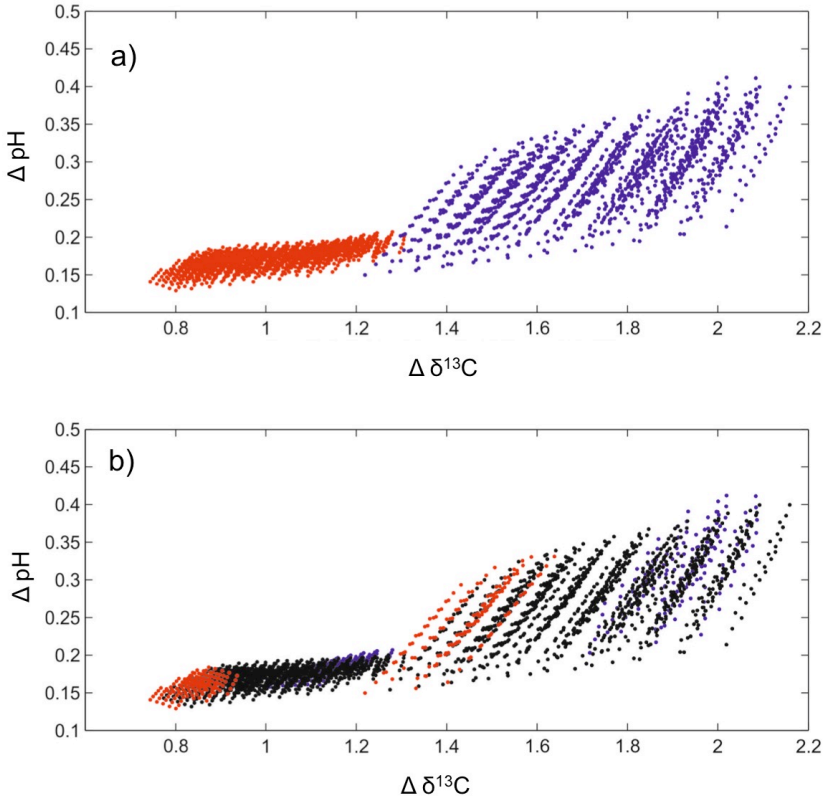

Figure 4-7: The output from sensitivity analysis of the relationship between pH gradient and $\delta^{13}C$ gradient (see text for model details). The effect of a range of carbon cycle perturbations, including those outlined in Hain et al., (2010) as well as different [Ca] (1x to 4x modern), CCD depths (3.5-5.5 km Pacific CCD depth) and CO_2 levels (200-1000 ppm) on the relationship between $\delta^{13}C$ gradient and pH gradient. Note panel (a) and (b) contain the same data. (a) Highlights the relationship between $\delta^{13}C$ gradient and pH gradient when GNAIW (blue) and NADW (red) formation is taking place. (b) Highlights the consistency of the relationship when atmospheric CO_2 is 200 ppm (blue), 300-900 ppm (black) and 1000 ppm (red).

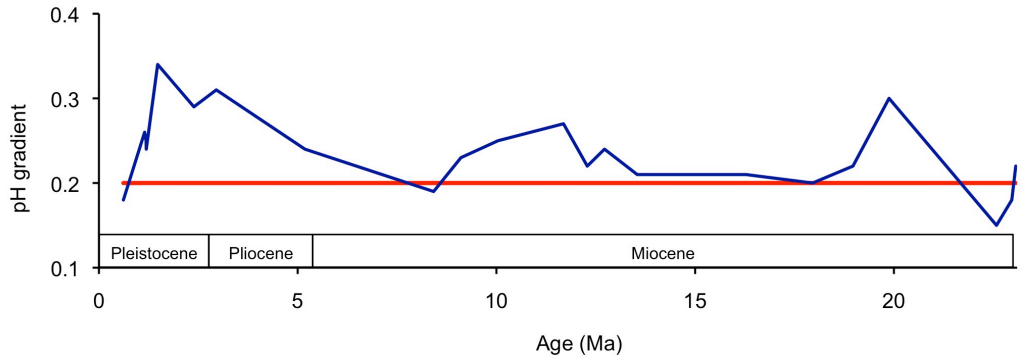

Figure 4-8: The pH gradient between surface and deep. Red line is the assumed constant gradient of 0.2. Blue is the variable pH gradient calculated from the $\delta^{13}C$ gradient and the output from the CYCLOPS model (see Section 4.3.3).

4.4.3 $\delta^{11}B_{sw}$ records through the Neogene

The $\delta^{11}B_{sw}$ values calculated using the constant pH method vary from 34.1 ‰ to 42.4 ‰ (± 0.68-5.6 ‰) across the Neogene with the predominance of higher values closer to the modern and minimum values in the middle Miocene (Fig. 4-9). When the individual time slices are smoothed to calculate the average $\delta^{11}B_{sw}$ it can be seen that mean values are 38.4 ‰ at 23 Ma and decrease to a minimum of 37.08 ‰ at ~ 14 Ma (± 0.47-1.26 ‰) (Fig. 4-10). $\delta^{11}B_{sw}$ then steadily increases through the late Miocene and Pliocene to modern values. The unadjusted modern estimate of 39.25 ‰ (± 0.74 ‰) is within uncertainty of the $\delta^{11}B_{sw}$ value measured from seawater today (39.61 ‰). The variability in the estimations of $\delta^{11}B_{sw}$ for each time slice and the associated uncertainty in our determinations suggest that $\delta^{11}B_{sw}$ is sensitive to the different input parameters, particularly the uncertainty in the pH gradient. Furthermore, the spread of the data suggests that the assumption that the pH gradient remained constant may not be correct on short (e.g. glacial-interglacial timescales) timescales. However, by smoothing the record we can focus on the long-term changes in the $\delta^{11}B$ difference between surface and deep.

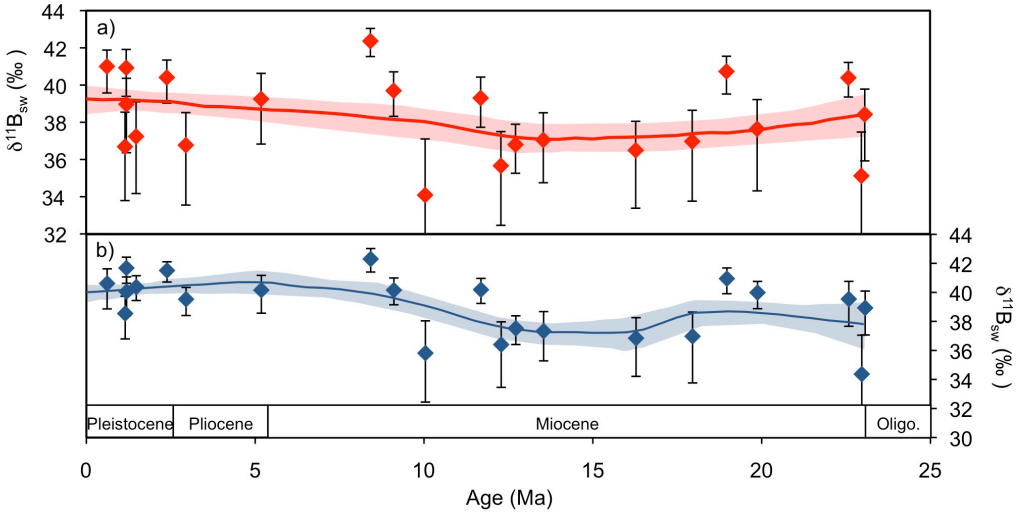

Figure 4-9: The calculated $\delta^{11}B_{sw}$ from the benthic-planktic $\delta^{11}B$ pairs assuming a) a constant pH gradient of 0.2 b) a variable pH gradient derived from $\delta^{13}C$. The uncertainty on each data point is determined using a Monte Carlo approach including uncertainties in temperature, salinity, $\delta^{11}B$ and the pH gradient (see text for details) The line of best fit is the probability maximum of a LOESS fit given the uncertainty in the calculated $\delta^{11}B_{sw}$. The shaded area highlights the 95% confidence interval.

The $\delta^{11}B_{sw}$ values calculated using the variable pH method yields very similar results to the fixed pH method. $\delta^{11}B_{sw}$ varies from 34.4 ‰ to 42.3 ‰ (± 0.60-5.74 ‰) across the Neogene with the predominance of higher values closer to the modern with the minimum values in the middle Miocene (Fig. 4-9). When the individual time slices are smoothed, $\delta^{11}B_{sw}$ is ~ 38 ‰ at 24 Ma and decreases to a minimum of 37.21 ‰ at ~ 14 Ma (± 0.35-1.68 ‰). $\delta^{11}B_{sw}$ then decreases sharply through the late Miocene and remains relatively constant thereafter to the modern (Fig. 4-10). The modern estimate of 40 ‰ (± 0.6 ‰) is within uncertainty of the $\delta^{11}B_{sw}$ value measured from seawater today (39.61 ‰). Similar to the individual records, the combined output from the LOESS Monte Carlo simulations derived using both the fixed pH gradient assumption and the $\delta^{13}C$ derived pH gradient approach the combined output is ~ 38 ‰ at 24 Ma and decreases to 37.3 ‰ during the middle Miocene (Fig. 4-11a). $\delta^{11}B_{sw}$ increases sharply to ~ 39 ‰ during the late Miocene before increasing more gradually through the Pliocene and Pleistocene to 39.63 ‰ at present (± 0.7-1.72 ‰). This value is in good agreement with the modern value (39.61 ‰).

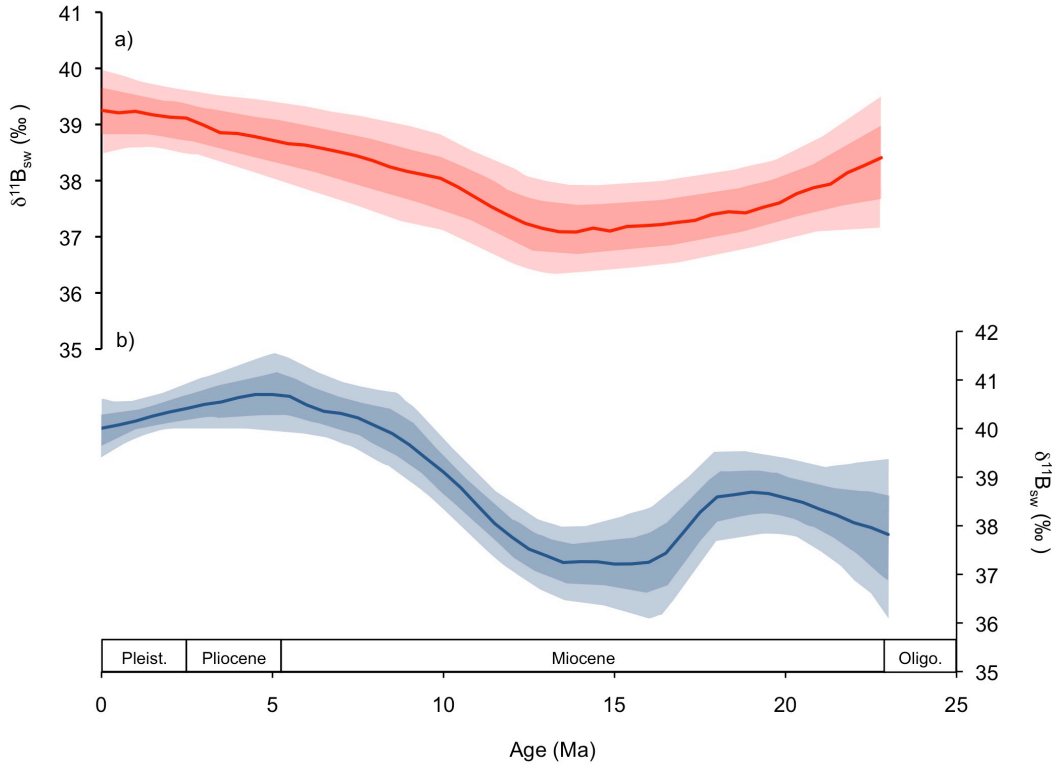

Figure 4-10: The $\delta^{11}B_{sw}$ curve calculated for a) a constant pH gradient of 0.2 b) a variable pH gradient derived from $\delta^{13}C$. The line of best fit is the probability maximum of a LOESS fit given the uncertainty in the calculated $\delta^{11}B_{sw}$. The darker shaded area highlights the 68% confidence interval and the lighter interval highlights the 95% confidence interval.

4.4.4 Comparison to other $\delta^{11}B_{sw}$ records

In order to compare our new $\delta^{11}B_{sw}$ record to those previously published, we adjust all the published $\delta^{11}B_{sw}$ curves so that at t=0, the isotopic composition is equal to the modern. A common feature of all the existing estimates of Neogene $\delta^{11}B_{sw}$ evolution is an increase through time between the middle Miocene and present (Fig 4-11a). Our new $\delta^{11}B_{sw}$ record matches the previously published estimates calculated using pH gradients in the surface ocean, in terms of shape and magnitude remarkably well except in the middle Miocene where the minimum in $\delta^{11}B_{sw}$ in our record is 1 ‰ lower (Fig. 4-11a) than the published estimates of Pearson and Palmer, (2000). The $\delta^{11}B_{sw}$ record calculated using benthic $\delta^{11}B$ and assumed pH changes (Raitzsch and Honisch, 2013) shows values in a similar range to the $\delta^{11}B_{sw}$ values reconstructed here, however, the amount of variability in the Raitzsch and Honisch, (2013) study is greater. For instance, a decrease in $\delta^{11}B_{sw}$ between 5 Ma and the modern is not evident in our study. The

modelling study of Lemarchand et al., (2002b) similarly shows an increase in $\delta^{11}B_{sw}$ between the middle Miocene and present, however, the increase is more gradual than suggested by the results presented here and continues through the entire Neogene (Fig. 4-11a). The model output is within uncertainty of our new $\delta^{11}B_{sw}$ record, however, the modelled values do not show the same level of variability, suggesting that some of the controls on the inputs and outputs of boron in to and out of the ocean are not fully understood. In line with the conclusions of previous studies (Raitzsch and Honisch, 2013), our data show that the $\delta^{11}B_{sw}$ signal in the fluid inclusions is mostly likely a combination of the $\delta^{11}B_{sw}$ and a poorly constrained fractionation factor between the seawater and the halite.

4.4.5 Comparison to the seawater isotopic ratios of Mg, Ca and Li

The overall form taken by our new record of $\delta^{11}B_{sw}$ is comparable to that shown by the pattern of secular change seen in other marine isotope records (Fig. 4-11). The $\delta^{7}Li_{sw}$ (Misra and Froelich, 2012) and $\delta^{44/40}Ca_{sw}$ (Griffith et al., 2008) both increase through the Neogene, whereas $\delta^{26}Mg_{sw}$ decreases (Pogge von Strandmann et al., 2014) suggesting that there is a similar control on the isotopic composition of all four elements across this time interval (Fig. 4-11). In order to better evaluate the extent of the correlation we fit a LOESS curve to the records of $\delta^{7}Li_{sw}$, $\delta^{26}Mg_{sw}$ and $\delta^{44/40}Ca_{sw}$ using the same method as for $\delta^{11}B_{sw}$ (see methods). The curve is then adjusted so that at t=0, the isotopic composition is equal to the modern. The curves are then sampled every 0.5 Ma and plotted against $\delta^{11}B_{sw}$ (Fig. 4-12). The crossplots suggest that the isotopic composition of $\delta^{11}B_{sw}$, $\delta^{7}Li_{sw}$ and $\delta^{44/40}Ca_{sw}$ seem to be well correlated between 14 Ma and present, however, this correlation is not evident between 23 and 15 Ma (Fig. 4-11). While a correlation exists between $\delta^{26}Mg_{sw}$ and $\delta^{11}B_{sw}$, the slope of the relationship appears to change at ~ 7 Ma suggesting that there may be a secondary control on the $\delta^{26}Mg_{sw}$ through this interval.

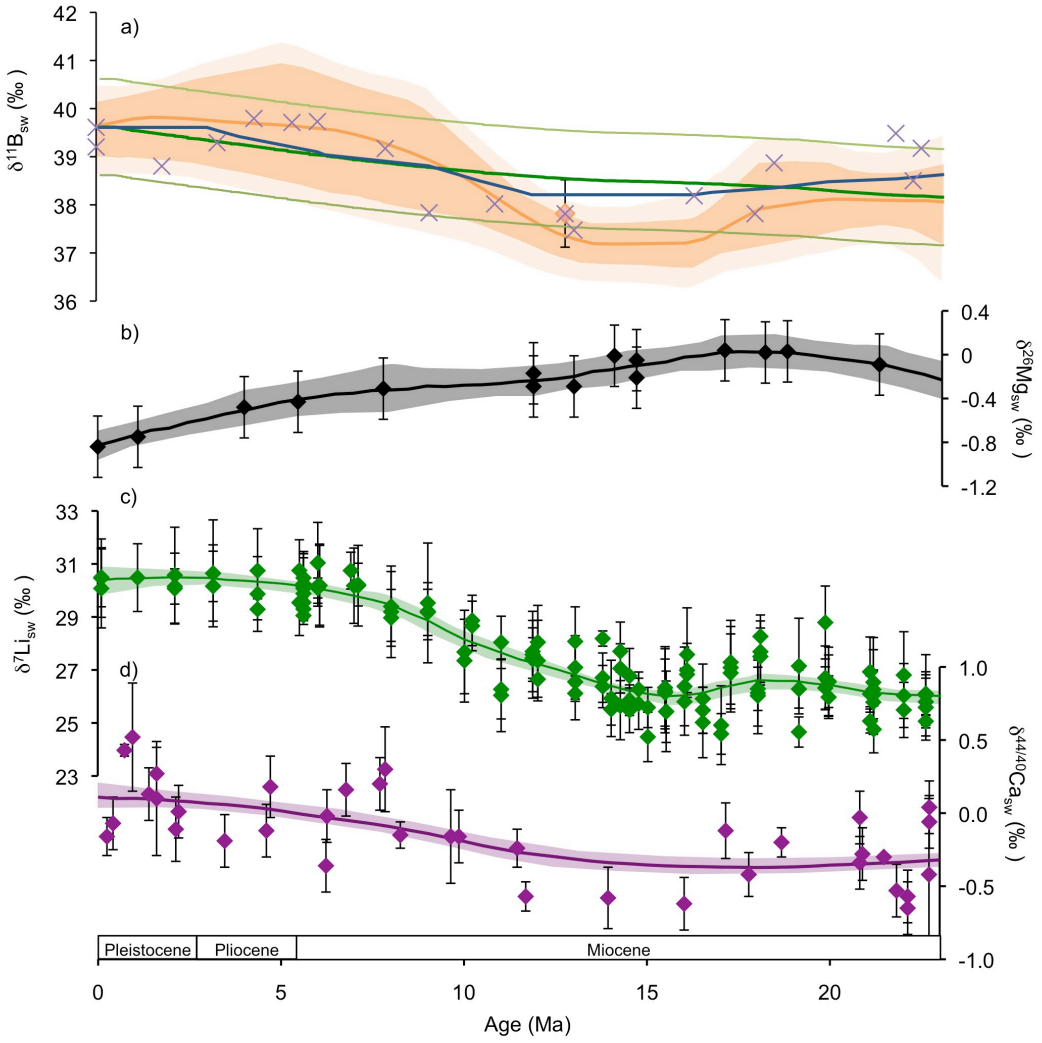

Figure 4-11: a) The $\delta^{11}B_{sw}$ curve calculated using the combined Monte Carlo simulations from the curve created assuming a constant pH gradient of 0.2 and a variable pH gradient derived from $\delta^{13}C$. The median (orange line), 68% (dark orange band) and 95% (light orange band) confidence intervals were calculated from the combined simulations. Plotted with a compilation of published $\delta^{11}B_{sw}$ records. Seawater composition reconstructed from foraminifera depth profiles (dark blue line and orange diamond) from Pearson and Palmer, (2000) and Foster et al., (2012) respectively, numerical modelling (dark green line), with light green lines shows ± 1 ‰ confidence interval (Lemarchand et al., 2002b) and benthic $\delta^{11}B$ (purple crosses) from Honisch et al., (2012). b) The $\delta^{26}Mg_{sw}$ record from Pogge von Strandmann et al., (2014). Probability maximum on the LOESS fit is highlighted by the black line, the grey band highlights the 95% confidence level. c) The $\delta^{7}Li_{sw}$ record from Misra and Froelich, (2012). Probability maximum on the LOESS fit is highlighted by the green line, the green band highlights the 95% confidence level. d) $\delta^{44/40}Ca_{sw}$ record from Griffith et al., (2008). Probability maximum on the LOESS fit is highlighted by the purple line, the purple band highlights the 95% confidence level. For (b-d) Nonparametric regressions (locally weighted scatterplot smoothing (LOESS)) were fitted to each realization, and the distributions of LOESS curves at each $\delta^{11}B_{sw}$ step were assessed, and the probability maximum, as well as the 68% and 95% probability intervals, was determined.

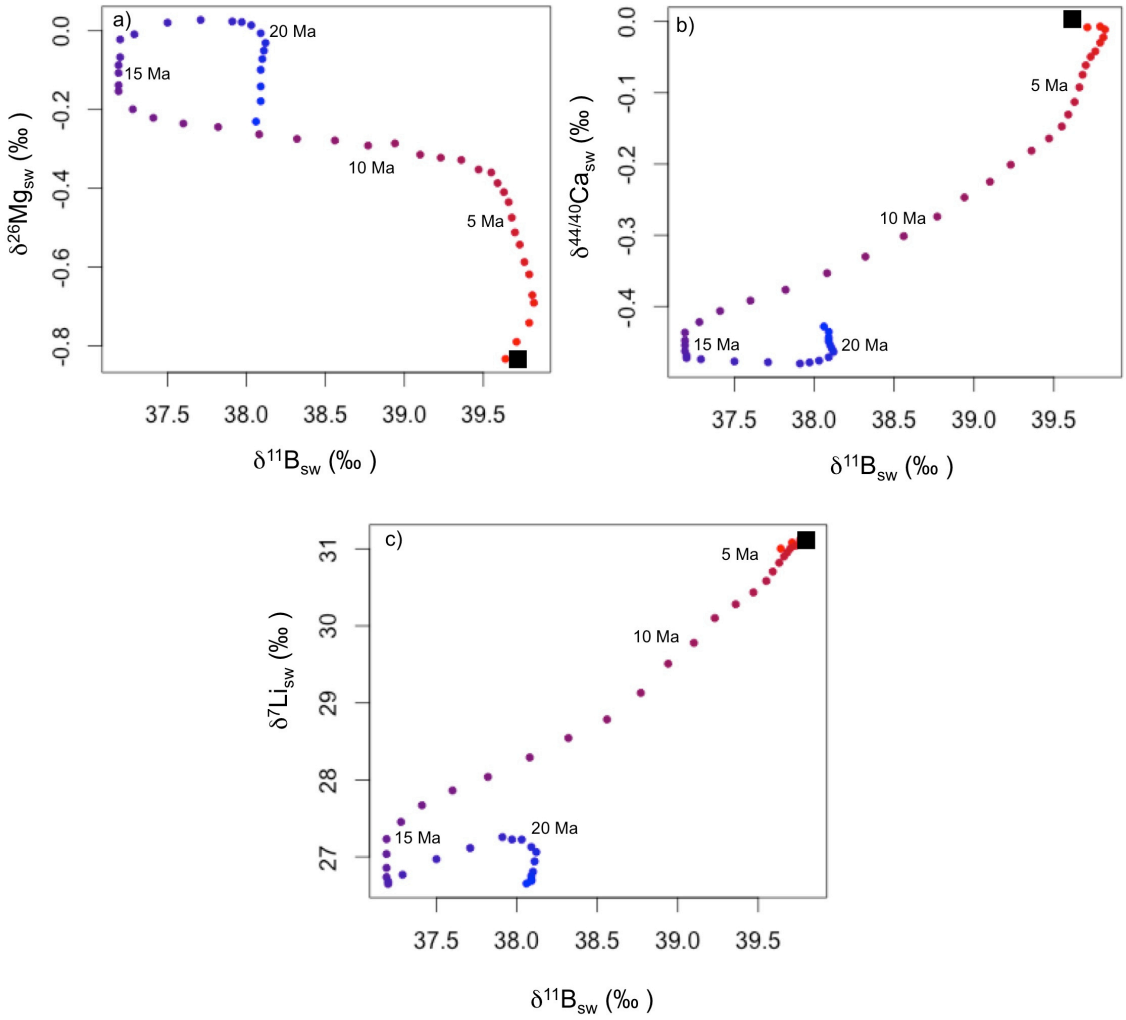

Figure 4-12: Crossplots of the smoothed records of a) $\delta^{11}B_{sw}$ and $\delta^{26}Mg_{sw}$ from Pogge von Strandmann et al., (2014). (b) $\delta^{11}B_{sw}$ and $\delta^{44/40}Ca_{sw}$ from Griffith et al., (2008). (c) $\delta^{11}B_{sw}$ and $\delta^{7}Li_{sw}$ from Misra and Froelich, (2012). The black square highlights modern conditions. The colour of the data points highlights the age of the data points where red = modern and blue = 23 Ma.

4.4.6 Controls on the seawater isotopic composition of B, Mg, Ca and Li

To better constrain the controls on $\delta^{11}B_{sw}$, $\delta^{7}Li_{sw}$, $\delta^{26}Mg_{sw}$ and $\delta^{44/40}Ca_{sw}$ it is instructive to compare the size and isotopic composition of the fluxes of boron, lithium, calcium and magnesium (Table 4-1). As noted previously, the major flux of boron into the ocean is via riverine input (Lemarchand et al., 2002b), although some studies suggest that atmospheric input may also play an important role (Park and Schlesinger, 2002). The outputs are dominated by absorption onto clays and the alteration of oceanic crust (Spivack and Edmond, 1987; Smith et al., 1995). Similar to boron the primary inputs of Li into the ocean come from hydrothermal sources and riverine input and the main outputs are ocean crust alteration and absorption onto sediments (Misra and Froelich,

2012). The two dominant controls on magnesium concentration and isotope ratio in the oceans is the riverine input, ocean crust alteration and dolomitisation (Table 4-1) (Tipper et al., 2006b). The main controls on the amount of calcium in the modern ocean and its isotopic composition is the balance between riverine and hydrothermal inputs and removal through $CaCO_3$ deposition and alteration of oceanic crust (Griffith et al., 2008). Dolomitisation has also been cited as playing a potential role in controlling $\delta^{44/40}Ca_{sw}$, although the contribution of this process through time is poorly constrained (Griffith et al., 2008).

Sources	**Isotopic Ratio**			
Oceanic Inputs	$\delta^{11}B_{sw}$ 39.61 ‰	$\delta^{7}Li_{sw}$ 31 ‰	$\delta^{26}Mg_{sw}$ −0.83 ‰	$\delta^{44/40}Ca_{sw}$ 0 ‰
Input from hydrothermal	20[a]	8.3[f]	N/A	–0.96[k]
Fluid from accretionary prisms	25[b]	15[f]	N/A	N/A
Riverine Inputs	10[c]	23[f]	−1.09[h]	-1.28[k]
Groundwater	N/A	N/A	-0.82[h]	−1.3[l]
Outputs				
Precipitation into carbonates	20[d]	28[g]	-3.6[i]	-1.15[k]
Ocean crust alteration	1.5[e]	15[f]	-0.83[h]	-1.2[k]
Dolomisation	N/A	N/A	-2.6[h]	??
Absorption onto sediment	15[a]	15[f]	-2.4[j]	N/A

Table 4-1: The average $\delta^{11}B$, $\delta^{26}Mg$, $\delta^{44/40}Ca$ and $\delta^{7}Li$ composition of major fluxes into and out of the ocean. Colour coding reflects the relative importance of each the processes (darker blue reflects greater importance). The colour coding for boron is based on Lemarchand et al., (2002b) and references therein, lithium from (Misra and Froelich, 2012) and references therein, magnesium from Tipper et al., (2006b) and calcium from Zhu and Macdougall, (1998) and references therein. The isotopic ratio of each process is: a) (Spivack and Edmond, 1987) b) (You et al., 1993) c) (Lemarchand et al., 2002b) d) (Hemming and Hanson, 1992) e) (Smith et al., 1995) f) (Misra and Froelich, 2012) and references therein g) (You and Chan, 1996) h) (Tipper et al., 2006b) i) (Wombacher et al., 2011) j) (Wimpenny et al., 2014) k) (Griffith et al., 2008) l) (Schmitt et al., 2003). $\delta^{26}Mg_{sw}$ and $\delta^{11}B_{sw}$ from Foster et al., (2010), $\delta^{7}Li_{sw}$ from Tomascak, (2004). In the analysis of $\delta^{44/40}Ca_{sw}$ seawater is used as a reference.

Riverine input is the common control on the isotopic ratio in seawater of all the ions analysed and consequently may be an important factor on the changing isotopic composition of B, Li, Ca and Mg over the late Neogene (Table 4-1). However, given the differences in the $\delta^{26}Mg_{sw}$ curve compared to the other elements, it may be that additional factors are also affecting this isotope system. A recent modelling study suggests a decrease in the rate of dolomitisation over the past 15 Myrs may be a control on $\delta^{26}Mg_{sw}$ (Pogge von Strandmann et al., 2014). Consequently, the following discussion of changes in the isotopic composition of Mg, Ca, B and Li in riverine input may not be as important a factor for Mg as for the other isotope systems. The isotopic composition of the riverine input of all four elements is dependent on the isotopic composition of the source rock and isotopic fractionation during weathering process, although the relative importance of these two factors varies between isotope systems. The $\delta^{11}B$ composition of rivers is primarily dependent on isotopic fractionation during the reaction of water with silicate rocks and to a lesser extent the isotopic composition of the source rock (i.e. the proportion of evaporites and silicate rocks) (Rose et al., 2000). The source rock also appears to have limited influence on the $\delta^{7}Li$ composition of rivers and riverine $\delta^{7}Li$ primarily varies with weathering intensity (Kısakűrek et al., 2005; Millot et al., 2010). The riverine input of calcium to the oceans is controlled by the composition of the primary continental crust (dominated by carbonate weathering) and the recycled component, although the relative influence of these two processes is not well understood (Tipper et al., 2006a). For Mg, the isotopic composition of the source rock is important for small rivers, however, lithology is of limited significance at a global scale in comparison to fractionation in the weathering environment may be more important (Tipper et al., 2006b). While the source rock only seems a significant factor for some of the isotope systems, weathering induced isotopic fractionation affects the isotopic composition of riverine input across all of the isotope systems. Next we explore some of the possible causes for changes in the isotopic composition/flux of riverine input over the past 15 Ma.

In this regard, of the four elements discussed here, Li isotopes are the most extensively studied. Indeed, the change in $\delta^{7}Li_{sw}$ has been attributed to an increase in the $\delta^{7}Li_{sw}$ composition of the riverine input (Hathorne and James, 2006; Misra and Froelich, 2012). The causes of the shift in $\delta^{7}Li$ riverine have been variably attributed to: 1) an increase in incongruent weathering of silicate rocks and secondary clay formation as a

consequence of Himalayan uplift (Misra and Froelich, 2012). 2) A reduction in weathering intensity (Hathorne and James, 2006). 3) An increase in silicate weathering rate (Liu et al., 2015). 4) An increase in the formation of floodplains and the increased formation of secondary minerals (Pogge von Strandmann and Henderson, 2014). In all four cases the lighter isotope of Li is retained on land in clay and secondary minerals. A mechanism associated with either an increase in secondary mineral formation or the retention of these minerals on land is also consistent across Mg, Ca and B isotope systems. For instance, clay minerals are preferentially enriched in the light isotope of B (Spivack and Edmond, 1987; Deyhle and Kopf, 2004; Lemarchand and Gaillardet, 2006) and Li (Pistiner and Henderson, 2003) and soil carbonates and clays are preferentially enriched in the light isotope of Ca (Tipper et al., 2006a; Hindshaw et al., 2013). The formation of secondary silicate minerals, such as clays, is assumed to preferentially take up isotopically heavy Mg into the solid phase (Tipper et al., 2006a; Tipper et al., 2006b; Pogge von Strandmann et al., 2008; Wimpenny et al., 2014), adequately explaining the inverse relationship between $\delta^{11}B_{sw}$ and $\delta^{26}Mg_{sw}$. Consequently the increased formation or retention on land of secondary minerals would alter the isotopic composition of the riverine input of all the examined isotope systems and could potentially explain the trends in all four isotope systems through the late Neogene (Fig. 4-11). However, the role of clay formation in controlling the isotopic composition of rivers is complicated. For instance, Mg and Li isotope ratios in the river waters of the Mackenzie Basin and Canadian Cordillera are strongly positively correlated, although evidence from other river systems suggests that Li and Mg isotopes should exhibit opposing isotope discrimination during weathering (Tipper et al., 2012). Misra and Froelich, (2012) suggest that tectonic uplift and an increase in incongruent weathering was the primary cause of the shift in the $\delta^{7}Li_{sw}$ through the Neogene. However, a recent study has shown that when uplift rates are high, congruent weathering increases as a consequence of an increase in the proportion of fresh faces for weathering (Pogge von Strandmann and Henderson, 2014). Alternatively, the cause of the shift in $\delta^{7}Li_{sw}$ may have been the formation of large floodplains associated with uplift, where secondary mineral formation was increased (Pogge von Strandmann and Henderson, 2014).

Whatever the cause of the Neogene evolution of oceanic B and these other isotopic systems, the correlation between $\delta^{11}B_{sw}$ and the isotopic composition of the other

elements is not evident between 14 and 23 Ma suggesting that across this interval, a different process unique to the boron cycle was the dominant control on the evolution of $\delta^{11}B_{sw}$. The atmospheric cycle of boron is an interesting aspect of the boron cycle that is poorly understood. The relative importance of this cycle is unknown, however, if the upper estimates of the atmospheric flux are considered, changes in this part of the boron cycle could have a significant influence on $\delta^{11}B_{sw}$ (Park and Schlesinger, 2002). Alternatively there could be another source or sink of boron to/from the ocean, which is as yet unidentified. The divergence of the isotopic composition of B from the evolution of the other elements could be due to some other controls, which are more/less dominant on $\delta^{11}B_{sw}$ than the other isotopic systems (Table 4.1). For instance, as previously discussed, changes in the rate of dolomite formation may play a significant role in the isotopic composition of Mg and Ca (Griffith et al., 2008; Pogge von Strandmann et al., 2014) but be less important for $\delta^{11}B_{sw}$. Explaining the divergence of $\delta^{11}B_{sw}$ and $\delta^{7}Li_{sw}$ is more difficult because the isotopic composition of both elements share many of the same inputs and outputs (Table 4.1). However, small differences in the relative size of some of the fluxes (e.g. processes involving oceanic crust alteration) may have caused the divergence of the two records.

4.5 Conclusions

Here we present a new $\delta^{11}B_{sw}$ record for the Neogene based on paired planktic-benthic $\delta^{11}B$ measurements. Our new record suggests that $\delta^{11}B_{sw}$ is ~ 38 ‰ at the Oligocene-Miocene boundary and decreases to a minimum of ~ 37 ‰ at 14 Ma. $\delta^{11}B_{sw}$ then increases to the modern value through the late Miocene and Pliocene. When the new $\delta^{11}B_{sw}$ record is compared to changes in the seawater isotopic composition of Li and Ca the shape of the records between 14 Ma and present is remarkably similar. Although the isotopic composition of Mg also changes through this interval, the correlation between $\delta^{26}Mg_{sw}$ and $\delta^{11}B_{sw}$ is not as strong as the other elements suggesting there may be a secondary control on Mg. In all four cases riverine input is cited as one of the key control of the isotopic composition of the elements in seawater. When we compare the isotopic fractionation of the elements associated with secondary mineral formation, the trends in the $\delta^{26}Mg_{sw}$, $\delta^{44/40}Ca_{sw}$ $\delta^{11}B_{sw}$ and $\delta^{7}Li_{sw}$ records are all consistent with an increase in secondary mineral formation through time. The qualitative treatment of multiple stable isotope systems presented here requires a more quantitative treatment.

The evolution of $\delta^{11}B_{sw}$ presented here provides important additional constraints on the processes responsible for the evolution of ocean chemistry through time.

Chapter 5: Middle Miocene climate instability associated with high amplitude CO_2 variability.

Acknowledgements:

The following chapter was accepted for publication as a research article in the journal "Paleoceanography" (August 2014). The contributions of co-authors to this work are detailed below.

Rosanna Greenop: data collection and analysis, CO_2 calculations, data interpretation, manuscript drafting and production of figures.

Paul A. Wilson: data interpretation and manuscript drafting

Gavin L. Foster: data interpretation and manuscript drafting

Caroline H. Lear: Provided the samples for $\delta^{11}B$ analysis, manuscript editing

Abstract:

The amplitude of climatic change, as recorded in the benthic oxygen isotope record, has varied throughout geological time. During the late Pleistocene changes in the atmospheric concentration of carbon dioxide (CO_2) are an important control on this amplitude of variability. The contribution of CO_2 to climate variability during the pre-Quaternary, however, is unknown. Here we present a new boron isotope based CO_2 record for the transition into the middle Miocene Climatic Optimum (MCO) between 15.5 and 17 Myrs that shows pronounced variability between 300 ppm and 500 ppm on a roughly 100 kyr time scale during the MCO. The CO_2 changes reconstructed for the Miocene are ~ 2 times larger in absolute terms (300 to 500 ppm compared to 180 to 280 ppm) than those associated with the late Pleistocene and ~15% larger in terms of climate forcing. In contrast, however, variability in the contemporaneous benthic oxygen isotope record (at ~1 ‰) is approximately two-thirds the amplitude of that seen during the late Pleistocene. These observations indicate a lower overall sensitivity to CO_2 forcing for Miocene (Antarctic only) ice sheets than their late Pleistocene (Antarctic plus lower latitude northern hemisphere) counterparts. When our Miocene

CO_2 record is compared to estimated changes in contemporaneous $\delta^{18}O_{sw}$ (ice volume), they point to the existence of two reservoirs of ice on Antarctica. One of these reservoirs appears stable while a second reservoir shows a level of dynamism that contradicts the results of coupled climate-ice sheet model experiments given the CO_2 concentrations that we reconstruct.

5.1 Introduction

Variations in the orbit of the Earth around the Sun have paced the Earth's climate cycles throughout geological time, however, the amplitude of the change in radiative forcing caused by orbital variations is too small to directly drive the observed magnitude of the climate change (Hays et al., 1976). Instead, feedbacks in the Earth system must exist to amplify the changes in orbital forcing (Imbrie et al., 1993; Shackleton, 2000). In the case of the glacial-interglacial cycles of the late Pleistocene when variability in the benthic oxygen isotope record was high (1.5 ‰) the changes in radiative forcing brought about by CO_2 change were relatively large (up to -2.4 W/m^2), identifying CO_2 as an important contributor to climate variability over the past 800,000 years (Lisiecki and Raymo, 2005; Lüthi et al., 2008; Köhler et al., 2010). However, it is not known whether the role played by CO_2 in climate variability over the past 800,000 years is unique to the late Pleistocene. In fact, the lack of suitable records has prevented analysis of the role of CO_2, in controlling climate variability in the pre-Quaternary.

One pre-Quaternary time interval that exhibits significant fluctuations in climate as recorded by change in the benthic $\delta^{18}O$ record is the middle Miocene Climatic Optimum (MCO) between 14.7-17 Ma (Holbourn et al., 2007; Holbourn et al., 2014). The MCO is a generally warm time interval punctuating the long term Cenozoic cooling trend (Fig. 5-1) (Zachos et al., 2008). Global mean temperatures are estimated to have been around 2 to 4 ºC warmer than the pre-industrial with the largest temperature differences to modern in the high latitudes (Warny et al., 2009; You et al., 2009). Palynological data from ANDRILL AND-2A, near the modern ice margin of the East Antarctic ice sheet in the Ross Sea, suggest that circum-Antarctic annual sea surface temperatures ranged from 0 to 11.5ºC (compared to ~ -1 to 3 ºC today; Schlitzer, 2000) with January mean land temperatures ~ 11ºC warmer than today during the peak MCO warmth (Warny et al., 2009). A further striking feature of the MCO is the smaller and more dynamic ice

sheet on Antarctica that is thought to have accompanied these warmer high latitude temperatures (Billups and Schrag, 2002; Shevenell et al., 2004; Holbourn et al., 2007; Warny et al., 2009; Fielding et al., 2011; Passchier et al., 2011; Holbourn et al., 2014). Sedimentary facies analysis conducted on AND-2A shows evidence for large-amplitude cyclicity in facies associations in middle Miocene strata. These cycles are interpreted to indicate changes from open water to ice-proximal deposition during the early middle Miocene with two discrete intervals of ice sheet and sea-ice minima at ~15.7 Ma and ~16.4 Ma (Acton et al., 2008-2009; Warny et al., 2009; Fielding et al., 2011; Passchier et al., 2011). A strong orbital control on climate variability in the middle Miocene is clearly seen in high-resolution benthic oxygen isotope records, which are characterized by high-amplitude (~1 ‰) variability during the MCO with a periodicity matching that of the short-term (~100 kyr) eccentricity cycle (Holbourn et al., 2007; Holbourn et al., 2014). A similar orbital pacing (94-99 kyrs) is seen in particle size data from AND-2A and interpreted to reflect the hydrodynamic effects of wave stirring in response to ice sheet growth and decay (intensity of wave stirring is controlled by the effect of the ice sheet on various high-latitude climate system parameters such as iceberg density) (Passchier et al., 2013). Yet, as with the well-documented climate cycles of the late Pleistocene, climate variations with an eccentricity pacing are difficult to explain. One long-standing problem is that the amplitude of change in radiative forcing brought about by eccentricity change is too small to drive climate variability directly (Imbrie et al., 1993; Shackleton, 2000). Another problem concerns the lack of evidence for major ice expansion during the minimum or 'node' in the obliquity amplitude modulation centered around 16.2 Ma when we might predict ice expansion in response to dampened seasonal extremes, particularly the suppression of ablation-inducing warm summers (Holbourn et al., 2007). In fact, this predicted expansion of glacial conditions is not seen until 2.4 Myr later, at the mid-Miocene Climatic Transition (MMCT), during a node in obliquity no more extreme than the one at 16.2 Ma. These observations indicate that orbital forcing alone cannot fully explain the observed mid-Miocene climate history and that some additional factor(s) must have exerted a fundamental control on the climate system at this time. A number of recent studies have suggested that variations in atmospheric CO_2 drive long-term Miocene climate change (Kürschner et al., 2008; Foster et al., 2012). Published estimates of atmospheric CO_2 fall in the range of 200 to 450 ppm during the MCO (Fig. 5-1e) (Kürschner et al., 2008; Foster et al., 2012). Yet, the resolution of these records is too crude and the discrepancies among different

proxies are currently too large to provide an insight into the possible role of CO_2 in amplifying shorter-term climate variability during the MCO. Here we present a new higher resolution boron isotope-based $\delta^{11}B$-CO_2 record and use this to assess the relationship between climate and CO_2 variability in the middle Miocene.

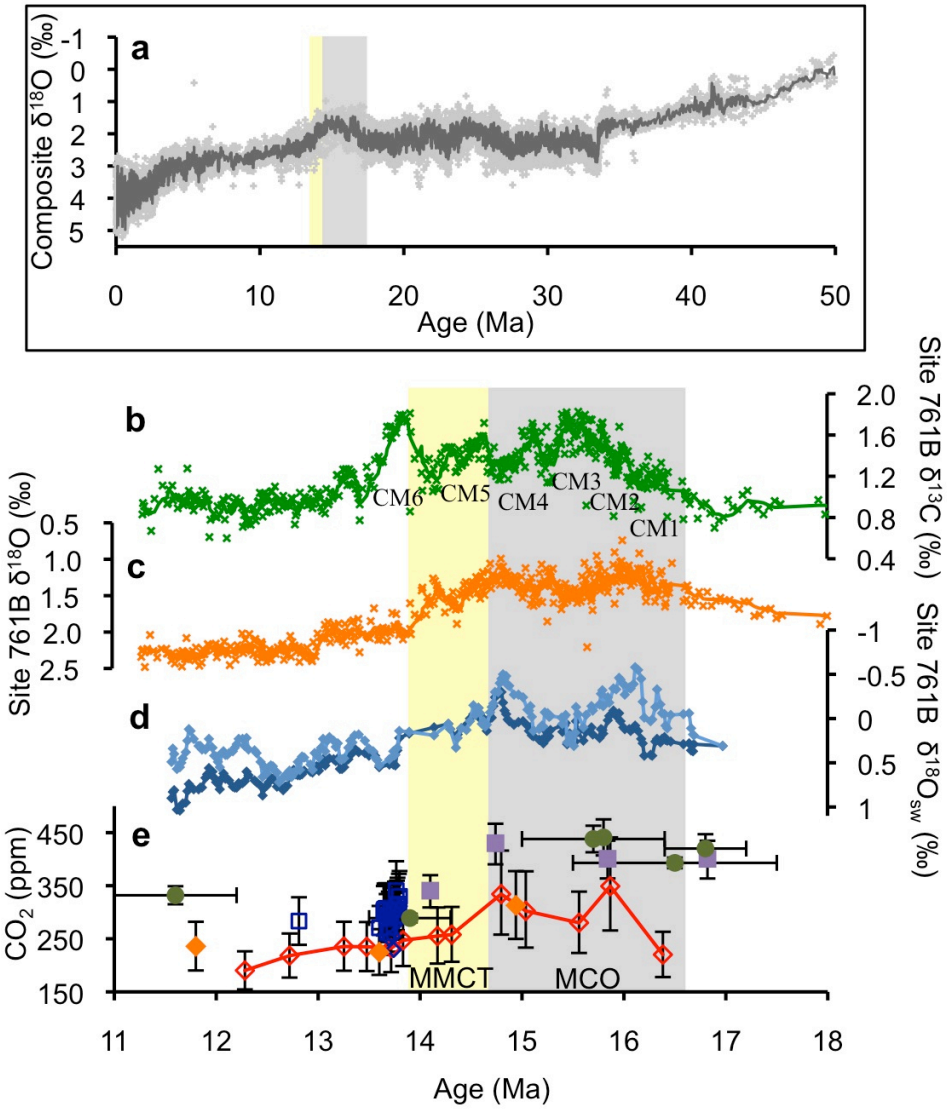

Figure 5-1: Long term climate and pCO_2 records from the middle Miocene. (a) Composite benthic $\delta^{18}O$ with 5 point moving average (Zachos et al., 2008). Grey and yellow bar indicates middle Miocene Climatic Optimum (MCO) and mid-Miocene Climatic Transition (MMCT) respectively. (b-c) Benthic $\delta^{13}C$ and $\delta^{18}O$ record from Site 761B with 5 point moving average (Holbourn et al., 2004; Lear et al., 2010). (CM) are carbon maxima events as identified at 761B in (Holbourn et al., 2004). (d) Seawater $\delta^{18}O$ (‰, vs PDB) (Lear et al., 2010). The light blue data points are calculated assuming a carbonate ion effect on the Mg/Ca ratios whilst the dark blue points are calculated assuming no carbonate ion effect on measured Mg/Ca. (e) CO_2, from boron isotopes ($\delta^{11}B$), (red open diamonds Site 761B; Foster et al., 2012, orange solid diamonds Site 926; Foster et al., 2012 and open dark blue diamonds; Badger et al., 2013), leaf stomata (dark green circles; Kürschner et al., 2008) and alkenones (open dark blue squares; Badger et al., 2013 and purple squares; Zhang et al., 2013).

5.2 Materials and Methods

To better understand the role of greenhouse gas forcing in climate variability across the MCO, a CO_2 record of higher temporal resolution is needed. We exploit sediments of Miocene age from ODP Hole 761B (16˚44.23'S, 115˚32.10'E) in the Indian Ocean (Fig. 5-2). The foraminifera sampled from ODP Hole 761B were taken from between 47 and 52 m below sea floor (mcd). The $\delta^{18}O$ and $\delta^{13}C$ stratigraphy for Hole 761B is not sufficiently structured to allow development of a reliable orbitally tuned age model but both of these records capture the characteristic structure that typically defines the long-term climate evolution of the middle Miocene seen at other sites (Figs. 5-1 & 5-3) (Holbourn et al., 2004; Lear et al., 2010). The oxygen isotope stratigraphy was used to capture the full range of climate variability and measurements were made with ~40 kyr spacing. Surface waters at this site today are close to equilibrium with the atmosphere with respect to CO_2 (Fig. 5-2) (Takahashi et al., 2009).

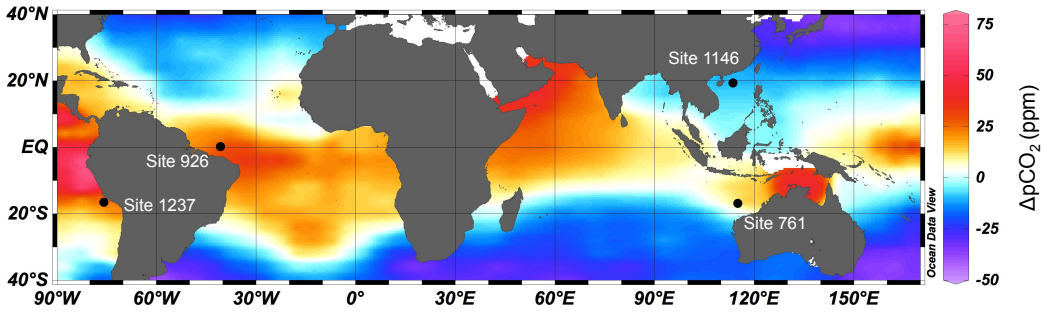

Figure 5-2: Map of study sites and mean annual air–sea disequilibria with respect to pCO_2. Black dots indicate the location of the sites referred to in this study. ODP 761 (16˚44.23'S, 115˚32.10'E) is from a water depth of 2179m. The modern extent of disequilibria at Site 761B is <25 ppm. ODP 926 (3˚43.148'N, 42˚54.507'W), ODP Site 1237 (16˚0.421′S, 76˚22.685′W) and ODP Site 1146 (19˚27.40′N, 116˚16.37′E) are also plotted for reference. Data from Takahashi et al., (2009).

Boron isotope measurements (described in delta notation as $\delta^{11}B$ – permil variation from the boric acid standard SRM 951; Catanzaro et al., 1970) were made on the $CaCO_3$ shells of the mixed layer dwelling foraminifera *Globigerinoides trilobus* (300-355 μm). Boron was first separated from the Ca matrix prior to analysis using the boron specific resin Amberlite IRA 743 following Foster, (2008). The boron isotopic composition was then determined using a sample-standard bracketing routine on a ThermoFisher Scientific Neptune multicollector inductively coupled plasma mass spectrometer (MC-

ICPMS) at the University of Southampton (closely following Henehan et al., 2013). $\delta^{11}B$ in planktic foraminiferal calcite, such as *G. trilobus* (Sanyal et al., 2001), correlates positively with pH and negatively with $CO_{2(aq)}$ (Sanyal et al., 2000; Foster, 2008). In the absence of changes in the local hydrography, variations of atmospheric CO_2 are the dominant influence on $CO_{2(aq)}$. Previous work at ODP Site 761 during the Miocene has shown that $\delta^{11}B$-derived CO_2 is reproducible at ODP Site 926 and in broad agreement with other methods of reconstructing CO_2 (Fig. 5-1), suggesting that variations in atmospheric CO_2 are the dominant control on $\delta^{11}B$ variability at our study site (Foster et al., 2012).

To put the relative changes in CO_2 during the middle Miocene captured by our $\delta^{11}B$ data set in context, it is instructive to make absolute reconstructions of CO_2. To calculate CO_2 from $\delta^{11}B$ several other parameters are needed. First sea surface temperatures (SST) and sea surface salinities (SSS) are required to calculate the pK_B of boric acid (Dickson, 1990). Here SSTs are calculated from tandem Mg/Ca analyses on *G. trilobus* with adjustments for Mg/Ca_{sw} from (Horita et al., 2002) (with a conservative ± 3ºC) using the calibration of (Anand et al., 2003) while SSS is held constant at 35 ± 3 ‰ for the entire record. These variables only have a minor affect on the calculated pH and pCO_2 (~30 ppm for a ± 3 ºC; ± ~10 ppm for a ± 3 ‰). Second $\delta^{11}B_{sw}$ during the middle Miocene is an important source of uncertainty and can have a significant effect on the calculation of absolute CO_2. The residence time of boron in the oceans is long (~ 10 to 20 Myrs) ensuring that major changes in $\delta^{11}B_{sw}$ are unlikely during our 1.5 Myr-long study (Lemarchand et al., 2002b). It is probable, however, that $\delta^{11}B_{sw}$ in the Miocene was different to the present value of 39.61 ‰ and here we use a $\delta^{11}B_{sw}$ value of 37.82 ± 0.7 ‰ determined for the middle Miocene using offsets in $\delta^{11}B$ between benthic and planktic foraminifera (Foster et al., 2010; Foster et al., 2012). Thirdly, to define atmospheric CO_2 a second carbonate system parameter is needed. Here we use a total alkalinity value of 1292 ± 300 μmol/kg determined by Foster et al., (2012) for the middle Miocene and constrained by reconstructions of the calcium carbonate compensation depth (CCD) (Sime et al., 2007) and deep water pH reconstructions (Foster et al., 2012). A change in the depth of the CCD by ± 500 m results in variations of ±100 μmol/kg in the estimation of deep-water alkalinity. The ± 300 μmol/kg uncertainty on the alkalinity estimate used in this study should therefore account for any rapid changes in CCD, across this interval, that may not be fully resolved in the lower

resolution CCD records (Sime et al., 2007). A full propagation of uncertainty on our CO_2 estimate is carried out using a Monte Carlo simulation (n=10000) using the uncertainty limits highlighted above. The Monte Carlo simulation allows us to fully account for the combined effect of the required parameters on the calculated CO_2 and our overall uncertainty in our CO_2 estimates using this technique is calculated to be ± 66-353 ppm (95% confidence interval). These estimates include uncertainties in the $\delta^{11}B$ measurement, SST, SSS, total alkalinity and $\delta^{11}B$ seawater as outlined above. The uncertainties in the other parameters needed to calculate CO_2, aside from the *G. trilobus* $\delta^{11}B$, are larger (by a factor of 1.5 to 2) in this study than those reported by Foster et al., (2012) to reflect greater potential variability in these parameters over the shorter timescales investigated here and any secular evolution between the time interval when $\delta^{11}B_{sw}$ and total alkalinty were determined by Foster et al., (2012) and this study interval (12.72 Ma vs. 15.5-17 Ma).

5.3 Results and Discussion

In Figure 5-3, alongside published stable isotope records we present a new boron isotope data set spanning 15.5 to 17 Myrs from Site 761B. This new boron isotope record shows high $\delta^{11}B$ values (16 to 17.5 ‰; hence lowest CO_2) during the interval 17 to 16.5 Ma leading up to the MCO. During the MCO (16.5 to 15.5 Ma) the $\delta^{11}B$ record shows pronounced variability with the presence of distinctly lower values (16.5 to 14.5 ‰; hence higher CO_2) (Fig. 5-3). The 1.5 to 2 ‰ changes in $\delta^{11}B$ suggests that CO_2 variability is closely linked to the observed pronounced variability in high latitude climate during the MCO. Our data therefore confirm inferences made from the % $CaCO_3$ content of deep ocean sediments from the equatorial Pacific (Holbourn et al., 2014) that large variations in the carbon cycle accompanied climate variability during the MCO. The minima in $\delta^{11}B$ in our record appear to occur with a rough 100 kyr spacing raising the question of whether they might be paced by the short eccentricity cycle. However, our $\delta^{11}B$ data are not of sufficiently high temporal resolution to address this question quantitatively. Furthermore, while comparison of records at Site 761B shows some similarities of the appropriate sign ($\delta^{11}B$ maxima with $\delta^{18}O$ minima), the 761B $\delta^{18}O$ record does not demonstrate clear 100 kyr cyclicity (Fig. 5-3). This lack of clear orbital cyclicity in the oxygen also prohibits detailed correlation of our $\delta^{11}B$ record to other, better-resolved oxygen isotope stratigraphies. Therefore, while our $\delta^{11}B$ record

documents the existence of short-term CO_2 variability in the pre-Quaternary, work elsewhere is required to gain a fuller understanding of the links between CO_2 and climate on orbital timescales during the middle Miocene.

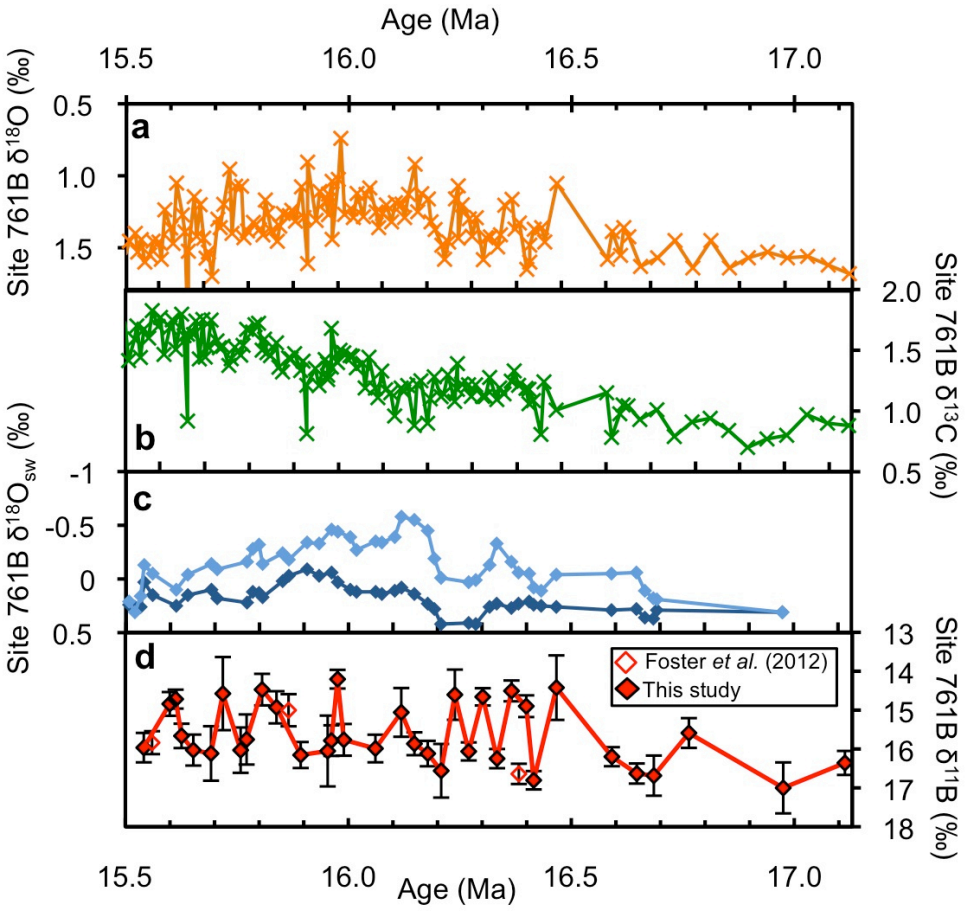

Figure 5-3: MCO climate proxies with the new boron isotope data ($\delta^{11}B$). (a-c) Benthic $\delta^{18}O$, $\delta^{13}C$ and seawater $\delta^{18}O$ record from Site 761B between 15.5-17.13 Myrs. For the $\delta^{18}O_{sw}$, light blue data points are calculated assuming a carbonate ion effect on the Mg/Ca ratios whilst the dark blue points are calculated assuming no carbonate ion effect on measured Mg/Ca (Holbourn et al., 2004; Lear et al., 2010) (d) $\delta^{11}B$ from Site 761B (solid diamonds from this study and open diamonds Foster et al., 2012). $\delta^{11}B$ are measured against NIST SRM boric acid standard 951. Note the inverted axis. Error bars show 2 s.d. external reproducibility.

Despite this inability to fully quantify the cyclicity within our new $\delta^{11}B$ record, our new data indicates that CO_2 oscillated from a baseline value of 250 to 350 ppm to a maximum of ~500 ppm, a value that is reached at several times during the MCO (±66-353 ppm, 95% confidence) (Fig. 5-4). The CO_2 minima and maxima in our new record fall close to the range of MCO values previously reported using a number of different

techniques (Kürschner et al., 2008; Foster et al., 2012; Zhang et al., 2013). The new record exhibits, however, considerably more structure than is seen in published data sets and goes some way to reconciling some of the differences among those existing CO_2 records. The maximum values for CO_2 that we calculate (~500 ppm) also fall within the range required in climate models to match the observed warmth during the MCO (e.g. 460-580 ppm You et al., 2009).

CO_2 exerts a logarithmic forcing on global climate defined by the relationship: Climate forcing = $5.35*\ln(C/C_0)$ W/m^2 where C is the CO_2 concentration in ppm and C_0 is the reference pre-industrial concentration (278 ppm) (Myhre et al., 1998). The range in CO_2 (interglacial-glacial) that we reconstruct is ~2 times larger in absolute terms than that associated with late Pleistocene climate change (Lüthi et al., 2008), but the logarithmic relationship between CO_2 and climate forcing means that the resulting increase in the range of radiative forcing is more modest (only ~15% larger than the late Pleistocene). Nevertheless, the larger range in radiative forcing for the Miocene than for the late Pleistocene contrasts sharply with the observed variability in climate as measured in the benthic oxygen isotope record (glacial-interglacial variability in benthic $\delta^{18}O$ during the Miocene is only about two thirds of that seen during the late Pleistocene; Lisiecki and Raymo, 2005; Holbourn et al., 2014). This observation suggests that larger CO_2 changes are required to induce changes in temperature and ice volume during the Miocene than for the late Pleistocene. We interpret this result to reflect the impact of the absence during the MCO of large ice sheets in the northern hemisphere (where ice sheets accumulate at lower latitudes than in the southern hemisphere and where the thermal response to transient CO_2 increase is greater because of a larger land area in the sensitive latitudinal range). In this interpretation, the absence of large ice sheets in the north acts to reduce the size of the reservoir of ice that is sensitive to subtle variations in atmospheric CO_2.

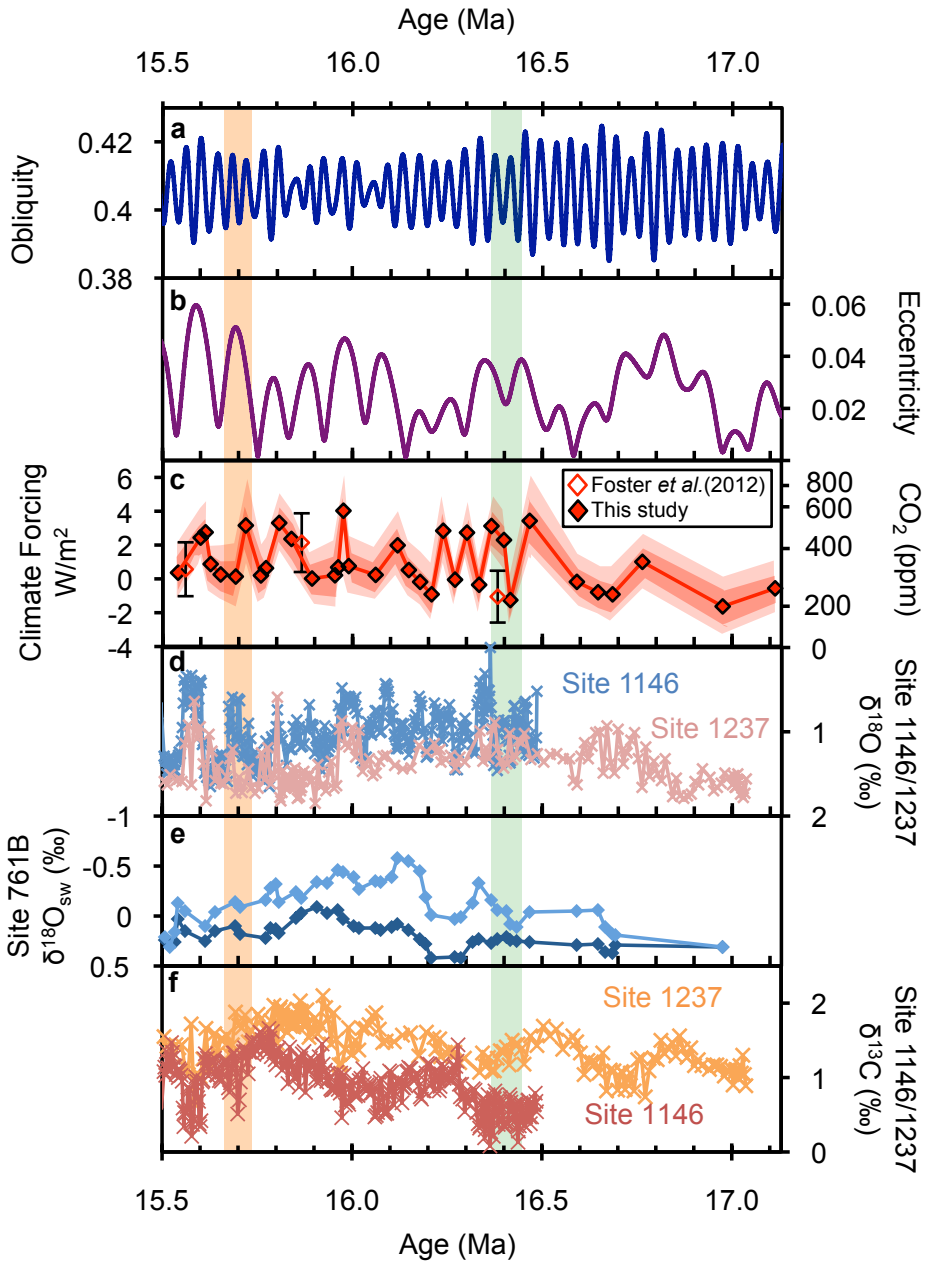

Figure 5-4: High amplitude changes in MCO climate records and CO_2. (a-b) Obliquity and eccentricity cycles (Laskar et al., 2004) (c) CO_2 reconstruction for ODP 761B plotted as CO_2 and climate forcing (Climate Forcing, $\Delta F = 5.35*\ln(C/C_0)$ W/m^2 where C is the CO_2 concentration in ppm and C_0 is the reference pre-industrial concentration (280 ppm) (Myhre et al., 1998), closed diamonds this study and open diamonds from Foster et al., (2012). CO_2 is calculated using a surface water total alkalinity (~1293 ± 300 μmol/kg) and a $\delta^{11}B_{sw}$ = 37.82 ± 0.7 ‰. The pale red band on δ^{11}B-CO_2 shows climate forcing/CO_2 uncertainty at 95% confidence level, dark red band at 68% confidence level for data from this study. The error bars on the Foster et al., (2012) data show climate forcing/CO_2 uncertainty at 95% confidence. (d) Benthic δ^{18}O record at ODP Site 1146 and ODP Site 1237 (Holbourn et al., 2007). (e) Seawater δ^{18}O (‰, vs PDB) (Lear et al., 2010). The light blue data points are calculated assuming a carbonate ion effect on the Mg/Ca ratios whilst the dark blue points are calculated assuming no carbonate ion effect on measured Mg/Ca (f) Benthic δ^{13}C record at ODP Site 1146 and ODP Site 1237 (Holbourn et al., 2007). Orange and green vertical bars highlights major ice sheet retreat at ~15.7 Ma and ~16.4 Ma respectively (Acton et al., 2008-2009; Warny et al., 2009; Fielding et al., 2011; Passchier et al., 2011).

Next we assess associations between CO_2 variability during the middle Miocene and rapid changes in ice sheet behavior by comparing our record with the ANDRILL records from the Antarctic margin. This task is not straightforward because of the lack of orbitally resolved age models both for the ANDRILL core and at Site 761. These uncertainties mean that we cannot directly correlate the detailed structure seen in our $\delta^{11}B$-CO_2 record with individual cycles in ice sheet behavior reconstructed from the ANDRILL records. Using the best stratigraphic age controls available, however, the two intervals of inferred dramatic ice sheet retreat (at ~15.7 Ma and ~16.4 Ma; coloured bands on Fig. 5-4) (Acton et al., 2008-2009; Warny et al., 2009; Fielding et al., 2011; Passchier et al., 2011; Feakins et al., 2012) fall during intervals of high amplitude variability in both obliquity and atmospheric CO_2, (Fig. 5-4), suggesting that warm summers brought about by a combination of high-tilt and high CO_2 are responsible for retreat of the Antarctic ice sheet in the middle Miocene. Further work on both the chronostratigraphy and paleoclimate history of AND-2A is needed to test this hypothesized relationship between atmospheric CO_2 and the stability of the Antarctic ice sheet.

In Figure 5-5, we compare CO_2 and ice volume between 12 and 17 Myrs by constructing cross plots of $\delta^{11}B$ and CO_2 forcing against $\delta^{18}O_{sw}$ (reconstructed from the benthic oxygen isotope record from which the temperature effect has been removed using Mg/Ca paleothermometry, Lear et al., 2010). We note that, at low levels of carbonate saturation, Mg/Ca in benthic foraminiferal calcite also responds to changes in carbonate saturation state (Elderfield et al., 2006; Yu and Elderfield, 2007). Uncertainties surrounding the threshold level of this effect led Lear et al., (2010) to calculate bottom water temperatures for two assumed scenarios, one in which Mg/Ca is unaffected by changes in saturation state and one in which Mg/Ca is affected by changes in saturation state. For the latter scenario paired Mg/Ca and Li/Ca records were used to correct for this effect. While that study demonstrated the potential of using paired trace metal records to correct for changes in carbonate saturation state it is important to acknowledge that uncertainties remain regarding the species-specific sensitivities and thresholds to both temperature and saturation state (Lear et al., 2010; Kender et al., 2014). Nevertheless, here we plot the $\delta^{18}O_{sw}$ calculated for both scenarios in Lear et al., (2010) to compare with our new CO_2 record. The Mg/Ca-temperatures are

based on modern seawater Mg/Ca and therefore the record should only be taken as an indication of $\delta^{18}O_{sw}$ variability. In order to better quantify the relationship between the $\delta^{11}B/CO_2$ forcing and $\delta^{18}O_{sw}$ we follow a probabilistic approach similar to Foster and Rohling, (2013) to fully account for the uncertainty in X and Y variables. This entailed generating 10,000 realizations of each data set by randomly perturbing each data point within its uncertainty (see Fig 5-5. caption for more details). Non-parametric regressions (LOWESS) were fitted to each realization and the distributions of LOWESS curves at each $\delta^{11}B/CO_2$ forcing step was assessed and the probability maximum, as well as the 68% and 95% probability intervals, was determined. Importantly, because we are only concerned here with relative change in climate forcing it is not necessary to propagate all of the uncertainties in CO_2 discussed above. For instance, whilst the absolute value of $\delta^{11}B_{sw}$ during the middle Miocene is uncertain (37.82 ± 0.7 permil), given the oceanic residence time of boron it is unlikely to change across our study interval and so can be ignored. Similarly, the uncertainty on the Mg/Ca based temperature is largely due to the correction in the Mg/Ca of seawater, which is uncertain in the middle Miocene but unlikely to vary significantly across the study interval (residence time of Mg and Ca is 14 and 1 Ma respectively), and so our SST uncertainty can be reduced to ± 1 ºC (reflecting the analytical uncertainty in Mg/Ca measurement). Finally, studies of the Quaternary glacial-interglacial cycles suggest that whole ocean alkalinity does not vary on these timescales by more than ± 150 μmol/kg (Hain et al., 2010), given this is likely an extreme case, we therefore reduce the TA uncertainty to ± 200 μmol/kg to cover the likely change in this variable across our record.

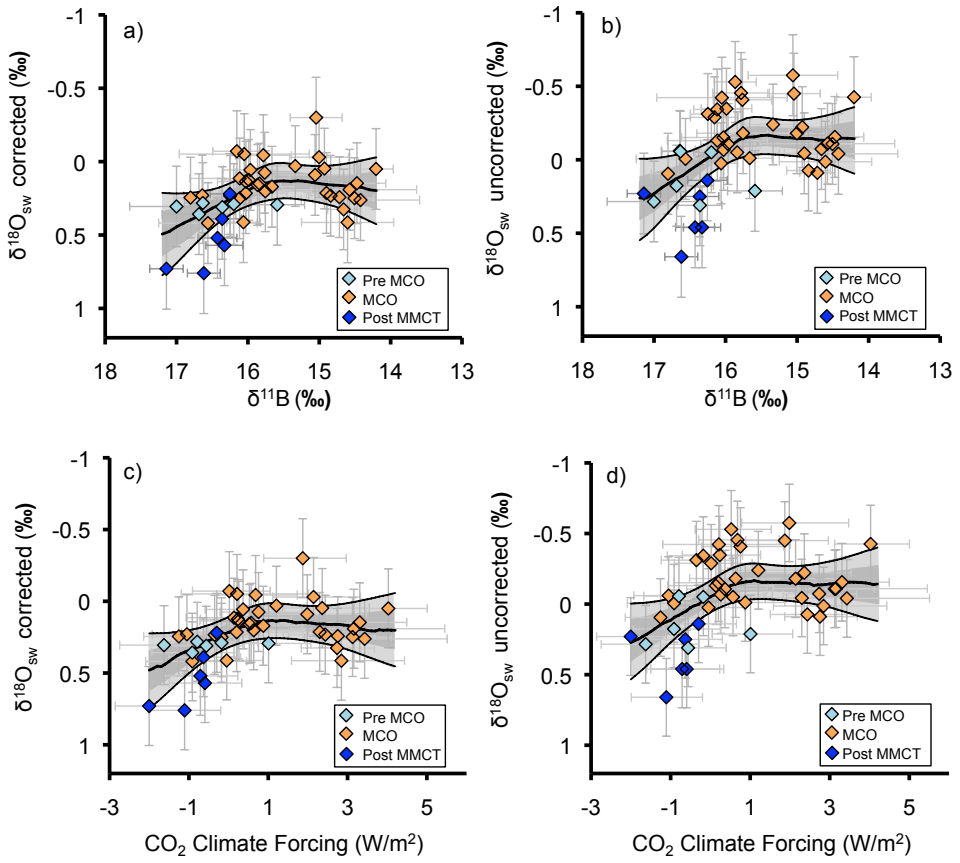

Figure 5-5: Cross plots of $\delta^{11}B$/climate forcing and $\delta^{18}O_{sw}$. For $\delta^{18}O_{sw}$ calculations see Lear et al., (2010). (a) $\delta^{18}O_{sw}$ calculated assuming a carbonate saturation state effect on Mg/Ca plotted with *G.trilobus* $\delta^{11}B$. (b) $\delta^{18}O_{sw}$ calculated assuming no carbonate saturation state effect on Mg/Ca plotted with *G.trilobus* $\delta^{11}B$. (c) $\delta^{18}O_{sw}$ calculated assuming a carbonate saturation state effect on Mg/Ca plotted with climate forcing (as defined in text). (d) $\delta^{18}O_{sw}$ calculated assuming no carbonate saturation state effect on Mg/Ca plotted with climate forcing. $\delta^{11}B$/climate forcing data from this study and Foster et al., (2012) and error bars show either analytical uncertainty (for $\delta^{11}B$) or reconstructed uncertainty (climate forcing, see text). In each plot the data are divided into Pre-MCO (light blue), MCO (orange) and Post MMCT (dark blue) and uncertainty on $\delta^{18}O_{sw}$ is ± 0.275 ‰ (at 68% confidence) due to the ± 1 ºC uncertainty (at 68% confidence) of the Mg/Ca-temperature calibration used in Lear et al., (2010). The black line describes the most likely relationship between the X and Y variables (the probability maximum) given the uncertainty in these variables, the light and dark grey areas are the 95% and 68% confidence intervals. Note the deep-water temperature used to estimates $\delta^{18}O_{sw}$ were calculated using modern seawater Mg/Ca ratio as in Lear et al., (2010) and should therefore only be interpreted in terms of relative change.

This treatment of the data clearly reveals a curvilinear relationship between $\delta^{11}B/CO_2$ forcing and ice volume, regardless of our choice of corrected or uncorrected $\delta^{18}O_{sw}$ (Fig. 5-5). The inflection point on these non-parametric regressions can be used to identify two distinct $\delta^{18}O_{sw}/CO_2$ forcing regimes (Fig. 5-5). Regime I is characterised by comparatively low levels of atmospheric CO_2 values and a near-linear relationship

between increasing CO_2 and decreasing ice volume ($\delta^{18}O_{sw}$) while Regime II is characterised by higher CO_2 but no additional change in ice volume. While ice existed on the continents of the northern hemisphere from at least Eocene/Oligocene boundary time (Eldrett et al., 2007), the global ice budget was almost certainly dominated by the Antarctic ice sheets until the late Pliocene (DeConto et al., 2008; Bailey et al., 2013; Rohling et al., 2014). Thus, there may have been a small contribution to the global ice budget from the northern hemisphere during intervals of peak $\delta^{18}O_{sw}$ (greatest ice volumes) during the mid-Miocene Climatic Transition but during the MCO, it is likely that ice sheet variability traced by changes in $\delta^{18}O_{sw}$ capture the waxing and waning of Antarctic ice sheets. The marine-based West Antarctic ice sheet today is certainly the most dynamic component of the Antarctic ice sheet system (Pollard and DeConto, 2009), however, recent ice-proximal provenance studies suggest that during the Pliocene Epoch (3-5 Ma) parts of the East Antarctic ice sheet may also have acted as a dynamic reservoir (Cook et al., 2013; Mengel and Levermann, 2014). Most of the data from the MCO lie in Regime II, or on the upper part of the steep limb that defines Regime I (Fig 5-5) suggesting that during this time interval two reservoirs of ice existed, one of which was stable (i.e. no change in $\delta^{18}O_{sw}$ for a given change in CO_2), even at the highest CO_2 levels seen in our record and another that is more dynamic at these low CO_2 levels than predicted by the results of classic coupled climate-Antarctic ice sheet models (Pollard and DeConto, 2005).

5.4 Conclusions

Our new $\delta^{11}B$ record indicates that high amplitude CO_2 variations accompanied the orbitally paced climatic changes observed in a range of climate records during the middle Miocene. In particular we show, using the best stratigraphic information available, that the two intervals of Antarctic ice sheet retreat identified in the AND-2A ANDRILL core occur during the MCO when the amplitudes of CO_2 and orbital obliquity variability are both high. A lack of late Pleistocene-like ice sheets in the northern hemisphere indicates that, while the overall climatic response to CO_2 change was muted in the middle Miocene, our results also indicate that there was a component of the continental ice budget, most likely on Antarctic, that was responding to CO_2. In detail our results point to the existence of two reservoirs of ice on Antarctica during the Miocene, one that is stable even at comparatively high CO_2 levels and one that is

dynamic at the lower end of the CO_2 range reconstructed. While our data do not distinguish the separated reservoirs, in light of the magnitude of $\delta^{18}O_{sw}$ variability we envisage a multi-component Antarctic ice sheet with at least one component (including a portion of the East Antarctic ice sheet) showing significant ice sheet variability at CO_2 concentrations lower than the threshold predicted by coupled climate-ice sheet models (Pollard and DeConto, 2005; Cook et al., 2013; Gasson et al., 2014; Mengel and Levermann, 2014). An important implication of this finding is that present day continental ice masses may become increasingly dynamic as the Earth-system approaches equilibrium with anthropogenic climate forcing.

Chapter 6: The relationship between ice volume and CO_2 across the Oligocene-Miocene boundary.

Acknowledgements:

The following chapter is written in the style of a research article with the intention of future publication. The contributions of co-authors to this work are detailed below.

Rosanna Greenop: data collection and analysis, calculating CO_2, data interpretation, manuscript drafting and production of figures.

Sindia S. Sosdian: aided in the collection of some of the $\delta^{11}B$ data

Gavin L. Foster: data interpretation and manuscript drafting

Paul A. Wilson: manuscript drafting

Caroline H. Lear: provided some of the Site 926 and all of the Site 872 samples for $\delta^{11}B$ analysis

Abstract:

The Mi-1 glaciation, coincident with the Oligocene-Miocene transition (OMT) is one of the major climatic events of the Cenozoic and interpreted to involve a large (estimated ~50 m sea level equivalent) rapid (200-300 kyrs) transient expansion and contraction in Antarctic ice volume. The causes of these events are poorly understood. Orbital forcing has long been cited as an important factor determining the timing of the ice sheet growth, however, the existence of a similar orbital configuration 1.2 million years prior to the event suggests that additional mechanisms play an important role. To improve our understanding of the mechanisms involved we present a boron isotope-based CO_2 record between 22 and 24 Myrs from two sites in the Atlantic Ocean (Ocean Drilling Program, ODP, Site 926 in the equatorial Atlantic and Integrated Ocean Drilling Program, IODP, Site U1406 in the North Atlantic) and one site in the Pacific Ocean (ODP Site 872). These records show that CO_2 was low (~240 ppm) and comparatively stable on the immediate run-up to the Mi-1 glaciation but increased to ~400-500 ppm during the subsequent deglaciation. When we combine our new CO_2 record with

published Oligocene data sets Mi-1 glaciation appears to be controlled by long-term decline in CO_2 levels below a critical threshold, as part of a long-term CO_2 decline, and a favourable orbital configuration, caused by a combination of low obliquity and low amplitude eccentricity. Large published estimates of ice volume change on Antarctica of (50 msle) across the OMT are difficult to reconcile with the relatively modest changes in CO_2 indicated in our records.

6.1 Introduction

Over the last 55 million years Earth's climate has gradually cooled and superimposed upon this long-term evolution are intervals of more rapid change (Zachos et al., 2008). The Oligocene-Miocene stratigraphic transition coincides with one of these events, the Mi-1 glaciation (terminology of Miller et al., 1991; ca. 23 Ma, see Fig. 6-1). This abrupt cooling event is evident in the oxygen isotope record as a transient two-step positive increase in benthic $\delta^{18}O$. The magnitude of this change has typically been estimated at approximately 1 ‰ (Miller et al., 1991; Paul et al., 2000; Pälike et al., 2006a; Pälike et al., 2006b; Liebrand et al., 2011), and interpreted to represent an expansion in continental ice volume of approximately ~50 m (s.l.e) and bottom water-cooling of approximately 2ºC (Mawbey and Lear, 2013). However, a recent re-evaluation of stacked benthic $\delta^{18}O$ records argues that the excursion was smaller (~ 0.6 ‰) and that previous work had placed too much emphasis on the extremes in the interpretation of the individual records (Mudelsee et al., 2014). While it is not possible to discount the involvement of Northern Hemisphere ice in contributing to the amplitude of the Mi-1 glaciation, it has been shown that at least some of the ice volume change occurred on Antarctica (Naish et al., 2001).

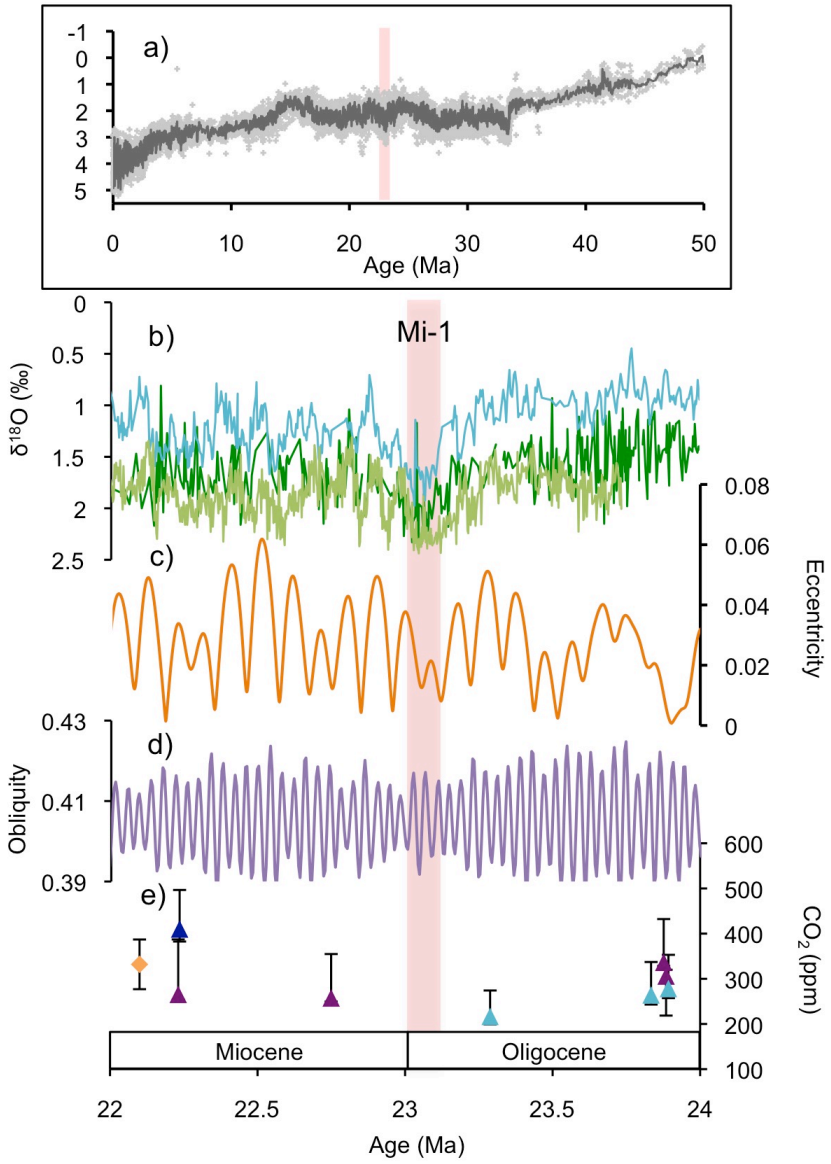

Figure 6-1: Climate and forcing over the Oligocene-Miocene transition. a) Cenozoic oxygen isotope composite (Zachos et al., 2008) (b) Oxygen isotope records from Site 926 (blue) (Pälike et al., 2006a), Site 1264 (light green) (Liebrand et al., 2011) and Site 1218 (dark green) (Pälike et al., 2006b and references therein). (c) Eccentricity orbital forcing and (d) Obliquity orbital forcing from Laskar et al., (2004). (e) Previously published CO_2 records from across the Mi-1 glaciation. Alkenone reconstructions (light blue and purple) from Pagani et al., (2005) and (dark blue) from Zhang et al., (2013) plotted on the age model of Pagani et al., (2011) updated to Gradstein et al., (2012). Leaf stomata CO_2 reconstruction (yellow diamond) from Kürschner et al., (2008). The Oligocene-Miocene transition is highlighted in red.

Orbital forcing plays a central role in the character of the Mi-1 glaciation, with deep-ocean cooling and ice sheet growth/retreat occurring as a number of orbitally paced steps (Naish et al., 2001; Zachos et al., 2001b; Pälike et al., 2006a; Pälike et al., 2006b; Liebrand et al., 2011; Mawbey and Lear, 2013;). For instance, following the Mi-1

glaciation, a strong 100 kyr cyclicity is evident in a number of benthic oxygen isotope records (Zachos et al., 2001b; Liebrand et al., 2011) and $\delta^{18}O_{sw}$ (calculated from coupled benthic oxygen isotope and Mg/Ca measurements) (Mawbey and Lear, 2013). It is evident from such high-resolution records of benthic $\delta^{18}O$ that the Mi-1 glaciation coincides with low obliquity, associated with the 1.2 Myr modulation of the Earth's orbit and axial tilt (an obliquity 'node'), as well as reduced amplitude of eccentricity (400 kyr long eccentricity cycle; i.e. a very circular orbit), both of which reduce seasonal extremes and increase the chances of winter snowfall surviving the summer ablation season (Zachos et al., 2001b; Pälike et al., 2006a) (Fig. 6-1). However, obliquity nodes occur with regular frequency throughout the late Oligocene (Laskar et al., 2004) and the amplitude of the previous one at 24.4 Ma is more extreme than that associated with the Oligocene-Miocene transition (Pälike et al., 2006a). Consequently, despite a clear orbital pacing to Mi-1, changes in other transition conditions are required in order to explain the exact timing of the climate perturbation.

Given the importance of atmospheric CO_2 as a determinant of the secular evolution of Earth's climate on these timescales, it is commonly suggested that the Mi-1 glaciation is also associated with a perturbation of the carbon cycle (Zachos et al., 1997; Paul et al., 2000; Mawbey and Lear, 2013). It has been well documented by numerous modeling studies (DeConto and Pollard, 2003b; Gasson et al., 2012) and a growing number of reconstructions (e.g. Pearson et al., 2009; Pagani et al., 2011; Foster et al., 2012; Greenop et al., 2014) that CO_2 plays an important role in controlling the timing of ice sheet growth and retreat throughout the Cenozoic. In the absence of a detailed CO_2 record across the Mi-1 glaciation the long-term increase of 0.8‰ in carbon isotopes from 24 to 22.9 Ma at Site 929 has been attributed to an increase in global organic carbon burial and the associated reduction in atmospheric CO_2 (Zachos et al., 1997; Paul et al., 2000). On the basis of deep ocean $CaCO_3$ preservation indicators, an increase in CO_2 has also been implicated as one of the driving forces of the deglaciation that followed the glacial maximum at 23 Ma (Mawbey and Lear, 2013). The published CO_2 records, however, do not have the required resolution to test these hypotheses, or to test for the CO_2 decline that would be expected to accompany an increase in organic carbon burial prior to Mi-1 glaciation (Fig. 6-1). A further complication with the traditional interpretation of the Mi-1 glaciation concerns the rapid, largely symmetrical, and orbitally paced nature of the ice growth and ice retreat across the event. Ice sheet

models for the Antarctic ice sheet suggest a relatively high threshold (>1000 ppm) for melting of the ice sheet once it has grown due to inherent hysteresis (Pollard and DeConto, 2005). If the Antarctic ice sheet does play a role in the ice sheet changes across the O-M transition (Naish et al., 2001), this dynamic behaviour must occur at a CO_2 level substantially below the modelled threshold. However, to better understand the timing and causes of Mi-1 glaciation it is clear that CO_2 data are required at substantially higher resolution that is currently available (Fig. 6-1). Here we present the first high-resolution, multi-site boron isotope based CO_2 record across the Mi-1 glaciation.

6.2 Methods and Site information

6.2.1 Site Location and Information

We utilise sediments from three open ocean sites: IODP Site 1406 from the Newfoundland Ridge (40°21.0′N, 51°39.0′W; water depth of 3798.9 m), ODP Hole 926B from Ceara Rise (3°43′N, 42°54′W; 3598 m water depth) and ODP Hole 872C situated in the tropical north Pacific gyre on the sedimentary caps of flat-topped seamounts (10°05.850'N, 162°51.960'E, water depth of 1287 m). All three sites are currently located in regions where surface water is close to equilibrium (+/- 25 ppm) with the atmosphere with respect to CO_2 (Fig. 6-2; (Takahashi et al., 2009)). Age models are based on (Expedition 342 Scientists, 2012) and (Pälike et al., 2006a and references therein) and (Pearson, 1995) for Site 1406, Site 926 and Site 872 respectively. The foraminifera sampled from IODP Site 1406 were taken from between 51 and 97 metres below sea floor (mcd). Foraminifera from ODP Site 926 were sampled from between 469 and 527 mcd. Foraminifera from ODP Site 872 were sampled from between 112 and 117 mcd. Visual inspection of the foraminifera from sites 926 and 1406 shows that, as a result of the greater burial depth, the foraminifera at ODP Site 926 have been subjected to more micro-crystalline recrystallisation than ODP Site 1406, where the preservation is exceptional for this time interval (Fig. 6-S1). Comparison of the two sites may thus allow us to assess potential diagenetic effects on our $\delta^{11}B$ data.

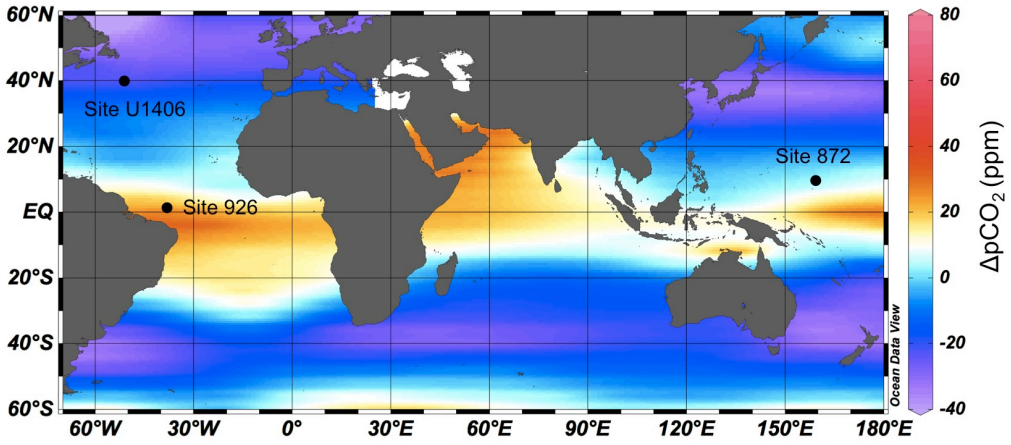

Figure 6-2: Map of study sites and mean annual air-sea disequilibria with respect to pCO_2. The black dots indicate the location of the sites used in this study. IODP Site U1406 (40°21.0′N, 51°39.0′W) is from a water depth of 3798.9 m and the modern extent of disequilibria is ~ -24 ppm. ODP Site 926 (3°43.148′N, 42°54.507′W) is at a water depth of 3598 m and the modern extent of disequilibria is ~ +22 ppm. ODP Site 872C (10°05.850'N, 162°51.960'E) is from a water depth of 1287 m and the modern extent of disequilibria is ~ 0 ppm. Data are from Takahashi et al., (2009).

6.2.2 Boron isotope measurements

Trace element and boron isotope (described in delta notation as $\delta^{11}B$ – permil variation from the boric acid standard SRM 951; Catanzaro et al., 1970) measurements were made on the $CaCO_3$ shells of the mixed-layer dwelling foraminifera *Globigerina praebulloides* (250-300 μm) at Sites 926 and 1406. At Site 872, mixed layer dwelling foraminifera *Globigerinoides trilobus* (300-355 μm) were analysed. The foraminifera were cleaned following the oxidative cleaning methodology of Barker et al., (2003) before dissolution by incremental addition of 0.5 M HNO_3. Trace element analysis was then conducted on a small aliquot of the dissolved sample at the University of Southampton using a ThermoFisher Scientific Element 2 XR to measure Mg/Ca for ocean temperature estimates and Al/Ca to assess the competency of the sample cleaning. For boron isotope analysis the boron was first separated from the Ca matrix using the boron specific resin Amberlite IRA 743 following (Foster et al., 2008). The boron isotopic composition was then determined using a sample-standard bracketing routine on a ThermoFisher Scientific Neptune multicollector inductively coupled plasma mass spectrometer (MC-ICPMS) at the University of Southampton (closely following Henehan et al., 2013).

6.2.3 The $\delta^{11}B$-pH proxy

Boron exists as two stable isotopes in the ocean, ^{10}B and ^{11}B in the proportions of 19.82% and 80.18% respectively. The two major dissolved species of boron in seawater are trigonally coordinated boric acid $B(OH)_3$ and the tetrahedrally-coordinated borate ion $B(OH)_4^-$. The proportions of these two species is pH dependent such that at low pH all dissolved boron is in the $B(OH)_3$ form and at high pH all dissolved boron is in the $B(OH)_4^-$ species (Zeebe and Wolf-Gladrow, 2001).

$$B(OH)_3 + 2H_2O = B(OH)_4^- + H_3O^+ \qquad (6.1)$$

A pronounced isotopic fractionation exists between the two aqueous boron species as a consequence of differences in coordination and vibration frequencies. Consequently given a change in pH both the proportion of the two species and their isotopic composition varies.

A large body of evidence suggests that only the charged species is predominantly incorporated into the foraminifer shell (Hemming and Hanson, 1992; Sanyal et al., 2000; Sanyal et al., 2001; Foster et al., 2008; Rae et al., 2011; Henehan et al., 2013) and consequently $\delta^{11}B$ in planktic foraminiferal calcite correlates positively with pH and negatively with $[CO_2]_{aq}$. The $\delta^{11}B$ of $B(OH)_4^-$ is related to pH by the following equation:

$$pH = pK_B^* - \log\left(\frac{\delta^{11}B_{SW} - \delta^{11}B_{CaCO_3}}{\delta^{11}B_{SW} - \propto_B . \delta^{11}B_{CaCO_3} - 1000\,.(\propto_B - 1)}\right) \qquad (6.2)$$

In the absence of changes in the local hydrography, variations of atmospheric CO_2 have a dominant influence on $[CO_2]_{aq}$. Although the $\delta^{11}B$ of foraminifera correlates well with pH and $[CO_2]_{aq}$, the $\delta^{11}B_{calcite}$ is often not exactly equal to $\delta^{11}B_{borate}$ (Fig. 6-3) (Sanyal et al., 2001; Foster, 2008; Henehan et al., 2013). For instance, while the pH sensitivity of $\delta^{11}B$ in modern *G. bulloides* is similar to the pH sensitivity of $\delta^{11}B$ in borate ion, the relationship between pH and $\delta^{11}B$ falls below the theoretical $\delta^{11}B_{borate}$-pH line (i.e a lower $\delta^{11}B$ for a given pH) (Martinez Boti et al., 2015b) (Fig. 6-3). This effect has been attributed to the dominance of respiration and calcification on the foraminifer's microenvironment in asymbiotic foraminifera, which both act to drive down local pH (Hönisch et al., 2003; Zeebe et al., 2003). In contrast, photosynthetic processes in symbiont-bearing foraminifera cause the pH of the micro-environment to be elevated above that of the external seawater (Henehan et al., 2013). Recent work, based on $\delta^{13}C$

and $\delta^{18}O$ changes with size fraction, has shown at the Oligocene-Miocene transition *G. praebulloides* appears to be symbiotic, in contrast to *G. bulloides* that is thought to be its nearest living relative (Chapter 3). Consequently the modern $\delta^{11}B$-pH calibration of *G. bulloides* is not applicable. The good agreement in absolute terms between $\delta^{11}B$ in *G. praebulloides* from this study and *G. trilobus* from Site 872 suggests that the *G. sacculifer* calibration may be more applicable (Fig. 6-3, 6-4, 6-5). In the absence of a *G. sacculifer* calibration for the 250-300 µm size fraction, following (Foster et al., 2012), we apply the *G. sacculifer* calibration of (Sanyal et al., 2001) with a modified intercept so that it passes through the core top value for *G. sacculifer* (300–355 µm) from ODP 999A (Seki et al., 2010).

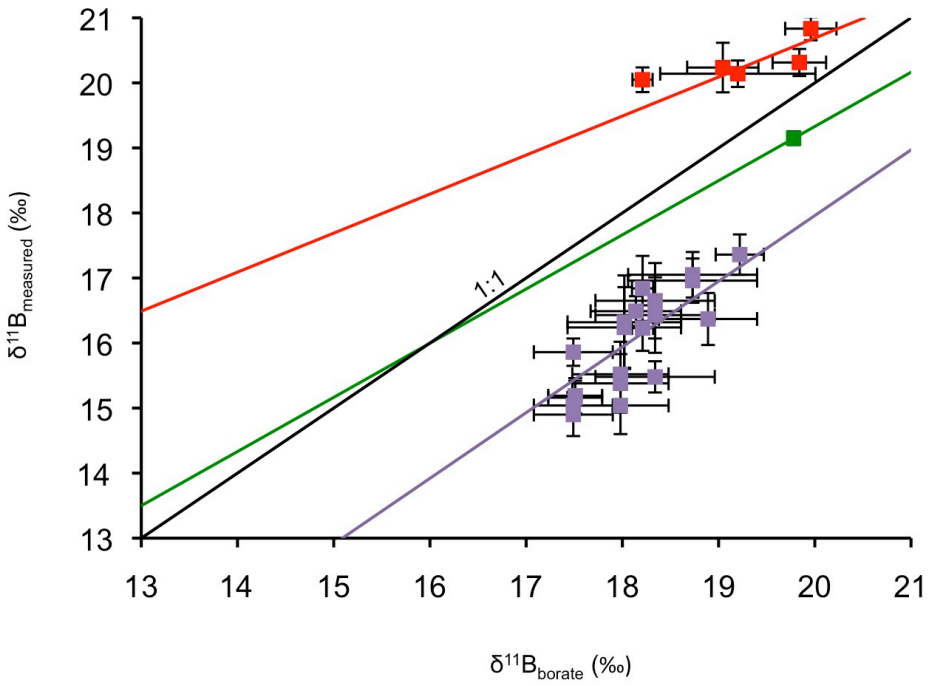

Figure 6-3: Offset between $\delta^{11}B_{measured}$ and $\delta^{11}B_{borate}$ for a range of modern species. The 1:1 line is the $\delta^{11}B$ of the borate ion. The calibration for *G. ruber* (red) is from Henehan et al., (2013) and the intercept is modified to go through the 250-300 µm size fraction data (red squares) from the same study. The calibration for *G. sacculifer* (green) is from Sanyal et al., (2001) and the intercept is modified to go through the 300-355 µm size fraction core top value (green square) from (Seki et al., 2010). The calibration for *G. bulloides* is from Martinez-Boti et al., (2015b) and core top data are a mix of size fractions (purple squares) from the same study as there is no systematic change in $\delta^{11}B$ with size fraction in this species.

6.2.4 Calculating CO_2

To further understand the role of CO_2 in driving the Mi-1 glaciation we need to put the relative changes of CO_2 indicated by $\delta^{11}B$ alone into a quantitative framework by making absolute reconstructions of CO_2. To do this we need the following additional information: temperature, salinity, $\delta^{11}B_{sw}$ and a second carbonate system parameter (e.g. Foster et al., 2012).

(i) Temperature and salinity changes are assessed using Mg/Ca derived temperatures alongside planktic stable oxygen isotopes. SSTs are calculated from tandem Mg/Ca analyses on *G. bulloides* using the generic Mg/Ca temperature calibration of Anand et al., (2003). Adjustments were made for changes in the Mg/Ca_{sw} using the record of Horita et al., (2002) and correcting for changes in dependence on Mg/Ca_{sw} following Evans and Muller, (2012) using H = 0.41 calculated from *G. sacculifer* (Delany et al., 1985; Hasiuk and Lohmann, 2010; Evans and Muller, 2012). After evaluation of the Mg/Ca temperature estimates (see Section 6.3.1) we elect to use the Mg/Ca derived temperatures at Site 926 and Site 872 and apply a conservative estimate of uncertainty in Mg/Ca-SST of ± 3 C, to account for analytical uncertainty, uncertainty in the magnitude of the Mg/Ca_{sw} correction and potential diagenetic alteration. As a result of issues with the Mg/Ca temperature estimates at Site 1406 (see Section 6.3.1), we use the temperature estimates from Site 926 and apply the modern temperature gradient of ~10ºC between Site 1406 and Site 926. The temperature effect on CO_2 calculated from $\delta^{11}B$ is ~ 10-15 ppm/ºC. Consequently small variations in SSTs have a limited effect on the calculated CO_2, however, this does become more significant when the variations are greater than 5ºC. Based on the planktic oxygen isotope record at Site 1406, we hypotheses that large changes in temperature are occurring at this site across the boundary (see section 6.3.1 for details). Consequently here we use a larger uncertainty of ± 5 ºC. We assume salinity remained the same as modern day at all three sites and apply a conservative estimate of ± 3 psu to account for any changes in this parameter through time. Salinity has a little effect on CO_2 uncertainty (± 3-14 ppm for a ± 3 ‰).

(ii) The $\delta^{11}B_{sw}$ during the middle Miocene is a large source of uncertainty and can have a significant effect on the calculation of absolute CO_2. Although the residence time of boron in the oceans (~ 10 to 20 Myrs) ensures that major changes in $\delta^{11}B_{sw}$ during the 2 Myr interval we assess here are unlikely (Lemarchand et al., 2002b), it is probable that

$\delta^{11}B_{sw}$ has shifted from the present value of 39.61 ‰ in the past 17 Myrs (Foster et al., 2010). Here we used the $\delta^{11}B_{sw}$ record from Chapter 4, calculated using $\delta^{11}B$ and $\delta^{13}C$ from planktic-benthic foraminifera pairs. Across this interval $\delta^{11}B_{sw}$ is 38.06-38.09 ‰ with an uncertainty of 0.99-1.52 ‰. While the absolute value of $\delta^{11}B_{sw}$ is uncertain, given the oceanic residence time of boron, it is unlikely to change across our study interval and so can be ignored in the calculation of relative changes of CO_2.

(iii) To define atmospheric CO_2 a second carbonate system parameter is needed. Carbon cycle modelling experiments have shown that surface water calcite saturation state ($\Omega_{calcite}$) is well regulated, varying by only around 0.5 from the modern mean global value of approximately 5.4 over the past 100 million years (Tyrrell and Zeebe, 2004; Ridgwell, 2005). If we assume that $\Omega_{calcite}$ remained constant and the [Ca] through time is known (e.g. from fluid inclusions; Horita et al., 2002), we can calculate CO_3^{2-} and hence CO_2 using the $\delta^{11}B$ derived pH. However, while surface water omega appears to remain relatively constant on long timescales (e.g. >100 kyrs) (Tyrrell and Zeebe, 2004; Ridgwell, 2005; Honisch et al., 2012), rapid perturbations in the ocean carbonate system can drive substantial changes in omega on timescales < 100 kyrs that are in fact correlated with pH change (Honisch et al., 2012). Consequently, here we assume the average omega of the whole record, rather than on each individual data points is equal to the modern, and has been used to determine and average total alkalinity. We calculate total alkalinity to be 1800 μmol/kg using the $\delta^{11}B$ at Site 926 and the [Ca] record of Horita et al., (2002) by adjusting total alkalinity until the surface water omega across the whole record averages the modern day value of 5.69 at Site 926. $\Omega_{calcite}$ at Site 1406 may have changed across the Oligocene-Miocene transition as a consequence of the location of the site at the transition between two surface water masses. Consequently we apply the alkalinity estimate from Site 1406 to this site. The limited data at Site 872 means that it is more difficult to calculate 'average' omega across the whole record here and we therefore apply the alkalinity estimation from Site 926. Given that the modern difference in total alkalinity between Site 926 and Site 872 is relatively small (~100 μmol/kg) we think this assumption is reasonable in light of the uncertainty on the total alkalinity estimate (± 800 μmol/kg). The alkalinity uncertainty is based on the uncertainty in [Ca] (± 0.0045 μmol/kg), omega (± 0.5) and the other parameters needed to calculate pH. Note we have chosen to use total alkalinity rather than CO_3^{2-} directly. This is because on these timescales pH and CO_3^2 should be positively correlated

(Honisch et al., 2012) and perturbing each variable independently in our Monte Carlo simulations (below) to fully propagate uncertainty causes the CO_2 uncertainty to be unjustifiably large. The effect of [Mg] and [Ca] on the equilibrium constants K1, K2 and K_{sp} was parameterised using the corrections from Ben-Yaakov and Goldhaber, (1973) following Tyrrell and Zeebe, (2004).

For each CO_2 data point a full propagation of uncertainty is carried out using a Monte Carlo simulation (n=10000) perturbing each data point within the uncertainty limits in the $\delta^{11}B$ measurement (± 0.16-0.85 ‰), SST (± 3 ºC at Sites 872 and 926, ± 5 ºC at Site 1406), SSS (± 3 psu), total alkalinity (± 800 μmol/kg) and $\delta^{11}B$ seawater (±0.94-1.66 ‰). Our overall uncertainty in our CO_2 record using this technique is estimated to be ± 70-186 ppm at Site 926, ± 64-627 ppm at Site 1406 and ± 97-137 ppm at Site 872 (95% confidence interval). These uncertainties are dominated by the uncertainties in alkalinity and $\delta^{11}B_{sw}$, which are both primarily associated with the calculation of absolute CO_2 levels. As noted above, the long residence time of boron in the ocean makes it unlikely that $\delta^{11}B_{sw}$ has changed significantly during the interval of study. In addition, studies of the Quaternary glacial-interglacial cycles suggest that that alkalinity changes are unlikely to be above 150 μmol/kg over these timescales (Hain et al., 2010). Consequently, for relative changes of CO_2, the uncertainty associated with $\delta^{11}B_{sw}$ can be ignored and the uncertainty associated with total alkalinity can be reduced (to ±150 μmol/kg). Overall this leads to significantly smaller uncertainties on the calculated relative CO_2 changes (± 30-190 ppm).

6.3 Results and discussion

6.3.1 Surface water temperature and salinity fluctuations

At Site 926 the available planktic $\delta^{18}O$ record suggests that the surface water conditions were relatively stable across the Mi-1 glaciation (variations of < 0.5 ‰) (Fig. 6-S2). Although the $\delta^{18}O$ record does not extend over the whole of our $\delta^{11}B$ record, the lack of variability over the Mi-1 glaciation, where we would expect to see the most change, suggests that the surface waters were relativity stable throughout the study interval. While diagenetic alteration may mean the absolute values of $\delta^{18}O$ are offset to higher values (and therefore lower paleotemperatures), on these timescales, it is likely the relative changes have been preserved (Sexton et al., 2006a). The Mg/Ca record shows

more variability (25-29ºC) including a sustained decrease of 1.5ºC at 23 Ma, however, there is no evidence of major changes in hydrography. No planktic oxygen isotope data exists for Site 872, however, the Mg/Ca estimates are relatively stable across the three data points, suggesting that there were no large oceanographic changes at this site across the Mi-1 event (see appendix E.1). Like $\delta^{18}O$, the Mg/Ca ratios of planktic foraminifera are also susceptible to diagenetic alteration and consequently the Mg/Ca ratios from Sites 962 and 872 may be reflecting both a primary temperature and a secondary diagenetic signal (Sexton et al., 2006a). However, although the degree of diagenetic alteration appears to vary with species, in general, foraminifera with poor preservation display only marginally higher Mg/Ca than the same species from a different site where preservation is good (Sexton et al., 2006a). The Mn/Ca ratio of foraminifera can be used as an indicator for the presence of ferromanganese coatings, which also contain Mg. The Mn/Ca ratios of the foraminifera are relatively low at Site 872 (~500 μmol/mol) but are elevated at Site 926 (~600-1000 μmol/mol). However, previous work has shown that most of the Mn at Site 926 is in manganese carbonate overgrowths, rather than ferromanganese coatings (Stewart, 2012). Consequently, as outlined above, for Site 926 and Site 872 we use the Mg/Ca derived temperature estimates with a ± 3 ºC temperature uncertainty.

At Site 1406, a low-resolution *G. praebulloides* $\delta^{18}O$ record from across the Oligocene-Miocene transition suggests that there are large changes in surface water conditions (Fig. 6-S3). The $\delta^{18}O_{planktic}$ increases by 2 ‰ between 22 and 23 Ma, suggesting that there are large temperature and/or salinity shifts across this interval. If the 2 ‰ increase was solely due to temperature it would result in a temperature increase of ~8ºC across the study interval. Given the position of the site on the transition between the Gulf Stream and the Labrador Current in the modern day, a temperature change of this magnitude could be caused by shifting circulation patterns associated with the warming out of the Mi-1 glaciation (Fig. 6-S4). However, the contemporaneous Mg/Ca record shows little structure and more worryingly the calculated temperatures are higher than those calculated at Site 926 (27-30ºC). A recent core top study has shown that salinity may have a secondary control on Mg/Ca in planktic foraminifers (Honisch et al., 2013). Consequently the Mg/Ca record at Site 1406 may also be recording the changes in salinity of the surface waters as circulations patterns shift. Alternatively, the high Mn/Ca ratio measured in these foraminifera (Mn/Ca of ~ 1000-2000 μmol/mol) may

suggest that Mg in ferromanganese coatings is causing the measured Mg/Ca to be elevated. The discrepancy between the $\delta^{18}O_{planktic}$ and Mg/Ca record, and the high reconstructed Mg/Ca temperatures at Site 1406 suggests that more work is needed before the Mg/Ca derived temperatures at this site can be used. Instead we use the temperature estimates from Site 926 and apply the modern temperature gradient of ~10ºC between Site 1406 and Site 926. While this temperature will give us an indication of the likely absolute temperature at Site 1406, we acknowledge it will not parameterise any changes in temperature at this site as a consequence of changes in surface water hydrography through time. Consequently a large uncertainty is applied to the temperature (± 5 ºC) estimates for this site. Salinity is assumed to have remained constant through time with an uncertainty of ± 3 ‰. As the age constraints at Site 1406 are improved and more geochemical records produced, further interpretation of the differences between the two records can be made.

6.3.2 $\delta^{11}B$ changes across the Oligocene-Miocene boundary

Our record from *G. praebulloides* at Site 926 shows high and relatively stable $\delta^{11}B$ values (17.5 ‰; hence lowest CO_2) prior to and during the Mi-1 glaciation (Fig. 6-4, 6-5). After 23 Ma, $\delta^{11}B$ decreases, reaching minimum values of 15.5 ‰ at 22.5 Ma (hence highest CO_2). The data from Site 872, where available, agree well with the data from Site 926. At Site 1406 while the $\delta^{11}B$ across the glaciation is in agreement with Site 926 and there is a similar decrease in $\delta^{11}B$ between 22.9 and 22.4 Ma, the magnitude of this change is considerably larger than in the record from Site 926 (4 ‰ compared to 2 ‰ at Site 926; Fig. 6-4). Another discrepancy between the two records is evident prior to the Mi-1 glaciation. While the record at Site 926 appears to be relatively invariant between 23 and 23.5 Ma, the record from Site 1406 shows a sharp decrease in $\delta^{11}B$ (increase in CO_2) around 23.5 Ma. It is possible that the record from Site 926 does not resolve this peak or that the shipboard age model at Site 1406 has led to the misalignment of the two records (e.g. with the peak of 23.7 Ma at Site 926). However, the differences in magnitude of the excursion may point to the influences of additional hydrographic effects as outlined above.

The differences between the $\delta^{11}B$ records at sites 926 and U1406 may be attributable to differential diagenesis at the two sites as a consequence of the different burial depths

and preservation (see above). However, previous work conducted at Site 926 across the middle Miocene suggests that, despite greater burial depths, the recorded $\delta^{11}B$ at this site is comparable to both the more shallowly buried Site 761 and 'glassy' foraminifera from the clay-rich Ras-il Pellegrin section in Malta (Foster et al., 2012; Badger et al., 2013). A similar lack of diagenetic overprint from recrystallisation has also been found in $\delta^{11}B$ records with different diagenetic histories across the Paleocene/Eocene Thermal Maximum and prior to the Mid-Eocene Climatic Optimum (Edgar et al., in review; Penman et al., 2014). A possible explanation for the lack of diagenetic effect on $\delta^{11}B$ is that the inorganic carbonate precipitated from the pore water, as the foraminifera recrystallises during burial, has a low B/Ca and therefore only comprises a small proportion of the analysed foraminifera (Edgar et al., in review). However, several studies have shown that if dissolution, rather than recrystallization, is the dominant diagenetic process altered foraminifera tend to show lower $\delta^{11}B$ (Seki et al., 2010). This is particularly evident in a depth transect of core top foraminifera that shows the $\delta^{11}B$ of *G. sacculifer* declines by ~ 0.7‰ from the shallowest to the deepest site (Seki et al., 2010). This effect is species-dependent because no comparable diagenetic signal is seen in *G. ruber*. The offset seen in the samples here is unlikely to be caused by partial dissolution as the foraminifera that have the lowest $\delta^{11}B$ values are at Site 1406 where the foraminifera are usually well-preserved. The difference between the $\delta^{11}B$ records may instead be caused by different hydrographic conditions at Site 1406, compared to Site 872 and Site 926, which are corrected for in the CO_2 calculations by our treatment of temperature at Site 1406. The $\delta^{11}B$ difference between sites 1406 and 926 alongside the $\delta^{18}O$ data from Site 1406 suggest that the surface waters above the site originated from the Gulf stream prior to, and during Mi-1, with a gradual cooling and acidifying of the surface waters during the 1 million years following the event (Fig. 6-S3, 6-S4).

6.3.3 The relationship between $\delta^{11}B$-CO_2 and climate across the boundary

To a first order it can be assumed that the changes in $\delta^{11}B$ are primarily driven by changes in CO_2. When comparing the benthic foraminiferal $\delta^{18}O$ record to our $\delta^{11}B$ data there appears to be a decoupling between CO_2 and climate in the lead up the glaciation (Fig. 6-4, 6-5). During the deglaciation phase, however, the $\delta^{11}B$ rise broadly follows the decrease in $\delta^{18}O$. Benthic $\delta^{18}O$ records salinity, ice volume and temperature changes. Salinity changes in the deep-sea are negligible and therefore if an independent

reconstruction of temperature can be made the ice volume component ($\delta^{18}O_{sw}$) of the $\delta^{18}O$ record can be isolated. At Site 926, a $\delta^{18}O_{sw}$ record was developed across the Oligocene-Miocene transition using Mg/Ca temperature estimates from *O. umbonatus* (Mawbey and Lear, 2013). In keeping with the interpretation made from $\delta^{18}O$ alone, a comparison of the $\delta^{18}O_{sw}$ and $\delta^{11}B$ records suggests that while ice sheet expansion was not associated with an increase in $\delta^{11}B$ (drop in CO_2) the decrease in ice volume coincided with a decrease in $\delta^{11}B$ (increase in CO_2) (Fig. 6-4, 6-5).

It has been widely hypothesised that a decrease in CO_2 prior to the Mi-1 glaciation may have been one of the key triggers of the event. (Zachos et al., 1997; Paul et al., 2000; Mawbey and Lear, 2013) The lack of $\delta^{11}B$ increase (CO_2 decrease) leading up to the Mi-1 glaciation is particularly hard to reconcile with this suggestion in light of the $\delta^{13}C$ increase prior to the event, which has traditionally been interpreted as an increase in organic carbon burial and CO_2 decrease (Zachos et al., 1997; Paul et al., 2000). However, the relationship between CO_2 and positive $\delta^{13}C$ excursions is complicated. For example, a $\delta^{13}C$ increase during the warming into the Miocene Climate Optimum coincides with a well-documented CO_2 increase (Foster et al., 2012; Greenop et al., 2014) suggesting that carbon burial is not the dominant control on CO_2 during this interval. Consequently, while carbon burial may be occurring prior to the O-M transition, it may not be the primary control on CO_2 and other factors may be acting to maintain constant CO_2. For instance, the establishment of the Antarctic circumpolar current, which both climate models and proxy data suggest occur 1 to 2 million years prior to the Mi-1 glaciation (Pfuhl and McCave, 2005; Lyle et al., 2007; Hill et al., 2013), may have influenced ocean carbon storage or the deep ocean $\delta^{13}C$ signal.

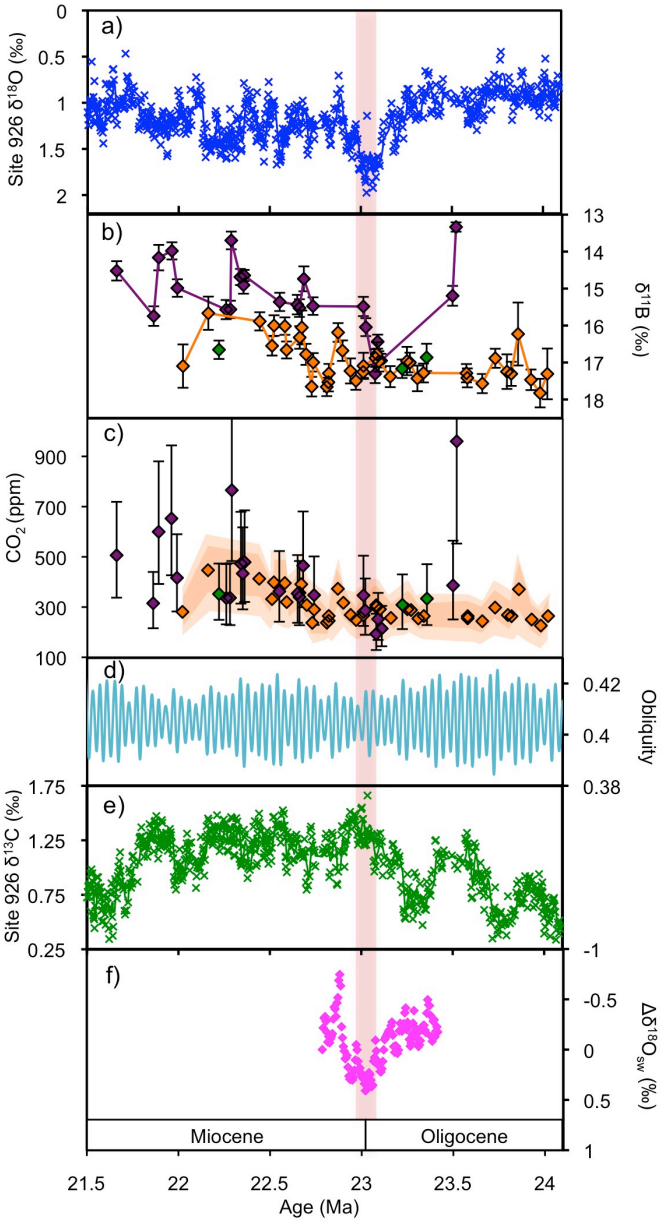

Figure 6-4: Oligocene-Miocene CO_2 and climate records. (a) $\delta^{18}O$ record from Site 926 (Pälike et al., 2006a) and references therein. (b) Oligocene-Miocene transition $\delta^{11}B$ from Site 926 (orange) and Site U1406 (purple) and Site 872 (green). The data are plotted on inverted axes and the error bars show the external reproducibility at 95% confidence. The $\delta^{11}B$ are measured against the National Institute of Standards and Technology SRM boric acid standard 951. (c) Oligocene-Miocene transition pCO_2 from Site 926 (orange) and Site U1406 (purple) and Site 872 (green). Dark and light orange bands show CO_2 uncertainty at the 95% confidence interval and the 68% confidence interval respectively at Site 926. Error bars show 95% confidential interval at Site 1406 and Site 872. Uncertainty was calculated using a Monte Carlo simulation (n=10000) and consists of uncertainty on temperature, salinity, alkalinity, $\delta^{11}B_{sw}$ and the $\delta^{11}B$ measurement. See text for details of the measurement and uncertainty. (d) Obliquity orbital forcing from Laskar et al. (2004). (e) $\delta^{13}C$ record from Site 926 (Pälike et al., 2006a and references therein). (f) $\delta^{18}O_{sw}$ record from Site 926 (Mawbey and Lear, 2013). Note relative changes are plotted where $\delta^{18}O_{sw}$ at 22.79 Ma is set to zero. Red shaded area highlights the Oligocene-Miocene transition.

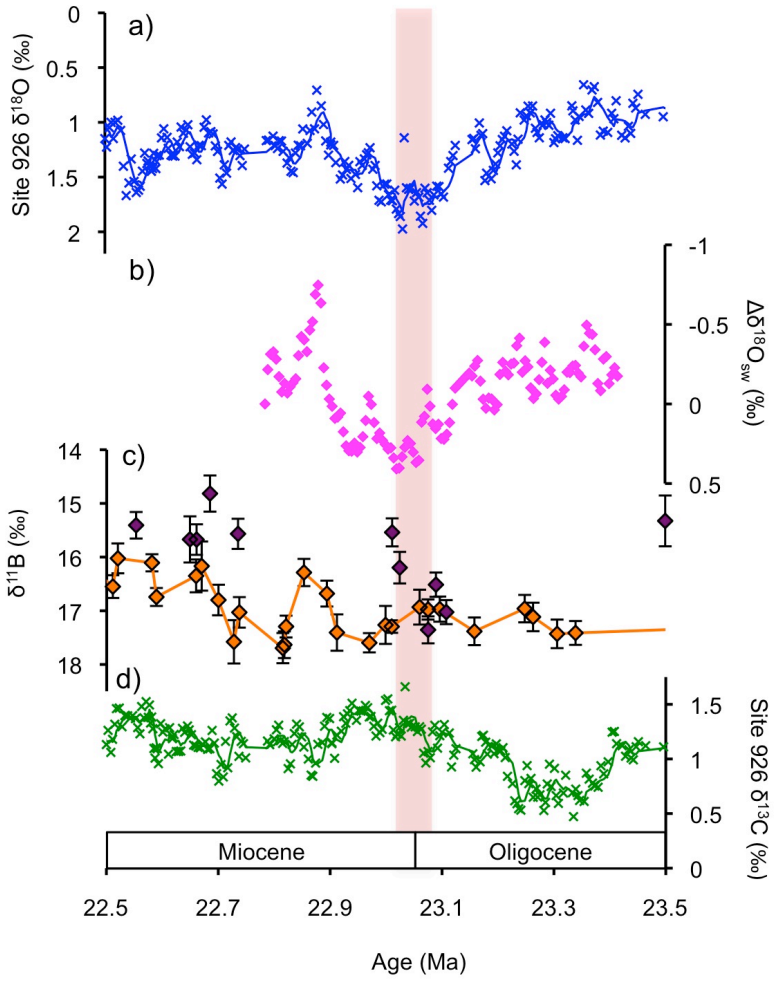

Figure 6-4: Zoomed in view of $\delta^{11}B$ between 22.5 Ma and 23.5 Ma. (a) $\delta^{18}O$ record from Site 926 (Pälike et al., 2006a) and references therein. (b) $\delta^{18}O_{sw}$ record from Site 926 (Mawbey and Lear, 2013). Note relative changes are plotted where $\delta^{18}O_{sw}$ at 22.79 Ma is set to zero. Red shaded area highlights the Oligocene-Miocene transition. c) Oligocene-Miocene transition $\delta^{11}B$ from Site 926 (orange) and Site U1406 (purple) and Site 872 (green). The data are plotted on inverted axes and the error bars show the external reproducibility at 95% confidence. The $\delta^{11}B$ are measured against the National Institute of Standards and Technology SRM boric acid standard 951. (d) $\delta^{13}C$ record from Site 926 (Pälike et al., 2006a and references therein).

6.3.4 The role of CO_2 in the Mi-1 glaciation

In order to better understand the role of atmospheric CO_2 in the Mi-1 glaciation it is instructive to make absolute reconstructions on CO_2 (Fig. 6-4). Our new $\delta^{11}B$-CO_2 data suggest that CO_2 rises from a baseline value of 250 ppm to a maximum of ~ 400-500 ppm following the deglaciation. While the uncertainty on the CO_2 estimates is quite large (± 70-186 ppm at Site 926, ± 64-627 ppm at Site 1406 and ± 97-137 ppm at Site 872; 95% confidence interval), primarily as a result of large uncertainties on $\delta^{11}B_{sw}$ and

total alkalinity estimates, our data do allow us to show that CO_2 declines below 400 ppm across the Oligocene-Miocene transition. Elsewhere it has been suggested that ~ 400 ppm may be an important threshold value for growth of the West Antarctic Ice Sheet, Greenland ice sheet and potentially a partially more mobile part of the East Antarctic ice sheet (Langebroek et al., 2009; Foster and Rohling, 2013). Our best estimate of CO_2 before and during the Mi-1 glaciation is also below the Pleistocene Northern Hemisphere glaciation threshold of ~280 ppm suggesting that the presence of Northern Hemisphere ice across the transition cannot be discounted (DeConto et al., 2008; Luthi et al., 2008). However, other boundary conditions are clearly different between the Quaternary and the Oligocene-Miocene transition and consequently these thresholds might not apply.

While there are large uncertainties associated with the absolute reconstructions of CO_2, there is greater certainty in relative CO_2 changes as a result of reduced uncertainties associated with $\delta^{11}B_{sw}$ and total alkalinity (± 30-190 ppm) (see above). The post Mi-1 deglaciation out of the event is associated with a CO_2 rise of ~ 120 ppm (± 82 ppm). This CO_2 rise is much smaller than coupled ice sheet- global circulation models suggest is needed to overcome the Antarctic ice sheet hysteresis and cause melting (Pollard and DeConto, 2005). Even when taking into account recent work in the Pliocene that suggests a dynamic East Antarctic ice sheet could contribute 3 to 16m of sea level equivalent (Cook et al., 2013), the Mi-1 deglaciation CO_2 change appears very modest in comparison to the ice volume changes of ~ 50 msle (Mawbey and Lear, 2013), based on our current knowledge of Antarctic ice sheet stability (Pollard and DeConto, 2005). The Northern Hemisphere ice sheets are more sensitive to changes in CO_2, although there is little evidence to suggest the presence of substantial ice sheets prior to the late Pliocene (DeConto et al., 2008; Bailey et al., 2013).

Previous estimates of CO_2 across the Oligocene-Miocene transition are sparse. Nonetheless, the absolute values of CO_2 reconstructed here agree well with the published alkenone records from (Pagani et al., 2005b) and leaf stomata CO_2 records from (Kürschner et al., 2008) (Fig. 6-1). Our CO_2 reconstructions here also matches well with the latest alkenone CO_2 reconstructed from Zhang et al. (2013) when the data are plotted on the age model in Pagani et al., (2011) and updated to the Geological Timescale 2012 (Gradstein et al., 2012). In combination with our new CO_2 data, the

alkenone record of Zhang et al., (2013) can also be used to better understand the role of CO_2 in the timing of the Mi-1 glaciation. In figure 6-5 we have plotted our new dataset, the Zhang et al., (2013) alkenone CO_2 record and the Pearson et al., (2009) boron isotope CO_2 record to evaluate the long-term trends in CO_2 leading up to the Mi-1 glaciation. Using these data sets we show that the Mi-1 glaciation appears to have occurred when CO_2 had fallen below a critical threshold (~ 400 ppm) and the orbital forcing was favourable for ice growth. The CO_2 decline begins at 29.5 Ma from values of ~1000 ppm to a minimum of ~230 ppm at 23.5 Ma. It appears the glaciation did not occur during the previous node in obliquity at 24.4 Ma when the variability was further reduced as CO_2 was still elevated (>400 ppm) (Fig. 6-6).

Despite a CO_2 decrease of ~ 500 ppm between the Eocene-Oligocene (E-O) and O-M boundaries (Fig. 6-6) little is known about the impact of this change on ice volume and global climate. The Oligocene oxygen isotope record shows a long-term increase (~ 0.5 ‰) between 27-31.5 Ma and this may be associated with ice sheet expansion and global cooling. Yet, the more prominent benthic $\delta^{18}O$ trend for the late Oligocene is a decrease of ~ 1‰, interpreted as an interval of climate warming and reduced ice volume (Zachos et al., 2001a; Mudelsee et al., 2014). This is particularly puzzling in light of the 500 ppm CO_2 decline between 27.5 Ma and 23.5 Ma. One possibility is that climate and CO_2 were decoupled during the late Oligocene. A second possibility is that the benthic $\delta^{18}O$ record captures an increase in bottom water temperature that is decoupled from Antarctic climate. A third possibility is the operation of a counter-intuitive links between Antarctic climate and deep-water temperature. A recent climate modelling study suggests that the emplacement of an Antarctic ice sheet at the Mid-Miocene Climatic Transition caused a short-term rise in global annual mean temperatures associated with cooling of deep waters (Knorr and Lohmann, 2014). The possible initiation or strengthening of the Antarctic circumpolar current (ACC) around this time (Pfuhl and McCave, 2005; Lyle et al., 2007; Hill et al., 2013; Ladant et al., 2014b) may have resulted in large oceanographic changes, with counterintuitive effects on global temperatures. It has been shown that a strong ACC is associated with increased sea ice cover in the Southern Ocean, which may have created cold and very salty waters and impacted the characteristics of deep-water formation in the Southern Hemisphere (Ladant et al., 2014b). A better understanding of the ice volume and global climate

changes of the Oligocene are therefore needed to better understand the interplay of CO_2, ice volume and climate across the Mi-1 glaciation.

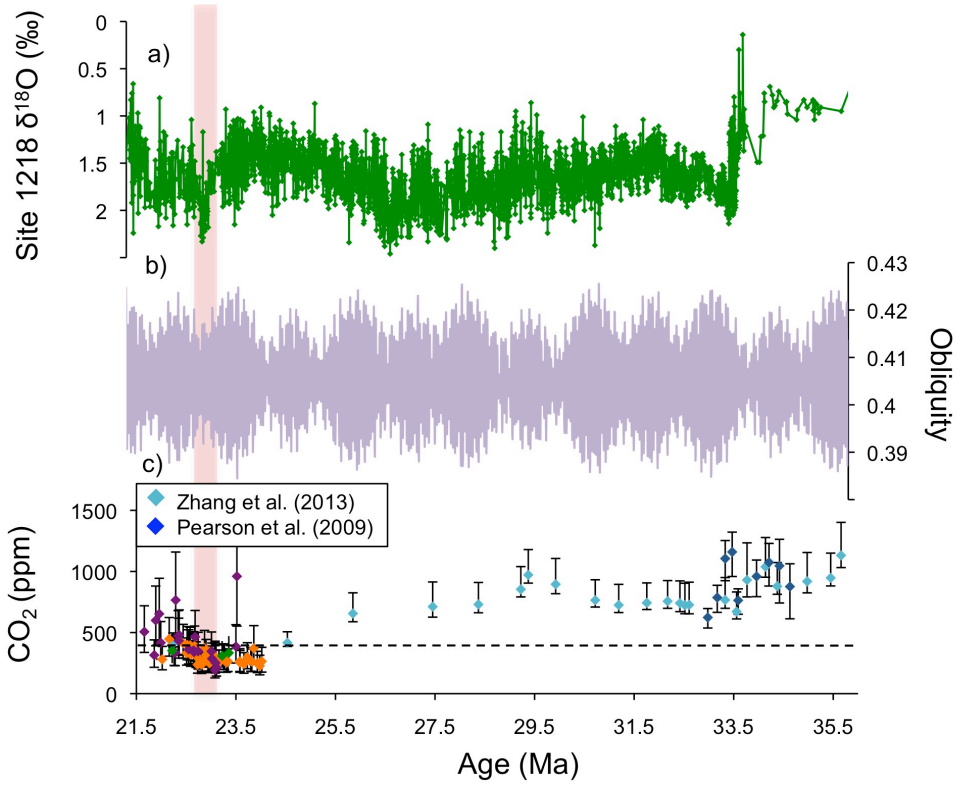

Figure 6-5: Long-term Oligocene climate and CO_2. (a) $\delta^{18}O$ record from Site 1218 (Pälike et al., 2006b) and references therein. (b) Obliquity orbital forcing from Laskar et al., (2004) (c) $\delta^{11}B$-CO_2 from Site 926 (this study) in orange, alkenone derived CO_2 from Zhang et al., (2013) in purple and $\delta^{11}B$-CO_2 from Pearson et al., (2009) in dark blue. For $\delta^{11}B$-derieved CO_2 records error bars represent two sigma uncertainty. Black bar marks the hypothesised 400 ppm threshold for ice sheet growth. Orange band marks Oligocene-Miocene boundary.

6.4 Conclusions

The new CO_2 data presented here, when combined with published Oligocene CO_2 data, show that the timing of the Mi-1 glaciation is controlled by a combination of declining CO_2 below a critical threshold and favourable orbital forcing of a node in obliquity and low amplitude eccentricity. This combination of factors has also been used to explain the first expansion of ice on Antarctica at the Eocene-Oligocene transition. Our best estimate of CO_2 suggests that values were around 250 ppm prior to, and during the Mi-1 glaciation. When the reconstructed CO_2 is evaluated in the context of the long-term

Oligocene record the O-M transition appears to mark the first time CO_2 levels fall below 400 ppm, a hypothesed threshold for Antarctic ice sheet growth during the Neogene. The post-Mi-1 deglaciation associated with the recovery out of the event is associated with a CO_2 rise of ~ 120 (± 82 ppm) ppm. Large published estimates of contemporaneous ice volume change on Antarctica of 50 msle are difficult to reconcile with the relatively modest CO_2 changes reconstructed here. Future work is needed in order to gain a better understanding of the background climate and CO_2 conditions during the late Oligocene so that the relative contribution of the different ice sheets to the ice volume changes associated with the Mi-1 glaciation can be better determined.

6.5 Supplementary Figures

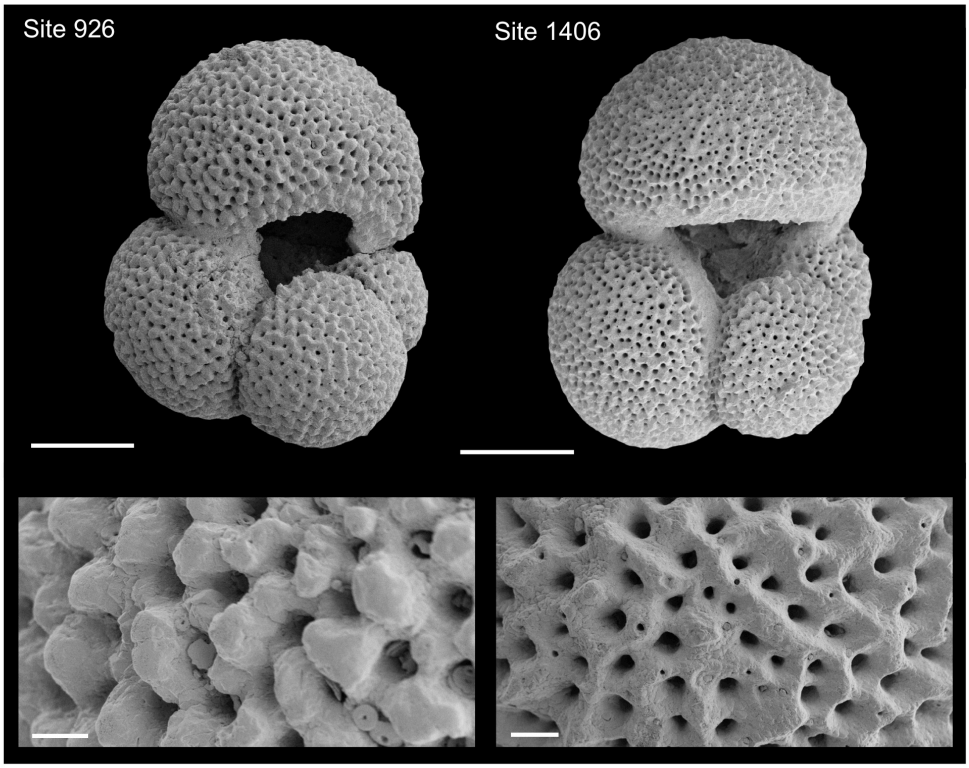

Figure 6-S1: SEM images of whole foraminifera and wall texture for *G. praebulloides* from Site 926 (926B 50 1W 48-52) and Site 1406 (1406A 8H 5W 72-74). The scale bar on whole foraminifera images is 100 μm and on wall texture images is 10 μm. Note the difference in preservation.

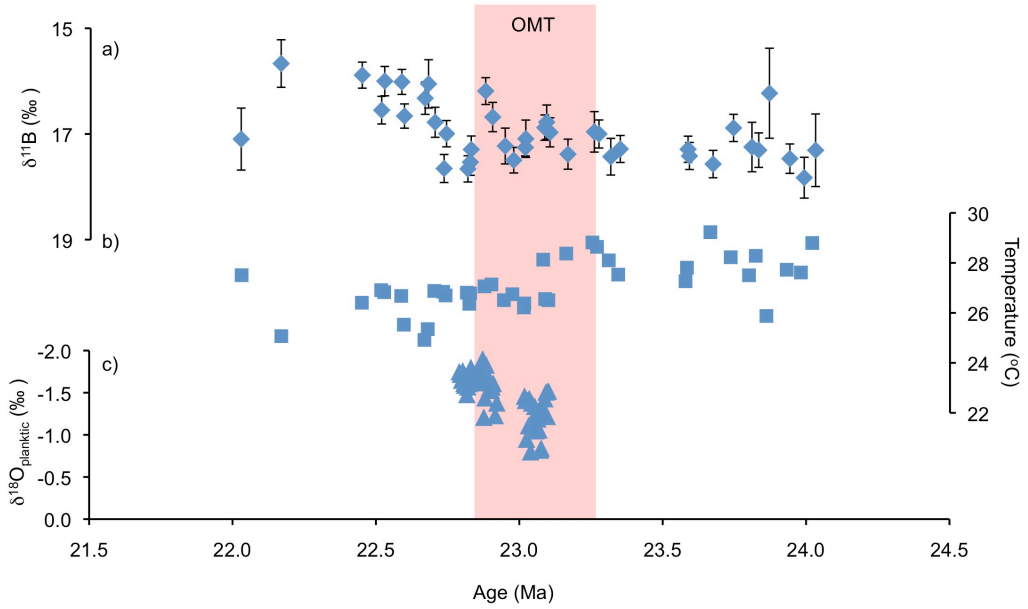

Figure 6-S2: Surface water hydrography at Site 926 (a) $\delta^{11}B$ plotted on inverted axes and the error bars show the external reproducibility at 95% confidence. (b) Mg/Ca based temperature reconstructions from tandem measurements of *G. bulloides*. (c) $\delta^{18}O_{planktic}$ record from Pearson et al., (1997). Shaded red bar shows the timing of Mi- glaciation oxygen isotope excursion.

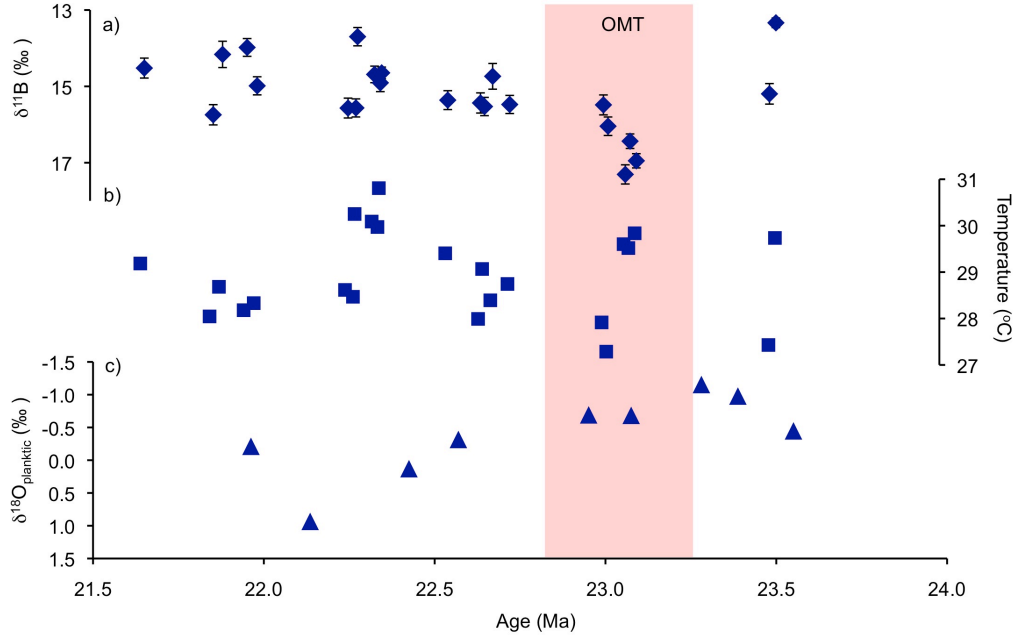

Figure 6-S3: Surface water hydrography at Site 1406 (a) $\delta^{11}B$ plotted on inverted axes and the error bars show the external reproducibility at 95% confidence. (b) Mg/Ca based temperature reconstructions from tandem measurements on *G. bulloides*. (c) $\delta^{18}O_{planktic}$ record (this study) increases by 2 ‰ through the study interval. Shaded red bar shows the timing of Mi- glaciation oxygen isotope excursion.

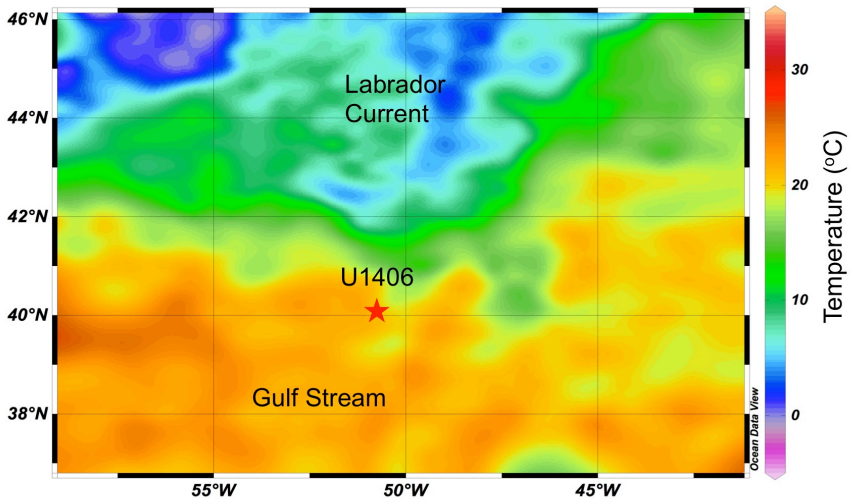

Figure 6-S4: Map of modern day surface water temperatures around Site U1406. Labelled are the Labrador Current and the Gulf Stream; the two predominant surface water currents in the area today. Data from Schlitzer, (2000).

Chapter 7: Conclusions

This thesis provides an important contribution to our understanding of the relationship between CO_2 and the cryosphere in the Miocene that could also have important implications for the rest of the Neogene, the present day and our warm future. Furthermore, in investigating some of the additional parameters needed to calculate CO_2 from $\delta^{11}B$ for the Miocene records, this thesis also provides important information that will support the interpretation of $\delta^{11}B$ records in other time intervals.

7.1 Chapters 3 and 4

The key aim of Chapters 3 and 4 was to gain a better understanding of some of the additional parameters needed to accurately estimate atmospheric CO_2 from the $\delta^{11}B$ of foraminifera. It is likely that some of the other boundary conditions and assumptions relating to the proxy are different from the modern during the Miocene epoch and therefore some of the additional parameters needed to calculate CO_2 from $\delta^{11}B$ may also have changed through time. This thesis has focused on what are considered to be the key unknowns: the boron isotopic composition of seawater ($\delta^{11}B_{sw)}$ and changes in the life habit of *Globigerina bulloides* (one of the important proxy carriers in the Miocene).

Understanding the extent to which modern calibrations can be applied further through geological time is key for the successful utilisation of the $\delta^{11}B$-pH proxy. The calibration applied to the foraminifer $\delta^{11}B$ can have a significant affect on the calculated CO_2 (see section 2.2.3). This offset is particularly large between symbiotic vs. non-symbiotic foraminifera. The results from Chapter 4 show that *G. bulloides (sensu lato)* hosted symbiotic symbionts and did not acquire its non-symbiotic lifestyle until the late Miocene. Therefore, if these foraminifera are used in palaeo-CO_2 reconstructions across the Oligocene-Miocene boundary and during the early/middle Miocene the modern calibration isn't applicable. It is unlikely that the change in life habit of *G. bulloides* through time is an isolated case. For instance, there is evidence for symbiont 'bleaching' associated with the warm conditions of the Middle Eocene Climate Optimum (Edgar et al., 2012). Therefore, the foraminifer ecology must be well understood a priori for the generation of long-term, single species CO_2 records, particularly over major Cenozoic climatic events.

Understanding the boron isotopic composition of seawater ($\delta^{11}B_{sw}$) is also key to calculating absolute estimates of CO_2 through time using $\delta^{11}B$. Based on the constraints of numerical modelling studies, the residence time of boron in the ocean is ~ 10-20 million years (Lemarchand et al., 2002b) and consequently the secular evolution of $\delta^{11}B_{sw}$ needs to be constrained for CO_2 calculations during the Miocene. Based on the data-led approach in Chapter 4, it appears that $\delta^{11}B_{sw}$ was ~ 38 ‰ at the Oligocene-Miocene boundary. $\delta^{11}B_{sw}$ then decreased to a minimum of ~ 37 ‰ during the middle Miocene before increasing through the late Miocene and Pliocene to modern day values. Not only is this finding key to the interpretation of the records presented in this thesis, but it will also have important implications for future $\delta^{11}B$-CO_2 records produced for the pre-Pliocene. The new $\delta^{11}B_{sw}$ record presented here may also provide important constraints on the changes in the fluxes of all the isotope systems both through the Neogene and further back in time. The correlation of the new $\delta^{11}B_{sw}$ record with the seawater isotopic compositions of Li and Ca (and to a less extent Mg) over the past 15 Myrs suggests there is a common control on the isotopic composition of all the elements across this interval.

7.2 Chapters 5 and 6

In Chapters 5 and 6 the changes in atmospheric CO_2 associated with two of the major climatic events of the Miocene have been reconstructed. Coupled with records of climate and ice volume these records have provided an insight into the stability of the cryosphere at atmospheric CO_2 levels of 250-500 ppm, the top end of which will most likely be reached before the end of the century (IPCC, 2013). One of the major implications of the CO_2 records reconstructed over both time intervals is that the east Antarctic ice sheet shows a level of dynamism at much lower CO_2 levels than expected by coupled global climate/ice sheet models.

The $\delta^{11}B$ record from the middle Miocene indicates that high-amplitude CO_2 variations (~ 300 to 500 ppm) accompanied the orbitally paced climatic changes observed in a range of climate records during the climatic optimum, suggesting a coupling between climate and CO_2. However, the lack of a substantial ice mass in the northern hemisphere means that the overall climatic response to CO_2 change was muted in the middle Miocene compared to the latest Pleistocene. A comparison of $\delta^{11}B$ and $\delta^{18}O_{sw}$ data also

indicates that there was a component of the continental ice budget, most likely on Antarctica that was responding to CO_2. In particular, this suggests that two reservoirs of ice existed on Antarctica during the Miocene, one that is stable even at comparatively high CO_2 levels and one that is dynamic at the lower end of the CO_2 range reconstructed. This finding does not support the long held belief that the EAIS has not undergone melting since it was first established 34 Ma, however, the data from the middle Miocene does provide some evidence that there is a portion of the Antarctic ice sheet which is stable at atmospheric CO_2 levels > 500 ppm.

The CO_2 data reconstructed for the Oligocene-Miocene boundary suggests that this major glaciation occurred once CO_2 fell below a threshold of 400 ppm and the orbital configuration was favourable. This is a similar to the mechanism that is evoked for the first emplacement of large ice sheets on Antarctica across the Eocene-Oligocene boundary (Coxall et al., 2005; DeConto et al., 2008). Little is known about the fate of the Antarctic ice sheet during the Oligocene, although variability in the high-resolution benthic oxygen isotope record does suggest a level of dynamism (Pälike et al., 2006b). The deglaciation of the event is associated with a CO_2 rise of ~ 120 ppm to a maximum of ~ 400-500 ppm. While this CO_2 rise may in part explain why the Mi-1 glaciation was transient in nature, the size of the CO_2 increase is small given the magnitude of the ice volume changes and assumed lack of northern hemisphere ice sheets. This again points at the existence of a dynamic component of the Antarctic ice sheet within the range of CO_2 that is expected for the next century (IPCC, 2013).

The findings from the two Miocene case studies clearly have implication for future climate change assuming that the Miocene is analogous for our warm future. There is growing consensus that the portion of the EAIS overlying the deep subglacial basins is mobile (Cook et al., 2013; Mengel and Levermann, 2014). Based on the findings here, the threshold for partial melting of the east Antarctic ice sheet will be passed during the next century. Estimations of sea level change as a result of the partial melting of the East Antarctic ice sheet are ~19 m (Mengel and Levermann, 2014). Coupled with approximately ~7 m from Greenland (Bamber et al., 2013), and ~3-4 m from the West Antarctic ice sheet (Bamber et al., 2009), then the total expected sea level change could be on the order of ~ 31 m once Earth system equilibrium is reached. However, less is known about the potential implications of a dynamic EAIS on shorter timescales (over millennial timescales). Large uncertainties remain about the rate and magnitude of sea

level change, largely as a result of the inability of ice sheet models to incorporate the dynamical processes into climate models involved with the growth and decay of the continental ice sheets (Meehl et al., 2012).

Future work

7.2.1 The Neogene CO_2 record

The CO_2 records in this thesis make an important contribution to our understanding of long term Neogene CO_2 changes. In addition to the work presented here, a collaboration with Caroline Lear and Sindia Sosdian at Cardiff University, has produced a long-term record of Neogene CO_2 that shows more CO_2 variability than previously identified, through the Miocene. Future work is needed to increase the resolution of this record so that changes in the variability of CO_2 (e.g. those identified in the middle Miocene; Chapter 5) can be better constrained through time. Advances in the analytical technique, such as an automated boron column chemistry machine, could increase the throughput of samples and efficiency of what is otherwise a time consuming analytical process.

7.2.2 The boron isotope composition of seawater

The next stage in understanding changes in the $\delta^{11}B_{sw}$ composition through time is to use a geochemical box model to quantitatively constrain the inputs and outputs. The aim of this project is to use changes in the seawater isotopic composition of the other elements highlighted in Chapter 4 (Li, Mg and Ca) to provide additional constraints on a model based $\delta^{11}B_{sw}$ record. Another facet of on going work is the application of an extension of the $\delta^{13}C$-pH gradient method to foraminifera that live in the surface ocean. The $\delta^{11}B$ and $\delta^{13}C$ of the entire foraminiferal assemblage is measured within a single sample in order to constrain the pH-$\delta^{13}C$ relationship in the surface ocean. The gradient of the relationship is then adjusted by changing $\delta^{11}B_{sw}$ until it reaches the gradient between pH and $\delta^{13}C$ in the ocean today. Preliminary $\delta^{11}B$ and $\delta^{13}C$ data has been run from ODP Site 999 for the modern and three Pleistocene time slices in order to test this approach.

7.2.3 Outstanding questions related to ice sheet hysteresis

While the contribution of this thesis means that there is a better understanding of the CO_2 range within which the east Antarctic ice sheet is stable, less is known about the type of response the EAIS has to CO_2 forcing. Coupled global climate- ice sheet modelling experiments have shown that the WAIS transitions relative rapidly (on the order of 1-3 kyrs) between different stable states given a linear change in forcing (Pollard and DeConto 2009). Consequently given the similar nature of the marine based WAIS and the areas of the EAIS situated in the subglacial basins, it is possible that partial melting of the EAIS may also exhibit a non-linear relationship to forcing. Current estimates of future sea level rise suggest that the contribution of the Antarctic ice sheet will increase linearly by 1.2m/^{o}C (Levermann et al., 2013), however, this assumption may need revising as the nature of Antarctic deglaciation is better understood.

Appendices

Appendix A: Teflon cleaning protocol

Carry out all stages in extract fume hood unless overpressured box is indicated.

1) Remove leftover sample - if want to run again: transfer to acid leached mini spin centrifuge tube & store. If it is a $\delta^{11}B$ sample, store in a Teflon screw top vial (its own an acid leached one).

2) Wipe outside of beakers & a/s vials with acetone: remove labels & organics.

3) Place in jar to rinse inside of beakers with MQ x3.

4) Wipe inside of beakers with Acetone

5) Use different white roll from step 2 and change gloves

6) Do not let Acetone dry inside beakers – drop immediately into MQ

7) Place in jar & rinse x3 MQ to ensure acetone completely removed.

8) ⅔ fill with 7 M HNO_3 & place on hotplate for 2hrs @ ~140 ˚C.

9) Make 7 M HNO_3 using 1L plastic bottle. No need to be precise, ½ MQ & ½ HNO_3 (REMEMBER – water first).

10) Ensure no trapped bubbles in bottom of Teflon centrifuge tubes

11) Empty beakers. If necessary, let cool for short period before handling (10 mins). Pour acid to waste – don't let cool for >30 min, if so, put back on hotplate for 1hr, start again.

12) Place in 1L Teflon jar & rinse x2 MQ.

13) Place all beakers & a/s vials facing upwards in jar, & fill with 7 M HNO_3.

14) To ensure no trapped air pockets, rattle jar & watch for bubbles.

15) Fill centrifuge tubes with squirty bottle & drop in, ensure no trapped air in end.

16) Hotplate @ 140 ˚C overnight.

17) Empty 7 M to waste, & rinse x2 MQ. If required: remove any residue inside centrifuge tubes w. clean pipette tip

18) Rearrange beakers & a/s vials in jar, again no air bubbles trapped. Fill w. ~ 2% HNO_3 & hotplate @ 140 ˚C overnight.

19) Wipe outside of the jar w. damp white roll to remove dust. In overpressured box remove 2% to waste & rinse x3 MQ. Put on lids completely & place in "clean beaker/vial" box.

20) Before use leach (cap closed) in 10% HNO_3 (TD) on hotplate @ 120-150°C for ½ hr, & rinse x2 MQ (with cap closed always). Rinsing must be in overpressured box.

Appendix B: Chapter 3 data table

Leg	Site	Core	Section	Sample (cm)	Age (Ma)	Species	Size fraction (µm)	$\delta^{13}C$	$\delta^{18}O$
342	1406A	6H	5W	72-74	22.0	*G. praebulloides*	180-212	-0.159	-0.036
342	1406A	6H	5W	72-74	22.0	*G. praebulloides*	212-250	0.353	-0.212
342	1406A	6H	5W	72-74	22.0	*G. praebulloides*	250-300	0.650	-0.044
342	1406A	6H	5W	72-74	22.0	*G. praebulloides*	300-355	0.560	0.065
342	1406C	9H	4W	44-46	23.1	*G. praebulloides*	180-212	0.487	-0.259
342	1406C	9H	4W	44-46	23.1	*G. praebulloides*	212-250	1.017	-0.685
342	1406C	9H	4W	44-46	23.1	*G. praebulloides*	250-300	1.363	-0.354
342	1406C	9H	4W	44-46	23.1	*G. praebulloides*	300-355	1.872	-0.856
208	1264B	24H	6W	19.5-20.5	22.5	*G. praebulloides*	180-212	1.698	0.729
208	1264B	24H	6W	19.5-20.5	22.5	*G. praebulloides*	212-250	1.916	0.955
208	1264B	24H	6W	19.5-20.5	22.5	*G. praebulloides*	250-300	1.874	0.944
208	1264B	24H	6W	19.5-20.5	22.5	*G. praebulloides*	300-355	1.848	0.712
208	1264B	24H	6W	19.5-20.5	22.5	*G. praebulloides*	300-355	1.700	0.756
208	1264B	24H	6W	19.5-20.5	22.5	*D. dehiscens*	180-212	1.642	0.950
208	1264B	24H	6W	19.5-20.5	22.5	*D. dehiscens*	250-300	1.747	0.960
208	1264B	24H	6W	19.5-20.5	22.5	*D. dehiscens*	300-355	1.866	1.003
208	1264B	24H	6W	19.5-20.5	22.5	*G. primordius*	212-250	2.201	0.633
208	1264B	24H	6W	19.5-20.5	22.5	*G. primordius*	212-250	2.309	0.520
208	1264B	24H	6W	19.5-20.5	22.5	*G. primordius*	250-300	2.343	0.652
208	1264B	24H	6W	19.5-20.5	22.5	*G. primordius*	300-355	2.601	0.580
154	925A	22R	7W	30-32	22.7	*G. praebulloides*	180-212	1.571	-1.893
154	925A	22R	7W	30-32	22.7	*G. praebulloides*	180-212	1.922	-1.550
154	925A	22R	7W	30-32	22.7	*G. praebulloides*	212-250	2.205	-1.540
154	925A	22R	7W	30-32	22.7	*G. praebulloides*	212-250	1.934	-1.805
154	925A	22R	7W	30-32	22.7	*P. siakensis/ mayeri*	180-212	1.445	-1.167
154	925A	22R	7W	30-32	22.7	*P. siakensis/ mayeri*	212-250	1.546	-0.743
154	925A	22R	7W	30-32	22.7	*P. bella*	180-212	1.469	-0.976
154	925A	22R	7W	30-32	22.7	*P. bella*	212-250	1.512	-0.514
154	925A	24R	1W	110-112	24.2	*G. praebulloides*	180-212	0.973	-2.302
154	925A	24R	1W	110-112	24.2	*G. praebulloides*	180-212	0.891	-2.087
154	925A	24R	1W	110-112	24.2	*P .bella*	180-212	0.659	-1.798
154	925A	24R	1W	110-112	24.2	*P .bella*	180-212	0.639	-1.840

Appendix C: Chapter 4 data tables

C.1 Benthic boron isotope and trace element data

Site	Core	Section	Interval (cm)	Species	Size fraction (µm)	Age (Ma)	Mg/Ca mmol/mol	$\delta^{11}B$ - 1	2sd	$\delta^{11}B$ - 2	2sd	$\delta^{11}B$ average	2sd average	Data Source
999A	4	47-49	*C. wuellestorfi*	>200	0.62	1.90	16.85	0.22	16.79	0.21	16.82	0.22	this study
758B	5	64-67	*C. wuellestorfi*	>200	1.15	1.03	15.26	0.26	15.70	0.26	15.48	0.26	this study
999A	3	10-12	*C. wuellestorfi*	250-300	1.19	1.43	16.61	0.22	16.82	0.21	16.72	0.21	this study
999A	3	27-29	*C. wuellestorfi*	>200	1.19	1.62	16.60	0.24	16.55	0.23	16.58	0.24	this study
758B	1	117-119	*C. wuellestorfi*	>200	1.48	1.08	15.70	0.27	15.93	0.27	15.82	0.27	this study
999A	3	78-80	*C. wuellestorfi*	>200	2.39	1.62	15.91	0.27	15.96	0.26	15.94	0.27	this study
999A	2	53-55	*C. wuellestorfi*	250-300	2.95	1.67	15.21	0.24	15.06	0.23	15.14	0.24	this study
926A	2	60.5-62	*C. wuellestorfi*	>200	5.19	1.39	15.57	0.24	15.83	0.22	15.70	0.23	this study
926A	3	65-66.5											
926A	3	26.5-28	*C. mundulus*	>200	8.45	1.70	15.65	0.21	15.94	0.20	15.79	0.21	this study
926A	3	52-53.5											
926A	2	106-108	*C. wuellestorfi*	>200	9.12	1.73	14.91	0.21	15.01	0.20	14.96	0.21	this study
926A	2	58-60	*C. wuellestorfi*	250-300	10.20	1.54	14.23	0.53	14.28	0.50	14.26	0.52	this study
926A	2	85-87											
926A	2	30-32	*C. wuellestorfi*	250-300	11.56	1.25	14.27	0.36	14.64	0.35	14.46	0.36	this study
926A	2	63-65											
926A	2	67.5-70	*C. wuellestorfi*	>200	12.29	1.14	14.02	0.26	14.32	0.27	14.17	0.26	this study
761B	4	123-125	*C. mundulus*	>250	12.72	2.01	13.18	0.26	13.37	0.22	13.28	0.27	Foster et al. (2012)
926A	3	130-132	*C. wuellestorfi*	>200	13.61	1.25	13.65	0.28	14.16	0.28	13.90	0.28	this study
926A	3	67-69	*C. mundulus*	>200	16.28	1.76	14.07	0.26	14.11	0.26	14.09	0.26	this study
926A	3	60-62											
926B	2	65-68	*C. mundulus*	>200	17.93	1.81	14.46	0.27	14.67	0.27	14.56	0.27	this study
926B	2	70-72											
926B	6	54-56.5											
926B	6	70-72											
926B	4	100-103	*C. mundulus*	>200	19.03	1.71	14.88	0.25	15.00	0.25	14.94	0.25	this study
926B	6	29-32											
926B	2	65-68	*C. mundulus*	>200	19.88	1.41	15.23	0.26	15.29	0.26	15.26	0.26	this study
926B	3	126.5-130	*C. mundulus*	>200	22.58	1.71	14.86	0.23	14.81	0.23	14.84	0.23	this study
926B	3	147-150	*C. mundulus*	250-300	22.96	2.12	14.48	0.61			14.48	0.61	this study
926B	5	99-104	*C. mundulus*	>200	23.05	1.70	14.78	0.24	14.93	0.23	14.86	0.24	this study

C.2 Planktic boron isotope and trace element data

Site	Core	Section	Interval (cm)	Species	Size fraction (µm)	Age (Ma)	Mg/Ca mmol/mol	$\delta^{11}B$ - 1	2sd	$\delta^{11}B$ - 2	2sd	$\delta^{11}B$ average	2sd average	Temp. °C	Data source
999A	3	4	47-49	*G.trilobus*	500-600	0.62	4.06	20.43	0.21	20.52	0.20	20.47	0.21	26.95	this study
758B	2	5	64-67	*G.trilobus*	300-355	1.15	3.10	19.05	0.27	18.68	0.26	18.87	0.26	23.99	this study
999A	5	3	10-12	*G.ruber*	300-355	1.19	3.75					20.57	0.41	26.12	Chalk et al. (in prep)
999A	5	3	27-29	*G.ruber*	300-355	1.19	3.47					20.95	0.15	25.26	Chalk et al. (in prep)
758B	3	1	117-119	*G.trilobus*	300-355	1.47	3.40	19.30	0.25	19.23	0.24	19.26	0.24	25.07	this study
999A	9	3	78-80	*G.ruber*	300-355	2.39	3.91					19.89	0.24	26.70	Martinez-Boti et al. (in press)
999A	11	2	53-55	*G.ruber*	300-355	2.95	3.06					19.90	0.20	24.01	Martinez-Boti et al. (in press)
926A	16	2	100-102	*G.trilobus*	300-355	5.17	3.54	17.47	0.31	17.66	0.29	17.56	0.30	25.87	Sosdian et al. (in prep)
926A	22	2	50-52	*G.trilobus*	300-355	8.36	3.77	16.50	0.44	16.26	0.40	16.38	0.42	26.88	Sosdian et al. (in prep)
926A	23	2	75-77	*G.trilobus*	300-355	9.10	3.83	16.51	0.30	16.58	0.28	16.54	0.29	27.11	Sosdian et al. (in prep)
926A	24	2	56-57.5	*G.trilobus*	300-355	9.73	3.58	17.59	0.20	17.50	0.19	17.54	0.20	26.44	Sosdian et al. (in prep)
926A	26	5	30-32	*G.trilobus*	300-355	11.94	3.39	16.02	0.09	16.16	0.11	16.09	0.21	25.98	Foster et al. (2012)
761B	5	4	13-15	*G.trilobus*	300-355	12.3	3.89	17.14	0.12	17.15	0.12	17.14	0.23	27.60	Foster et al. (2012)
761B	5	4	123-125	*G.trilobus*	300-355	12.7	4.00	16.50	0.08	16.73	0.07	16.62	0.15	27.94	Foster et al. (2012)
761B	5	6	8-10	*G.trilobus*	300-355	13.5	4.06	16.3	0.22	16.42	0.16	16.36	0.27	28.16	Foster et al. (2012)
926A	33	3	67-68.5	*G.trilobus*	300-355	16.28	3.81	16.58	0.21	16.64	0.21	16.61	0.21	27.73	Sosdian et al. (in prep)
926B	35	6	54-56.5	*G.trilobus*	300-355	18.0	4.33	16.95	0.24	17.20	0.24	17.08	0.24	29.29	Sosdian et al. (in prep)
926B	38	4	100-103	*G.trilobus*	300-355	18.9	3.45	15.90	0.24	15.96	0.24	15.93	0.24	26.88	Sosdian et al. (in prep)
926B	41	2	65-68	*G.trilobus*	300-355	19.9	3.55	17.50	0.22	17.53	0.22	17.51	0.22	27.27	Sosdian et al. (in prep)
926B	49	3	126.5-130	*G.praebull oides*	250-300	22.58	3.29	15.86	0.24	16.17	0.23	16.02	0.24	26.68	Greenop et al. (in prep)
926B	50	4	14-19	*G.praebull oides*	250-300	22.97	3.42	17.39	0.25	17.60	0.24	17.50	0.24	27.14	Greenop et al. (in prep)
926B	50	5	121-124	*G. praebulloi des*	250-300	23.08	3.24	16.75	0.33	16.80	0.32	16.78	0.32	26.55	Greenop et al. (in prep)

C.3 δ^{13}C planktic and benthic data

δ^{13}C planktic								**δ^{13}C benthic**							**δ^{13}C DIC**		**Gradients**	
Lab	Age (Ma)	Site	Core	Section	Interval (cm)	Planktic species	δ^{13}C planktic	Lab	Age (Ma)	Site	Core	Section	Interval (cm)	Benthic species	δ^{13}C benthic	δ^{13}C DIC surface	δ^{13}C DIC deep	δ^{13}C gradient	pH gradient
Bremen	0.62	999A	3	4	47-49	*G. ruber*	1.13	Cardiff	0.62	999A	3	4	47-49	*C.wuellestorfi*	0.82	2.07	0.82	1.25	0.18
Cardiff	1.15	758B	2	5	64-67	*G. trilobus*	1.27	Cardiff	1.15	758B	2	5	64-67	*C.wuellestorfi*	0.09	1.73	0.09	1.63	0.26
Soton Greenop	1.19	999A	5	3	10-12	*G. ruber*	1.07	Soton Chalk	1.19	999A	5	3	10-12	*C.wuellestorfi*	0.43	2.01	0.43	1.58	0.25
Bremen	1.19	999A	5	3	27-29	*G. ruber*	1.35	Soton Chalk	1.19	999A	5	3	27-29	*C.wuellestorfi*	0.74	2.29	0.74	1.55	0.24
Cardiff	1.48	758B	3	1	117-119	*G. trilobus*	1.78	Cardiff	1.48	758B	3	1	117-119	*C.wuellestorfi*	0.10	2.24	0.10	2.14	0.34
Cardiff	2.39	999A	9	3	78-80	*G. ruber*	1.67	Haug and Tiedemann (1998)	2.39	999A	9	3	75-77	*C.wuellestorfi*	0.79	2.61	0.79	1.82	0.29
Cardiff	2.95	999A	11	2	53-55	*G.ruber*	1.49	Haug and Tiedemann (1998)	2.95	999A	11	2	55-57	*C.wuellestorfi*	0.43	2.43	0.43	2.00	0.31
Cardiff	5.17	926A	16	2	100-102	*G. trilobus*	2.13	Cardiff	5.2	926A	16	2	60.5-62	*C.mundulus*	0.64	2.59	1.11	1.48	0.24
Cardiff	8.36	926A	22	2	50-52	*G. trilobus*	2.55	Cardiff	5.2 8.44	926A 926A	16 22	3 3	65-66.5 26.5-28	*C.mundulus* *C.mundulus*	0.64 1.44	3.01	1.91	1.10	0.19
Cardiff	9.10	926A	23	2	75-77	*G. trilobus*	2.63	Cardiff	8.46 9.12	926A 926A	22 23	3 2	52-53.5 106-107 .5	*C.mundulus*	1.28	3.09	1.75	1.35	0.23
Cardiff	9.73	926A	24	2	56-57.5	*G. trilobus*	2.57	Cardiff	9.32 9.73	926A 926A	23 24	3 2	35-36.5 58-60	*C.mundulus*	1.00	3.03	1.47	1.56	0.25
Cardiff	11.94	926A	26	5	30-32	*G. trilobus*	2.44	Cardiff	10.66 11.55 11.57	926A 926A 926A	25 26 26	2 2 2	85-87 30-32 62-65	*C.wuellestorfi*	1.13	2.90	1.13	1.77	0.27
Cardiff	12.3	761B	5	4	13-15	*G. trilobus*	1.90	Cardiff	12.29	926A	27	2	67.5-69. 5	*C.wuellestorfi*	1.09	2.36	1.09	1.27	0.22
Foster et al (2012)	12.7	761B	5	4	123-125	*G. trilobus*	2.30	Lear et al (2010)	12.7	761B	5	4	123-125	*C.mundulus*	0.92	2.76	1.39	1.38	0.24
Cardiff	13.5	761B	5	6	8-10	*G. trilobus*	2.14	Cardiff	13.61	926A	29	3	130-132	*C.wuellestorfi*	1.40	2.60	1.40	1.21	0.21
Cardiff	16.28	926A	33	3	67-68.5	*G. trilobus*	3.19	Cardiff	16.28	926A	33	3	67-68.5	*C.mundulus*	1.97	3.65	2.44	1.21	0.21
Cardiff	18.0	926B	35	6	54-56.5	*G. trilobus*	1.74	Cardiff	16.28 17.8 18.0	926A 926B 926B	33 35 35	3 2 6	60-62 70-72 54-56.5	*C.mundulus*	0.55	2.20	1.02	1.17	0.2
Cardiff	18.9	926B	38	4	100-103	*G. trilobus*	2.26	Cardiff	18.0 18.9	926B 926B	35 38	6 4	70-72 100-103	*C.mundulus*	0.91	2.72	1.38	1.33	0.22
Cardiff	19.9	926B	41	2	65-68	*G. trilobus*	2.36	Cardiff	19.0 19.9	926B 926B	38 41	6 3	29-32 72-75	*C.mundulus*	0.46	2.82	0.93	1.89	0.3
Cardiff	22.58	926B	49	3	126.5-30	*G. praebulloides*	2.37	Cardiff	22.58	926B	49	3	126.5-1 30	*C.mundulus*	1.53	2.83	2.00	0.83	0.15
Cardiff	22.96	926B	50	3	147-150	*G. praebulloides*	2.39	Cardiff	22.96	926B	50	3	147-150	*Cibs spp*	1.38	2.85	1.85	1.00	0.18
Cardiff	23.08	926A	50	5	121-124	*G. trilobus*	2.74	Cardiff	23.05	926B	50	5	99-104	*C.mundulus*	1.43	3.20	1.90	1.30	0.22

C.4 $\delta^{11}B_{sw}$ output

Fixed pH gradient				Variable pH gradient			
Age	$\delta^{11}B$ seawater	Negative 2σ Monte Carlo simulation (n=1000)	Positive 2σ Monte Carlo simulation (n=1000)	Age	$\delta^{11}B$ seawater	Negative 2σ Monte Carlo simulation (n=1000)	Positive 2σ Monte Carlo simulation (n=1000)
0.62	41.00	1.43	0.88	0.62	40.61	1.75	1.01
1.15	36.69	2.90	1.85	1.15	38.54	1.75	1.19
1.19	40.93	1.54	0.98	1.19	41.68	1.05	0.75
1.19	38.97	2.61	1.39	1.19	40.05	1.66	1.02
1.48	37.24	3.07	1.86	1.48	40.37	0.93	0.78
2.39	40.41	1.38	0.94	2.39	41.51	0.80	0.60
2.95	36.77	3.22	1.75	2.95	39.53	1.12	0.81
5.18	39.25	2.42	1.38	5.18	40.16	1.59	1.02
8.42	42.36	0.83	0.68	8.42	42.30	0.90	0.72
9.11	39.70	1.38	1.01	9.11	40.16	1.01	0.84
10.04	34.09	5.61	3.01	10.04	35.81	3.37	2.22
11.69	39.31	1.57	1.12	11.69	40.18	0.94	0.78
12.29	35.66	3.20	1.84	12.29	36.40	2.95	1.57
12.72	36.80	1.54	1.09	12.72	37.52	1.11	0.86
13.54	37.05	2.30	1.46	13.54	37.33	2.05	1.35
16.28	36.49	3.11	1.56	16.28	36.85	2.63	1.41
17.95	36.97	3.21	1.67	17.95	36.97	3.21	1.67
18.97	40.73	1.21	0.82	18.97	40.95	1.04	0.74
19.88	37.64	3.33	1.58	19.88	39.99	1.11	0.77
22.58	40.39	1.03	0.82	22.58	39.54	1.88	1.22
22.97	35.12	3.50	2.36	22.97	34.37	5.74	2.68
23.07	38.43	2.50	1.36	23.07	38.93	1.86	1.16

C.5 $\delta^{11}B_{sw}$ smoothed

Fixed pH gradient				Variable pH gradient				Combined			
Age	δ11B seawater	2.5 percentile Monte Carlo simulation (n=10000)	97.5 percentile Monte Carlo simulation (n=10000)	Age	δ11B seawater	2.5 percentile Monte Carlo simulation (n=10000)	97.5 percentile Monte Carlo simulation (n=10000)	Age	δ11B seawater	2.5 percentile Monte Carlo simulation (n=20000)	97.5 percentile Monte Carlo simulation (n=20000)
0	39.25	38.48	39.97	0	40.01	39.38	40.55	0.0	39.64	38.60	40.46
0.5	39.21	38.54	39.86	0.5	40.07	39.62	40.53	0.5	39.71	38.64	40.46
1	39.23	38.57	39.77	1	40.15	39.79	40.55	1.0	39.79	38.67	40.49
1.5	39.17	38.57	39.70	1.5	40.26	39.90	40.63	1.5	39.82	38.66	40.57
2	39.13	38.54	39.63	2	40.34	39.97	40.75	2.0	39.81	38.63	40.68
2.5	39.11	38.49	39.59	2.5	40.41	39.98	40.89	2.5	39.79	38.58	40.82
3	38.99	38.42	39.55	3	40.50	39.98	41.03	3.0	39.76	38.51	40.96
3.5	38.85	38.34	39.50	3.5	40.55	40.00	41.14	3.5	39.73	38.42	41.05
4	38.84	38.23	39.47	4	40.64	39.99	41.25	4.0	39.70	38.34	41.15
4.5	38.79	38.13	39.44	4.5	40.70	39.97	41.38	4.5	39.68	38.25	41.27
5	38.72	38.02	39.42	5	40.70	39.95	41.51	5.0	39.66	38.15	41.39
5.5	38.66	37.93	39.37	5.5	40.66	39.92	41.42	5.5	39.63	38.05	41.30
6	38.63	37.84	39.31	6	40.49	39.88	41.22	6.0	39.59	37.95	41.11
6.5	38.58	37.74	39.24	6.5	40.36	39.81	41.06	6.5	39.55	37.86	40.96
7	38.51	37.64	39.18	7	40.31	39.71	40.94	7.0	39.47	37.77	40.83
7.5	38.45	37.54	39.12	7.5	40.22	39.56	40.84	7.5	39.36	37.67	40.74
8	38.36	37.44	39.06	8	40.06	39.37	40.78	8.0	39.23	37.57	40.67
8.5	38.25	37.33	39.01	8.5	39.90	39.17	40.73	8.5	39.10	37.47	40.60
9	38.17	37.25	38.94	9	39.67	38.94	40.54	9.0	38.94	37.39	40.41
9.5	38.11	37.19	38.87	9.5	39.38	38.67	40.18	9.5	38.77	37.31	40.06
10	38.04	37.11	38.80	10	39.11	38.35	39.81	10.0	38.56	37.24	39.70
10.5	37.89	36.99	38.64	10.5	38.79	38.05	39.43	10.5	38.32	37.12	39.32
11	37.71	36.85	38.50	11	38.41	37.73	39.08	11.0	38.08	36.98	38.98
11.5	37.53	36.70	38.36	11.5	38.04	37.38	38.74	11.5	37.82	36.84	38.65
12	37.38	36.55	38.21	12	37.77	37.08	38.47	12.0	37.60	36.68	38.39
12.5	37.24	36.42	38.08	12.5	37.52	36.84	38.25	12.5	37.41	36.54	38.19
13	37.15	36.36	38.00	13	37.39	36.67	38.09	13.0	37.28	36.47	38.05
13.5	37.09	36.32	37.94	13.5	37.24	36.51	37.98	13.5	37.19	36.40	37.96
14	37.08	36.35	37.93	14	37.26	36.47	37.99	14.0	37.19	36.40	37.96
14.5	37.15	36.39	37.92	14.5	37.26	36.41	38.03	14.5	37.19	36.40	37.99
15	37.10	36.42	37.92	15	37.21	36.33	38.12	15.0	37.19	36.37	38.04
15.5	37.18	36.44	37.93	15.5	37.22	36.23	38.22	15.5	37.20	36.33	38.11
16	37.20	36.44	37.95	16	37.25	36.11	38.34	16.0	37.20	36.25	38.19
16.5	37.22	36.47	37.97	16.5	37.44	36.26	38.55	16.5	37.29	36.37	38.37
17	37.26	36.53	38.01	17	37.85	36.77	38.86	17.0	37.50	36.59	38.70
17.5	37.29	36.58	38.06	17.5	38.28	37.25	39.19	17.5	37.71	36.69	39.04
18	37.40	36.62	38.10	18	38.59	37.68	39.51	18.0	37.91	36.75	39.36
18.5	37.44	36.69	38.15	18.5	38.64	37.76	39.51	18.5	37.97	36.82	39.36
19	37.43	36.77	38.19	19	38.69	37.83	39.51	19.0	38.03	36.88	39.37
19.5	37.52	36.86	38.28	19.5	38.66	37.86	39.45	19.5	38.09	36.96	39.32
20	37.60	36.93	38.38	20	38.57	37.86	39.39	20.0	38.12	37.05	39.27
20.5	37.77	37.02	38.53	20.5	38.48	37.72	39.28	20.5	38.11	37.13	39.14
21	37.87	37.08	38.68	21	38.34	37.51	39.21	21.0	38.10	37.18	39.08
21.5	37.94	37.12	38.85	21.5	38.22	37.24	39.22	21.5	38.09	37.16	39.09
22	38.14	37.14	39.04	22	38.06	36.94	39.26	22.0	38.09	37.04	39.15
22.5	38.27	37.15	39.24	22.5	37.96	36.63	39.32	22.5	38.09	36.80	39.27
23	38.41	37.15	39.48	23	37.82	36.14	39.34	23.0	38.06	36.38	39.43

Appendix D: Data from Chapter 5

Site	Core	Section	Interval	mcd	Age	Mg/Ca	$\delta^{11}B$ - 1	2sd	$\delta^{11}B$ - 2	2sd	$\delta^{11}B$	2sd	Temp.	CO_2	2.5 percentile Monte Carlo simulation (n=10000)	97.5 percentile Monte Carlo simulation (n=10000)
		(cm)		(m)	(Ma)	mmol/mol					average	average	°C	ppm		
G. trilobus (300-355 µm)																
761B	6	3	96-98	47.06	15.54	4.73	15.97	0.38			15.97	0.38	32	300	208	413
761B	6	3	118-120	47.28	15.60	4.35	14.57	0.31	15.11	0.30	14.84	0.31	32	442	300	618
761B	6	3	123-125	47.33	15.61	4.50	14.58	0.25	14.86	0.24	14.72	0.24	32	469	319	656
761B	6	3	128-130	47.38	15.63	4.69	15.50	0.32	15.83	0.31	15.66	0.31	32	330	229	453
761B	6	3	138-140	47.48	15.65	4.65	16.08	0.41	15.98	0.39	16.03	0.40	32	294	202	406
761B	6	4	3-5	47.63	15.69	4.74	16.38	0.71	15.85	0.69	16.11	0.70	32	287	189	417
761B	6	4	13-15	47.73	15.72	4.36	15.03	0.95	14.12	0.93	14.58	0.94	31	505	296	858
761B	6	4	28-30	47.88	15.76	4.54	16.05	0.62	16.01	0.55	16.03	0.58	32	291	196	413
761B	6	4	33-35	47.93	15.77	4.29	15.86	0.63	15.65	0.66	15.76	0.64	31	315	207	452
761B	6	4	46-48	48.06	15.81	4.40	14.54	0.41	14.40	0.40	14.47	0.41	32	520	344	757
761B	6	4	58-60	48.18	15.84	4.56	14.93	0.42	14.93	0.40	14.93	0.41	32	435	292	619
761B	6	4	78-80	48.38	15.89	4.71	16.04	0.34	16.27	0.33	16.15	0.33	32	281	194	385
761B	6	4	100-102	48.60	15.95	4.47	16.60	0.92	15.51	0.90	16.05	0.91	32	291	181	448
761B	6	4	103-105	48.63	15.96	4.64	15.62	0.40	15.95	0.39	15.78	0.39	32	318	219	440
761B	6	4	108-110	48.68	15.98	4.75	14.17	0.24	14.24	0.24	14.20	0.24	32	595	398	859
761B	6	4	113-115	48.73	15.99	4.77	15.67	0.42	15.86	0.39	15.76	0.41	33	322	220	451
761B	6	4	138-140	48.98	16.06	4.42	15.97	0.36	16.01	0.35	15.99	0.36	32	293	201	402
761B	6	5	8-10	49.18	16.12	4.26	15.52	0.62	14.60	0.63	15.06	0.63	31	406	262	601
761B	6	5	18-20	49.28	16.15	4.66	15.75	0.30	15.98	0.29	15.87	0.29	32	309	214	423
761B	6	5	28-30	49.38	16.18	3.99	15.96	0.33	16.28	0.33	16.12	0.33	31	271	188	373
761B	6	5	38-40	49.48	16.21	3.97	16.77	0.71	16.35	0.67	16.56	0.69	31	236	157	338
761B	6	5	48-50	49.58	16.24	3.97	14.34	0.65	14.87	0.64	14.60	0.65	30	477	304	728
761B	6	5	58-60	49.68	16.27	4.08	16.09	0.23	16.03	0.23	16.06	0.23	31	278	193	378
761B	6	5	68-70	49.78	16.30	4.14	14.66	0.22	14.66	0.22	14.66	0.22	31	467	317	655
761B	6	5	78-80	49.88	16.33	4.06	16.11	0.25	16.38	0.24	16.25	0.25	31	262	183	357
761B	6	5	88-90	49.98	16.37	4.19	14.51	0.27			14.51	0.27	31	502	341	710
761B	6	5	98-100	50.08	16.40	4.30	14.90	0.28			14.90	0.28	32	430	293	602
761B	6	5	103-105	50.13	16.42	4.25	16.80	0.24	16.81	0.24	16.80	0.24	31	221	156	300
761B	6	5	118-120	50.28	16.47	4.15	14.90	0.83	13.94	0.83	14.42	0.83	31	532	319	870
761B	6	6	3-5	50.63	16.59	4.26	16.14	0.25	16.26	0.24	16.20	0.25	31	271	188	368
761B	6	6	18-20	50.78	16.65	4.70	16.61	0.26	16.66	0.26	16.63	0.26	32	242	167	327
761B	6	6	28-30	50.88	16.69	4.38	16.75	0.51	16.62	0.52	16.69	0.52	32	236	162	329
761B	6	6	48-50	51.08	16.76	4.41	15.50	0.39	15.68	0.37	15.59	0.38	32	338	231	472
761B	6	6	98-100	51.58	16.98	3.96	16.94	0.67	17.07	0.65	17.00	0.66	31	207	138	293
761B	6	6	128-130	51.88	17.11	4.03	16.33	0.32	16.39	0.30	16.36	0.31	31	252	177	342

Appendix E : Data from Chapter 6

E.1 Data from Sites 1406 and 872

Site	Core	Section	Interval	mcd	Age	Mg/Ca	$\delta^{11}B$ - 1	2sd	$\delta^{11}B$ - 2	2sd	$\delta^{11}B$	2sd	CO_2	2.5 percentile Monte Carlo simulation (n=10000)	97.5 percentile Monte Carlo simulation (n=10000)
			(cm)	(m)	(Ma)	mmol/mol					average	average	ppm		
G. praebulloides (250-300 µm)															
1406B	6	5	122-124	51.49	21.66	4.12	14.40	0.26	14.64	0.26	14.52	0.26	506	337	719
1406A	6	3	132-134	55.29	21.86	3.70	15.70	0.27	15.79	0.26	15.74	0.27	315	216	440
1406A	6	4	44-46	55.91	21.89	3.91	14.23	0.35	14.09	0.34	14.16	0.34	600	392	880
1406A	6	5	72-74	57.69	21.96	3.76	14.02	0.23	13.94	0.23	13.98	0.23	653	427	944
1406A	6	6	2-4	58.49	21.99	3.87	15.04	0.24	14.93	0.23	14.99	0.24	416	282	590
1406A	7	5	46-48	67.53	22.26	3.91	15.60	0.26	15.53	0.26	15.57	0.26	336	231	471
1406A	7	5	132-134	68.39	22.28	3.96	15.45	0.24	15.68	0.23	15.56	0.24	337	228	475
1406C	7	3	12-14	68.57	22.29	4.56	13.66	0.24	13.73	0.24	13.70	0.24	765	483	1159
1406C	7	4	44-46	70.39	22.34	4.48	14.59	0.22	14.78	0.21	14.69	0.22	473	314	679
1406C	7	4	104-106	70.99	22.35	4.43	14.78	0.23	15.03	0.23	14.91	0.23	434	291	618
1406C	7	4	118-120	71.13	22.36	4.74	14.56	0.16	14.73	0.15	14.65	0.15	479	320	685
1406A	8	5	72-74	77.29	22.55	4.23	15.40	0.25	15.32	0.25	15.36	0.25	363	242	523
1406B	9	4	14-16	79.88	22.65	3.80	15.32	0.27	15.55	0.26	15.43	0.26	354	237	507
1406B	9	4	44-46	80.18	22.66	4.00	15.49	0.24	15.57	0.24	15.53	0.24	340	228	483
1406B	9	4	104-106	80.78	22.68	3.84	14.68	0.34	14.79	0.34	14.74	0.34	465	299	681
1406B	9	5	74-76	81.99	22.74	3.90	15.50	0.24	15.45	0.23	15.47	0.24	348	229	502
1406C	9	3	72-74	87.84	23.01	3.81	15.48	0.26	15.49	0.26	15.49	0.26	346	225	505
1406C	9	3	98-100	88.10	23.02	3.57	16.09	0.24	16.00	0.24	16.04	0.24	286	190	414
1406C	9	4	44-46	89.06	23.08	4.29	17.36	0.25	17.26	0.25	17.31	0.25	193	129	273
1406C	9	4	70-72	89.32	23.09	4.27	16.38	0.19	16.49	0.19	16.44	0.19	252	169	356
1406C	9	4	104-106	89.66	23.11	4.42	16.96	0.19	16.94	0.18	16.95	0.19	214	144	305
1406A	10	5	12-14	96.29	23.50	3.51	15.33	0.27	15.06	0.27	15.20	0.27	386	251	564
1406A	10	5	42-44	96.59	23.52	4.28	13.30	0.13	13.37	0.12	13.33	0.13	960	553	1587

Site	Core	Section	Interval	mcd	Age	Mg/Ca	$\delta^{11}B$ - 1	2sd	$\delta^{11}B$ - 2	2sd	$\delta^{11}B$	2sd	Temp.	CO_2	2.5 percentile Monte Carlo simulation (n=10000)	97.5 percentile Monte Carlo simulation (n=10000)
			(cm)	(m)	(Ma)	mmol/mol					average	average	°C	ppm		
G.trilobus (300-350 µm)																
872C	13	4	20-22	110	22.22	4.42	16.63	0.25	16.68	0.25	16.66	0.25	29.93	352	249	473
872C	13	6	20-22	112.64	23.22	4.88	17.23	0.25	17.11	0.25	17.17	0.25	31.10	309	212	430
872C	14	1	20-22	115.7	23.36	4.04	16.76	0.38	16.96	0.36	16.86	0.37	29.02	334	228	471
872C	14	1	78-80	116.28												

E.2 Data from Site 926

Site	Core	Section	Interval	mcd	Age	Mg/Ca	$\delta^{11}B$ - 1	2sd	$\delta^{11}B$ - 2	2sd	$\delta^{11}B$	2sd	Temp.	CO_2	2.5 percentile	97.5 percentile
											average	average			Monte Carlo simulation (n=10000)	Monte Carlo simulation (n=10000)
G. praebulloides (250-300 µm)			(cm)	(m)	(Ma)	mmol/mol							°C	ppm		
926B	47	5	137.5-139.5	469.61	22.02	3.56	17.09	0.59	17.10	0.58	17.10	0.59	28	281	195	386
926B	48	2	47-49	473.90	22.16	2.86	15.68	0.45	15.65	0.45	15.67	0.45	25	447	307	623
926B	49	1	43.5-46	481.97	22.44	3.22	15.86	0.25	15.91	0.25	15.89	0.25	26	413	290	567
926B	49	2	97-99.5	484.01	22.51	3.36	16.70	0.26	16.40	0.26	16.55	0.26	27	332	233	456
926B	49	2	124-126.5	484.28	22.52	3.34	16.14	0.28	15.86	0.28	16.00	0.28	27	399	277	549
926B	49	3	126.5-130	485.81	22.58	3.29	15.86	0.24	16.17	0.23	16.02	0.24	27	395	275	544
926B	49	4	20-24	486.25	22.59	2.97	16.59	0.23	16.73	0.22	16.66	0.23	26	320	224	435
926B	49	5	63-65	488.16	22.66	2.81	16.19	0.31	16.45	0.30	16.32	0.31	25	357	246	494
926B	49	5	91-93.5	488.45	22.67	2.92	16.06	0.46	16.05	0.45	16.05	0.46	25	391	265	553
926B	49	5	147-149	489.00	22.7	3.35	16.66	0.28	16.90	0.29	16.78	0.28	27	308	214	424
926B	49	6	76.5-79	489.78	22.73	3.34	17.52	0.27	17.79	0.26	17.65	0.27	27	237	167	324
926B	49	cc	9-12	489.99	22.74	3.29	16.83	0.25	17.16	0.24	16.99	0.25	27	290	202	397
926B	50	1	65-69	491.86	22.81	3.32	17.63	0.25	17.69	0.24	17.66	0.25	27	238	165	325
926B	50	1	70-73	492.11	22.82	3.19	17.38	0.25	17.69	0.25	17.53	0.25	26	246	171	336
926B	50	1	90-93	492.13												
926B	50	1	94-99	492.20	22.82	3.32	17.34	0.26	17.24	0.25	17.29	0.26	27	265	183	364
926B	50	2	29-32	493.02	22.87	3.40	16.17	0.25	16.21	0.25	16.19	0.25	27	373	255	517
926B	50	2	66-68	493.37												
926B	50	2	75-78	493.48												
926B	50	2	78-80	493.49												
926B	50	2	117-121	493.90												
926B	50	2	130-133	494.04	22.9	3.42	16.74	0.28	16.62	0.27	16.68	0.28	27	317	218	443
926B	50	3	17-20	495.29	22.94	3.23	17.27	0.34	17.18	0.34	17.23	0.34	27	269	185	372
926B	50	3	106-109	494.40												
926B	50	3	147-150	495.70												
926B	50	4	14-19	495.90	22.97	3.30	17.39	0.25	17.60	0.24	17.50	0.24	27	249	172	344
926B	50	4	125-130	497.01	23.01	3.15	17.07	0.17	17.44	0.15	17.26	0.16	26	267	184	370
926B	50	4	88-90	496.60	23.01	3.19	17.04	0.36	17.14	0.35	17.09	0.35	26	280	191	389
926B	50	4	134-137	497.07												
926B	50	5	28-31	497.51												
926B	50	6	10-16	498.87	23.08	3.74	16.81	0.24	16.95	0.24	16.88	0.24	28	300	205	417
926B	50	5	121-124	498.44	23.08	3.24	16.75	0.33	16.80	0.32	16.78	0.32	27	307	210	429
926B	50	6	16-19	498.89												
926B	50	6	61-64	499.34												
926B	50	6	106-109	499.42												
926B	50	6	56-59	499.30	23.1	3.23	17.21	0.28	16.73	0.27	16.97	0.28	27	291	200	402
926B	51	1	12-16	500.97	23.16	3.82	17.58	0.30	17.18	0.28	17.38	0.28	28	257	176	356
926B	51	2	109-111.5	503.43	23.25	3.97	16.96	0.45	16.96	0.34	16.96	0.38	29	291	198	408
926B	51	3	0-3	503.84	23.27	3.91	16.79	0.27	17.21	0.26	17.00	0.27	29	288	198	399
926B	51	3	121.5-124	505.05	23.31	3.72	17.39	0.39	17.47	0.32	17.43	0.35	28	255	175	354
926B	51	4	64-69	506.00	23.34	3.53	17.18	0.26	17.39	0.25	17.28	0.26	28	264	181	367
926B	51	6	120-122	509.51	23.58	3.44	17.22	0.25	17.36	0.24	17.29	0.25	27	264	182	368
926B	51	6	130-134	509.65	23.58	3.62	17.40	0.26	17.43	0.25	17.42	0.26	28	255	175	353
926B	52	2	57.5-60	512.39	23.66	4.11	17.32	0.26	17.82	0.26	17.57	0.26	29	244	167	335
926B	52	3	90-95	514.21	23.73	3.75	16.73	0.26	17.04	0.25	16.89	0.26	28	298	204	417
926B	52	4	95-98	515.76	23.8	3.51	17.02	0.72	17.47	0.36	17.25	0.47	28	268	183	378
926B	52	4	138-140	516.21	23.82	3.77	17.24	0.33	17.37	0.33	17.31	0.33	28	264	180	365
926B	52	5	72-74	517.05	23.86	3.03	16.29	0.86	16.17	0.84	16.23	0.85	26	371	238	557
926B	52	6	101-103	518.84	23.93	3.58	17.67	0.28	17.27	0.28	17.47	0.28	28	250	173	347
926B	53	1	10-12	520.13	23.98	3.54	17.29	0.39	18.37	0.38	17.83	0.39	28	226	154	314
926B	53	2	39.5-41.5	521.93	24.02	3.94	17.10	0.69	17.52	0.69	17.31	0.69	29	264	176	379

Appendix F : Auxillary data

F.1 Benthic trace element data from Chapter 4

Site	Core	Section	Interval (cm)	B11/ Ca43 (µmol/ mol)	B11/ Ca48 (µmol/ mol)	Na23/ Ca48 (mmol /mol)	Na23/ Ca43 (mmol /mol)	Mg24/ Ca43 (mmol /mol)	Mg24/ Ca48 (mmol /mol)	Mg25/ Ca43 (mmol /mol)	Mg25/ Ca48 (mmol /mol)	Al27/ Ca43 (µmol/ mol)	Al27/ Ca48 (µmol/ mol)	Mn55/ Ca43 (µmol/ mol)	Mn55/ Ca48 (µmol/ mol)	Sr86/ Ca43 (mmol/ mol)	Sr86/ Ca48 (mmol/ mol)	Sr87/ Ca43 (mmol/ mol)	Sr87/ Ca48 (mmol/ mol)	Cd111/ Ca43 (µmol/ mol)	Cd111/ Ca48 (µmol/ mol)	Ba138/ Ca43 (µmol/ mol)	Ba138/ Ca48((µmol/ mol)	Nd146/ Ca43 (µmol/ mol)	Nd146/ Ca48 (µmol/ mol)	U238/ Ca43 (nmol/ mol)	U238/ Ca48 (nmol/ mol)
999A	3	4	47-49	207	207	5.38	5.37	1.87	1.88	1.92	1.92	23.62	23.68	612	614	1.33	1.34	1.34	1.34	0.12	0.12	2.98	2.99	0.39	0.39	7	8
758B	2	5	64-67	120	120	6.35	6.33	1.08	1.07	0.99	0.98	6.63	6.61	670	668	1.23	1.23	1.15	1.14	0.40	0.40	7.18	7.15	1.33	1.33	12	12
999A	5	3	10-12	183	182	5.29	5.28	1.38	1.38	1.43	1.43	23.98		750		1.28				0.11	0.11	2.28		0.50			40
999A	5	3	27-29	201	202	5.00	4.99	1.61	1.62	1.63	1.63	37.78	37.88	678	680	1.32	1.32	1.31	1.32	0.08	0.08	2.40	2.41	0.67	0.67	24	24
758B	3	1	117-119	121	121	7.47	7.46	1.12	1.12	1.05	1.05	40.66	40.61	620	619	1.24	1.24	1.15	1.15	0.32	0.32	5.79	5.78	1.16	1.16	10	10
999A	9	3	78-80	182	181	5.83	5.89	1.61	1.59	1.64	1.63	60.82	60.28	1646	1631	1.19	1.18	1.14	1.13	0.19	0.19	3.27	3.24	1.42	1.41	75	75
999A	11	2	53-55	174	173	5.84	5.83	1.60	1.59	1.67	1.67	19.10		1376				1.21		0.31	0.31	3.33		1.08			38
926A	16	2	60.5-62	181	181	4.04	4.04	1.38	1.38	1.40	1.40	10.29	10.27	309	309	1.12	1.11	1.12	1.11	0.15	0.15	2.40	2.40	0.71	0.71	15	15
926A	16	3	65-66.5																								
926A	22	3	26.5-28	133	132	3.18	3.19	1.71	1.71	1.68	1.68	14.48	14.43	339	338	0.97	0.97	0.98	0.98	0.10	0.10	1.59	1.58	1.45	1.45	22	22
926A	22	3	52-53.5																								
926A	23	2	106-108	185	185	4.50	4.47	1.70	1.71	1.76	1.77	11.56	11.62	245	247	1.11	1.12	1.11	1.12	0.11	0.11	2.05	2.06	1.23	1.24	15	15

Site	Core	Section	Interval (cm)	B11/ Ca43 (µmol/ mol)	B11/ Ca48 (µmol/ mol)	Na23/ Ca48 (mmol /mol)	Na23/ Ca43 (mmol /mol)	Mg24/ Ca43 (mmol /mol)	Mg24/ Ca48 (mmol /mol)	Mg25/ Ca43 (mmol /mol)	Mg25/ Ca48 (mmol /mol)	Al27/ Ca43 (µmol/ mol)	Al27/ Ca48 (µmol/ mol)	Mn55/ Ca43 (µmol/ mol)	Mn55/ Ca48 (µmol/ mol)	Sr86/ Ca43 (mmol/ mol)	Sr86/ Ca48 (mmol/ mol)	Sr87/ Ca43 (mmol/ mol)	Sr87/ Ca48 (mmol/ mol)	Cd111/ Ca43 (µmol/ mol)	Cd111/ Ca48 (µmol/ mol)	Ba138/ Ca43 (µmol/ mol)	Ba138/ Ca48((µmol/ mol)	Nd146/ Ca43 (µmol/ mol)	Nd146/ Ca48 (µmol/ mol)	U238/ Ca43 (nmol/ mol)	U238/ Ca48 (nmol/ mol)
926A	24	2	58-60	172	172	6.24	6.24	1.61	1.61	1.54	1.54	27.87		265				1.13		0.11	0.11	2.48		1.38			16
926A	25	2	85-87																								
926A	26	2	30-32	147	148	6.01	6.06	1.29	1.30	1.25	1.26	27.35		1006				1.12		0.20	0.20	3.44		1.96			34
926A	26	2	63-65																								
926A	27	2	67.5-70	169	169	1.96	1.97	1.14	1.13	1.15	1.14	22.97	22.90	1094	1090	1.14	1.14	1.14	1.14	0.16	0.16	2.84	2.83	1.79	1.79	22	22
926A	29	3	130-132	149	149	2.01	2.01	1.27	1.27	1.24	1.24	37.81	37.85	1130	1131	1.20	1.20	1.18	1.18	0.16	0.16	5.93	5.94	2.44	2.44	50	50
926A	33	3	67-69	110	110	2.04	2.04	1.75	1.75	1.76	1.76	29.99	29.99	594	594	1.18	1.18	1.17	1.17	0.14	0.14	4.30	4.30	2.21	2.21	28	28
926A	33	3	60-62																								
926B	35	2	65-68	118	118	1.98	1.99	1.80	1.79	1.83	1.82	35.37	35.23	449	447	1.10	1.10	1.11	1.10	0.13	0.13	3.96	3.95	1.75	1.74	26	26
926B	35	2	70-72																								
926B	35	6	54-56.5																								
926B	35	6	70-72																								
926B	38	4	100-103	126	126	3.02	3.02	1.70	1.70	1.72	1.72	52.27	52.38	447	448	1.08	1.08	1.08	1.08	0.13	0.13	8.26	8.28	1.20	1.21	44	44
926B	38	6	29-32																								
926B	41	2	65-68	114	114	1.83	1.82	1.41	1.41	1.42	1.42	51.01	51.15	728	730	1.13	1.13	1.13	1.13	0.10	0.11	5.66	5.67	1.83	1.83	105	105
926B	49	3	126.5-130	142	142	1.71	1.72	1.69	1.69	1.72	1.72	44.12	43.90	844	840	1.12	1.12	1.13	1.12	0.13	0.13	7.98	7.94	1.09	1.09	50	50
926B	50	3	147-150																								
926B	50	5	99-104	119	119	1.44	1.45	1.70	1.68	1.72	1.71	48.49	48.19	707	703	1.18	1.17	1.17	1.16	0.12	0.12	8.01	7.96	1.76	1.75	69	68

F.2 Oxygen isotope data from Chapter 4

δ18O planktic								**δ18O benthic**						
Lab	Age (Ma)	Site	Core	Section	Interval (cm)	Planktic species	δ18O planktic	Lab	Age (Ma)	Site	Core	Section	Interval (cm)	Benthic species	δ18O benthic
Bremen	0.62	999A	3	4	47-49	*G. ruber*	-0.80	Cardiff	0.62	999A	3	4	47-49	*C.wuellestorfi*	2.749
Cardiff	1.15	758B	2	5	64-67	*G. trilobus*	-1.54	Cardiff	1.15	758B	2	5	64-67	*C.wuellestorfi*	3.046
Soton Greenop	1.19	999A	5	3	10-12	*G. ruber*	-0.53	Cardiff	1.48	758B	3	1	117-119	*C.wuellestorfi*	2.846
Bremen	1.19	999A	5	3	27-29	*G. ruber*	-0.56	Cardiff	5.2	926A	16	2	60.5-62	*C.mundulus*	2.497
Cardiff	1.48	758B	3	1	117-119	*G. trilobus*	-1.62		5.2	926A	16	3	65-66.5		
Cardiff	2.39	999A	9	3	78-80	*G. ruber*	-1.27	Cardiff	8.44	926A	22	3	26.5-28	*C.mundulus*	2.543
Cardiff	2.95	999A	11	2	53-55	*G.ruber*	-1.25		8.46	926A	22	3	52-53.5		
Cardiff	5.17	926A	16	2	100-102	*G. trilobus*	-1.26	Cardiff	9.12	926A	23	2	106-107.5	*C.mundulus*	2.433
									9.32	926A	23	3	35-36.5		
Cardiff	8.36	926A	22	2	50-52	*G. trilobus*	-1.20	Cardiff	9.73	926A	24	2	58-60	*C.mundulus*	1.981
									10.66	926A	25	2	85-87		
Cardiff	9.10	926A	23	2	75-77	*G. trilobus*	-0.86	Cardiff	11.55	926A	26	2	30-32	*C.wuellestorfi*	1.988
									11.57	926A	26	2	62-65		
Cardiff	9.73	926A	24	2	56-57.5	*G. trilobus*	-0.90	Cardiff	12.29	926A	27	2	67.5-69.5	*C.wuellestorfi*	1.644
								Cardiff	13.61	926A	29	3	130-132	*C.wuellestorfi*	1.723
Cardiff	11.94	926A	26	5	30-32	*G. trilobus*	-1.54	Cardiff	16.28	926A	33	3	67-68.5	*C.mundulus*	1.432
									16.28	926A	33	3	60-62		
Cardiff	12.3	761B	5	4	13-15	*G. trilobus*	-0.89	Cardiff	17.8	926B	35	2	70-72	*C.mundulus*	1.041
Cardiff	13.5	761B	5	6	8-10	*G. trilobus*	-0.67		18.0	926B	35	6	54-56.5		
Cardiff	16.28	926A	33	3	67-68.5	*G. trilobus*	-1.75		18.0	926B	35	6	70-72		
								Cardiff	18.9	926B	38	4	100-103	*C.mundulus*	1.328
Cardiff	18.0	926B	35	6	54-56.5	*G. trilobus*	-1.44		19.0	926B	38	6	29-32		
								Cardiff	19.9	926B	41	3	72-75	*C.mundulus*	0.974
								Cardiff	22.58	926B	49	3	126.5-130	*C.mundulus*	1.497
Cardiff	18.9	926B	38	4	100-103	*G. trilobus*	-1.51	Cardiff	22.96	926B	50	3	147-150	*Cibs spp*	1.409
								Cardiff	23.05	926B	50	5	99-104	*C.mundulus*	1.656
Cardiff	19.9	926B	41	2	65-68	*G. trilobus*	-1.74								
Cardiff	22.58	926B	49	3	126.5-30	*G. praebulloides*	-1.73								
Cardiff	22.96	926B	50	3	147-150	*G. praebulloides*	-1.60								
Cardiff	23.08	926A	50	5	121-124	*G. trilobus*	-1.41								

F.3 Trace element data from Chapter 5

Site	Core	Section	Interval (cm)	mcd (m)	Age (Ma)	B/Ca (µmol/mol)	Na/Ca (mmol/mol)	Mg/Ca (mmol/mol)	Al/Ca (µmol/mol)	Mn/Ca (µmol/mol)	Sr/Ca (mmol/mol)	Cd/Ca (µmol/mol)	Ba/Ca (µmol/mol)	Nd/Ca (µmol/mol)	U/Ca (nmol/mol)
G. trilobus (300-355 µm)															
761B	6	3	96-98	47.06	15.54	55.1	3.98	4.69	309.7	212.8	1.08	0.102	1.34	11.28	29.2
761B	6	3	118-120	47.28	15.60	53.0	3.62	4.37	104.1	204.3	1.12	0.137	1.70	1.04	13.5
761B	6	3	123-125	47.33	15.61	52.5	4.55	4.48	79.4	208.6	1.10	0.134	2.14	1.00	13.3
761B	6	3	128-130	47.38	15.63	53.0	3.81	4.59	169.2	190.2	1.08	0.103	1.38	8.81	30.0
761B	6	3	138-140	47.48	15.65	51.5	4.18	4.66	95.1	171.3	1.06	0.100	1.45	6.93	28.2
761B	6	4	3-5	47.63	15.69	57.7	5.97	4.70	223.0	215.6	1.09	0.104	1.62	8.58	27.3
761B	6	4	13-15	47.73	15.72	55.4	4.26	4.33	77.6	184.9	1.10	0.144	1.70	0.97	13.5
761B	6	4	28-30	47.88	15.76	50.4	3.26	4.51	166.6	193.7	1.07	0.140	3.02	1.04	14.8
761B	6	4	33-35	47.93	15.77	52.9	3.53	4.30	54.8	213.3	1.09	0.134	1.82	0.95	14.0
761B	6	4	46-48	48.06	15.81	45.8	4.03	4.43	74.9	186.5	1.09	0.103	1.19	5.91	25.9
761B	6	4	58-60	48.18	15.84	47.2	4.46	4.60	81.2	181.0	1.09	0.102	1.46	9.05	28.3
761B	6	4	78-80	48.38	15.89	52.6	3.60	4.64	185.6	232.4	1.07	0.102	1.52	11.61	31.5
761B	6	4	100-102	48.60	15.95	46.5	4.08	4.43	52.7	197.6	1.07	0.102	1.55	8.78	31.1
761B	6	4	103-105	48.63	15.96	53.4	4.20	4.64	68.9	213.6	1.06	0.171	2.30	1.16	14.9
761B	6	4	108-110	48.68	15.98	43.9	4.05	4.70	176.6	203.8	1.04	0.098	1.54	12.83	31.1
761B	6	4	113-115	48.73	15.99	59.6	4.63	4.74	127.9	185.3	1.05	0.100	1.55	8.72	30.5
761B	6	4	138-140	48.98	16.06	49.5	3.43	4.40	16.9	148.1	1.07	0.101	1.49	6.28	28.2
761B	6	5	8-10	49.18	16.12	52.1	3.60	4.26	323.3	194.1	1.05	0.176	2.38	1.01	14.5
761B	6	5	18-20	49.28	16.15	72.6	6.85	4.62	172.2	177.2	1.05	0.100	1.76	11.04	28.5
761B	6	5	28-30	49.38	16.18	56.2	4.03	3.97	78.3	192.3	1.08	0.148	1.99	1.02	14.1
761B	6	5	38-40	49.48	16.21	58.7	3.86	3.97	98.7	198.2	1.08	0.103	1.41	6.59	26.0
761B	6	5	48-50	49.58	16.24	82.9	4.08	3.91	161.2	165.5	1.10	0.134	1.66	0.87	14.0
761B	6	5	58-60	49.68	16.27	94.1	4.52	4.04	90.4	173.8	1.10	0.104	1.44	6.43	25.3
761B	6	5	68-70	49.78	16.30	60.4	3.81	4.12	87.5	196.4	1.07	0.144	1.83	0.97	14.4
761B	6	5	78-80	49.88	16.33	79.7	3.75	4.08	181.1	168.3	1.10	0.104	1.33	7.17	30.7
761B	6	5	88-90	49.98	16.37	63.7	3.51	4.16	159.8	181.3	1.09	0.134	2.17	1.01	14.6
761B	6	5	98-100	50.08	16.40	63.6	3.61	4.30	168.6	181.1	1.06	0.146	2.29	1.08	15.5
761B	6	5	103-105	50.13	16.42	69.6	3.71	4.20	53.5	210.5	1.07	0.154	2.19	1.12	15.2
761B	6	5	118-120	50.28	16.47	87.8	4.11	4.15	97.7	172.7	1.10	0.147	2.10	1.00	15.1
761B	6	6	3-5	50.63	16.59	63.2	3.98	4.26	52.4	172.8	1.07	0.100	1.44	6.94	36.1
761B	6	6	18-20	50.78	16.65	65.4	3.76	4.61	178.2	177.6	1.05	0.100	1.27	9.13	32.4
761B	6	6	28-30	50.88	16.69	65.2	4.59	4.39	123.1	179.7	1.05	0.099	1.44	7.16	32.7
761B	6	6	48-50	51.08	16.76	58.0	3.28	4.40	275.3	179.0	1.01	0.163	2.29	1.13	15.7
761B	6	6	98-100	51.58	16.98	67.0	4.11	3.92	78.5	162.6	1.06	0.100	1.36	6.96	30.4
761B	6	6	128-130	51.88	17.11	67.8	3.33	4.00	72.8	169.6	1.04	0.098	1.32	15.21	29.8

F.4 Trace element data from Chapter 6

Site	Core	Section	Interval (cm)	mcd (m)	Age (Ma)	B11/Ca43 (µmol/mol)	B11/Ca48 (µmol/mol)	Na23/Ca43 (mmol/mol)	Na23/Ca48 (mmol/mol)	Mg24/Ca43 (mmol/mol)	Mg24/Ca48 (mmol/mol)	Mg25/Ca43 (mmol/mol)	Mg25/Ca48 (mmol/mol)	Mn55/Ca43 (µmol/mol)	Cd111/Ca43 (µmol/mol)	Cd111/Ca48 (µmol/mol)	Ba138/Ca43 (µmol/mol)	Nd146/Ca43 (µmol/mol)	U238/Ca43 (nmol/mol)	Sr87/Ca43 (mmol/mol)	Al27/Ca43 (µmol/mol)
G. praebulloides (250-300 µm)																					
926B	47	5	137.5-139.5	469.61	22.02	57	57	3.49	3.50	3.46	3.46	3.67	3.67	792	0.10	0.10	5.43	1.76	94	1.12	16
926B	48	2	47-49	473.90	22.16	56	56	3.01	3.00	2.79	2.78	2.94	2.92	606	0.09	0.09	4.04	1.20	46	1.15	23
926B	49	1	43.5-46	481.97	22.44	62	63	3.44	3.37	3.20	3.27	3.16	3.23	758	0.09	0.09	6.47	1.28	61	1.14	59
926B	49	2	97-99.5	484.01	22.51					3.32	3.33	3.40	3.41	711	0.04	0.05	2.56	1.89	43	1.16	107
926B	49	2	124-126.5	484.28	22.52	57	56	3.57	3.60	3.37	3.34	3.34	3.31	736	0.10	0.10	8.62	1.68	77	1.16	173
926B	49	3	126.5-130	485.81	22.58					3.23	3.22	3.36	3.36	877	0.13	0.13	5.45	1.39	67	1.14	171
926B	49	4	20-24	486.25	22.59					3.02	3.04	2.90	2.91	786	0.08	0.08	6.64	2.50	64	1.17	190
926B	49	5	63-65	488.16	22.66	53	52	3.03	3.08	2.84	2.80	2.82	2.78	641	0.08	0.08	8.38	1.60	50	1.19	105
926B	49	5	91-93.5	488.45	22.67	49	49	3.23	3.24	2.92	2.93	2.91	2.92	612	0.07	0.07	10.92	1.72	40	1.17	97
926B	49	5	147-149	489.00	22.7	62	61	3.80	3.83	3.38	3.35	3.35	3.32	770	0.07	0.07	15.37	1.87	67	1.17	333
926B	49	6	76.5-79	489.78	22.73	66	67	4.20	4.22	3.34	3.36	3.32	3.33	976	0.09	0.09	9.12	1.56	94	1.16	204
926B	49	cc	9-12	489.99	22.74	54	54	2.67	2.68	3.34	3.32	3.27	3.25	994	0.07	0.07	18.03	1.83	102	1.17	236
926B	50	1	65-69	491.86	22.81	53	53	2.43	2.44	3.34	3.34	3.31	3.31	1056	0.08	0.08	18.18	1.90	118	1.16	217
926B	50	1	70-73	492.11	22.82	60	60	3.31	3.30	3.23	3.23	3.16	3.16	903	0.10	0.10	3.52	2.39	107	1.17	71
926B	50	1	90-93	492.13						3.28	3.27	3.36	3.35	897	0.11	0.11	3.04	2.00	103	1.19	128
926B	50	1	94-99	492.20	22.82					3.28	3.27	3.36	3.35	897	0.11	0.11	3.04	2.00	103	1.19	128
926B	50	2	29-32	493.02	22.87	59	59	3.02	3.02	3.41	3.41	3.38	3.39	795	0.07	0.07	2.43	1.94	72	1.18	55
926B	50	2	66-68	493.37																	
926B	50	2	75-78	493.48																	
926B	50	2	78-80	493.49																	

Site	Core	Section	Interval (cm)	mcd (m)	Age (Ma)	B11/Ca43 (µmol/mol)	B11/Ca48 (µmol/mol)	Na23/Ca43 (mmol/mol)	Na23/Ca48 (mmol/mol)	Mg24/Ca43 (mmol/mol)	Mg24/Ca48 (mmol/mol)	Mg25/Ca43 (mmol/mol)	Mg25/Ca48 (mmol/mol)	Mn55/Ca43 (µmol/mol)	Cd111/Ca43 (µmol/mol)	Cd111/Ca48 (µmol/mol)	Ba138/Ca43 (µmol/mol)	Nd146/Ca43 (nmol/mol)	U238/Ca43 (nmol/mol)	Sr87/Ca43 (µmol/mol)	Al27/Ca43 (µmol/mol)
926B	50	2	117-121	493.90	22.9					3.41	3.38	3.47	3.43	781	0.07	0.07	3.08	1.80	58	1.12	92
926B	50	2	130-133	494.04																	
926B	50	3	17-20	495.29	22.94	57	58	3.37	3.35	3.22	3.24	3.23	3.24	870	0.07	0.07	3.57	2.06	63	1.17	96
926B	50	3	106-109	494.40																	
926B	50	3	147-150	495.70																	
926B	50	4	14-19	495.90	22.97					3.23	3.28	3.32	3.38	972	0.07	0.07	8.91	1.92	53	1.16	235
926B	50	4	125-130	497.01	23.01					3.21	3.24	3.06	3.09	852	0.11	0.11	8.53	1.82	77	1.21	243
926B	50	4	88-90	496.60	23.01	71	71	3.71	3.72	3.21	3.20	3.18	3.18	883	0.09	0.09	2.71	1.79	84	1.27	55
926B	50	4	134-137	497.07																	
926B	50	5	28-31	497.51																	
926B	50	6	10-16	498.87	23.08					3.67	3.68	3.79	3.80	832	0.08	0.08	5.93	2.51	106	1.24	255
926B	50	5	121-124	498.44	23.08	62	62	3.50	3.53	3.26	3.23	3.25	3.23	869	0.10	0.10	2.32	2.32	122	1.22	35
926B	50	6	16-19	498.89																	
926B	50	6	61-64	499.34																	
926B	50	6	106-109	499.42																	
926B	50	6	56-59	499.30	23.1					3.22	3.21	3.25	3.23	859	0.09	0.09	2.85	2.21	91	1.18	63
926B	51	1	12-16	500.97	23.16					3.78	3.75	3.89	3.86	963	0.10	0.10	2.66	2.56	82	1.24	49
926B	51	2	109-111.5	503.43	23.25					3.97	3.95	3.99	3.97	1106	0.10	0.10	4.29	2.66	88	1.14	59
926B	51	3	0-3	503.84	23.27	62	63	3.08	3.07	3.91	3.94	3.88	3.90	992	0.09	0.09	2.72	2.30	135	1.11	59
926B	51	3	121.5-124	505.05	23.31					3.72	3.71	3.73	3.72	1044	0.13	0.13	3.47	2.59	78	1.20	102
926B	51	4	64-69	506.00	23.34					3.50	3.52	3.54	3.57	1020	0.08	0.09	4.89	2.70	62	1.10	217
926B	51	6	120-122	509.51	23.58	53	53	2.78	2.79	3.54	3.53	3.36	3.35	1043	0.09	0.09	11.64	1.90	90	1.14	111
926B	51	6	130-134	509.65	23.58					3.56	3.61	3.62	3.67	935	0.07	0.08	6.95	1.82	65	1.13	272
926B	52	2	57.5-60	512.39	23.66	52	52	2.64	2.64	4.08	4.08	4.13	4.13	1063	0.08	0.08	8.61	2.50	82	1.15	130
926B	52	3	90-95	514.21	23.73	47	47	2.40	2.41	3.88	3.87	3.63	3.62	1039	0.09	0.09	15.90	2.17	63	1.13	53
926B	52	4	95-98	515.76	23.8	51	51	5.67	5.69	3.55	3.54	3.48	3.47	1129	0.11	0.11	10.42	2.73	70	1.15	84
926B	52	4	138-140	516.21	23.82	62	62	4.46	4.46	3.77	3.78	3.75	3.76	1085	0.11	0.11	13.87	3.09	150	1.12	220
926B	52	5	72-74	517.05	23.86	82	82	4.13	4.12	2.97	2.97	3.10	3.09	1013	0.13	0.13	9.47	2.26	73	1.24	265
926B	52	6	101-103	518.84	23.93	76	76	4.27	4.26	3.59	3.58	3.57	3.56	1038	0.10	0.10	16.12	2.04	71	1.14	215
926B	53	1	10-12	520.13	23.98	81	81	4.26	4.27	3.44	3.45	3.63	3.65	945	0.16	0.16	4.95	2.79	90	1.27	134
926B	53	2	39.5-41.5	521.93	24.02	58	58	3.63	3.64	3.83	3.84	4.03	4.04	1004	0.09	0.09	7.01	1.94	185	1.12	242

Site	Core	Section	Interval	mcd	Age	B11/ Ca43 (µmol/ mol)	B11/ Ca48 (µmol/ mol)	Na23/ Ca43 (mmol/ mol)	Na23/ Ca48 (mmol/ mol)	Mg24/ Ca43 (mmol/ mol)	Mg24/ Ca48 (mmol/ mol)	Mg25/ Ca43 (mmol/ mol)	Mg25/ Ca48((mmol/ mol)	Mn55/ Ca43 (µmol/ mol)	Cd111/ Ca43 (µmol/ mol)	Cd111/ Ca48 (µmol/ mol)	Ba138/ Ca43 (µmol/ mol)	Nd146/ Ca43 (µmol/ mol)	U238/ Ca43 (nmol/ mol)	Sr87/ Ca43 (mmol/ mol)	Al27/ Ca43((µmol/ mol)	
			(cm)	(m)	(Ma)																	
G. praebulloides (250-300 µm)																						
1406B	6	5	122-124	51.49	21.66	53	53	4.35	4.37	4.14	4.12	4.11	4.10	969	0.08	0.08	2.05	0.91	15.50	1.29	5	
1406A	6	3	132-134	55.29	21.86	68	67	5.40	5.47	3.73	3.69	3.72	3.67	924	0.10	0.10	2.10	0.92	30.34	1.31	35	
1406A	6	4	44-46	55.91	21.89	42	42	12.73	12.74	3.95	3.95	3.87	3.87	907	0.07	0.07	2.06	0.84	22.04	1.24	78	
1406A	6	5	72-74	57.69	21.96	57	56	4.74	4.72	3.78	3.76	3.76	3.74	1406	0.20	0.20	2.01	0.82	49.10	1.30	12	
1406A	6	6	2-4	58.49	21.99	48	48	7.70	7.67	3.83	3.84	3.89	3.91	823	0.13	0.13	2.77	1.43	29.08	1.30	5	
1406A	7	5	46-48	67.53	22.26	52	52	5.14	5.19	3.93	3.90	3.93	3.90	1087	0.09	0.09	2.33	1.13	28.02	1.31	22	
1406A	7	5	132-134	68.39	22.28					3.88	3.86	4.06	4.05	1201	0.07	0.07	2.43	0.95	25.50	1.27	14	
1406C	7	3	12-14	68.57	22.29	47	47	4.40	4.39	4.55	4.57	4.54	4.56	1419	0.09	0.09	2.03	1.07	37.75	1.29	23	
1406C	7	4	44-46	70.39	22.34	58	58	5.64	5.66	4.49	4.47	4.50	4.48	1305	0.08	0.08	3.01	1.59	22.90	1.32	16	
1406C	7	4	104-106	70.99	22.35	55	54	4.52	4.55	4.44	4.41	4.46	4.43	1391	0.10	0.10	2.69	1.97	42.42	1.30	23	
1406C	7	4	118-120	71.13	22.36	53	52	6.00	6.08	4.79	4.72	4.76	4.69	1445	0.14	0.14	2.83	1.18	35.92	1.31	16	
1406A	8	5	72-74	77.29	22.55	52	52	8.36	8.31	4.22	4.24	4.22	4.24	1137	0.14	0.14	2.44	0.79	37.04	1.31	22	
1406B	9	4	14-16	79.88	22.65					3.71	3.75	3.85	3.88	1114	0.07	0.07	1.98	0.86	39.90	1.31	6	
1406B	9	4	44-46	80.18	22.66					4.09	4.09	3.91	3.91	1317	0.10	0.10	3.20	1.26	46.76	1.31	9	
1406B	9	4	104-106	80.78	22.68	51	51	4.27	4.29	3.85	3.86	3.82	3.83	1035	0.06	0.07	1.89	1.21	42.37	1.32	8	
1406B	9	5	74-76	81.99	22.74	55	55	8.26	8.23	3.97	3.99	3.81	3.82	988	0.05	0.05	2.14	1.07	31.80	1.31	4	
1406C	9	3	72-74	87.84	23.01	43	43	6.60	6.63	3.69	3.71	3.91	3.93	931	0.09	0.09	3.26	2.05	24.26	1.35	41	
1406C	9	3	98-100	88.10	23.02					3.49	3.52	3.63	3.66	1329	0.11	0.11	6.35	2.18	28.12	1.34	22	
1406C	9	4	44-46	89.06	23.08	66	66	5.67	5.66	4.29	4.30	4.28	4.28	2333	0.10	0.10	3.28	1.78	61.50	1.33	38	
1406C	9	4	70-72	89.32	23.09					4.26	4.27	4.26	4.28	2230	0.13	0.13	4.32	2.09	59.05	1.35	24	
1406C	9	4	104-106	89.66	23.11					4.39	4.46	4.39	4.46	2247	0.41	0.41	2.94	2.29	208.90	1.34	11	
1406A	10	5	12-14	96.29	23.50	51	51	5.18	5.20	3.53	3.51	3.52	3.50	1334	0.08	0.08	3.59	0.88	18.82	1.36	9	
1406A	10	5	42-44	96.59	23.52					4.35	4.38	4.19	4.22	1537	0.09	0.09	4.04	1.26	17.70	1.36	7	

Site	Core	Section	Interval	mcd	Age	B11/ Ca43 (µmol/ mol)	B11/ Ca48 (µmol/ mol)	Na23/ Ca43 (mmol/ mol)	Na23/ Ca48 (mmol/ mol)	Mg24/ Ca43 (mmol/ mol)	Mg24/ Ca48 (mmol/ mol)	Mg25/ Ca43 (mmol/ mol)	Mg25/ Ca48 (mmol/ mol)	Al27/ Ca43 (µmol/ mol)	Al27/ Ca48 (µmol/ mol)	Mn55/ Ca43 (mmol/ mol)	Mn55/ Ca48 (mmol/ mol)	Sr86/ Ca43 (µmol/ mol)	Sr86/ Ca48 (µmol/ mol)	Sr87/ Ca43 (mmol/ mol)	Sr87/ Ca48 (µmol/ mol)	Cd111/ Ca43 (µmol/ mol)	Cd111/ Ca48 (µmol/ mol)	Ba138/ Ca43 (µmol/ mol)	Ba138 /Ca43 (µmol/ mol)	Ba138/ Ca48 (µmol/ mol)	Nd146/ Ca43 (µmol/ mol)	Nd146/ Ca48 (µmol/ mol)	U238/ Ca43 (nmol/ mol)
			(cm)	(m)	(Ma)																								
G.trilobus (300-350 µm)																													
872C	13	4	20-22	110	22.22	87	86.54	5.15	5.17	4.49	4.48	4.42	4.41	23.66	23.61	22.67	22.61	1.15	1.15	1.16	1.15	0.665	0.663	1.21	1.21	1.84	1.83	30.05	
872C	13	6	20-22	112.64	23.22	97	97.02	5.46	5.44	4.89	4.91	4.88	4.89	13.13	13.18	13.15	13.19	1.12	1.12	1.12	1.13	0.755	0.758	1.35	1.36	1.46	1.46	55.91	
872C	14	1	20-22	115.7	23.36	64	63.82	5.51	5.53	4.07	4.06	4.04	4.03	20.72	20.67	15.01	14.97	1.1	1.1	1.1	1.1	0.638	0.636	1.75	1.74	1.32	1.32	34.91	
872C	14	1	78-80	116.28																									

List of References

Abe-Ouchi, A., Saito, F., Kawamura, K., Raymo, M., Okuno, J., Takahashi, K., and Blatter, H., 2013, Insolation-driven 100,000-year glacial cycles and hysteresis of ice-sheet volume: Nature, v. 500, no. 7461, p. 190-193.

Acton, G., Crampton, J., Di Vincenzo, G., Fielding, C. R., Florindo, F., Hannah, M., Harwood, D., Ishman, S., Johnson, K., Jovane, L., Levy, R., Lum, B., Marcano, M. C., Mukasa, S., Ohneiser, C., Olney, M. P., Riesselman, C., Sagnotti, L., Stefano, C., Strada, E., Taviani, M., Tuzzi, E., Verosub, K. L., Wilson, G. S., Zattin, M., and Team, A.-S. S., 2008-2009, Preliminary Integrated Chronostratigraphy of the AND-2A Core, ANDRILL Southern McMurdo Sound Project, Antarctica: Terra Antarctica, v. 15, no. 1, p. 211-220.

Al-Ammar, A. S., Gupta, R. K., and Barnes, R. M., 2000, Elimination of boron memory effect in inductively coupled plasma-mass spectrometry by ammonia gas injection into the spray chamber during analysis: Spectrochimica Acta Part B-Atomic Spectroscopy, v. 55, no. 6, p. 629-635.

Al-Rousan, S., Pätzold, J., Al-Moghrabi, S., and Wefer, G., 2004, Invasion of anthropogenic CO_2 recorded in planktonic foraminifera from the northern Gulf of Aqaba: International Journal of Earth Sciences, v. 93, no. 6, p. 1066-1076.

Allen, K.A., and Honisch, B., 2012, The planktic foraminiferal B/Ca proxy for seawater carbonate chemistry: A critical evaluation: Earth and Planetary Science Letters, v. 345, p. 203-211.

Allen, K.A., Honisch, B., Eggins, S., and Rosenthal, Y., 2012, Environmental controls on B/Ca in calcite tests of the tropical planktic foraminifer species Globigerinoides ruber and Globigerinoides sacculifer: Earth and Planetary Science Letters, v. 351, p. 270-280.

Allen, K. A., Honisch, B., Eggins, S. M., Yu, J. M., Spero, H. J., and Elderfield, H., 2011, Controls on boron incorporation in cultured tests of the planktic foraminifer Orbulina universa: Earth and Planetary Science Letters, v. 309, no. 3-4, p. 291-301.

Anand, P., Elderfield, H., and Conte, M. H., 2003, Calibration of Mg/Ca thermometry in planktonic foraminifera from a sediment trap time series: Paleoceanography, v. 18, no. 2, p. doi 10.1029/2002kpa000846.

Armstrong McKay, D. I., Tyrrell, T., Wilson, P. A., and Foster, G. L., 2014, Estimating the impact of the cryptic degassing of Large Igneous Provinces: A mid-Miocene case-study: Earth and Planetary Science Letters, v. 403, no. 0, p. 254-262.

Badger, M. P. S., Lear, C. H., Pancost, R. D., Foster, G. L., Bailey, T. R., Leng, M. J., and Abels, H. A., 2013, CO_2 drawdown following the middle Miocene expansion of the Antarctic Ice Sheet: Paleoceanography, v. 28, no. 1, p. 42-53.

Bailey, I., Hole, G. M., Foster, G. L., Wilson, P. A., Storey, C. D., Trueman, C. N., and Raymo, M. E., 2013, An alternative suggestion for the Pliocene onset of major northern hemisphere glaciation based on the geochemical provenance of North Atlantic Ocean ice-rafted debris: Quaternary Science Reviews, v. 75, no. 0, p. 181-194.

Bamber, J. L., Griggs, J. A., Hurkmans, R. T. W. L., Dowdeswell, J. A., Gogineni, S. P., Howat, I., Mouginot, J., Paden, J., Palmer, S., Rignot, E., and Steinhage, D., 2013, A new bed elevation dataset for Greenland: The Cryosphere, v. 7, no. 2, p. 499-510.

Bamber, J. L., Riva, R. E. M., Vermeersen, B. L. A., and LeBrocq, A. M., 2009, Reassessment of the Potential Sea-Level Rise from a Collapse of the West Antarctic Ice Sheet: Science, v. 324, no. 5929, p. 901-903.

Barker, S., Greaves, M., and Elderfield, H., 2003, A study of cleaning procedures used for foraminiferal Mg/Ca paleothermometry: Geochemistry Geophysics Geosystems, v. 4, DOI: 10.1029/2003GC000559

Barrett, J., 2007, Cenozoic climate and sea level history from glacimarine strata off the Victoria Land Coast, Cape Roberts Project, Antarctica: In: M. J. Hambrey, P. Christoffersen, N. F. Glasser, & B. Hubbart (Eds). Glacial Processes and Products, International Association of Sedimentologists Special Publication, v. 39, p. 259-287.

Barrett, P., 2008, Chapter 3 A History of Antarctic Cenozoic Glaciation - View from the Margin, *in* Fabio, F., and Martin, S., eds., Developments in Earth and Environmental Sciences, Volume Volume 8, Elsevier, p. 33-83.

Bart, P. J., 2003, Were West Antarctic Ice Sheet grounding events in the Ross Sea a consequence of East Antarctic Ice Sheet expansion during the middle Miocene?: Earth and Planetary Science Letters, v. 216, no. 1-2, p. 93-107.

Beerling, D. J., and Royer, D. L., 2002, Reading a CO_2 signal from fossil stomata: New Phytologist, v. 153, no. 3, p. 387-397.

Beerling, D. J., and Royer, D. L., 2011, Convergent Cenozoic CO_2 history: Nature Geoscience, v. 4, no. 7, p. 418-420.

Ben-Yaakov, S., and Goldhaber, M. B., 1973, The influence of sea water composition on the apparent constants of the carbonate system: Deep Sea Research and Oceanographic Abstracts, v. 20, no. 1, p. 87-99.

Berger, W. H., Killingley, J. S., and Vincent, E., 1978, Stable isotopes in deep- sea carbonates: Box core ERDC-92, west equatorial Pacific: Oceanologica Acta, v. 1, p. 203–216.

Berner, R. A., and Kothavala, Z., 2001, GEOCARB III: A revised model of atmospheric CO_2 over phanerozoic time: American Journal of Science, v. 301, no. 2, p. 182-204.

Bidigare, R. R., Fluegge, A., Freeman, K. H., Hanson, K. L., Hayes, J. M., Hollander, D., Jasper, J. P., King, L. L., Laws, E. A., Milder, J., Millero, F. J., Pancost, R., Popp, B. N., Steinberg, P. A., and Wakeham, S. G., 1997, Consistent fractionation of $\delta^{13}C$ in nature and in the laboratory: Growth-rate effects in some haptophyte algae: Global Biogeochemical Cycles, v. 11, no. 2, p. 279-292.

Billups, K., Channell, J. E. T., and Zachos, J., 2002, Late Oligocene to early Miocene geochronology and paleoceanography from the subantarctic South Atlantic: Paleoceanography, v. 17, no. 1, p. 4-1-4-11.

Billups, K., and Schrag, D. P., 2002, Paleotemperatures and ice volume of the past 27 Myr revisited with paired Mg/Ca and $^{18}O/^{16}O$ measurements on benthic foraminifera: Paleoceanography, v. 17, no. 1, p. 3-1-3-11.

Birch, H., Coxall, H. K., Pearson, P. N., Kroon, D., and O'Regan, M., 2013, Planktonic foraminifera stable isotopes and water column structure: Disentangling ecological signals: Marine Micropaleontology, v. 101, p. 127-145.

Blow, W. H., and Banner, F. T., 1962, The Mid-Tertiary (Upper Eocene to Aquitanian) Globigerinaceae, *in* Eames, F. E., Banner, F. T., W.H., B., and Clarke, W. J., eds., Fundamentals of Mid-Tertiary Stratigraphical Correlation: London, Cambridge University Press.

Bohaty, S. M., Zachos, J. C., and Delaney, M. L., 2012, Foraminiferal Mg/Ca evidence for Southern Ocean cooling across the Eocene–Oligocene transition: Earth and Planetary Science Letters, v. 317–318, no. 0, p. 251-261.

Bolton, C. T., and Stoll, H. M., 2013, Late Miocene threshold response of marine algae to carbon dioxide limitation: Nature, v. 500, no. 7464, p. 558-562.

Bornemann, A., and Norris, R. D., 2007, Size-related stable isotope changes in Late Cretaceous planktic foraminifera: Implications for paleoecology and photosymbiosis: Marine Micropaleontology, v. 65, no. 1-2, p. 32-42.

Bostock, H., Hayward, B., Neil, H., Currie, K., and Dunbar, G., 2011, Deep-water carbonate concentrations in the southwest Pacific: Deep-Sea Research Part I-Oceanographic Research Papers, v. 58, no. 1, p. 72-85.

Brading, P., Warner, M., Davey, P., Smith, D., Achterberg, E., and Suggett, D., 2011, Differential effects of ocean acidification on growth and photosynthesis among phylotypes of Symbiodinium (Dinophyceae): Limnology and Oceanography, v. 56, no. 3, p. 927-938.

Bowen, G. J., and Beerling, D. J., 2004, An integrated model for soil organic carbon and CO_2: Implications for paleosol carbonate pCO_2 paleobarometry: Global Biogeochemical Cycles, v. 18, no. 1, p. GB1026.

Catanzaro, E. J., Champion, C., Garner, E., Marinenko, G., Sappenfield, K., and Shields, W., 1970, Boric acid: isotopic and assay standard reference materials.: Number 260-17 in NBS (US) Special Publications. National Bureau of Standards, Institute for Materials Research, Washington D.C.

Cerling, T. E., 1991, Carbon dioxide in the atmosphere; evidence from Cenozoic and Mesozoic Paleosols: American Journal of Science, v. 291, no. 4, p. 377-400.

Cerling, T. E., Harris, J. M., MacFadden, B. J., Leakey, M. G., Quade, J., Eisenmann, V., and Ehleringer, J. R., 1997, Global vegetation change through the Miocene/Pliocene boundary: Nature, v. 389, no. 6647, p. 153-158.

Chalk, T. B., Foster, G. L., Cherry, S. G., Badger, M. P. S., Sexton, P. F., Pancost, R. D., Rohling, E. J., Pälike, H., and Wilson, P. A., in prep., Multiple drivers of the Mid Pleistocene Transition.

Chen, J., Farrell, J. W., Murray, D. W., and Prell, W. L., 1995, Timescale and paleoceanographic implications of a 3.6 m.y. oxygen isotope record from the northeast Indian Ocean (Ocean Drilling Program Site 758): Paleoceanography, v. 10, no. 1, p. 21-47.

Chow, J. M., and Bart, P. J., 2003, West Antarctic ice sheet grounding events on the Ross Sea outer continental shelf during the middle Miocene: Palaeogeography Palaeoclimatology Palaeoecology, v. 198, no. 1-2, p. 169-186.

Cifelli, R., 1982, Textural observations on some living species of Planktonic Foraminifera: Smithsonian Contributions to Paleobiology, v. 45, p. 1-45.

Conrad, C. P., 2013, The solid Earth's influence on sea level: Geological Society of America Bulletin, v. 125, no. 7-8, p. 1027-1052.

Cook, C. P., Van de Flierdt, T., Williams, T., Hemming, S. R., Iwai, M., Kobayashi, M., Jimenez-Espejo, F. J., Escutia, C., Gonzalez, J. J., Khim, B.K., McKay, R.M., Passchier, S., Bohaty, S.M., Riesselman, C.R., Tauxe, L., Sugisaki, S., Galindo, A.L., Patterson, M.O., Sangiorgi, F., Pierce, E.L., Brinkhuis, H., and IODP Expedition 318 Scientists, 2013, Dynamic behaviour of the East Antarctic ice sheet during Pliocene warmth: Nature Geoscience, v. 6, no. 9, p. 765-769.

Coxall, H. K., Wilson, P. A., Palike, H., Lear, C. H., and Backman, J., 2005, Rapid stepwise onset of Antarctic glaciation and deeper calcite compensation in the Pacific Ocean: Nature, v. 433, no. 7021, p. 53-57.

Cramer, B., Miller, K., Barrett, P., and Wright, J., 2011, Late Cretaceous-Neogene trends in deep ocean temperature and continental ice volume: Reconciling records of benthic foraminiferal geochemistry ($\delta^{18}O$ and Mg/Ca) with sea level history: Journal of Geophysical Research-Oceans, v. 116, DOI: 10.1029/2011JC007255

Darling, K. F., Kucera, M., Wade, C. M., von Langen, P., and Pak, D., 2003, Seasonal distribution of genetic types of planktonic foraminifer morphospecies in the Santa Barbara Channel and its paleoceanographic implications: Paleoceanography, v. 18, no. 2, DOI: 10.1029/2001PA000723.

De Boer, B., Van De Wal, R. S. W., Bintanja, Lourens, L. J., and Tuenter, E., 2010, Cenozoic global ice-volume and temperature simulations with 1-D ice-sheet models forced by benthic $\delta^{18}O$ records: Annals of Glaciology, v. 51, p. 23-33.

DeConto, R. M., and Pollard, D., 2003a, A coupled climate-ice sheet modeling approach to the Early Cenozoic history of the Antarctic ice sheet: Palaeogeography Palaeoclimatology Palaeoecology, v. 198, no. 1-2, p. 39-52.

DeConto, R. M., and Pollard, D, 2003b, Rapid Cenozoic glaciation of Antarctica induced by declining atmospheric CO_2: Nature, v. 421, no. 6920, p. 245-249.

DeConto, R. M., Pollard, D., Wilson, P. A., Palike, H., Lear, C. H., and Pagani, M., 2008, Thresholds for Cenozoic bipolar glaciation: Nature, v. 455, no. 7213, p. 652-U652.

Delany, M. L., Be, A. W. H., and Boyle, E. A., 1985, Li, Sr, Mg and Na in foraminiferal calcite shells from laboratory culture, sediment traps, and sediment cores: Geochimica et Cosmochimica Acta, v. 49, no. 6, p. 1327-1341.

Demicco, R. V., Lowenstein, T. K., and Hardie, L. A., 2003, Atmospheric pCO_2 since 60 Ma from records of seawater pH, calcium, and primary carbonate mineralogy: Geology, v. 31, no. 9, p. 793-796.

Deyhle, A., and Kopf, A., 2004, Possible influence of clay contamination on B isotope geochemistry of carbonaceous samples: Applied Geochemistry, v. 19, no. 5, p. 737-745.

Dickson, A. G., 1990, Thermodynamics of the dissociation of boric acid in synthetic seawater from 273.15 to 318.15 K: Deep Sea Research Part A. Oceanographic Research Papers, v. 37, no. 5, p. 755-766.

Edgar, K. M., Anagnostou, E., Pearson, P. N., and Foster, G. L., in review, Assessing the impact of diagenesis on $\delta^{11}B$, $\delta^{13}C$, $\delta^{18}O$, Sr/Ca and B/Ca values in fossil planktic foraminiferal calcite: Geochimica et Cosmochimica Acta.

Edgar, K. M., Bohaty, S. M., Gibbs, S. J., Sexton, P. F., Norris, R. D., and Wilson, P. A., 2012, Symbiont 'bleaching' in planktic foraminifera during the Middle Eocene Climatic Optimum: Geology. v. 41, no.1, p. 15–18.

Ehleringer, J. R., Cerling, T. E., and Helliker, B. R., 1997, C4 photosynthesis, atmospheric CO_2, and climate: Oecologia, v. 112, no. 3, p. 285-299.

Ehrmann, W., 1998, Implications of late Eocene to early Miocene clay mineral assemblages in McMurdo Sound (Ross Sea, Antarctica) on paleoclimate and ice dynamics: Palaeogeography Palaeoclimatology Palaeoecology, v. 139, no. 3-4, p. 213-231.

Elderfield, H., Vautravers, M., and Cooper, M., 2002, The relationship between shell size and Mg/Ca, Sr/Ca, $\delta^{18}O$, and $\delta^{13}C$ of species of planktonic foraminifera: Geochemistry, Geophysics, Geosystems, v. 3, no. 8, p. 1-13.

Elderfield, H., Yu, J., Anand, P., Kiefer, T., and Nyland, B., 2006, Calibrations for benthic foraminiferal Mg/Ca paleothermometry and the carbonate ion hypothesis: Earth and Planetary Science Letters, v. 250, no. 3-4, p. 633-649.

Eldrett, J. S., Harding, I. C., Wilson, P. A., Butler, E., and Roberts, A. P., 2007, Continental ice in Greenland during the Eocene and Oligocene: Nature, v. 446, no. 7132, p. 176-179.

Ennyu, A., and Arthur, M. A., 2004, Early to Middle Miocene Paleoceanography in the Southern High Latitudes Off Tasmania: The Cenozoic Southern Ocean: Tectonics, Sedimentation, and Climate Change Between Australia and Antarctica Geophysical Monograph Series 151, American Geophysical Union., p. 215-233.

Evans, D., and Muller, W., 2012, Deep time foraminifera Mg/Ca paleothermometry: Nonlinear correction for secular change in seawater Mg/Ca: Paleoceanography, v. 27, no. 4, DOI: 10.1029/2012PA002315

Expedition 342 Scientists, 2012, Integrated Ocean Drilling Program Expedition 342 Preliminary Report: Paleogene Newfoundland Sediment Drifts, *in* doi:10.2204/iodp.pr.342.2012, ed., Integrated Ocean Drilling Program Management International, Inc., for the Integrated Ocean Drilling Program

Ezard, T. H. G., Edgar, K. M., and Hull, P. M., 2015, Environmental and biological controls on size specific $\delta^{13}C$ and $\delta^{18}O$ in recent planktonic foraminifera, Paleoceanography, DOI: 10.1002/2014PA002735

Farrell, W. E., and Clark, J. A., 1976, Postglacial Sea-Level: Geophysical Journal of the Royal Astronomical Society, v. 46, no. 3, p. 647-667.

Feakins, S. J., Warny, S., and Lee, J.-E., 2012, Hydrologic cycling over Antarctica during the middle Miocene warming: Nature Geoscience, v. 5, no. 8, p. 557-560.

Fielding, C. R., Browne, G. H., Field, B., Florindo, F., Harwood, D. M., Krissek, L. A., Levy, R. H., Panter, K. S., Passchier, S., and Pekar, S. F., 2011, Sequence stratigraphy of the ANDRILL AND-2A drillcore, Antarctica: A long-term, ice-proximal record of Early to Mid-Miocene climate, sea-level and glacial dynamism: Palaeogeography Palaeoclimatology Palaeoecology, v. 305, no. 1-4, p. 337-351.

Flower, B. P., and Kennett, J. P., 1994, The middle Miocene climatic transition: East Antarctic ice sheet development, deep ocean circulation and global carbon cycling: Palaeogeography, Palaeoclimatology, Palaeoecology, v. 108, no. 3-4, p. 537-555.

Flower, B. P., Zachos, J. Z., and Martin, Z., 1997, Latest Oligocene through early Miocene isotopic stratigraphy and deep water paleoceanography of thje western equatorial Atlantic: Sites 926 and 929.: Shackleton, N.J., Curry, W.B., Richter, C., and Bralower, T.J. (Eds.), in Proceedings of the Ocean Drilling Program, Scientific Results, Vol. 154.

Foster, G. L., Honisch, B., Paris, G., Dwyer, G., Rae, J., Elliott, T., Gaillardet, J., Hemming, N., Louvat, P., and Vengosh, A., 2013, Interlaboratory comparison of boron isotope analyses of boric acid, seawater and marine $CaCO_3$ by MC-ICPMS and NTIMS: Chemical Geology, v. 358, p. 1-14.

Foster, G. L., Lear, C. H., and Rae, J., 2012, The evolution of pCO_2, ice volume and climate during the middle Miocene: Earth and Planetary Science Letters, v. 341-344, p. 243-254.

Foster, G. L., 2008, Seawater pH, pCO_2 and $[CO_3^{2-}]$ variations in the Caribbean Sea over the last 130 kyr: A boron isotope and B/Ca study of planktic forminifera: Earth and Planetary Science Letters, v. 271, no. 1-4, p. 254-266.

Foster, G. L., Ni, Y. Y., Haley, B., and Elliott, T., 2006, Accurate and precise isotopic measurement of sub-nanogram sized samples of foraminiferal hosted boron by total evaporation NTIMS: Chemical Geology, v. 230, no. 1-2, p. 161-174.

Foster, G. L., Pogge von Strandmann, P. A. E., and Rae, J. W. B., 2010a, Boron and magnesium isotopic composition of seawater: Geochemistry Geophysics Geosystems, v. 11, no. 8, p. Q08015, doi 08010.01029/02010GC003201

Foster, G. L., Rae, J., and Elliott, T., 2008, Boron isotope measurements of marine carbonate using MC-ICPMS: Geochimica et Cosmochimica Acta, v. 72, no. 12, p. A279-A279.

Foster, G. L., and Rohling, E. J., 2013, Relationship between sea level and climate forcing by CO_2 on geological timescales: Proceedings of the National Academy of Sciences of the United States of America, v. 110, no. 4, p. 1209-1214.

Friedrich, O., Schiebel, R., Wilson, P. A., Weldeab, S., Beer, C. J., Cooper, M. J., and Fiebig, J., 2012, Influence of test size, water depth, and ecology on Mg/Ca, Sr/Ca, $\delta^{18}O$ and $\delta^{13}C$ in nine modern species of planktic foraminifers: Earth and Planetary Science Letters, v. 319, p. 133-145.

Gasperi, J., and Kennett, J. P., 1992, Isotopic Evidence for Depth Stratification and Paleoecology of Miocene Planktonic Foraminifera: Western Equatorial Pacific DSDP Site 289: In: Tsuchi, R., and J.C. Ingle, eds., IGCP-246 Pacific Neogene: Environment, Evolution and Events, University of Tokyo Press, v. 117-147.

Gasson, E., Lunt, D. J., DeConto, R., Goldner, A., Heinemann, M., Huber, M., LeGrande, A. N., Pollard, D., Sagoo, N., Siddall, M., Winguth, A., and Valdes, P. J., 2014, Uncertainties in the modelled CO_2 threshold for Antarctic glaciation: Climate of the Past, v. 10, no. 2, p. 451-466.

Gasson, E., Siddall, M., Lunt, D. J., Rackham, O. J. L., Lear, C. H., and Pollard, D., 2012, Exploring Uncertainties in the Relationship between Temperature, Ice Volume, and Sea Level over the Past 50 Million Years: Reviews of Geophysics, v. 50, no. 1, DOI: 10.1029/2011RG000358

Gradstein, F. M., Ogg, J. G., and Schmitz, M., 2012, The Geologic Time Scale 2012, Amsterdam, Elsevier.

Grant, K. M., and Dickens, G. R., 2002, Coupled productivity and carbon isotope records in the southwest Pacific Ocean during the late Miocene-early Pliocene biogenic bloom: Palaeogeography Palaeoclimatology Palaeoecology, v. 187, no. 1-2, p. 61-82.

Greenop, R., Foster, G. L., Wilson, P. A., and Lear, C. H., 2014, Middle Miocene climate instability associated with high-amplitude CO_2 variability: Paleoceanography, v. 29, no. 9, p. 2014PA002653.

Griffith, E., Paytan, A., Caldeira, K., Bullen, T., and Thomas, E., 2008, A Dynamic Marine Calcium Cycle During the Past 28 Million Years: Science, v. 322, no. 5908, p. 1671-1674.

Hain, M., Sigman, D., and Haug, G., 2010, Carbon dioxide effects of Antarctic stratification, North Atlantic Intermediate Water formation, and subantarctic nutrient drawdown during the last ice age: Diagnosis and synthesis in a geochemical box model: Global Biogeochemical Cycles, v. 24, no. 4, DOI: 10.1029/2010GB003790

Hansen, J., Sato, M., Russell, G., and Kharecha, P., 2013, Climate sensitivity, sea level and atmospheric carbon dioxide: Philosophical Transactions of the Royal Society A: Mathematical, Physical and Engineering Sciences, v. 371, no. 2001, DOI: 10.1098/rsta.2012.0294

Hasiuk, F., and Lohmann, K., 2010, Application of calcite Mg partitioning functions to the reconstruction of paleocean Mg/Ca: Geochimica et Cosmochimica Acta, v. 74, no. 23, p. 6751-6763.

Hathorne, E. C., and James, R. H., 2006, Temporal record of lithium in seawater: A tracer for silicate weathering?: Earth and Planetary Science Letters, v. 246, no. 3–4, p. 393-406.

Haug, G. H., and Tiedemann, R., 1998, Effect of the formation of the Isthmus of Panama on Atlantic Ocean thermohaline circulation: Nature, v. 393, no. 6686, p. 673-676.

Hays, J. D., Imbrie, J., and Shackleton, N. J., 1976, Variations in the Earth's Orbit: Pacemaker of the Ice Ages: Science, v. 194, no. 4270, p. 1121-1132.

Hemleben, C., Spindler, M., and Anderson, O. R., 1989, Modern Planktonic Foraminifera, New York, Springer-Verlag.

Hemming, N. G., and Hanson, G. N., 1992, Boron isotopic composition and concentration in modern marine carbonates: Geochimica et Cosmochimica Acta, v. 56, no. 1, p. 537-543.

Hemming, N. G., and Hanson, G. N., 1994, A Procedure for the Isotopic Analysis of Boron by Negative Thermal Ionization Mass-Spectrometry: Chemical Geology, v. 114, no. 1-2, p. 147-156.

Henderiks, J., and Pagani, M., 2007, Refining ancient carbon dioxide estimates: Significance of coccolithophore cell size for alkenone-based pCO_2 records: Paleoceanography, v. 22, no. 3, DOI: 10.1029/2006PA001399.

Henehan, M. J., 2013, Ground-truthing the Boron-based Proxies [PhD thesis]: University of Southampton.

Henehan, M. J., Foster, G. L., Rae, J. W. B., Prentice, K. C., Erez, J., Bostock, H. C., Marshall, B. J., and Wilson, P. A., in review, Testing the utility of B/Ca ratios in planktic foraminifera as a proxy for the carbonate system: A case study in *Globigerinoides ruber*.: Geochemistry, Geophysics, Geosystems.

Henehan, M. J., Rae, J. W. B., Foster, G. L., Erez, J., Prentice, K. C., Kucera, M., Bostock, H. C., Martìnez-Botì, M. A., Milton, J. A., Wilson, P. A., Marshall, B. J., and Elliott, T., 2013, Calibration of the boron isotope proxy in the planktonic foraminifera Globigerinoides ruber for use in palaeo-CO_2 reconstruction: Earth and Planetary Science Letters, v. 364, no. 0, p. 111-122.

Herold, N., Huber, M., and Müller, R. D., 2011, Modeling the Miocene Climatic Optimum. Part I: Land and Atmosphere: Journal of Climate, v. 24, no. 24, p. 6353-6372.

Hill, D., Haywood, A., Valdes, P., Francis, J., Lunt, D., Wade, B., and Bowman, V., 2013, Paleogeographic controls on the onset of the Antarctic circumpolar current: Geophysical Research Letters, v. 40, no. 19, p. 5199-5204.

Hindshaw, R. S., Bourdon, B., Pogge von Strandmann, P. A. E., Vigier, N., and Burton, K. W., 2013, The stable calcium isotopic composition of rivers draining basaltic catchments in Iceland: Earth and Planetary Science Letters, v. 374, no. 0, p. 173-184.

Holbourn, A., Kuhnt, W., Lyle, M., Schneider, L., Romero, O., and Andersen, N., 2014, Middle Miocene climate cooling linked to intensification of eastern equatorial Pacific upwelling: Geology, DOI: 10.1130/G34890.34891.

Holbourn, A., Kuhnt, W., Schulz, M., and Erlenkeuser, H., 2005, Impacts of orbital forcing and atmospheric carbon dioxide on Miocene ice-sheet expansion: Nature, vol. 438, no. 7067, p. 483-487.

Holbourn, A., Kuhnt, W., Schulz, M., Flores, J., and Andersen, N., 2007, Orbitally-paced climate evolution during the middle Miocene "Monterey" carbon-isotope excursion: Earth and Planetary Science Letters, v. 261, no. 3-4 p. 534-550.

Holbourn, A., Kuhnt, W., Simo, J., and Li, Q., 2004, Middle miocene isotope stratigraphy and paleoceanographic evolution of the northwest and southwest Australian margins (Wombat Plateau and Great Australian Bight): Palaeogeography Palaeoclimatology Palaeoecology, v. 208, no. 1-2, p. 1-22.

Honisch, B., Allen, K., Lea, D., Spero, H., Eggins, S., Arbuszewski, J., deMenocal, P., Rosenthal, Y., Russell, A., and Elderfield, H., 2013, The influence of salinity on Mg/Ca in planktic foraminifers - Evidence from cultures, core-top sediments and complementary delta $\delta^{18}O$: Geochimica et Cosmochimica Acta, v. 121, p. 196-213.

Hönisch, B., Bickert, T., and Hemming, N. G., 2008, Modern and Pleistocene boron isotope composition of the benthic foraminifer Cibicidoides wuellerstorfi: Earth and Planetary Science Letters, v. 272, no. 1-2, p. 309-318.

Hönisch, B., and Hemming, N. G., 2005, Surface ocean pH response to variations in pCO_2 through two full glacial cycles: Earth and Planetary Science Letters, v. 236, no. 1-2, p. 305-314.

Hönisch, B., Bijma, J., Russell, A. D., Spero, H. J., Palmer, M. R., Zeebe, R. E., and Eisenhauer, A., 2003, The influence of symbiont photosynthesis on the boron isotopic composition of foraminifera shells: Marine Micropaleontology, v. 49, no. 1-2, p. 87-96.

Hönisch, B., Hemming, N. G., Archer, D., Siddall, M., and McManus, J. F., 2009, Atmospheric Carbon Dioxide Concentration Across the Mid-Pleistocene Transition: Science, v. 324, no. 5934, p. 1551-1554.

Hönisch, B., Hemming, N. G., Grottoli, A. G., Amat, A., Hanson, G. N., and Buma, J., 2004, Assessing scleractinian corals as recorders for paleo-pH: Empirical calibration and vital effects: Geochimica et Cosmochimica Acta, v. 68, no. 18, p. 3675-3685.

Hönisch, B., Ridgwell, A., Schmidt, D., Thomas, E., Gibbs, S., Sluijs, A., Zeebe, R., Kump, L., Martindale, R., Greene, S., Kiessling, W., Ries, J., Zachos, J., Royer, D., Barker, S., Marchitto, T., Moyer, R., Pelejero, C., Ziveri, P., Foster, G., and Williams, B., 2012, The Geological Record of Ocean Acidification: Science, v. 335, no. 6072, p. 1058-1063.

Hooper, P. R., Binger, G. B., and Lees, K. R., 2002, Ages of the Steens and Columbia River flood basalts and their relationship to extension-related calc-alkalic volcanism in eastern Oregon: Geological Society of America Bulletin, v. 114, no. 1, p. 43-50.

Horita, J., Zimmermann, H., and Holland, H. D., 2002, Chemical evolution of seawater during the Phanerozoic: Implications from the record of marine evaporites: Geochimica et Cosmochimica Acta, v. 66, no. 21, p. 3733-3756.

Imbrie, J., Berger, A., Boyle, E. A., Clemens, S. C., Duffy, A., Howard, W. R., Kukla, G., Kutzbach, J., Martinson, D. G., McIntyre, A., Mix, A. C., Molfino, B., Morley, J. J., Peterson, L. C., Pisias, N. G., Prell, W. L., Raymo, M. E., Shackleton, N. J., and Toggweiler, J. R., 1993, On the structure and origin of major glaciation cycles 2. The 100,000-year cycle: Paleoceanography, v. 8, no. 6, p. 699-735.

IPCC, 2013, Climate Change 2013: The Physical Science Basis. Working Group I Contribution to the 5th Assessment Report of the Intergovernmental Panel on Climate Change.

Kahn, M. I., and Williams, D. F., 1981, Oxygen and carbon isotopic composition of living planktonic foraminifera from the northeast Pacific Ocean: Palaeogeography, Palaeoclimatology, Palaeoecology, v. 33, no. 1–3, p. 47-69.

Kakihana, H., and Kotaka, M., 1977, Equilibrium constants for boron isotope-exchange reactions: Bulletin Of The Research Laboratory For Nuclear Reactors, v. 2, p. 1-12.

Kakihana, H., Kotaka, M., Satoh, S., Nomura, M., and Okamoto, M., 1977, Fundamental studies on ion-exchange separation of boron isotopes: Bulletin of the Chemical Society of Japan, v. 50, no. 1, p. 158-163.

Kender, S., Yu, J., and Peck, V., 2014, Deep ocean carbonate ion increase during mid Miocene CO_2 decline: Scientific Reports, v. 4, no. 4187, DOI: 10.1038/srep04187

Key, R. M., Kozyr, A., Sabine, C. L., Lee, K., Wanninkhof, R., Bullister, J. L., Feely, R. A., Millero, F. J., Mordy, C., and Peng, T. H., 2004, A global ocean carbon climatology: Results from Global Data Analysis Project (GLODAP): Global Biogeochemical Cycles, v. 18, no. 4, p. GB4031.

Kısakűrek, B., James, R. H., and Harris, N. B. W., 2005, Li and δ^7Li in Himalayan rivers: Proxies for silicate weathering?: Earth and Planetary Science Letters, v. 237, no. 3–4, p. 387-401.

Klochko, K., Cody, G. D., Tossell, J. A., Dera, P., and Kaufman, A. J., 2009, Re-evaluating boron speciation in biogenic calcite and aragonite using B-11 MAS NMR: Geochimica et Cosmochimica Acta, v. 73, no. 7, p. 1890-1900.

Klochko, K., Kaufman, A. J., Yao, W. S., Byrne, R. H., and Tossell, J. A., 2006, Experimental measurement of boron isotope fractionation in seawater: Earth and Planetary Science Letters, v. 248, no. 1-2, p. 276-285.

Knorr, G., and Lohmann, G., 2014, Climate warming during Antarctic ice sheet expansion at the Middle Miocene transition: Nature Geoscience, v. 7, no. 5, p. 376-381.

Kominz, M. A., and Pekar, S. F., 2001, Oligocene eustasy from two-dimensional sequence stratigraphic backstripping: Geological Society of America Bulletin, v. 113, no. 3, p. 291-304.

Koornneef, J. M., Bouman, C., Schwieters, J. B., and Davies, G. R., 2013, Use of 10^12 ohm current amplifiers in Sr and Nd isotope analyses by TIMS for application to sub-nanogram samples: Journal of Analytical Atomic Spectrometry, v. 28, no. 5, p. 749-754.

Kürschner, W. M., Kvaček, Z., and Dilcher, D. L., 2008, The impact of Miocene atmospheric carbon dioxide fluctuations on climate and the evolution of terrestrial ecosystems: Proceedings of the National Academy of Sciences of the United States of America, v. 105, no. 2, p. 449-453.

Ladant, J.B., Donnadieu, Y., Lefebvre, V., and Dumas, C., 2014a, The respective role of atmospheric carbon dioxide and orbital parameters on ice sheet evolution at the Eocene-Oligocene transition: Paleoceanography, v. 29, no. 8, p. 2013PA002593.

Ladant, J. B., Donnadieu, Y., and Dumas, C., 2014b, Links between CO_2, glaciation and water flow: reconciling the Cenozoic history of the Antarctic Circumpolar Current: Climate of the Past, v. 10, no. 6, p. 1957-1966.

Langebroek, P. M., Paul, A., and Schulz, M., 2009, Antarctic ice-sheet response to atmospheric CO2 and insolation in the Middle Miocene: Climate of the Past, v. 5, no. 4, p. 633-646.

Laskar, J., Robutel, P., Joutel, F., Gastineau, M., Correia, A. C. M., and Levrard, B., 2004, A long-term numerical solution for the insolation quantities of the Earth: Astronomy & Astrophysics, v. 428, no. 1, p. 261-285.

Lear, C. H., Bailey, T. R., Pearson, P. N., Coxall, H. K., and Rosenthal, Y., 2008, Cooling and ice growth across the Eocene-Oligocene transition: Geology, v. 36, no. 3, p. 251-254.

Lear, C. H., Elderfield, H., and Wilson, P. A., 2000, Cenozoic deep-sea temperatures and global ice volumes from Mg/Ca in benthic foraminiferal calcite: Science, v. 287, no. 5451, p. 269-272.

Lear, C. H., Mawbey, E. M., and Rosenthal, Y., 2010, Cenozoic benthic foraminiferal Mg/Ca and Li/Ca records: Toward unlocking temperatures and saturation states: Paleoceanography, v. 25, no. 4, DOI: 10.1029/2009PA001880

Lee, K., Kim, T. W., Byrne, R. H., Millero, F. J., Feely, R. A., and Liu, Y. M., 2010, The universal ratio of boron to chlorinity for the North Pacific and North Atlantic oceans: Geochimica Et Cosmochimica Acta, v. 74, no. 6, p. 1801-1811.

LeGrande, A. N., and Schmidt, G. A., 2011, Water isotopologues as a quantitative paleosalinity proxy: Paleoceanography, v. 26, no. 3, DOI: 10.1029/2010PA002043.

Lemarchand, D., and Gaillardet, J., 2006, Transient features of the erosion of shales in the Mackenzie basin (Canada), evidences from boron isotopes: Earth and Planetary Science Letters, v. 245, no. 1–2, p. 174-189.

Lemarchand, D., Gaillardet, J., Gopel, C., and Manhes, G., 2002a, An optimized procedure for boron separation and mass spectrometry analysis for river samples: Chemical Geology, v. 182, no. 2-4, p. 323-334.

Lemarchand, D., Gaillardet, J., Lewin, E., and Allegre, C. J., 2002b, Boron isotope systematics in large rivers: implications for the marine boron budget and paleo-pH reconstruction over the Cenozoic: Chemical Geology, v. 190, no. 1-4, p. 123-140.

Levermann, A., Clark, P. U., Marzeion, B., Milne, G. A., Pollard, D., Radic, V., and Robinson, A., 2013, The multimillennial sea-level commitment of global warming: Proceedings of the National Academy of Sciences, v. 110, no. 34, p. 13745-13750.

Lewis, A. R., Marchant, D. R., Ashworth, A. C., Hemming, S. R., and Machlus, M. L., 2007, Major middle Miocene global climate change: Evidence from East Antarctica and the Transantarctic Mountains: Geological Society of America Bulletin, v. 119, p. 1449-1461.

Lewis, A. R., Marchant, D. R., Kowalewski, D. E., Baldwin, S. L., and Webb, L. E., 2006, The age and origin of the Labyrinth, western Dry Valleys, Antarctica: Evidence for extensive middle Miocene subglacial floods and freshwater discharge to the Southern Ocean: Geology, v. 34, no. 7, p. 513-516.

Liebrand, D., Lourens, L. J., Hodell, D. A., de Boer, B., van de Wal, R. S. W., and Palike, H., 2011, Antarctic ice sheet and oceanographic response to eccentricity forcing during the early Miocene: Climate of the Past, v. 7, no. 3, p. 869-880.

Lisiecki, L., and Raymo, M., 2005, A Pliocene-Pleistocene stack of 57 globally distributed benthic $\delta^{18}O$ records: Paleoceanography, v. 20, no. 1. DOI: 10.1029/2004pa001071.

Liu, W. G., Xiao, Y. K., Peng, Z. C., An, Z. S., and He, X. X., 2000, Boron concentration and isotopic composition of halite from experiments and salt lakes in the Qaidam Basin: Geochimica Et Cosmochimica Acta, v. 64, no. 13, p. 2177-2183.

Liu, X.M., Wanner, C., Rudnick, R. L., and McDonough, W. F., 2015, Processes controlling $\delta^{7}Li$ in rivers illuminated by study of streams and groundwaters draining basalts: Earth and Planetary Science Letters, v. 409, no. 0, p. 212-224.

Lüthi, D., Le Floch, M., Bereiter, B., Blunier, T., Barnola, J., Siegenthaler, U., Raynaud, D., Jouzel, J., Fischer, H., Kawamura, K., and Stocker, T., 2008, High-resolution carbon dioxide concentration record 650,000-800,000 years before present: Nature, v. 453, no. 7193, p. 379-382.

Lyle, M., Gibbs, S., Moore, T., and Rea, D., 2007, Late Oligocene initiation of the Antarctic circumpolar current: Evidence from the South Pacific: Geology, v. 35, no. 8, p. 691-694.

Lythe, M. B., Vaughan, D. G., and Consortium, B., 2001, BEDMAP: A new ice thickness and subglacial topographic model of Antarctica: Journal of Geophysical Research-Solid Earth, v. 106, no. B6, p. 11335-11351.

Majewski, W., and Bohaty, S. M., 2010, Surface-water cooling and salinity decrease during the Middle Miocene climate transition at Southern Ocean ODP Site 747 (Kerguelen Plateau): Marine Micropaleontology, v. 74, no. 1-2, p. 1-14.

Martìnez-Botì, M. A., Foster, G. L., Chalk, T. B., Rohling, E. J., Sexton, P. F., Lunt, D. J., Pancost, R. D., Badger, M. P. S., and Schmidt, D. N., 2015a, Plio-Pleistocene climate sensitivity from on a new high-resolution CO_2 record: Nature, v. 518, p. 49-54.

Martìnez-Botì, M.A., Marino, G., Foster, G. L., Ziveri, P., Henehan, M. J., Rae, J. W. B., Mortyn, P. G. and Vance, D., 2015b, Boron isotope evidence for oceanic CO_2 leakage during the last deglaciation: Nature, v. 518, p. 219-222.

Mawbey, E. M., and Lear, C. H., 2013, Carbon cycle feedbacks during the Oligocene-Miocene transient glaciation: Geology, v. 41, no. 9, p. 963-966.

McCorkle, D. C., Corliss, B. H., and Farnham, C. A., 1997, Vertical distributions and stable isotopic compositions of live (stained) benthic foraminifera from the North Carolina and California continental margins: Deep Sea Research Part I: Oceanographic Research Papers, v. 44, no. 6, p. 983-1024.

Meehl, G. A., Hu, A., Tebaldi, C., Arblaster, J. M., Washington, W. M., Teng, H., Sanderson, B. M., Ault, T., Strand, W. G., and White, J. B., 2012, Relative outcomes of climate change mitigation related to global temperature versus sea-level rise: Nature Climate Change, v. 2, no. 8, p. 576-580.

Mengel, M., and Levermann, A., 2014, Ice plug prevents irreversible discharge from East Antarctica: Nature Climate Change, v. 4, no. 6, p. 451-455.

Miller, K. G., Fairbanks, R. G., and Mountain, G. S., 1987, Tertiary oxygen isotope synthesis, sea level history, and continental margin erosion: Paleoceanography, v. 2, no. 1, p. 1-19.

Miller, K. G., Mountain, G. S., Wright, J. D., and Browning, J. V., 2011, A 180-Million-Year Record of Sea Level and Ice Volume Variations from Continental Margin and Deep-Sea Isotopic Records: Oceanography, v. 24, no. 2, p. 40–53.

Miller, K. G., Wright, J. D., Browning, J. V., Kulpecz, A., Kominz, M., Naish, T. R., Cramer, B. S., Rosenthal, Y., Peltier, W. R., and Sosdian, S., 2012, High tide of the warm Pliocene: Implications of global sea level for Antarctic deglaciation: Geology, v. 40, no. 5, p. 407-410.

Miller, K. G., Wright, J. D., and Fairbanks, R. G., 1991, Unlocking the Ice House - Oligocene-Miocene Oxygen Isotopes, Eustasy, and Margin Erosion: Journal of Geophysical Research-Solid Earth and Planets, v. 96, no. B4, p. 6829-6848.

Millot, R., Vigier, N., and Gaillardet, J., 2010, Behaviour of lithium and its isotopes during weathering in the Mackenzie Basin, Canada: Geochimica et Cosmochimica Acta, v. 74, no. 14, p. 3897-3912.

Misra, S., and Froelich, P., 2012, Lithium Isotope History of Cenozoic Seawater: Changes in Silicate Weathering and Reverse Weathering: Science, v. 335, no. 6070, p. 818-823.

Mitrovica, J. X., Gomez, N., and Clark, P. U., 2009, The Sea-Level Fingerprint of West Antarctic Collapse: Science, v. 323, no. 5915, p. 753-753.

Mudelsee, M., Bickert, T., Lear, C. H., and Lohmann, G., 2014, Cenozoic climate changes: A review based on time series analysis of marine benthic δ18O records: Reviews of Geophysics, v. 52, no. 3, p. 333-374.

Myhre, G., Highwood, E. J., Shine, K. P., and Stordal, F., 1998, New estimates of radiative forcing due to well mixed greenhouse gases: Geophysical Research Letters, v. 25, no. 14, p. 2715-2718.

Naik, S., and Naidu, P., 2014, Boron/calcium ratios in Globigerinoides ruber from the Arabian Sea: Implications for controls on boron incorporation: Marine Micropaleontology, v. 107, p. 1-7.

Naish, T., Powell, R., Barrett, J., Levy, R., Henrys, S., Wilson, G., Krissek, L., Niessen, F., Pompilio, M., Ross, J., Scherer, R., Talarico, F., Pyne, A., and team, S.M S., 2008, Late Cenozoic Climate History of the Ross Embayment from the AND-1B Drill Hole: Culmination of Three Decades of Antarctic Margin Drilling: In: Cooper, A. K., P. J. Barrett, H. Stagg, B. Storey, E. Stump, W. Wise, and the 10th ISAES editorial team, eds. (2008). Antarctica: A Keystone in a Changing World. Proceedings of the 10th International Symposium on Antarctic Earth Sciences. Washington, DC: The National Academies Press., p. 71-82.

Naish, T. R., Woolfe, K. J., Barrett, P. J., Wilson, G. S., Atkins, C., Bohaty, S. M., Bucker, C. J., Claps, M., Davey, F. J., Dunbar, G. B., Dunn, A. G., Fielding, C. R., Florindo, F., Hannah, M. J., Harwood, D. M., Henrys, S. A., Krissek, L. A., Lavelle, M., van der Meer, J., McIntosh, W. C., Niessen, F., Passchier, S., Powell, R. D., Roberts, A. P., Sagnotti, L., Scherer, R. P., Strong, C. P., Talarico, F., Verosub, K. L., Villa, G., Watkins, D. K., Webb, P. N., and Wonik, T., 2001, Orbitally induced oscillations in the East Antarctic ice sheet at the Oligocene/Miocene boundary: Nature, v. 413, no. 6857, p. 719-723.

Ni, Y. Y., Foster, G. L., and Elliott, T., 2010, The accuracy of $\delta^{11}B$ measurements of foraminifers: Chemical Geology, v. 274, no. 3-4, p. 187-195.

Norris, R. D., 1996, Symbiosis as an Evolutionary Innovation in the Radiation of Paleocene Planktic Foraminifera: Paleobiology, v. 22, no. 4, p. 461-480.

Norris, R.D, Corfield R.M., 1998, Recognition and macroevolutionary significance of photosymbiosis in molluscs, corals, and foraminifera: Isotope Paleobiology and Paleoecology. The Paleontological Society, v. 4, p. 68-100.

Oerlemans, J., 1982, A Model of the Antarctic Ice-Sheet: Nature, v. 297, no. 5867, p. 550-553.

Oerlemans, J., 2004, Antarctic ice volume and deep-sea temperature during the last 50 Myr: a model study: Annals of Glaciology, v. 39, p. 13-19.

Pagani, M., 2002, The alkenone-CO_2 proxy and ancient atmospheric carbon dioxide: Philosophical Transactions of the Royal Society of London Series A-Mathematical, Physical and Engineering Sciences, v. 360, no. 1793, p. 609-632.

Pagani, M., Arthur, M. A., and Freeman, K. H., 1999, Miocene evolution of atmospheric carbon dioxide: Paleoceanography, v. 14, no. 3, p. 273-292.

Pagani, M., Huber, M., Liu, Z., Bohaty, S., Henderiks, J., Sijp, W., Krishnan, S., and DeConto, R., 2011, The Role of Carbon Dioxide During the Onset of Antarctic Glaciation: Science, v. 334, no. 6060, p. 1261-1264.

Pagani, M., Lemarchand, D., Spivack, A., and Gaillardet, J., 2005a, A critical evaluation of the boron isotope-pH proxy: The accuracy of ancient ocean pH estimates: Geochimica et Cosmochimica Acta, v. 69, no. 4, p. 953-961.

Pagani, M., Zachos, J. C., Freeman, K. H., Tipple, B., and Bohaty, S., 2005b, Marked decline in atmospheric carbon dioxide concentrations during the Paleogene: Science, v. 309, no. 5734, p. 600-603.

Pahnke, K., Zahn, R., Elderfield, H., and Schulz, M., 2003, 340,000-Year Centennial-Scale Marine Record of Southern Hemisphere Climatic Oscillation: Science, v. 301, no. 5635, p. 948-952.

Pälike, H., Frazier, J., and Zachos, J., 2006a, Extended orbitally forced palaeoclimatic records from the equatorial Atlantic Ceara Rise: Quaternary Science Reviews, v. 25, no. 23-24, p. 3138-3149.

Pälike, H., Norris, R. D., Herrle, J. O., Wilson, P. A., Coxall, H. K., Lear, C. H., Shackleton, N. J., Tripati, A. K., and Wade, B. S., 2006b, The Heartbeat of the Oligocene Climate System: Science, v. 314, no. 5807, p. 1894-1898.

Pälike, H., Lyle, M., Nishi, H., Raffi, I., Ridgwell, A., Gamage, K., Klaus, A., Acton, G., Anderson, L., Backman, J., Baldauf, J., Beltran, C., *et al*. 2012, A Cenozoic record of the equatorial Pacific carbonate compensation depth: Nature, v. 488, no. 7413, p. 609-614.

Pälike, H., Norris, R. D., Herrle, J. O., Wilson, P. A., Coxall, H. K., Lear, C. H., Shackleton, N. J., Tripati, A. K., and Wade, B. S., 2006b, The Heartbeat of the Oligocene Climate System: Science, v. 314, no. 5807, p. 1894-1898.

Palmer, M. R., Pearson, P. N., and Cobb, S. J., 1998, Reconstructing past ocean pH-depth profiles: Science, v. 282, no. 5393, p. 1468-1471.

Palmer, M. R., Spivack, A. J., and Edmond, J. M., 1987, Temperature and pH controls over isotopic fractionation during adsorption of boron on marine clay: Geochimica et Cosmochimica Acta, v. 51, no. 9, p. 2319-2323.

Paris, G., Gaillardet, J., and Louvat, P., 2010, Geological evolution of seawater boron isotopic composition recorded in evaporites: Geology, v. 38, no. 11, p. 1035-1038.

Park, H., and Schlesinger, W. H., 2002, Global biogeochemical cycle of boron: Global Biogeochemical Cycles, v. 16, no. 4, p. 1072.

Passchier, S., Browne, G., Field, B., Fielding, C. R., Krissek, L. A., Panter, K., Pekar, S. F., and Team, A.-S. S., 2011, Early and middle Miocene Antarctic glacial history from the sedimentary facies distribution in the AND-2A drill hole, Ross Sea, Antarctica: Geological Society of America Bulletin, v. 123, no. 11-12, p. 2352-2365.

Passchier, S., Falk, C. J., and Florindo, F., 2013, Orbitally-paced shifts in the particle size Antarctic continental shelf sediments in response to ice dynamics during the Miocene Climatic Optimum: Geosphere, v. 9, no. 1, p. 54-62.

Paul, H., Zachos, J., Flower, B., and Tripati, A., 2000, Orbitally induced climate and geochemical variability across the Oligocene/Miocene boundary: Paleoceanography, v. 15, no. 5, p. 471-485.

Pearson, P. N., 1995, Planktonic foraminifer biostratigraphy and the development of pelagic caps on guyots in the Marshall Islands group: *In* Haggerty, J.A., Premoli Silva, I., Rack, F., and McNutt, M.K. (Eds.), *Proc. ODP, Sci. Results,* 144: College Station, TX (Ocean Drilling Program), p. 21–59.

Pearson, P. N., Ditchfield, P. W., Singano, J., Harcourt-Brown, K. G., Nicholas, C. J., Olsson, R. K., Shackleton, N. J., and Hall, M. A., 2001, Warm tropical sea

surface temperatures in the Late Cretaceous and Eocene epochs: Nature, v. 413, no. 6855, p. 481-487.

Pearson, P. N., Foster, G. L., and Wade, B. S., 2009, Atmospheric carbon dioxide through the Eocene-Oligocene climate transition: Nature, v. 461, no. 7267, p. 1110-1204.

Pearson, P. N., and Palmer, M. R., 1999, Middle Eocene seawater pH and atmospheric carbon dioxide concentrations: Science, v. 284, no. 5421, p. 1824-1826.

Pearson, P. N., and Palmer, M. R., 2000, Atmospheric carbon dioxide concentrations over the past 60 million years: Nature, v. 406, no. 6797, p. 695-699.

Pearson, P. N., Shackleton, N. J., Weedon, G. P., and M.A., H., 1997, Multi- species planktonic foraminifer stable isotope stratigraphy through Oligocene/Miocene boundary climatic cycles, Site 926: in Shackleton, N.J., et al., eds., Proceedings of the Ocean Drilling Program, Scientific Results, Volume 154: College Station, Texas, Ocean Drilling Program, p. 441–449.

Pearson, P. N., and Wade, B. S., 2009, Taxonomy and Stable Isotope Paleoecology of Well-Preserved Planktonic Foraminifera from the Uppermost Oligocene of Trinidad: Journal of Foraminiferal Research, v. 39, no. 3, p. 191-217.

Peeters, F. J. C., Brummer, G.-J. A., and Ganssen, G., 2002, The effect of upwelling on the distribution and stable isotope composition of Globigerina bulloides and Globigerinoides ruber (planktic foraminifera) in modern surface waters of the NW Arabian Sea: Global and Planetary Change, v. 34, no. 3-4, p. 269-291.

Penman, D. E., Hönisch, B., Zeebe, R. E., Thomas, E., and Zachos, J. C., 2014, Rapid and sustained surface ocean acidification during the Paleocene-Eocene Thermal Maximum: Paleoceanography, v. 29, no. 5, DOI: 2014PA002621.

Pfuhl, H., and McCave, I., 2005, Evidence for late Oligocene establishment of the Antarctic Circumpolar Current: Earth and Planetary Science Letters, v. 235, no. 3-4, p. 715-728.

Pistiner, J. S., and Henderson, G. M., 2003, Lithium-isotope fractionation during continental weathering processes: Earth and Planetary Science Letters, v. 214, no. 1–2, p. 327-339.

Pogge von Strandmann, P. A. E., Burton, K. W., James, R. H., van Calsteren, P., Gislason, S. R., and Sigfússon, B., 2008, The influence of weathering processes on riverine magnesium isotopes in a basaltic terrain: Earth and Planetary Science Letters, v. 276, no. 1–2, p. 187-197.

Pogge von Strandmann, P. A. E., Forshaw, J., and Schmidt, D. N., 2014, Modern and Cenozoic records of seawater magnesium from foraminiferal Mg isotopes: Biogeosciences, v. 11, no. 18, p. 5155-5168.

Pogge von Strandmann, P. A. E., and Henderson, G. M., 2014, The Li isotope response to mountain uplift: Geology, DOI: 10.1130/G36162.1

Pollard, D., and DeConto, R. M., 2005, Hysteresis in Cenozoic Antarctic ice-sheet variations: Global and Planetary Change, v. 45, no. 1-3, p. 9-21.

Pollard, D., and DeConto, R. M., 2009, Modelling West Antarctic ice sheet growth and collapse through the past five million years: Nature, v. 458, no. 7236, p. 329-389.

Pollard, D., DeConto, R. M., and Nyblade, A. A., 2005, Sensitivity of Cenozoic Antarctic ice sheet variations to geothermal heat flux: Global and Planetary Change, v. 49, no. 1-2, p. 63-74.

Prell, W., and Curry, W. B., 1981, Faunal and isotopic indices of monsoonal upwelling: Western Arabian Sea: Oceanologica Acta, v. 4, no. 1, p. 91-98.

Rae, J. W., 2011, Boron isotopes in benthic foraminifera: measurement, calibration

and glacial CO_2. [PhD thesis]: University of Bristol.
Rae, J. W. B., Foster, G. L., Schmidt, D. N., and Elliott, T., 2011, Boron isotopes and B/Ca in benthic foraminifera: Proxies for the deep ocean carbonate system: Earth and Planetary Science Letters, v. 302, no. 3-4, p. 403-413.
Raitzsch, M., and Honisch, B., 2013, Cenozoic boron isotope variations in benthic foraminifers: Geology, v. 41, no. 5, p. 591-594.
Rathmann, S., Hess, S., Kuhnert, H., and Mulitza, S., 2004, Mg/Ca ratios of the benthic foraminifera Oridorsalis umbonatus obtained by laser ablation from core top sediments: Relationship to bottom water temperature: Geochemistry, Geophysics, Geosystems, v. 5, no. 12, DOI: 10.1029/2004GC000808.
Ravelo, A. C., and Fairbanks, R. G., 1995, Carbon isotopic fractionation in multiple species of planktonic foraminifera from core-tops in the tropical Atlantic: Journal of Foraminiferal Research, v. 25, p. 53-74.
Ridgwell, A., 2005, A mid Mesozoic revolution in the regulation of ocean chemistry: Marine Geology, v. 217, no. 3-4, p. 339-357.
Roberts, C. D., and Tripati, A. K., 2009, Modeled reconstructions of the oceanic carbonate system for different histories of atmospheric carbon dioxide during the last 20 Ma: Global Biogeochemical Cycles, v. 23, no. 1, DOI: 10.1029/2008GB003310.
Rohling, E. J., Foster, G. L., Grant, K. M., Marino, G., Roberts, A. P., Tamisiea, M. E., and Williams, F., 2014, Sea-level and deep-sea-temperature variability over the past 5.3 million years: Nature, v. 508, no. 7497, p. 477-482.
Rohling, E. J., Grant, K., Bolshaw, M., Roberts, A. P., Siddall, M., Hemleben, C., and Kucera, M., 2009, Antarctic temperature and global sea level closely coupled over the past five glacial cycles: Nature Geoscience, v. 2, p. 500 - 504
Rose, E. F., Chaussidon, M., and France-Lanord, C., 2000, Fractionation of boron isotopes during erosion processes: the example of Himalayan rivers: Geochimica et Cosmochimica Acta, v. 64, no. 3, p. 397-408.
Rose-Koga, E. F., Sheppard, S. M. F., Chaussidon, M., and Carignan, J., 2006, Boron isotopic composition of atmospheric precipitations and liquid–vapour fractionations: Geochimica et Cosmochimica Acta, v. 70, no. 7, p. 1603-1615.
Rosenthal, Y., Boyle, E. A., and Slowey, N., 1997, Temperature control on the incorporation of magnesium, strontium, fluorine, and cadmium into benthic foraminiferal shells from Little Bahama Bank: Prospects for thermocline paleoceanography: Geochimica et Cosmochimica Acta, v. 61, no. 17, p. 3633-3643.
Royer, D. L., Berner, R. A., and Beerling, D. J., 2001, Phanerozoic atmospheric CO_2 change: evaluating geochemical and paleobiological approaches: Earth-Science Reviews, v. 54, no. 4, p. 349-392.
Rustad, J. R., Bylaska, E. J., Jackson, V. E., and Dixon, D. A., 2010, Calculation of boron-isotope fractionation between $B(OH)_{3(aq)}$ and $B(OH)_{4\ (aq)}^-$: Geochimica et Cosmochimica Acta, v. 74, no. 10, p. 2843-2850.
Sadekov, A., Eggins, S., and De Deckker, P., 2005, Characterization of Mg/Ca distributions in planktonic foraminifera species by electron microprobe mapping: Geochemistry Geophysics Geosystems, v. 6, no. 12, DOI: 10.1029/2005GC000973
Sadekov, A. Y., Bush, F., Kerr, J., Ganeshram, R., and Elderfield, H., 2014, Mg/Ca composition of benthic foraminifera Miliolacea as a new tool of paleoceanography: Paleoceanography, v. 29, no. 10, p. 990-1001.

Salisbury, E. J., 1928, On the Causes and Ecological Significance of Stomatal Frequency, with Special Reference to the Woodland Flora: Philosophical Transactions of the Royal Society of London. Series B, Containing Papers of a Biological Character, v. 216, no. 431-439, p. 1-65.

Sanyal, A., Bijma, J., Spero, H., and Lea, D. W., 2001, Empirical relationship between pH and the boron isotopic composition of Globigerinoides sacculifer: Implications for the boron isotope paleo-pH proxy: Paleoceanography, v. 16, no. 5, p. 515-519.

Sanyal, A., Hemming, N. G., Broecker, W. S., Lea, D. W., Spero, H. J., and Hanson, G. N., 1996, Oceanic pH control on the boron isotopic composition of foraminifera: Evidence from culture experiments: Paleoceanography, v. 11, no. 5, p. 513-517.

Sanyal, A., Nugent, M., Reeder, R. J., and Buma, J., 2000, Seawater pH control on the boron isotopic composition of calcite: Evidence from inorganic calcite precipitation experiments: Geochimica et Cosmochimica Acta, v. 64, no. 9, p. 1551-1555.

Sautter, L. R., and Sancetta, C., 1992, Seasonal associations of phytoplankton and planktic foraminifera in an upwelling region and their contribution to the seafloor: Marine Micropaleontology, v. 18, no. 4, p. 263-278.

Sautter, L. R., and Thunell, R. C., 1991, Seasonal Variability in the $\delta^{18}O$ and $\delta^{13}C$ of Planktonic Foraminifera from an Upwelling Environment: Sediment Trap Results from the San Pedro Basin, Southern California Bight: Paleoceanography, v. 6, no. 3, p. 307-334.

Schlitzer, R., 2000, Electronic atlas of WOCE hydrographic and tracer data now available: Eos Trans. AGU, v. 81, no. 5, p. 45-45.

Schmidt, D. N., Thierstein, H. R., and Bollmann, J., 2004a, The evolutionary history of size variation of planktic foraminiferal assemblages in the Cenozoic: Palaeogeography, Palaeoclimatology, Palaeoecology, v. 212, no. 1–2, p. 159-180.

Schmidt, D. N., Thierstein, H. R., Bollmann, J., and Schiebel, R., 2004b, Abiotic Forcing of Plankton Evolution in the Cenozoic: Science, v. 303, no. 5655, p. 207-210.

Schmidt, G. A., G.R., B., and E.J., R., 1999 Global Seawater $\delta^{18}O$ Database - v1.20: http://data.giss.nasa.gov/o18data/.

Schmidt, M. W., Spero, H. J., and Lea, D. W., 2004c, Links between salinity variation in the Caribbean and North Atlantic thermohaline circulation: Nature, v. 428, no. 6979, p. 160-163.

Schmitt, A.D., Chabaux, F., and Stille, P., 2003, The calcium riverine and hydrothermal isotopic fluxes and the oceanic calcium mass balance: Earth and Planetary Science Letters, v. 213, no. 3–4, p. 503-518.

Seki, O., Foster, G. L., Schmidt, D. N., Mackensen, A., Kawamura, K., and Pancost, R. D., 2010, Alkenone and boron-based Pliocene pCO_2 records: Earth and Planetary Science Letters, v. 292, no. 1-2, p. 201-211.

Sexton, P. F., Wilson, P. A., and Pearson, P. N., 2006a, Microstructural and geochemical perspectives on planktic foraminiferal preservation: "Glassy" versus "Frosty": Geochemistry Geophysics Geosystems, v. 7, DOI: 10.1029/2006GC001291.

Sexton, P. F., Wilson, P. A., and Pearson, P. N, 2006b, Palaeoecology of late middle Eocene planktic foraminifera and evolutionary implications: Marine Micropaleontology, v. 60, no. 1, p. 1-16.

Shackleton, N. J., 2000, The 100,000-Year Ice-Age Cycle Identified and Found to Lag Temperature, Carbon Dioxide, and Orbital Eccentricity: Science, v. 289, no. 5486, p. 1897-1902.

Shackleton, N.J., Hall, M., Raffi, I., Tauxe, L., and Zachos, J., 2000, Astronomical calibration age for the Oligocene-Miocene boundary: Geology, v. 28, no. 5, p. 447-450.

Shevenell, A. E., Kennett, J. P., and Lea, D. W., 2004, Middle Miocene Southern Ocean cooling and Antarctic cryosphere expansion: Science, v. 305, no. 5691, p. 1766-1770.

Siddall, M., Rohling, E. J., Almogi-Labin, A., Hemleben, C., Meischner, D., Schmelzer, I., and Smeed, D. A., 2003, Sea-level fluctuations during the last glacial cycle: Nature, v. 423, no. 6942, p. 853-858.

Sime, N. G., De La Rocha, C. L., Tipper, E. T., Tripati, A., Galy, A., and Bickle, M. J., 2007, Interpreting the Ca isotope record of marine biogenic carbonates: Geochimica et Cosmochimica Acta, v. 71, no. 16, p. 3979-3989.

Simon, L., Lecuyer, C., Marechal, C., and Coltice, N., 2006, Modelling the geochemical cycle of boron: Implications for the long-term $\delta^{11}B$ evolution of seawater and oceanic crust: Chemical Geology, v. 225, no. 1-2, p. 61-76.

Smith, H. J., Spivack, A. J., Staudigel, H., and Hart, S. R., 1995, The boron isotopic composition of altered oceanic crust: Chemical Geology, v. 126, no. 2, p. 119-135.

Sosdian, S. M., Greenop, R., Lear, C. H., and Foster, G., in prep., Neogene CO_2 decline driven by increased silicate weathering rates.

Spero, H., Mielke, K., Kalve, E., Lea, D., and Pak, D., 2003, Multispecies approach to reconstructing eastern equatorial Pacific thermocline hydrography during the past 360 kyr: Paleoceanography, v. 18, no. 1, DOI: 10.1029/2002PA000814.

Spero, H. J., and DeNiro, M. J., 1987, The influence of photosynthesis on the $\delta^{18}O$ and $\delta^{13}C$ values of planktonic foraminiferal shell calcite: Symbiosis, v. 4, p. 213-228.

Spero, H. J., and Lea, D. W., 1993, Intraspecific stable isotope variability in the planktic foraminifera Globigerinoides sacculifer: Results from laboratory experiments: Marine Micropaleontology, v. 22, no. 3, p. 221-234.

Spero, H. J., and Lea, D. W., 1993, 1996, Experimental determination of stable isotope variability in Globigerina *bulloides*: Implications for paleoceanographic reconstructions: Marine Micropaleontology, v. 28, no. 3-4, p. 231-246.

Spivack, A. J., and Edmond, J. M., 1987, Boron isotope exchange between seawater and the oceanic crust: Geochimica et Cosmochimica Acta, v. 51, no. 5, p. 1033-1043.

Steckler, M., Watts, A. B., and Thorne, J., 1988, Subsidence and basin modelling at U.S. Atlantic passive margin. : In Sheridan, R.E., Grow, J.A. (Eds.) The Atlantic Continental Margin. The Geology of North America, U.S. Geological Society of America, Boulder, CO., v. 1-2, p. 399-416.

Steineck, P. L., and Fleisher, R. L., 1978, Towards the classical evolutionary reclassification of the Cenozoic Globigerinacea (Foraminiferida): Journal of Paleontology, v. 52, no. 3, p. 618-635.

Stewart, J. A., 2012, Variation in silicate weathering across the Oligocene-Miocene boundary: evidence from lithium and neodymium isotopes [PhD thesis]: University of Southampton.

Stewart, J. A., Wilson, P. A., Edgar, K. M., Anand, P., and James, R. H., 2012, Geochemical assessment of the palaeoecology, ontogeny, morphotypic

variability and palaeoceanographic utility of "*Dentoglobigerina*" *venezuelana*: Marine Micropaleontology, v. 84-85, p. 74-86.

Stocchi, P., Escutia, C., Houben, A. J. P., Vermeersen, B. L. A., Bijl, P. K., Brinkhuis, H., DeConto, R. M., Galeotti, S., Passchier, *et al.*, 2013 , Relative sea-level rise around East Antarctica during Oligocene glaciation: Nature Geosci, v. 6, no. 5, p. 380-384.

Takahashi, T., Sutherland, S. C., Wanninkhof, R., Sweeney, C., Feely, R. A., Chipman, D. W., Hales, B., Friederich, G., Chavez, F., *et al.*, 2009, Climatological mean and decadal change in surface ocean pCO_2, and net sea-air CO_2 flux over the global oceans: Deep-Sea Research Part I-Oceanographic Research Papers, v. 56, no. 11, p. 2075-2076.

Talarico, F. M., and Sandroni, S., 2009, Provenance signatures of the Antarctic Ice Sheets in the Ross Embayment during the Late Miocene to Early Pliocene: The ANDRILL AND-1B core record: Global and Planetary Change, v. 69, no. 3, p. 103-123.

Thorn, V. C., and DeConto, R., 2006, Antarctic climate at the Eocene/Oligocene boundary - climate model sensitivity to high latitude vegetation type and comparisons with the palaeobotanical record: Palaeogeography Palaeoclimatology Palaeoecology, v. 231, no. 1-2, p. 134-157.

Tipper, E. T., Calmels, D., Gaillardet, J., Louvat, P., Capmas, F., and Dubacq, B., 2012, Positive correlation between Li and Mg isotope ratios in the river waters of the Mackenzie Basin challenges the interpretation of apparent isotopic fractionation during weathering: Earth and Planetary Science Letters, v. 333–334, no. 0, p. 35-45.

Tipper, E. T., Galy, A., and Bickle, M. J., 2006a, Riverine evidence for a fractionated reservoir of Ca and Mg on the continents: Implications for the oceanic Ca cycle: Earth and Planetary Science Letters, v. 247, no. 3–4, p. 267-279.

Tipper, E. T., Galy, A., Gaillardet, J., Bickle, M. J., Elderfield, H., and Carder, E. A., 2006b, The magnesium isotope budget of the modern ocean: Constraints from riverine magnesium isotope ratios: Earth and Planetary Science Letters, v. 250, no. 1–2, p. 241-253.

Tomascak, P. B., 2004, Developments in the Understanding and Application of Lithium Isotopes in the Earth and Planetary Sciences: Reviews in Mineralogy and Geochemistry, v. 55, no. 1, p. 153-195.

Tyrrell, T., and Zeebe, R. E., 2004, History of carbonate ion concentration over the last 100 million years: Geochimica et Cosmochimica Acta, v. 68, no. 17, p. 3521-3530.

Urey, H. C., 1947, The thermodynamic properties of isotopic substances: Journal of the Chemical Society (Resumed), no. 0, p. 562-581.

Vengosh, A., Starinsky, A., Kolodny, Y., Chivas, A. R., and Raab, M., 1992, Boron Isotope Variations during Fractional Evaporation of Sea-Water - New Constraints on the Marine Vs Nonmarine Debate: Geology, v. 20, no. 9, p. 799-802.

Warny, S., Askin, R. A., Hannah, M. J., Mohr, B. A. R., Raine, J. I., Harwood, D. M., Florindo, F., and Team, S. M. S. S., 2009, Palynomorphs from a sediment core reveal a sudden remarkably warm Antarctica during the middle Miocene: Geology, v. 37, no. 10, p. 955-958.

Weertman, J., 1961, Stability of Ice-Age Ice Sheets: Journal of Geophysical Research, v. 66, no. 11, p. 3783-3792.

Weertman, J., 1976, Milankovitch Solar-Radiation Variations and Ice Age Ice Sheet Sizes: Nature, v. 261, no. 5555, p. 17-20.

Wei, K.Y., and Kennett, J. P., 1986, Taxonomic evolution of Neogene planktonic foraminifera and paleoceanographic relations: Paleoceanography, v. 1, no. 1, p. 67-84.

Wieser, M. E., and Schwieters, J. B., 2005, The development of multiple collector mass spectrometry for isotope ratio measurements: International Journal of Mass Spectrometry, v. 242, no. 2–3, p. 97-115.

Wilson, D. S., Jamieson, S. S. R., Barrett, P. J., Leitchenkov, G., Gohl, K., and Larter, R. D., 2012a, Antarctic topography at the Eocene–Oligocene boundary: Palaeogeography, Palaeoclimatology, Palaeoecology, v. 335–336, no. 0, p. 24-34.

Wilson, G. S., Levy, R. H., Naish, T. R., Powell, R. D., Florindo, F., Ohneiser, C., Sagnotti, L., Winter, D. M., Cody, R., Henrys, S., Ross, J., 2012b, Neogene tectonic and climatic evolution of the Western Ross Sea, Antarctica — Chronology of events from the AND-1B drill hole: Global and Planetary Change, v. 96–97, no. 0, p. 189-203.

Wilson, D. S., and Luyendyk, B. P., 2009, West Antarctic paleotopography estimated at the Eocene-Oligocene climate transition: Geophysical Research Letters, v. 36, DOI: 10.1029/2009GL039297

Wilson, D. S., Pollard, D., DeConto, R. M., Jamieson, S. S. R., and Luyendyk, B. P., 2013, Initiation of the West Antarctic Ice Sheet and estimates of total Antarctic ice volume in the earliest Oligocene: Geophysical Research Letters, v. 40, no. 16, p. 4305-4309.

Wimpenny, J., Colla, C. A., Yin, Q.-Z., Rustad, J. R., and Casey, W. H., 2014, Investigating the behaviour of Mg isotopes during the formation of clay minerals: Geochimica et Cosmochimica Acta, v. 128, no. 0, p. 178-194.

Wombacher, F., Eisenhauer, A., Böhm, F., Gussone, N., Regenberg, M., Dullo, W. C., and Rüggeberg, A., 2011, Magnesium stable isotope fractionation in marine biogenic calcite and aragonite: Geochimica et Cosmochimica Acta, v. 75, no. 19, p. 5797-5818.

Woodruff, F., and Savin, S. M., 1991, Mid-Miocene Isotope Stratigraphy in the Deep Sea: High-resolution correlations, paleoclimatic cycles, and sediment preservation: Paleoceanography, v. 6, no. 6, p. 755-806.

Woodward, F. I., 1987, Stomatal numbers are sensitive to increases in CO_2 from pre-industrial levels: Nature, v. 327, no. 6123, p. 617-618.

Woodward, R. S., 1888, On the form and position of mean sea level: United States Geological Survey Bulletin, v. 48, p. 87-170.

Wright, J. D., Miller, K. G., and Fairbanks, R. G., 1992, Early and Middle Miocene stable isotopes: Implications for deepwater circulation and climate: Paleoceanography, v. 7, no. 3, p. 357-389.

You, C.F., and Chan, L.-H., 1996, Precise determination of lithium isotopic composition in low concentration natural samples: Geochimica et Cosmochimica Acta, v. 60, no. 5, p. 909-915.

You, Y., Huber, M., Muller, R. D., Poulsen, C. J., and Ribbe, J., 2009, Simulation of the Middle Miocene Climate Optimum: Geophysical Research Letters, v. 36, DOI: 04700.01029/02008GL036571.

You, C.F., Spivack, A. J., Smith, J. H., and Gieskes, J. M., 1993, Mobilization of boron in convergent margins: Implications for the boron geochemical cycle: Geology, v. 21, no. 3, p. 207-210.

Yu, J.M., Thornalley, D., Rae, J., and McCave, N., 2013, Calibration and application of B/Ca, Cd/Ca, and $\delta^{11}B$ in *Neogloboquadrina pachyderma (sinistral)* to constrain CO_2 uptake in the subpolar North Atlantic during the last deglaciation: Paleoceanography, v. 28, no. 2, p. 237-252.

Yu, J. M., and Elderfield, H., 2007, Benthic foraminiferal B/Ca ratios reflect deep water carbonate saturation state: Earth and Planetary Science Letters, v. 258, no. 1-2, p. 73-86.

Yu, J. M., Elderfield, H., and Honisch, B., 2007, B/Ca in planktonic foraminifera as a proxy for surface seawater pH: Paleoceanography, v. 22, no. 2, DOI: 10.1029/2006PA001347.

Yu, J. M., Foster, G. L., Elderfield, H., Broecker, W. S., and Clark, E., 2010, An evaluation of benthic foraminiferal B/Ca and delta B-11 for deep ocean carbonate ion and pH reconstructions: Earth and Planetary Science Letters, v. 293, no. 1-2, p. 114-120.

Zachos, J., Pagani, M., Sloan, L., Thomas, E., and Billups, K., 2001a, Trends, rhythms, and aberrations in global climate 65 Ma to present: Science, p. 686-693.

Zachos, J., Shackleton, N., Revenaugh, J., Palike, H., and Flower, B., 2001b, Climate response to orbital forcing across the Oligocene-Miocene boundary: Science, p. 274-278.

Zachos, J. C., Dickens, G. R., and Zeebe, R. E., 2008, An early Cenozoic perspective on greenhouse warming and carbon-cycle dynamics: Nature, v. 451, no. 7176, p. 279-283.

Zachos, J. C., Flower, B. P., and Paul, H., 1997, Orbitally paced climate oscillations across the Oligocene/Miocene boundary: Nature, v. 388, no. 6642, p. 567-570.

Zeebe, R. E., 2005, Stable boron isotope fractionation between dissolved $B(OH)_3$ and $B(OH)_4^-$: Geochimica et Cosmochimica Acta, v. 69, no. 11, p. 2753-2766.

Zeebe, R. E., and Wolf-Gladrow, D. A., 2001, CO_2 in seawater, equilibrium, kinetics, isotopes IN Elsevier oceanography series, Amsterdam, PAYS-BAS, Elsevier, XIII.

Zeebe, R. E., Wolf-Gladrow, D. A., Bijma, J., and Honisch, B., 2003, Vital effects in foraminifera do not compromise the use of $\delta^{11}B$ as a paleo-pH indicator: Evidence from modeling: Paleoceanography, v. 18, no. 2, DOI: 10.1029/2003PA000881.

Zeeden, C., Hilgen, F., Westerhold, T., Lourens, L., Röhl, U., and Bickert, T., 2013, Revised Miocene splice, astronomical tuning and calcareous plankton biochronology of ODP Site 926 between 5 and 14.4 Ma: Palaeogeography, Palaeoclimatology, Palaeoecology, v. 369, no. 0, p. 430-451.

Zhang, C., Wang, Y., Deng, T., Wang, X., Biasatti, D., Xu, Y., and Li, Q., 2009, C4 expansion in the central Inner Mongolia during the latest Miocene and early Pliocene: Earth and Planetary Science Letters, v. 287, no. 3–4, p. 311-319.

Zhang, Y. G., Pagani, M., Liu, Z. H., Bohaty, S., and DeConto, R., 2013, A 40-million-year history of atmospheric CO_2: Philosophical Transactions of the Royal Society A: Mathematical, Physical and Engineering Sciences, v. 371, no. 2001. DOI: 10.1098/rsta.2013.0096.

Zhu, P., and Macdougall, J. D., 1998, Calcium isotopes in the marine environment and the oceanic calcium cycle: Geochimica et Cosmochimica Acta, v. 62, no. 10, p. 1691-1698.